VIRUS MITIGATION USING CONVENTIONAL CHEMICAL COAGULATION AND ELECTROCOAGULATION: CHEMISTRY AND VIRAL COMPONENT ALTERATIONS

A Dissertation

by

KYUNGHO KIM

Submitted to the Graduate and Professional School of
Texas A&M University
in partial fulfillment of the requirements for the degree of

DOCTOR OF PHILOSOPHY

Chair of Committee,	Shankar Chellam
Committee Members,	Arthur Laganowsky
	Hongmin Qin
	Zong Liu
Head of Department,	Zachary Grasley

December 2021

Major Subject: Civil Engineering

ABSTRACT

This research investigates virus behavior during coagulation processes including conventional chemical coagulation with $Al_2(SO_4)_3$ or $FeCl_3$, and electrocoagulation (EC) with sacrificial elemental Al or Fe anodes focusing on viral component alterations. Bacteriophages MS2 and ϕ6 were employed as surrogates for non-enveloped and enveloped viruses, respectively.

Iron EC was shown to simultaneously remove (via sweep flocculation) and inactivate a non-enveloped virus surrogate (MS2) especially under slightly acidic conditions resulting in highly effective virus control. MS2 phages are shown to be removed/inactivated via the plaque assay using their bacterial host *Escherichia coli* and via the reverse transcription quantitative polymerase chain reaction (RT-qPCR). In addition to these existing means of assessing virus mitigation, a novel technique of correlating transmission electron micrographs of electrocoagulated MS2 with their computationally altered 3-dimensional electron density maps was developed to provide direct visual evidence of capsid morphological damages during electrocoagulation.

Additionally, the extent and mechanisms of removal and/or inactivation of the enveloped bacteriophage ϕ6 by conventional $FeCl_3$ coagulation and iron EC were evaluated. Both coagulation methods appeared to be highly effective in controlling enveloped viruses during surface water treatment. ϕ6 phage adhesion to freshly precipitated iron (hydr)oxide was accompanied by envelope damage causing inactivation in both coagulation techniques. Fourier transform infrared spectroscopy revealed oxidative damages to ϕ6 lipids only for electrocoagulation consistent with electro-Fenton reactions, since both Fe(II) and H_2O_2 were detected in the bulk solution. Monitoring ϕ6 dsRNA by a novel reverse transcription quantitative polymerase chain reaction method quantified significantly lower viral removal/inactivation compared with the plaque assay

demonstrating that relying solely on RT-qPCR assays may overstate human health risks arising from viruses. Transmission electron microscopy and computationally generated electron density maps of ϕ6 showed severe morphological damages to virus' envelope and loss of capsid volume accompanying coagulation.

Further, the behavior of both MS2 and ϕ6 in four different coagulation approaches (iron electrocoagulation, iron conventional coagulation, aluminum conventional coagulation, and aluminum electrocoagulation) were compared. Infectivity of the MS2 phage was shown to persist during conventional iron and aluminum coagulation and aluminum electrocoagulation but not iron electrocoagulation. The ϕ6 phage was vulnerable to any type of coagulation, resulting in damages to its lipid envelope and nucleocapsid. Iron electrocoagulation compromised the structure of both phages, potentially via the electro-Fenton mechanism.

In addition to the virus research described above, microfiltration of *Acholeplasma laidlawii* was also empirically investigated to evaluate potential effects of cell deformability on membrane fouling and retention. This work demonstrated worse fouling due to "soft" particle penetration and cake compression compared with rigid silica particles of similar size and concentration.

DEDICATION

먼 곳에서 항상 나를 응원해준

사랑하는 나의 가족에게,

그리고 훗날

이 시간을 항상 기억할 내 자신에게

To my family who has been in my heart all the time,

and to myself who will always remember this moment

ACKNOWLEDGEMENTS

There used to be a lot to say, but it is not so easy for me to write all down well. Taking an opportunity to dedicate this section for acknowledgements, I would like to express my gratitude to all those who helped me complete my doctoral training.

First and foremost, I must give the greatest appreciation to my advisor, Dr. Shankar Chellam. From the moment I joined his lab, he has always given me honest evaluation and advices, for which I sometime felt too direct. However, as he said to me one day that he would rather be a tough advisor than an 'easy' advisor if necessary to make his students fully ready for their next career, I do not question his true intention to complete me as a highly competent researcher by having me objectively realize where I am and by pushing me to the limit. Owing to all these support and advice, I have been able to reach where I am standing now. Also, while I was working with him, I could witness what is being professional and what is required to become professional. His unlimited endeavor as a teacher, a researcher, and an advisor was far beyond being enough to inspire me. I would like to thank him again for his dedication to train me as a researcher. Someday in my life, I hope to become a such person to someone.

I also express my appreciation to committee members, Dr. Arthur Laganowsky, Dr. Hongmin Qin, and Dr. Zong Liu for sparing their precious time out of their busy schedules to provide me with valuable comments and guidance to improve my doctoral research.

Whenever I was going through a hard time, I used to recall what Dr. Mutiara Ayu Sari told us in her last lab meeting, 'never give up, Dr. Chellam is there to help you'. She may not even remember, but this single sentence has been a great cheer and support to me. Although I did not

spend much time together with Darpan Chorghe, his bright personality was always joyful to everyone.

I should not omit my battle buddies, Sourav Das, Dr. Kunal Gupta, and Bilal Abada, who joined the group almost together with me. I have learned many things from them. I will never forget this time we went through together. There has been countless moments I would like to mention, but I will save them for the future. Without these friends, I would have not been able to complete the training. Sadly, we will be in different places soon pursing each one's dream. I hope we all will succeed in what we do, and reunite someday with big smiles. Samantha Wilson, who worked with me as an undergraduate student on membrane experiments, also should be acknowledged for her assistance and dedication to research.

Dr. Anindito Sen and Dr. Jothikumar Narayanan provided me with astonishingly fruitful discussion as well as technical support. It was a unique opportunity to work with Dr. Narayanan at Centers for Disease Control and Prevention for genome assay. Also, Dr. Sen helped me introduce electron micrograph and image analysis to analyze the virus behavior, which is a novel approach in environmental engineering field.

Lastly, I would like to thank my brother Kyungmin Kim for his support and sacrifice. He strongly encouraged me to go for doctoral degree if I truly wanted it. He stayed in Korea taking care of our parents so that I could fully focus on my degree course.

CONTRIBUTORS AND FUNDING SOURCES

Contributors

This work was supervised by a dissertation committee consisting of Professor Shankar Chellam (advisor) and Professor Arthur Laganowsky of the Department of Chemistry and Professor Hongmin Qin of the Department of Biology and Professor Zong Liu of the Department of Biological and Agricultural Engineering.

All work for the dissertation was completed independently by the student.

Funding Sources

This work was made possible in part by National Science Foundation (Grant number CBET 1605088). Its contents are solely the responsibility of the authors and do not necessarily represent the official view of the sponsor.

TABLE OF CONTENTS

Page

ABSTRACT ii

DEDICATION iv

ACKNOWLEDGEMENTS v

CONTRIBUTORS AND FUNDING SOURCES vii

TABLE OF CONTENTS viii

LIST OF FIGURES xi

LIST OF TABLES xix

CHAPTER I INTRODUCTION 1

- Introduction 1
- Research goal and objectives 3
- Dissertation organization 4

CHAPTER II VIRUS REMOVAL AND INACTIVATION MECHANISMS DURING IRON ELECTROCOAGULATION: CAPSID AND GENOME DAMAGES AND ELECTRO-FENTON REACTIONS 6

- Introduction 6
- Materials and methods 8
  - Phage preparation, enumeration, and analysis 8
  - Electrocoagulation 9
  - Electron microscopy 10
  - ATR-FTIR and RT-qPCR protocols 10
- Results and discussion 11
  - Virus removal and inactivation at different pH 11
  - Direct evidence for capsid damage 13
  - Protein oxidation and alterations to secondary structures 18
  - Identifying clues to intermediate species responsible for inactivation 20
- Conclusions 23

CHAPTER III REMOVAL AND INACTIVATION OF AN ENVELOPED VIRUS SURROGATE BY IRON CONVENTIONAL COAGULATION AND ELECTROCOAGULATION 26

Introduction 26
Materials and methods 27
ϕ6 preparation and enumeration 27
TaqMan assay design 28
RT-qPCR assay 29
Microscopy and spectroscopy 30
Coagulation 30
Iron and hydrogen peroxide measurement 31
Results and discussion 32
Infective virus control by conventional- and electrocoagulation 32
Conventional coagulation and electrocoagulation damage ϕ6 structure 34
Coagulation alters ϕ6 biochemical composition 38
Viral RNA loss during coagulation 42
Electro-Fenton reactions during electrocoagulation 44
Conclusions 44

CHAPTER IV VIRUS MITIGATION USING CONVENTIONAL COAGULATION AND ELECTROCOAGULATION: COMPARISION OF NON-ENVELOPED AND ENVELOPED VIRUS 46

Introduction 46
Materials and methods 47
Virus stock preparation 47
Coagulation experiment 48
Transmission electron microscopy. 49
Fourier-transformed infrared spectroscopy 50
Results and discussion 50
Al and Fe (electro)coagulation of non-enveloped and enveloped virus 50
Virus removal and inactivation during coagulation. 53
Viral morphology alteration induced by coagulation 55
Spectral investigation of viral deformation/transformation upon coagulation 63
Conclusions 66

CHAPTER V REJECTION AND FOULING OF *ACHOLEPLASMA LAIDLAWII* DURING MICROFILTRATION 68

Introduction 68
Materials and methods 69
Preparation and quantification of *A. laidlawii* and silica particles 69
Membranes 71
Filtration experiment 72
Data process for blocking laws analysis 72

Sample preparation for SEM analysis..... 73
Results and discussion 74
Penetration of *A. laidlawii* cells through sterilizing-grade filters..... 74
Worsened fouling by *A. laidlawii* cells compared with silica particle 76
Identification of blocking mechanisms using integrated blocking models..... 78
Compressible cake of *A. laidlawii* cells..... 86
Conclusions.....87

CHAPTER VI CONCLUSIONS AND RECOMMENDATIONS FOR FUTURE WORK ...89

Conclusions.....89
Recommendations for future work 90
Optimization of iron EC process in complex water matrices 90
Investigation on other viruses..... 90

REFERENCES 92

APPENDICES 115

Supporting information for chapter II.....115
Supporting information for chapter III 148
Supporting information for chapter IV 159

LIST OF FIGURES

Page

Figure II-1. Temporal concentration profiles of infective MS2 virions in bulk water (A and C) and those extracted from flocs (B and D) at different total iron dosages (5 mg/L, 10 mg/L, and 20 mg/L corresponding to electrolysis times of 78 s, 156 s, and 312 s, respectively as shown in Section A4) and pH values (6.4 and 8.2) measured via the plaque assay. The entire EC experiment i.e. electrolysis + flocculation lasted 2 hours. Virus extraction from flocs is described in Section A5. 12

Figure II-2. (A) Transmission electron micrograph of untreated MS2 phage (scale bar equals 10 nm and applies to B and C as well), (B) computationally-filtered image of A depicting the gray-value profile, (C) Gaussian fitting of the gray-value profile and reading of full-width at half maximum (FWHM) values as capsid thicknesses. Note that the gray profile values (i.e., y-axis of bottom right panel) is arbitrary. Original TEM image is shown in Figure A-9A. 14

Figure II-3. (A) Electron micrograph of MS2 phages damaged by EC (pH 6.4, 10 mg/L total iron, 120 minutes) at 70,000X magnification. The black arrow shows a MS2 particle that has lost ~50% of the capsid protein. The white arrows point to other virions that were damaged to a smaller extent (~ 10%). Scale bar in (A) equals 50 nm. [B, C, and D] explain the capsid damage quantification procedure. (B) shows a boxed-out damaged virion as an example taken from Figure A-9B (scale bar in (B) is 10 nm), (C) shows a series of projection images of the band-pass computationally-altered electron density map of MS2 with the yellow-circle being the view that best matches the image in B (black vertical scale bar on the left in (C) is 50 nm). (D) is the corresponding 3D electron density map of the damaged particle in (B) (scale bar in (D) is 10 nm). 15

Figure II-4. Damaged MS2 after EC (pH 6.4, 10 mg/L total iron, 120 minutes) are shown in the first row with damages to protein capsids marked with yellow arrows [A – G]. The second row shows corresponding computationally-altered electron density maps [A1 – G1] used to quantitatively analyze structural damages. In other words, A1 is the electron density map of A and so on. A 10 nm scale bar is shown only on the top row leftmost image, which applies to all images in the first two rows. The bottom row shows frequency distributions of digitally measured capsid thicknesses. (H) depicts a monomodal distribution with an average of 2.3 nm for untreated MS2 (60 virions analyzed). (I) depicts a bimodal distribution after EC (50 damaged virions analyzed). Gaussian distributions were fitted to calculate statistical properties of capsid thickness (average and standard deviation). Original TEM is shown in Figure A-9B. 17

Figure II-5. Left panel (A) shows ATR-FTIR spectra of untreated MS2 (top, black color) and electrocoagulated MS2 at pH 6.4, 120 minutes, 10 mg/L total iron dosage (bottom, red color). Only representative peaks appearing in EC-treated viruses are shown (see Figure A-14 for complete identification). Right panel (B) compares relative areas of secondary structures of untreated and electrocoagulated MS2. 19

Figure II-6. Total infective MS2 in control experiments after adding Fe(II) (blue curve) and Fe(III) (red curve) salts and comparison with EC (green curve) at 10 mg/L total iron and pH 6.4 measured using the plaque assay. EC data shown here are the sum of data shown earlier in Figure II-1A and 1B. Figure A-17 depicts the same infective virus data separately as those extracted from the flocs and the bulk water..... 21

Figure II-7. (A) Total iron and Fe(II) concentrations during EC (B) H_2O_2 production (detection limit = 170 μg/L) and dissipation at different pH at a target total iron dosage of 10 mg/L. 22

Figure III-1. Facile reduction of ϕ6 by both electrocoagulation and conventional chemical coagulation at 10 mg Fe/L, pH 6.4, and N_0 ~10^8 PFU/mL. Error bars represent one standard deviation of a minimum of four measurements. The left panel (A) denotes viruses in the bulk water. Very few infective viruses were recovered from the flocs, which continuously declined over time (B, right panel). 33

Figure III-2. (A) TEM of complete native ϕ6 (black arrows), nucleocapsids (yellow arrows) and innermost capsid (red arrow) in the left panel. (B) boxed-out images of a native ϕ6, (E) the nucleocapsid and (H) the innermost capsid. The gray scale plots show the density distribution along the lines drawn through the boxed-out particles (C, F, I). The black arrowheads represent the edges of the particles providing us their size shown in (B, E, H). Size distributions of native viruses (n=100), nucleocapsids (n=32), and inner capsids (n=30) are shown on the rightmost panels (D), (G), and (J), respectively, where n is the number of particles analyzed. The mean and standard deviation are shown in each panel. Scale bars: (A) 100 nm and (B, E, H) 20 nm. 34

Figure III-3. (A) Image of iron flocs distributed on the TEM grid surface. (B) TEM image of a group of damaged ϕ6 particles trapped in the iron floc after 2.6 minutes appearing in lighter color with yellow arrows pointing to damaged phages. Scale bars: 100 nm. 35

Figure III-4. TEM images of native, conventionally coagulated, and electrocoagulated damaged ϕ6 particles are shown in (A), (E) and (I), respectively (coagulation was performed for 2.6 minutes). The image on the top left shows the multi-layer structure of intact virions (marked with white arrows). Scale bar: 100 nm. (B), (F) and (J) represent the

boxed out native, conventionally coagulated and electrocoagulated damaged ϕ6 particles with lines drawn across them showing the position the gray scale profiles generated. Scale bar: 20 nm. (C), (G) and (K) represent gray scale profiles corresponding to the boxed out particle on their left. The two valleys, marked with black arrows confirm the presence of nucleocapsid and inner capsid layers. (D) Iso-surface representation of electron density map of native bacteriophage ϕ6 (EMD-1301). Altered electron density maps of ϕ6 shown in (H) and (L) represent the 3D structures that matches best to (F) and (J) respectively. Scale bar: 10 nm. (M) and (N) shows computationally analyzed capsid volume damage induced by conventional and electrocoagulation, respectively obtained by analyzing 70 viruses in each case. 37

Figure III-5. FTIR spectra of native (top, brown color), conventionally coagulated (middle purple color), and electrocoagulated (bottom, orange color) ϕ6 after 2.6 minutes. See Table A-7 for comprehensive peak assignment. 40

Figure III-6. Coagulation (10 mg Fe/L at pH 6.4) effects on RNA recovery from bulk water (left panel, A) and flocs (right panel, B). Error bars represent one standard deviation of a minimum of four measurements. Our RT-qPCR assay only targets a short region (0.5%) of the ϕ6 genome. N_0 is the number of viral particles (expressed as RNA copies) in the bulk water initially spiked to the experimental set-up. 43

Figure IV-1. Coagulation of MS2 and ϕ6 with $Al_2(SO_4)_3$, $FeCl_3$, Al electrocoagulation, and Fe electrocoagulation at 0.18 mM Al or Fe and pH 6.4. Infective virus concentration in bulk water was normalized by initial bulk concentration, N_0. Negative controls (black solid lines) ensured that only coagulant addition was attributed to decline of infective virus fraction. 51

Figure IV-2. Inactivation of MS2 ϕ6 during the course of coagulation process. Total infective virus concentration (bulk water + flocs) was normalized by initial bulk concentration, N_0. 53

Figure IV-3. Electron micrographs of untreated viruses. Intact MS2 virions show a single layer of protein capsid (A, scale: 50 nm). Hexagonal structure of representative MS2 virions confirm their icosahedral capsids (A1-A3, shared scale: 10 nm). Intact ϕ6 virions appear to have a layered-structure (B, scale: 100 nm) with a hexagon inside (B1-B3, shared scale: 25 nm). 56

Figure IV-4. (A-D) Electron micrographs of MS2 virions after each coagulation treatment as labeled (scale bar equals 50 nm and shared with A-D). (E) enlarges the yellow-boxed area in (D), and is followed by (F) which is a computationally-simulated damaged structure of a yellow-circled MS2 particle in (E). Scale bars in (E) and (F) equal 10

nm. (G) and (H) depict capsid thickness (20 ~ 30 virions analyzed for each case) and remaining capsid volume distribution of untreated and coagulated MS2 (15 ~ 25 virions analyzed for each case), respectively. 58

Figure IV-5. Large-view electron micrographs of ϕ6 particles after each coagulation treatment as labeled (first column, A1-D1, shared scale: 100 nm) followed by enlarged-view to probe morphological changes (second column, A2-D2, shared scale: 50 nm) and computationally-generated best-matching damaged particles circled in yellow in A2-D2 to confirm and quantify nucleocapsid damage (third column, A3-D3, shared scale: 10 nm). 61

Figure IV-6. FTIR spectra of untreated and coagulated viruses, MS2 (A) and ϕ6 (B). Changes in relative amount of secondary structures of MS2 (C) and ϕ6 (D). 64

Figure V-1. Scanning electron micrograph of unpressurized A. laidlawii cells (A), silica particles (B), and 0.2 (C) and 0.1 μm rated track-etched membrane filters (D). All scale bars equal 200 nm. It is noted that the fraction of multiples are exaggerated in these micrographs. See Table 1 for the pore characterization results. 70

Figure V-2. Distribution of equivalent pore diameter of membranes (4439 and 2622 pores were analyzed for 0.1 and 0.2 μm-rated membrane, respectively) and particles (55 and 100 particles were analyzed for A. laidlawii and silica colloid, respectively). Both types of particles were found to be virtually bigger than pores. 71

Figure V-3. Log removal of A. laidlawii cells under various filtration conditions (A), and a comparison of log-removal values in this study with previous results (B). The results of this study (black symbols) in (B) are the average of log removals during the filtration shown in (A). In (B), filtration pressures and pore sizes are denoted in units of kPa and μm, respectively. Also, the average size of *A. laidlawii* cells are presented near the symbols in matching colors. 74

Figure V-4. Scanning electron micrographs of the permeate side of 0.2 μm (A) and 0.1 μm rated (B) membranes. Severely deformed bacterial cells near the pores (yellow arrows) were observed. Scale bars equal 200 nm. 75

Figure V-5. Normalized flux decline profiles of *A. laidlawii* and silica particles under different conditions. 77

Figure V-6. Model predictions on filtrate volume using integrated form models in three different scenarios in comparison with experimental data. 81

Figure V-7. Comparison of blocking laws analysis using integral and differential approaches. . 82

Figure V-8. Comparison of blocking parameters obtained by integral approach and differential approach. 84

Figure V-9. Model predictions on filtrate volume using sequential integral and differential approaches in comparison with experimental data. 85

Figure V-10. Characterization of cakes formed by A. laidlawii cells and silica particles. Specific cake resistance of silica colloids (A) and A. laidlawii cells (B). The dashed-lines shown in (A) represent the 95 % confidence band. 87

Figure A-1. Linear relation between log plaque counts and log dilution factors was only valid when plaque count was more than 10 PFU for both assays. The bulk water data are shown on the left panel and results from the flocs are on the right panel. Individual symbols represent plaque counts from different plates. 116

Figure A-2. Strong evidence of Fe(II) production during electrocoagulation via excellent agreement between Faraday's law and experimental measurements of total iron in all cases. A 2-electron transfer quantitatively explains our experimental observations without any fitting demonstrating anodic oxidation produces Fe(II). 119

Figure A-3. Complete recovery of MS2 phages using 6 % beef extract solution from iron flocs generated with $FeCl_3$ at all dosages used in this study at pH 6.4 (A) and 8.2 (B). It is noted that the phages were extracted at the end of flocculation (t= 120 min). *t* test between sorbed and recovered phage concentrations indicated insignificant differences at all conditions. 121

Figure A-4. Time series of MS2 recovery from the flocs at pH 6.4 when 10 mg/L Fe was added as $FeCl_3$. t test between sorbed and recovered phage concentrations indicated insignificant differences at all time points. 121

Figure A-5. Standard curve of MS2 RNA RT-qPCR. 124

Figure A-6. Comparison of log-reduction in bulk water at the end of flocculation (t= 120 min) in EC and $FeCl_3$ coagulation at pH 6.4 (A), at pH 8.2 (B), and the relative reduction between EC and $FeCl_3$ calculated by dividing EC reductions by $FeCl_3$ reductions (C). The *t* test performed between EC and $FeCl_3$ (n= 3 ~ 6, $p < 0.05$ for statistically significant difference) at each dose revealed that mean reductions were statistically different at all doses at pH 6.4 whereas EC and $FeCl_3$ did not show significant differences at pH 8.2. 126

Figure A-7. Visualization of phages captured by iron flocs at 10 mg/L total iron and pH 6.4 (A) along with various controls (B), (C), and (D). Bright field images and corresponding fluorescence images (excitation at 480 nm and emission at 510 nm, exposure time 200 ms) are shown next each other. 128

Figure A-8. Duplication of Figure A-7 at 10 mg/L total iron and pH 8.2. Microscopic analysis details are same as the previous figure. 129

Figure A-9. Representative TEMs of untreated (A) and electrocoagulated MS2 (B). Scale bars equal 50 nm. The white arrows with labels in Figure A-9B depict the particles that were chosen to be represented in the main manuscript. Particle 'b' is represented in Figure II-3B, and particles 'a-g' were used for the boxed-out images in Figure II-4A-4G matching the alphabetical sequence. 130

Figure A-10. Electron micrograph of electrocoagulated MS2 phages. MS2 particles with deformed/damaged capsids are shown in the white circle while severely damaged particles are pointed by white arrows. 130

Figure A-11. Visualization of phages in iron flocs with low (A) and high defocusing (B). The use of high defocusing generated electron micrographs that clearly differentiated relatively intact virion (green-dotted circle) and structurally-deformed virions (red-dotted circles). Scale bars equal 50 nm. 131

Figure A-12. Artifactual effect of defocusing on capsid thickness measurement. 132

Figure A-13. Reproducibility of FTIR spectrum of untreated (A), chemically coagulated (B), and electrocoagulated MS2 (C). Correlation coefficient among replicated spectra were found to be 0.88-0.96, 0.78, and 0.73 for untreated MS2, after $FeCl_3$, and after EC, respectively. 134

Figure A-14. Comparison of untreated and coagulated MS2 with complete peak identifications. 135

Figure A-15. Decomposition of FTIR spectrum of untreated (A), $FeCl_3$ coagulated (B), and electrocoagulated MS2 (C)..... 137

Figure A-16. Comparison of relative secondary structure areas before and after conventional coagulation and electrocoagulation. 137

Figure A-17. Comparison of infective virus concentration profiles by $FeCl_2$, $FeCl_3$, and electrocoagulation. Experimental conditions were pH 6.4 and 10 mg/L total iron dosage. 139

Figure A-18. Dissolved oxygen consumption under various conditions at total iron dosage of 10 mg/L. 140

Figure A-19. Negligible effect of DMSO (25 mM) on MS2 control by EC at pH 6.4 and 10 mg/L total iron. 141

Figure A-20. Total inactivation of MS2 phages during EC at pH 6.4 and pH 8.2. 142

Figure A-21. Negligible effect of $^{\bullet}O_2^-$ on MS2 inactivation during EC (pH 6.4, 10 mg/L total iron) proven by addition of superoxide dismutase. 143

Figure A-22. Negligible effect of H_2O_2 on MS2 phage inactivation. 144

Figure A-23. Suppression of virus inactivation due to Fe(II) complexation with 1,10-phenanthroline (4.4 mM) and deaeration in (A) $FeCl_2$ and (B) EC. 144

Figure A-24. Inhibition of MS2 inactivation by Na_2SO_3 in EC when 10 mg/L total iron was targeted at pH 6.4. 145

Figure A-25. RNA measured in bulk water (left panel, A) and flocs (right panel, B) during EC. Error bars are one standard deviation of at least four measurements. N_0 is the number of RNA copies measured immediately after adding viruses to the EC apparatus..... 146

Figure A-26. Standard curve of RT-qPCR. 149

Figure A-27.Negligible impact of Na_2SO_3 on ϕ6 infectivity. 152

Figure A-28. Segmentation of electron density map of intact ϕ6 (after computationally removing the outermost lipid layer) with accession number EMD-1301 (https://www.emdataresource.org/). (A) Electron density map of intact ϕ6 nucleocapsid (vertical scale bar: 60 nm). (B) Side views and tilted views of computationally altered maps. 153

Figure A-29.Example of computational image analysis to quantitatively assess damages induced by electrocoagulation (black scale bar in bottom panel of (B): 100 nm). 154

Figure A-30. Decomposition of amide I region for protein secondary structure relative amount of native (A), and after conventional coagulation (B) and electrocoagulation (C). 157

Figure A-31. Comparison of relative amount of protein secondary structure before and after conventional coagulation and electrocoagulation. 157

Figure A-32. Al(III) and Fe(II) generation during the electrolysis of Al^0 and Fe^0 anode for electrocoagulation. It is noted that the different current density of 4.2 and 2.8 mA/cm2 was applied for Al and Fe electrocoagulation, respectively to introduce Al(III) and Fe(II) at the same molar concentration rate of 1.15 μM/s. 159

Figure A-33. Temporal profiles of infective virus fractions extracted from Al or Fe flocs 160

Figure A-34. MS2 capsid thickness measurement protocol. 161

Figure A-35. Computationally analyzed remaining capsid volume after each coagulation approach. 20~25 virions were used for each case. 162

Figure A-36. Amide I peak decomposition to calculate relative amount of protein secondary structures. 164

LIST OF TABLES

Page

Table V-1. Summary of membrane characterization. 71

Table V-2. Summary of blocking laws models used in this study..... 79

Table V-3. Summary of blocking laws analysis results using integrated form models..... 80

Table A-1. Comparison of experimental set-ups and conditions for electrocoagulation of various target contaminant. 117

Table A-2. Identified FTIR band positions and corresponding assignments..... 135

Table A-3. Comparison of secondary structure relative areas of untreated and coagulated MS2 phage. 138

Table A-4. Summary of electrochemical reactions in EC. 147

Table A-5. Similarity between two approaches to calculate log reductions. High linearities ($r \geq 0.94$) demonstrated that both approaches generate statistically identical log reduction values in this study. 150

Table A-6. Summary of reproducibility estimation. 150

Table A-7. Summary of FTIR band identification, assignments, and contributors. 155

Table A-8. Comparison of secondary structure relative areas of native and coagulated ϕ6..... 158

Table A-9. Summary of FTIR peak assignment and contributor. 163

CHAPTER I

INTRODUCTION

Introduction

Enteric viruses are pathogens of concern for drinking water treatment as they have been known to cause chronic diseases as well as gastric and respiratory symptoms [1], several of which have been identified as etiological agents associated with drinking water outbreaks [2]. Indeed, The Centers for Disease Control and Prevention has estimated that roughly 8% of all waterborne disease outbreaks associated with drinking water reported in the United States from 1971 to 2006 are attributed to viruses [2, 3]. Moreover, some enteric viruses show low infectious doses and/or high tolerance to harsh environments including conventional water treatment [1, 4]. Inclusion of four enteric viruses in Contaminant Candidate List 4 (CCL4) as emerging pathogenic agents also emphasizes the importance of enteric virus control in drinking water treatment by removing and/or inactivating them [5].

In conventional drinking water treatment, chemical coagulation is used to destabilize and aggregate suspended colloids into larger particles for the effective removal in subsequent sedimentation and filtration processes [6-8]. Electrocoagulation (EC) is an emerging technology as an alternative to convention chemical coagulation wherein a sacrificial anode is oxidized to add hydrolyzing metal ions such as iron or aluminum *in-situ* which reduces the risk of transporting, storing and handling corrosive chemicals required for conventional coagulation. Moreover, other advantages such as portability, low alkalinity consumption, easy automation, and suitability for packaged plant bring attention to EC technology [9-12].

Previous studies have shown that viruses can be effectively controlled by EC achieving more than 4-log removal/inactivation [7, 13-15]. Mechanistic studies have shown that during aluminum and iron EC, viruses are not only removed by Al/Fe precipitates but also inactivated by other electrochemically-produced species [13-16]. Free chlorine production during the electrolysis of Al anode was found to be responsible for virus inactivation in aluminum EC of saline water [16]. For iron EC, evidence has been presented that Fe(II) oxidation by dissolved oxygen is involved in viral inactivation [14, 15]. Nonetheless, to the best of our knowledge, no studies so far have provided any mechanistic information on aqueous phase reactive intermediates or modifications to virus structure, proteins, or genome [15, 17].

Meanwhile, the behavior of enveloped viruses during water and wastewater treatment including coagulation has not gained much attention presumably due to the common belief that these viruses normally do not persist in water [18-20]. However, recent evidence points to enveloped mammalian viruses and bacteriophages remaining infectious in surface water and sterilized sewage for several days [21-24] necessitating more attention on the fate of these viruses in contaminated water supplies and their behavior during water treatment. In addition, previous studies on the control of enveloped viruses in water and wastewater have largely focused on chemical disinfection, which justifies the need of pursuing research on their behavior during coagulation, which might serve as another barrier during water purification.

Another topic pursued was the bacterial fouling of microfiltration membranes and cell passage across filters with pore diameters smaller than the cell size.

Research goal and objectives

The overall goals of my research are to understand the fundamentals of microorganism behavior in two specific water treatment processes including (1) virus behavior during conventional chemical coagulation and electrocoagulation and (2) bacterial fouling of microfiltration membranes. The overarching hypothesis of the virus research is that, in addition to physical removal of viruses via sorption onto aluminum and iron flocs, viruses are inactivated by these flocs and/or *in-situ* generated virucidal species such as reactive oxygen species (ROS). Bacterial filtration research is based on the hypothesis that deformable cells will worsen fouling compared with rigid particles of similar size.

The specific research objectives were:

a. Identify virus control mechanisms during iron EC and compare with conventional $FeCl_3$ coagulation using the non-enveloped bacteriophage MS2 and investigate changes in viral components.

b. Compare the efficacy of conventional $FeCl_3$ coagulation and iron EC to attenuate the enveloped bacteriophage ϕ6 with respect to removal and inactivation and investigate associated mechanisms.

c. Compare the behavior of MS2 and ϕ6 phages in response to four different coagulation approaches, $Al_2(SO_4)_3$ coagulation, $FeCl_3$ coagulation, aluminum EC, and iron EC, and investigate viral capsid damages.

d. Evaluate fouling of microfiltration membranes by *Acholeplasma laidlawii* and compare with rigid silica particles.

Dissertation organization

The main components of this dissertation are four manuscripts (chapter II – V), two of which have been published, and third and fourth ones will be submitted for peer-review in the near future. Each of these chapters follows the same format as the published articles; each beginning with an introduction, followed by the material and methods, results and discussion, and the concluding remarks. The final chapter of the dissertation summarizes the key findings of all the chapters and recommends future research directions.

Chapter II demonstrates that iron EC can simultaneously remove and inactivate a non-enveloped surrogate virus. Inactivation of the bacteriophage MS2 was facilitated under slightly acidic conditions resulting in loss of viral capsid integrity potentially due to *in-situ* triggered Fenton's reactions. Detailed findings can be found in K. Kim, N. Jothikumar, A. Sen, and S. Chellam, Virus Removal and Inactivation Mechanisms during Iron Electrocoagulation: Capsid and Genome Damages and Electro-Fenton Reactions, *Environmental Science and Technology*, (2021) https://doi.org/10.1021/acs.est.0c04438 [25].

Chapter III evaluates the extent and mechanisms of removal and/or inactivation of an enveloped virus surrogate (bacteriophage ϕ6) by conventional $FeCl_3$ coagulation and iron EC. Both conventional and electro- coagulation appeared to be highly effective in controlling enveloped viruses during surface water treatment. This work has been published in K. Kim, N. Jothikumar, A. Sen, J. L. Murphy and S. Chellam, Removal and Inactivation of an Enveloped Virus Surrogate by Iron Conventional Coagulation and Electrocoagulation, *Environmental Science and Technology*, **55** (2021) 2674-2683 [26].

Chapter IV highlights different behaviors of non-enveloped (MS2) and enveloped (ϕ6) phages in four different coagulation approaches namely conventional $Al_2(SO_4)_3$ coagulation,

conventional $FeCl_3$ coagulation, aluminum EC, and iron EC. The structural integrity of MS2 phage was only compromised by iron EC whereas ϕ6 phage was found to be vulnerable to all coagulation approaches. This work will soon be submitted for peer-review.

Additional research work is presented in Chapter V. A comparison of microfilter fouling by flexible *A. laidlawii* cells and rigid silica particles illustrated that particle flexibility worsens the fouling via pore penetration and cake compression. This work also will soon be submitted.

CHAPTER II

VIRUS REMOVAL AND INACTIVATION MECHANISMS DURING IRON ELECTROCOAGULATION: CAPSID AND GENOME DAMAGES AND ELECTRO-FENTON REACTIONS [*]

Introduction

The estimated upper bound of annual cases of acute gastrointestinal illness associated with publicly-available water in the United States is between 12 million [27] and 32 million [28] even though only 780 drinking water disease outbreaks were reported in the 35-year period 1971-2006 [2]. Contaminated drinking water has an even higher global public health burden especially in developing nations [29] although fecal-oral disease transmission has consistently decreased in the last 3 decades worldwide [30]. A substantial portion of drinking water health risks can be attributed to viruses because they are copiously excreted in feces, generally exhibit a low infectious dose, and survive longer in surface- and groundwater than bacteria and protozoa [3, 31]. Surveillance reporting by the Centers for Disease Control and Prevention has shown that viruses account for approximately 8% of all waterborne disease outbreaks associated with drinking water reported in the United States from 1971 to 2006 [2, 3], which is almost certainly an underestimation given current detection limitations [32]. Additionally, because viruses are commonly present in surface- and groundwater and probably disproportionately responsible for waterborne diseases of unknown

[*] Reprinted with permission from "Virus removal and inactivation mechanisms during iron electrocoagulation: Capsid and genome damages and electro-Fenton reactions", K. Kim, N. Jothikumar, A. Sen, and S. Chellam, 2021, Environmental Science and Technology, https://doi.org/10.1021/acs.est.0c04438, Copyright 2021 by American Chemical Society.

etiology, they pose a significant risk in drinking water [2, 3, 31, 33] necessitating appropriate treatment to remove and/or inactivate them.

Enhancing virus coagulation is important in the context of the multiple-barrier approach to water treatment. Another consideration is that water is likely more contaminated in rural areas around the world [29], due to poor operation and maintenance of treatment plants, as revealed by numerous regulatory violations by small systems even in the United States [34, 35]. This motivates research into new coagulation technologies that are easy to install and amenable to automation and therefore suitable for small drinking water plants. One option in this context is electrocoagulation (EC), where hydrolyzing metal ions such as aluminum and iron are electrolytically added *in situ* via oxidation of a sacrificial anode thereby reducing transportation, storage, and handling of corrosive chemicals that are central to conventional chemical coagulation. EC units are compact, skid-mountable, amenable to automation, and nearly eliminate the need for acids/bases since alkalinity is not consumed (unlike external addition of alum or iron salts that behave as Brønsted acids to consume buffering capacity [36]). Thus, EC is a modular process that can rapidly respond to a wide range of feedwater chemistries and alleviates many safety concerns associated with hazardous chemicals currently employed for water treatment. EC has been shown to well-control viruses [4, 10] from natural and synthetic water via effective sweep flocculation by aluminum and iron (hydr)oxides [36], with little to no inactivation [13, 14, 16]. Evidence has also been recently presented linking overall Fe(II) oxidation to virus inactivation, without providing any mechanistic information on aqueous phase reactive intermediates or modifications to virus structure, proteins, or genome [15, 17].

The objectives of this research targeting iron EC are to (1) evaluate total virus attenuation and separate removal and inactivation, (2) directly visualize capsid damage via computational

image analysis using 3-D electron density maps of viruses, (3) quantify capsid structural modifications by measuring and comparing thickness of untreated and treated viruses using transmission electron microscopy (TEM), (4) provide plausible evidence for oxidative alterations to viral protein secondary structures using attenuated total reflectance − Fourier transform infrared spectroscopy (ATR-FTIR), (5) attribute virus inactivation to likely electro-Fenton reactions, and (6) monitor genomic alterations using the reverse transcription quantitative polymerase chain reaction (RT-qPCR). The MS2 bacteriophage was used as a model nonenveloped virus given its ubiquitous use in water purification investigations.

Materials and methods

Phage preparation, enumeration, and analysis

Enriched MS2 (ATCC 15597-B1) stock was prepared by propagating with *Escherichia coli* (ATCC 15597) followed by a series of purification and concentration steps as detailed in Section A1 [37, 38]. Briefly, MS2 was inoculated after growing its host to mid-log phase and further incubated (16 h, 37 °C). The resulting suspension was centrifuged (13,500 g, 20 minutes) and filtered successively using 0.2 μm and 0.1 μm polyethersulfone (PES) syringe filters. The filtrate was rinsed with phosphate buffer and viruses were extracted using a 100 kDa PES membrane centrifugal filter (5,900 g, 20 minutes). The stock titer of infective viruses was of the order of 10^{12} plaque forming units (PFU)/mL measured using the double-agar layer method [37, 38]. Our procedure is similar to earlier publications [13-17, 39, 40] and more details are given in Section A1.

Dynamic light scattering (Litesizer 500, Anton Paar) measured a hydrodynamic diameter of 31.0±1.8 nm similar to an earlier report [41]. Additionally, a low polydispersity index

(0.140±0.011) and coefficient of variance (5.8%) demonstrated that we prepared relatively monodispersed viruses with minimal impurities. MS2 is a F-specific single stranded RNA (ssRNA) coliphage and is employed as an example of nonenveloped enteric viruses without loss of generality since it allows direct comparison with others' results [4, 10, 13-17, 39-41]. We recognize differences between behavior of MS2 and other (pathogenic) viruses during iron EC [15]. Nevertheless this bacteriophage is a very common surrogate for assessing virus control technologies and mechanisms [17, 39, 40, 42, 43].

Electrocoagulation

Batch electrolysis was performed in a custom fabricated, baffled cylindrical reactor (6 cm diameter, 17 cm high, ~450 mL effective volume). We employed an annular electrode configuration with a cylindrical sacrificial iron anode (99.95 % metal basis purity, 35.9 cm^2 initial effective area) placed within a perforated dimensionally stable 316 stainless steel cathode (2 mm electrode gap) [13, 14, 16]. All experiments were performed using phages at an initial concentration of ~10^8 PFU/mL suspended in synthetic water (3 mM $NaHCO_3$ and 1 mM $CaCl_2$ in deionized water) that was initially nearly saturated with oxygen (8.3±0.16 mg/L). Two pH values (6.4±0.2 or 8.2±0.2) were chosen covering the range of low iron solubility [36]. The Faradaic electrolysis time was varied to attain the target total iron dosage at a constant current density of 2.8 mA/cm^2 under well-mixed conditions (78, 156, and 312 seconds to obtain 5, 10, and 20 mg/L of total iron respectively, see Figure A-2). This current density is in the range of other iron EC investigations [15, 44] and ensures that dissolved oxygen will not be rapidly depleted allowing H_2O_2 production to persist during electrolysis. Holding the current density constant also ensured the same ferric (oxy)hydroxide solid phase (probably lepidocrocite [45-47]) in all cases. Total iron and Fe(II) were measured using colorimetry (HACH methods 8112 and 8146, Section A6). After

electrolysis, the entire suspension was slowly stirred (flocculated) for a total time (electrolysis + flocculation) of 2 h to provide viruses with an extended contact with electrolysis products. Ten mL samples were collected at predetermined intervals, flocs separated by centrifugation (12,000 g, 30 minutes), and floc pellets dissolved in 6% beef extract after elevating pH to 9.5 [13-16, 48, 49]. Next, infective viruses were enumerated using plaque assay and RNA was quantified by RT-qPCR both in the supernatant (i.e. bulk water) and flocs (i.e. dissolved floc pellet). Section A2-A6 has more details on electrocoagulation protocols including reactor cleaning, sample preparation, electrolysis time, iron and H_2O_2 measurement, and phage recovery from flocs.

Electron microscopy

The morphology of untreated and electrocoagulated MS2 phages was visualized by TEM (F20 Thermo Fisher Scientific). 50 ml of electrocoagulated suspension was sampled, vigorously shaken, and briefly sonicated (to detach phages from flocs), and centrifuged at 3,000 g for 10 min to remove large flocs (to improve visualization). Afterwards, the supernatant was ultracentrifuged at 150,000 g for 10 hours to pelletize electrocoagulated MS2 particles, which was later resuspended in 1 ml of PBS. 5 μL of sample was placed on 300 mesh formvar-coated carbon grids prepared by glow-discharging. Conventional negative staining was performed using 5 μL of 2 % uranyl acetate solution (pH unadjusted). Excessive liquid was blotted out from the grid followed by air drying. All images were captured at an accelerating voltage of 200 keV either on a Gatan K2 or a Gatan Tridiem GIF-CCD camera.

ATR-FTIR and RT-qPCR protocols

Protein oxidation and structural alterations were monitored by collecting ATR-FTIR spectra (Nicolet iS10, Thermo Fisher) after directly mounting samples on a diamond iTX accessory (more details in Section A7). Viral RNA concentrations both in the bulk water and flocs

were quantified using one-step real-time RT-qPCR (Section A8) [16, 50]. The chosen amplicon (77 bp) targets 2.2% of the genome and is widely employed because of its high sensitivity and specificity [16, 50-52].

Results and discussion

Virus removal and inactivation at different pH

Figure II-1 depicts temporal changes in plaque assay measurements of infective MS2 concentrations in bulk water and flocs during EC at different total iron dosages and pH. Constant virus concentrations were measured by this method in the negative controls, i.e., no electrolysis (black lines in Figure II-1A and C). Hence, the apparatus and its components did not attenuate infective viruses. In other words, any attenuation measured during iron EC experiments could be directly attributed to changes induced by electrolysis.

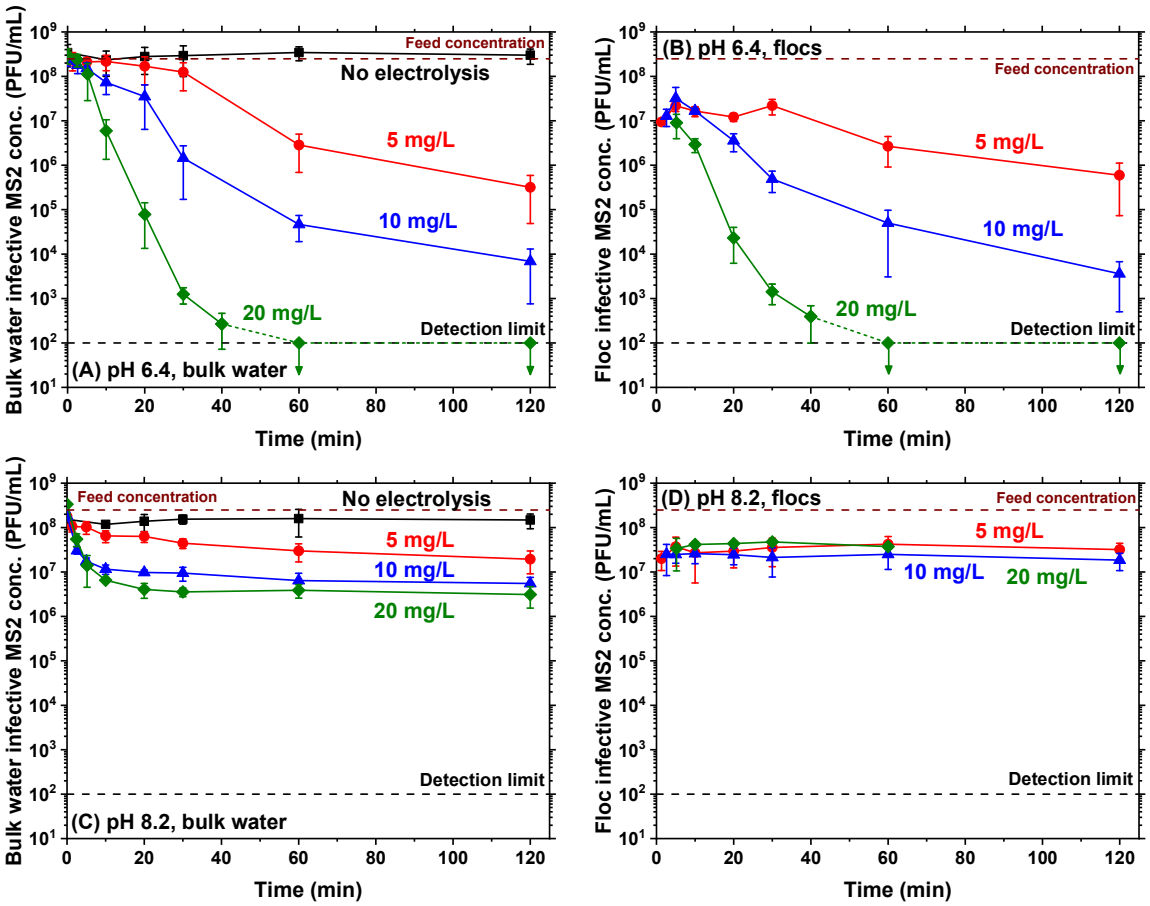

Figure II-1. Temporal concentration profiles of infective MS2 virions in bulk water (A and C) and those extracted from flocs (B and D) at different total iron dosages (5 mg/L, 10 mg/L, and 20 mg/L corresponding to electrolysis times of 78 s, 156 s, and 312 s, respectively as shown in Section A4) and pH values (6.4 and 8.2) measured via the plaque assay. The entire EC experiment i.e. electrolysis + flocculation lasted 2 hours. Virus extraction from flocs is described in Section A5.

At pH 6.4, total infective virus concentrations in the water column continuously decreased with time and total iron dosage even exceeding 6-log at 20 mg/L and 1 hour (Figure II-1A). A portion of viruses were simply removed from bulk water after sorbing onto flocs as evidenced by partial recovery of infective MS2 from iron precipitates (Figure II-1B). The gradual decline of infective viruses in EC flocs in Figure II-1B suggests that they were also inactivated as further discussed in Section A9. MS2 behaved differently at pH 8.2 wherein its infective concentrations in the bulk water reduced only initially and remained relatively constant thereafter (Figure II-1C). Additionally, the number of infective viruses in flocs at pH 8.2 remained constant throughout the

2-hours (Figure II-1D) unlike those at pH 6.4 (Figure II-1B). Differences in EC performance with pH are discussed later in the section "Identifying Clues to Intermediate Species Responsible for Inactivation" and elsewhere below.

Uptake of viruses on iron precipitates was confirmed by performing experiments with virions conjugated with fluorescein isothiocyanate isomer 1 (FITC) prior to EC. Section A10 and Figure A-7 and A-8 show corresponding bright field and fluorescence images of EC flocs (along with appropriate controls). Epifluorescence only of flocs incorporating FITC-labeled viruses provides direct evidence of MS2 enmeshment by iron precipitates, i.e. sweep flocculation [36] during EC at both pH values. EC-induced physicochemical alterations to viruses are pursued next.

Direct evidence for capsid damage

Because viruses were better attenuated at pH 6.4, they were imaged before and after EC at this pH value to assess their morphology (Figure II-2, 3, and 4). Intact MS2 consists of 180 copies of the coat protein structured as 90 dimers forming an icosahedral capsid shell (triangulation number = 3) with 5-, 3-, and 2-fold symmetry axes [53, 54], which are well defined in Figure II-2A [55]. The capsid thickness was measured using a MATLAB code which (1) imported a boxed-out MS2 particle micrograph (e.g., Figure II-2A), (2) computationally band-pass filtered it (Figure II-2B), (3) developed the gray-value profile across the virus particle (using the built-in function *improfile*), fit the profile to Gaussian distributions, and measured the full width at half maximum (FWHM) values [56] of distributions corresponding to the viral capsid (Figure II-2C). For each MS2 particle image, approx. 50 readings were made across the viral capsid by rotating the image to obtain the thickness distribution. This computational image analysis procedure was performed for 60 untreated viruses revealing that the capsid thickness of undamaged MS2 was monodispersed

and centered at 2.3 ± 0.4 nm (Figure II-4H), agreeing closely with small angle neutron scattering measurements of ~2.1 nm [57, 58].

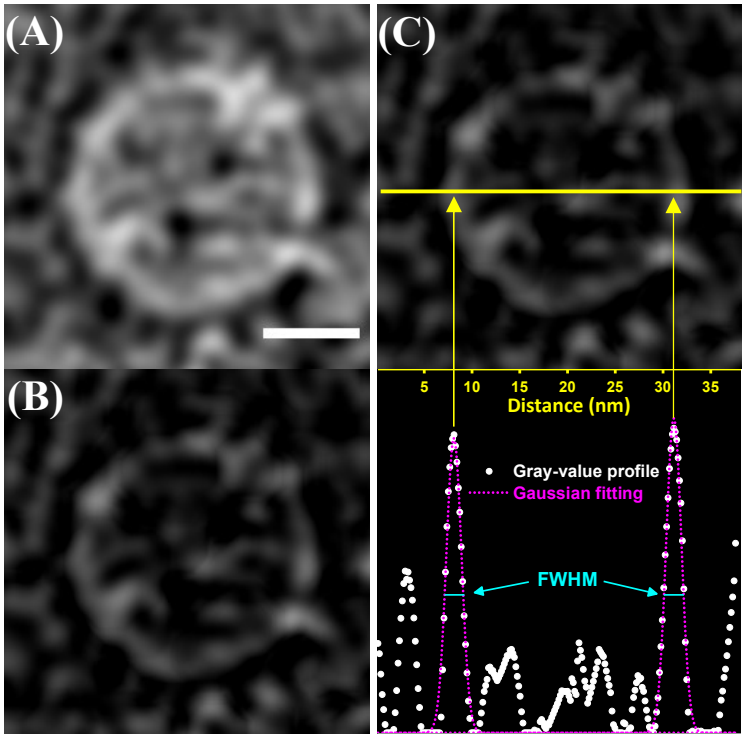

Figure II-2. (A) Transmission electron micrograph of untreated MS2 phage (scale bar equals 10 nm and applies to B and C as well), (B) computationally-filtered image of A depicting the gray-value profile, (C) Gaussian fitting of the gray-value profile and reading of full-width at half maximum (FWHM) values as capsid thicknesses. Note that the gray profile values (i.e., y-axis of bottom right panel) is arbitrary. Original TEM image is shown in Figure A-9A.

TEM images of electrocoagulated MS2 divulged clusters of MS2 particles lodged in iron flocs (Figure A-10) where the white circle highlights a set of MS2 particles with deformed/damaged capsids and severely damaged particles are marked by white arrows. Figure II-3A, recorded at 70,000X magnification, shows three viruses that lost a portion of their capsid shells appearing like hollow empty bowls due to their orientation on the grid surface. One with major damage is pointed by the black arrow and two with minor damages are marked by white arrows. Additionally, one virus also appeared to lose its icosahedral shape becoming elongated (yellow arrow), which is indicative of further capsid deformation and/or damage.

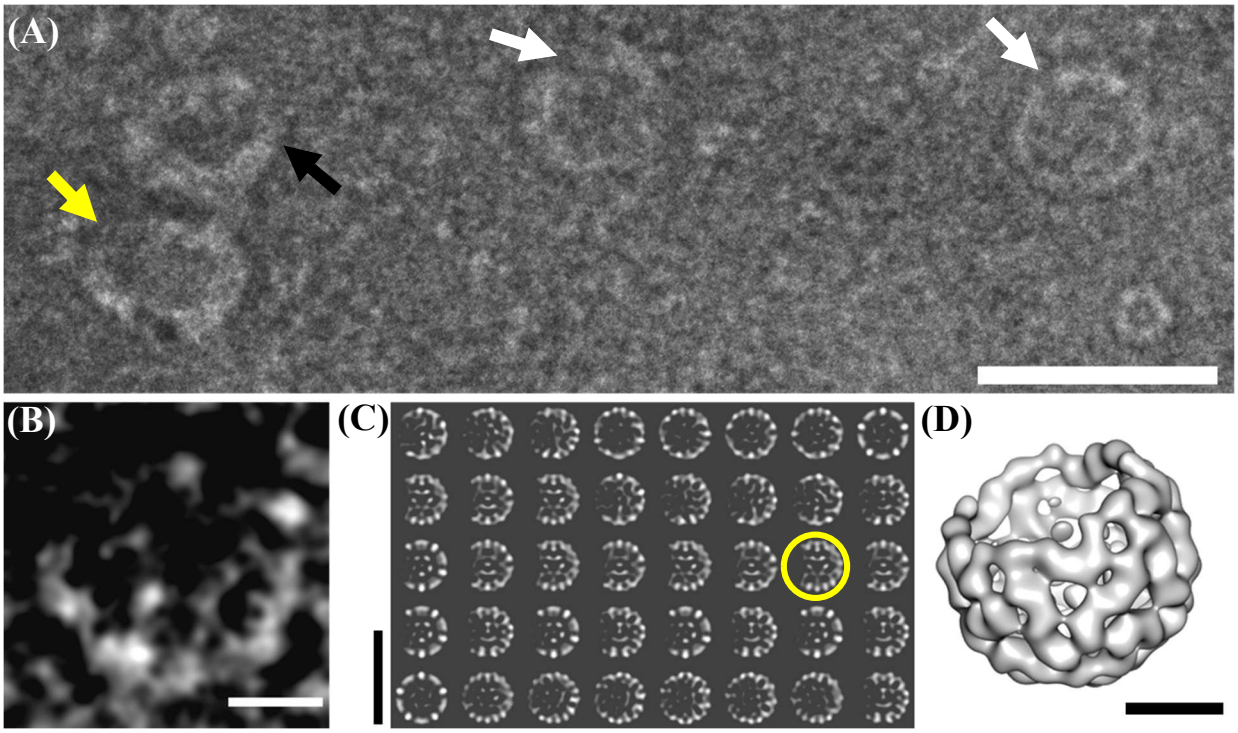

Figure II-3. (A) Electron micrograph of MS2 phages damaged by EC (pH 6.4, 10 mg/L total iron, 120 minutes) at 70,000X magnification. The black arrow shows a MS2 particle that has lost ~50% of the capsid protein. The white arrows point to other virions that were damaged to a smaller extent (~ 10%). Scale bar in (A) equals 50 nm. [B, C, and D] explain the capsid damage quantification procedure. (B) shows a boxed-out damaged virion as an example taken from Figure A-9B (scale bar in (B) is 10 nm), (C) shows a series of projection images of the band-pass computationally-altered electron density map of MS2 with the yellow-circle being the view that best matches the image in B (black vertical scale bar on the left in (C) is 50 nm). (D) is the corresponding 3D electron density map of the damaged particle in (B) (scale bar in (D) is 10 nm).

In order to estimate capsid damages to the virion particles, we employed 3-D information of the MS2 phage electron density map (accession number EMD-1431) [55]. All computational work was performed using Bsoft and University of California San Francisco (UCSF) Chimera software programs [59, 60]. It is noted that inner density of the map was computationally removed to only consider viral capsid, and the map was band-pass filtered at 20 Å resolution because negative staining bounds the micrograph information limit to ~15-20 Å. For a boxed-out virion particle (e.g., Figure II-3B), arrays of density maps of MS2 capsids damaged to various extents were generated by altering the original electron density map of intact MS2 (EMD-1431). During this procedure, various portions of the capsid shell at 5, 3, and 2-fold regions were computationally

erased eliminating 10 ~ 60 % of the total capsid shell to simulate different degree of damages [59-61]. (It is emphasized that we could only identify damages ≥ ~10% since smaller capsid damages could be hidden based on the virion's orientation on the TEM grid surface and/or obscured by iron flocs. In addition, capsid damage > 60% was not considered because remnants of virions that suffered such major damages would be too small and/or distorted to be recognized as even being a part of the capsid. Doing so necessitates cryo-electron microscopy, which is one of our next steps but is beyond the scope of the current manuscript.) Then, sets of projections of these altered density maps at different angles were generated to identify the angular view that best-matched the boxed-out damaged virion particle (yellow-circle in Figure II-3C) by estimating their cross-correlations [62-64]. Because the density map in Figure II-3D is missing nearly 30% of MS2's shell volume, the damage to the boxed-out virion in Figure II-3B was quantified as 30%. This procedure was implemented on 50 MS2 virion particles to estimate EC-induced damages.

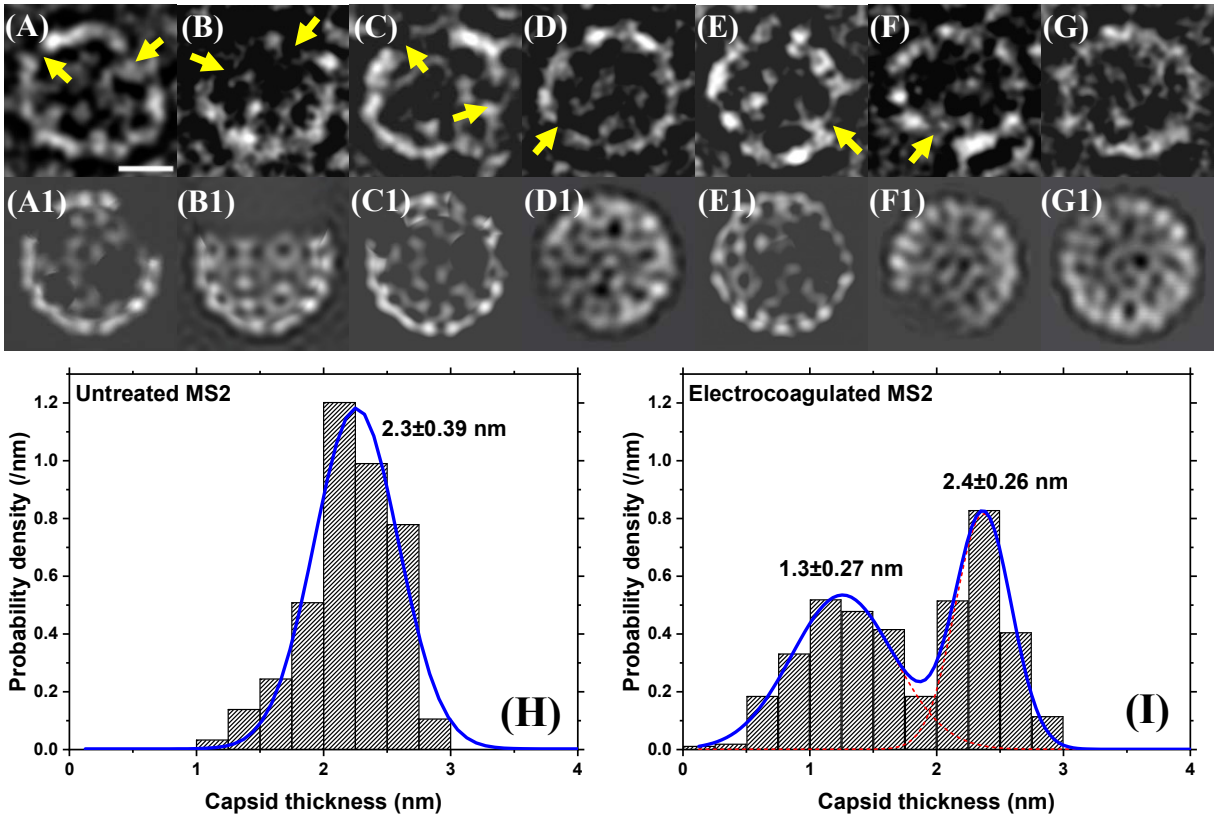

Figure II-4. Damaged MS2 after EC (pH 6.4, 10 mg/L total iron, 120 minutes) are shown in the first row with damages to protein capsids marked with yellow arrows [A – G]. The second row shows corresponding computationally-altered electron density maps [A1 – G1] used to quantitatively analyze structural damages. In other words, A1 is the electron density map of A and so on. A 10 nm scale bar is shown only on the top row leftmost image, which applies to all images in the first two rows. The bottom row shows frequency distributions of digitally measured capsid thicknesses. (H) depicts a monomodal distribution with an average of 2.3 nm for untreated MS2 (60 virions analyzed). (I) depicts a bimodal distribution after EC (50 damaged virions analyzed). Gaussian distributions were fitted to calculate statistical properties of capsid thickness (average and standard deviation). Original TEM is shown in Figure A-9B.

A representative TEM of electrocoagulated viruses is shown in Figure A-9B from which seven viruses were digitally extracted, magnified, and included in the first row of Figure II-4 where capsid damage locations are marked by yellow arrows. Capsid damage was not readily apparent in a few virions even after EC and one such example is the rightmost image G. Corresponding altered electron density maps of the seven representative electrocoagulated virions in the first row are shown in the second row of Figure II-4, which validate rupture of the protein coat following iron EC. Computational image analysis revealed that the majority of electrocoagulated MS2 lost

at least 10-60% of its capsid shell losing a minimum of one of the 5-fold regions and two of its 3 and 2-fold regions.

The capsid thickness of electrocoagulated viruses was bimodally distributed (Figure II-4I) dissimilar to untreated MS2 (Figure II-4H). One peak was centered at 1.3 nm, which is lower than the thinnest known capsid for an infective icosahedral virus [65] whereas the second peak at 2.4 nm was close to the intact capsid. Negligible shifting of capsid thickness noted via the second peak demonstrates only minimal artifactual measurements due to a defocusing (see Section A13). Therefore, these observations demonstrate decimation of the original protein coat suggestive of an extremely harsh physicochemical environment experienced by viruses during EC-treatment and corresponding loss of infectivity monitored via the plaque assay depicted in Figure II-1.

Protein oxidation and alterations to secondary structures

Figure II-5 compares FTIR spectra (1800 – 1500 cm^{-1}) of untreated and electrocoagulated viruses under the same conditions as the previous section (pH 6.4, 120 minutes, 10 mg/L total iron dosage). A negative control ($FeCl_3$ conventional coagulation) is shown in Figure A-14. The two broad amide I (1700~1600 cm^{-1}) and amide II (1580~1510 cm^{-1}) peaks of untreated MS2 (top black curve) [66] were provisionally assigned to protein secondary structures (using well-accepted amide I wavenumbers of peptides and proteins of known structures), amino acid side chains, and ring bases of RNA (Section A14) [58, 67-69]. Table A-2 comprehensively summarizes peak assignments [70-72]. It is emphasized that spectral interpretations are only indicative of functionalities and structural transformations by EC (i.e., not definitive) because of potentially severe peak overlaps arising from the virus' complex structure [73, 74].

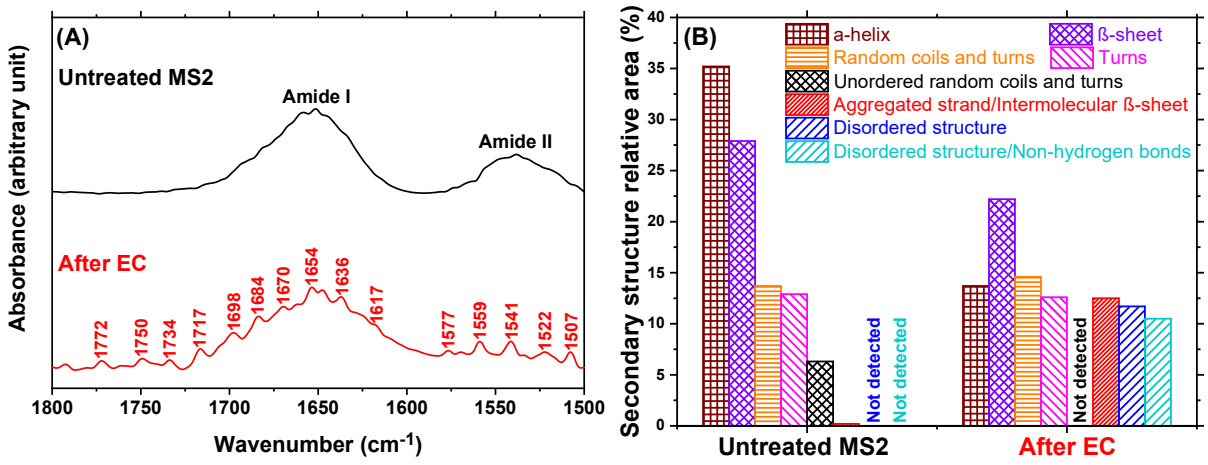

Figure II-5. Left panel (A) shows ATR-FTIR spectra of untreated MS2 (top, black color) and electrocoagulated MS2 at pH 6.4, 120 minutes, 10 mg/L total iron dosage (bottom, red color). Only representative peaks appearing in EC-treated viruses are shown (see Figure A-14 for complete identification). Right panel (B) compares relative areas of secondary structures of untreated and electrocoagulated MS2.

The spectrum of electrocoagulated MS2 (red curve in Figure II-5A) appeared to be significantly different from untreated phages. For example, the amide II relative peak area decreased from 26% to 17% and several peaks that could be assigned to amino acid side chains such as tryptophan, lysine, glutamic, and aspartic acid were resolved from a single broad amide II band [69]. (Note that corresponding amino acid peaks were not resolved in the untreated virus spectrum.) Since amide II is commonly attributed to N-H bending and C-N stretching of the protein backbone [68], the decrease in peak area suggests EC-induced structural changes to the protein backbone and damages to amino acid side chains as previously reported for bacteria [75-77]. Oxidative damages can also be inferred via evolution of new individual peaks above 1700 cm^{-1} corresponding to carbonyl groups, aldehydes, and ketones (1750, 1734, and 1717 cm^{-1}) that were absent for undamaged/untreated phages (and for $FeCl_3$ coagulated viruses in Figure A-14) [75, 78, 79].

EC-induced changes to protein secondary structures were also analyzed by enhancing spectral resolution in the amide I region (1700 – 1600 cm^{-1}) to decompose and separate overlapping

peaks [68, 73, 80]. Peak locations were identified using second derivatives of the original spectrum, assigned to secondary structures [68, 73, 81], and their relative areas were measured assuming a Lorentzian shape (Figure A-15) [82-84]. As summarized in Figure II-5B and Table A-3, EC appears to have increased the relative amount of aggregated strands/intermolecular β-sheets and disordered structures including non-hydrogen bonds. Simultaneously, EC seems to have decreased relative fractions of α-helices, β-sheets, and unordered random coils and turns. Substantial modifications to proteins' secondary structures are indicative of structural modifications arising from unfolding and enhancements of non-specific protein-protein and intermolecular interactions or aggregation [85]. Protein subunits can potentially unfold due to changing α-helical structures and β-structures [86] also reducing the required tensional energy needed to maintain the capsid's structural integrity [57]. Changes in capsid strain energy storage suggests that MS2's ability to inject its genomic RNA into its bacterial host can be impeded even in the absence of explicit rupture (e.g. images G and G1 in the far right of Figure II-4 rows 1 and 2) manifesting as inactivation [57, 87]. These arguments along with those in the previous section indicate both biophysical and biochemical capsid modifications accompanied iron EC.

Identifying clues to intermediate species responsible for inactivation

Several control experiments and measurements were performed to obtain insights into chemical mechanisms underlying the observed virus inactivation. First, since EC generates Fe(II) that oxidizes *in situ* to Fe(III) to achieve sweep flocculation [14], a control experiment was performed by externally adding Fe(III) (i.e. conventional $FeCl_3$ coagulation and no Fe(II)) at pH 6.4. Nearly all seeded viruses were extracted and enumerated using the plaque assay (red line in Figure II-6) demonstrating that Fe(III) only coagulates viruses and does not inactivate them. This was supported by the virtually identical IR spectra of MS2 before and after $FeCl_3$ coagulation

including protein secondary structures (Section A14) demonstrating negligible biochemical changes induced by $FeCl_3$ addition. Hence, Fe(III) and its hydrolysis products including the precipitates do not affect MS2 infectivity pointing to the critical role of Fe(II) for inactivation during iron EC [15, 17, 42, 49, 88].

Second, since EC releases Fe(II) via anodic Fe(0) oxidation [14] (see also Figure II-7 and Figure A-2), a positive control was also performed to evaluate virus control by externally adding Fe(II) in the form of $FeCl_2$ at pH 6.4. In contrast to Fe(III), the chemically added Fe(II) inactivated viruses [17, 88] (a total of ~1.7-log reduction from $2x10^8$ to $5x10^6$ PFU/mL, blue line in Figure II-6) over 2-hours. EC inactivated ~4.1 log viruses in 2-hours (from $2x10^8$ to 10^4 PFU/mL, green line in Figure II-6), which is ~500 times (2.7-log) more than direct Fe(II) addition. This suggests a separate inactivation mechanism during EC.

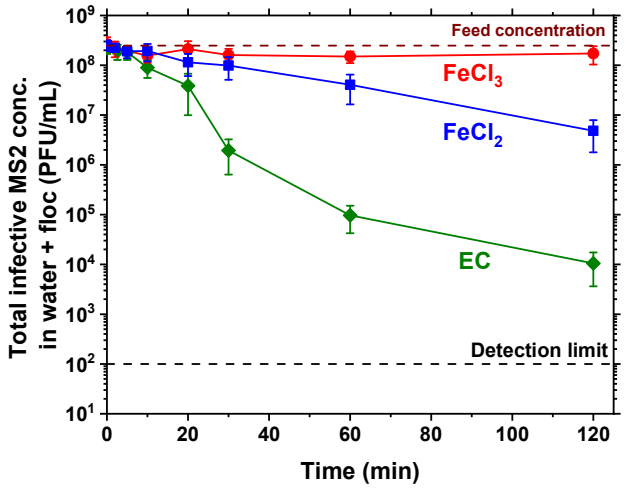

Figure II-6. Total infective MS2 in control experiments after adding Fe(II) (blue curve) and Fe(III) (red curve) salts and comparison with EC (green curve) at 10 mg/L total iron and pH 6.4 measured using the plaque assay. EC data shown here are the sum of data shown earlier in Figure II-1A and 1B. Figure A-17 depicts the same infective virus data separately as those extracted from the flocs and the bulk water.

Significantly more virus inactivation by EC compared with $FeCl_2$ at an identical total iron concentration and pH suggests that electrolysis produces additional virucidal species. Importantly, Fe(II) and H_2O_2 were measured to reach peak values of 7 mg/L and ~800 µg/L , respectively at the

end of electrolysis at pH 6.4 before dissipating (Figure II-7A and 7B). Dissolved oxygen was correspondingly depleted consistent with cathodic O_2 reduction (Figure A-18). Simultaneous presence of Fe(II) and H_2O_2 during EC can potentially trigger electro-Fenton reactions [89] releasing $^{\bullet}OH$ [90] and high-valent oxoiron(IV) ions [89, 91] (Table A-4). Although these reactive species were not independently measured herein, they have been implicated in phage inactivation [42, 88, 92] potentially explaining the greater efficacy of EC towards viruses depicted in Figure II-6.

Further, the short lifetimes of $^{\bullet}OH$ [93] and oxoiron(IV) [94], indicates that viruses had to be in very close proximity of these highly reactive intermediates to be effectively inactivated [95], similar to viral disinfection by photoactivated nanoparticles [39, 96]. Indirect evidence for this behavior was obtained when overlapping infective virus concentration profiles were measured in the presence and absence of a scavenger, dimethyl sulfoxide (Section A17) suggesting that only viruses within the limited diffusion radius of the reactive oxygen species were inactivated.

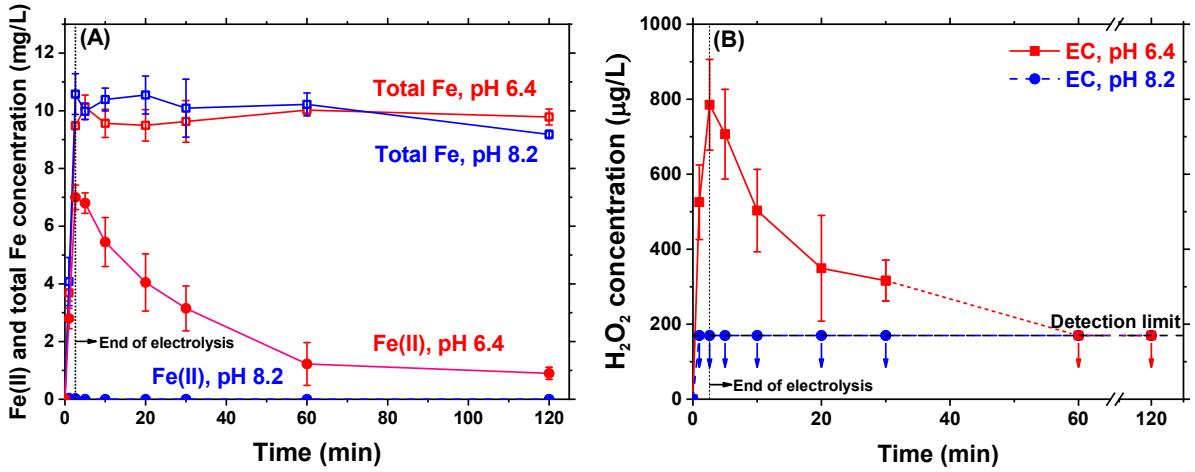

Figure II-7. (A) Total iron and Fe(II) concentrations during EC (B) H_2O_2 production (detection limit = 170 µg/L) and dissipation at different pH at a target total iron dosage of 10 mg/L.

In contrast to pH 6.4, at the higher pH of 8.2, Fe(II) oxidation is extremely rapid (~10^4 times the rate at pH 6.4) [97] "instantaneously" depleting ferrous ions (Figure II-7A). Additionally,

Fe(III) is substantially less soluble at pH 8.2 compared with 6.4 [36]. Further, H_2O_2 was always below detection limits at higher pH (Figure II-7B) since its cathodic generation is low under alkaline conditions (Section A16). This suggests that electro-Fenton reactions did not proceed significantly at pH 8.2 [89, 91, 95] thereby substantially lowering viral inactivation compared with pH 6.4. In other words, viruses were inactivated during EC at higher pH largely only when both Fe(II) and H_2O_2 were continuously generated, i.e. during electrolysis (green curve in Figure II-1C). After terminating electrolysis at pH 8.2, infectivity was maintained over the entire flocculation period manifested as nearly horizontal lines in Figure II-1C and 1D (i.e., no inactivation, also Section A18 and Figure A-20).

Several other controls were also performed to identify potentially responsible intermediates in the context of Fenton's chemistry (Section A19). For example, $^{\bullet}O_2^-$ only played a minor role in virus inactivation [43] (Figure A-21) demonstrating that direct Fe(II) oxidation by molecular oxygen (Section A21) was not the dominant inactivation pathway during EC. Similarly, H_2O_2 alone did not inactivate MS2 over the 2-hour duration of experiments (Figure A-22). Further, inactivation was completely suppressed during $FeCl_2$ coagulation and EC at pH 6.4 by (i) chelating Fe(II) using 1,10-phenanthroline [88, 92] or (ii) N_2 purging to deoxygenate the water and consequently preventing Fe(II) oxidation (DO $\leq$ 0.3±0.1 mg/L, Figure A-23). These controls confirm that both Fe(II) and dissolved oxygen species are necessary to inactivate MS2 during EC. Separately, the important role of peroxide was established by completely inhibiting inactivation by adding Na_2SO_3 as an anti-oxidant and H_2O_2 scavenger at the end of electrolysis (Figure A-24).

Conclusions

Iron EC under slightly acidic pH controls viruses by simultaneous physical removal and

chemical inactivation similar to polyaluminum chloride [48, 49]. This is unlike conventional chemical coagulation performed with metal salts such as alum, $Fe_2(SO_4)_3$, and $FeCl_3$ as well as aluminum EC [16] of chloride-depleted waters where nonenveloped viruses are only removed (by aggregation) but not inactivated. Additionally, the reverse transcription quantitative polymerase chain reaction revealed consistently lower RNA loss from the bulk water compared with infective viruses detected as plaque forming units (Section A20 and Figure A-25) demonstrating the need for both assays to monitor virus behavior. Decimation of capsids and significant damages to genomic content by iron EC at pH 6.4 is similar to virus deterioration documented after free chlorine attack [40, 98] demonstrating that EC technology presents a very harsh environment towards viruses. The two-pronged ability to concurrently remove and inactivate viruses at pH 6.4 allows iron EC to significantly outperform aluminum EC (e.g., > 6-log in Figure II-1A at 60 minutes by iron compared with only 2.3 log at 60 minutes by aluminum [16]). Note that this was accomplished in the same reactor, electrode assembly, and water chemistry by passing 36% lesser charge (69 C/L for Fe and 107 C/L for Al) because only two electrons are transferred in iron rather than three in aluminum.

Non-specific attack potentially by reactive oxygen species such as $^{\bullet}OH$ and/or oxoiron(IV) during iron EC indicates that this technology is potentially well-suited to inactivate a wide range of viruses including human pathogens [15]. Being effective against a wide spectrum of microbial and physicochemical contaminants suggests that EC may be suitable for small drinking water systems, allowing them to better comply with federal regulations [34, 35]. However, several process engineering and water chemistry issues need to be resolved before iron EC can be recommended for field implementation since Fenton reactions are strongly affected by water chemistry including presence of organics and long-term electrode behavior is not yet fully

understood [44]. Additionally, a thorough understanding of redox reactions, electrochemistry, and mass transfer mechanisms including electrode passivation is paramount to elucidate process capabilities and limitations, necessary to broaden and optimize adoption of EC technology. The role of natural organic matter (NOM) also needs to be established since it is known to play an important role in iron EC of natural waters [14] and virus behavior [14, 99] but experiments reported herein were performed in its absence similar to numerous previous virus-treatment investigations [15-17, 39, 40, 42, 43, 48, 71, 72, 88, 92, 98, 100]. Importantly, inactivation can possibly be significantly enhanced by lowering the pH during iron EC to operate under "enhanced coagulation" conditions where Fenton's reactions are accelerated [89, 91, 92]. However, acidic conditions along with NOM presence will slow Fe(II) oxidation kinetics and in turn inactivation rates, requiring careful process optimization.

Spectroscopic techniques such as FTIR and Raman can also detect/identify other intact viruses [66, 101-103], probe capsid alterations induced by reactive oxygen species [26, 96, 104], and investigate viral protein structures [26, 105-107]. Electron microscopy coupled with computational image processing has also been used to detail the role of capsid stability in infectivity [26, 61, 108] and capsid protein interactions [109] for adenoviruses and bacteriophage ϕ6. Hence, techniques employed herein to elucidate viral structure modifications may be applicable to other virus systems. However, because natural water components such as particulate matter and NOM can interfere with spectroscopy and microscopy by obscuring viruses during imaging and producing peaks that overlap with those associated with viruses, these techniques might be predominantly applicable only to simplified water chemistries lacking turbidity, NOM and other interferents.

CHAPTER III

REMOVAL AND INACTIVATION OF AN ENVELOPED VIRUS SURROGATE BY IRON CONVENTIONAL COAGULATION AND ELECTROCOAGULATION [*]

Introduction

The fate of enveloped viruses during water and wastewater treatment has not yet been well-established largely due to prevailing beliefs that they are not present in sufficiently high concentrations and that they can be easily inactivated [18-20]. However, this conventional wisdom needs to be reevaluated because enveloped animal and bacterial viruses have been shown to persist in surface water and sterilized sewage for several days [21-24] and their genome has been recently detected in raw sewage [110] and sludge [111]. Even though more still needs to be learned regarding the persistence and transmission of infective enveloped human viruses through aqueous environments [112-115], wastewater contamination of water supplies is common, with many municipalities practicing *de facto* wastewater reuse [116, 117]. Consequently, it is essential to better understand the fate of enveloped viruses during water purification [117]. Herein, we focus on coagulation by $FeCl_3$, which is commonly employed for colloid destabilization during conventional treatment [36]. We also evaluate its electrically-driven analog; Fe(0) electrocoagulation because it shows promise for small-scale water treatment [118].

Another consideration is that the vast majority of investigations of enveloped virus control from (waste)waters have targeted disinfection [119-122] with only limited research pursuing "physical" treatment methods [123]. Importantly, turbidity can protect viruses from disinfectants

[*] Reprinted with permission from "Removal and inactivation of an enveloped virus surrogate by iron conventional coagulation and electrocoagulation", K. Kim, N. Jothikumar, A. Sen, J. L. Murphy and S. Chellam, 2021, Environmental Science and Technology, 55**,** 2674-2683, Copyright 2021 by Americal Chemical Society.

[16, 122, 124], which in the case of enveloped viruses is particularly noteworthy since the hydrophobic outer lipid layer can enhance their uptake onto solids [125, 126] thereby necessitating investigations of their control via physical treatment processes as another barrier against them.

Our overarching goal was to quantify the removal/inactivation of an enveloped virus surrogate (ϕ6) by iron conventional coagulation and electrocoagulation. ϕ6 is a triple layered virion with an inner capsid encapsulating three RNA segments, which is surrounded by a nucleocapsid shell with turrets-like proteins at the 5-fold regions followed by a shell composed of proteins and lipids with spikes surrounding the entire outermost surface [127, 128]. Specific objectives were to obtain clues to underlying mechanisms by (i) visualizing native and treated viruses using Transmission Electron Microscopy (TEM) to assess capsid structural damages, (ii) identifying biochemical modifications to the virus envelope and capsids upon electrocoagulation and conventional coagulation using Attenuated Total Reflectance − Fourier Transform Infrared spectroscopy (ATR-FTIR), and (iii) monitoring stability of viral dsRNA using a newly-developed reverse transcription quantitative polymerase chain reaction (RT-qPCR) method.

Materials and methods

ϕ6 preparation and enumeration

As with all bacteriophages, ϕ6 is an imperfect Biosafety Level 1 surrogate but its structural similarity (i.e. phospholipid layer and spike proteins) makes it well-suited for treatment investigations of pathogenic enveloped human viruses [20, 113, 126, 129-131]. ϕ6 and its host *Pseudomonas syringae* (provided by Dr. M. Worth Calfee, United States Environmental Protection Agency, USEPA) were propagated using methods similar to previous publications [20, 24, 119, 130]. Employing a bacteriophage facilitated laboratory work as it did not present health risks to

humans, was easily and reproducibly cultivated, did not require animal cell lines and other relatively expensive infrastructure, and was easily disposed after completing experiments. Importantly, ϕ6 shares biophysical surface characteristics with coronaviruses such as the phospholipid envelope and spike proteins making it a good surrogate. Further, ϕ6 has been extensively studied [24, 119, 126, 132] and recommended as a coronavirus surrogate [20, 113, 126, 129-131] facilitating comparisons of our results with those that have already been published.

ϕ6 stock was prepared by inoculating it after growing its host bacterium to mid-log phase and further incubation (9 h, 26 °C). The resulting suspension was centrifuged (10,000 g, 20 minutes) and filtered with 0.2 μm polyethersulfone (PES) filters. Phages were then concentrated by ultracentrifugation at 104,000 g (2 h, 4 °C). The collected phage pellet was resuspended in SM buffer (10 mM Tris-HCl, NaCl 100 mM, $MgSO_4$ 50 mM, gelatin 0.01%, pH 7.5) which was then passed through a sucrose gradient layer (10% - 40%) prepared in SM buffer at 104,000 g (1 h, 4 °C). The recovered phage band was subject to a 100 kDa PES membrane centrifugal filter (5,900 g, 20 minutes) to further purify it and replace sucrose solution with SM buffer. Infective ϕ6 was enumerated using the double top layer method resulting in a stock titer of 10^{11} PFU/mL. Section A22 provides more details .

TaqMan assay design

Forward primer (JP6F, 5'-CGTACAACCGAGTAGGTTCGT-3', positions 47-67), reverse primer (JP6R, 5-GTTAGGCGTCGGGACCATC-3', positions 116-98) and probe (JP6P, FAM5-TCATCCTGCAAGCGTCGCCAATTAAGGC-3BHQ-1, positions 96-69) targeting a highly conserved non-structural protein (P12) of S segment were selected based on the sequences available in the GenBank database. Positions described are based on the ϕ6 isolate Slow2 segment S partial sequence (GenBank accession number KF615861). The TaqMan probe was labeled with

6-carboxyfluorescein (FAM) and with Black Hole Quencher 1 (BHQ-1) at the 5’ and 3' ends, respectively.

RT-qPCR assay

Nucleic acid was extracted using 400 µL of sample following the UNEX extraction protocol [133] and eluted in Tris-EDTA buffer to a final volume of 80 µL. The RT-qPCR assay was performed with PrimeDirect™ Probe RT-qPCR Mix (TaKaRa, USA). This kit was chosen to perform all three steps; dsRNA denaturation, reverse transcription, and amplification in a single reaction tube. The kit’s reverse transcriptase enzyme is thermostable and denaturation of the ϕ6 dsRNA at 95 °C for 30 s was followed by reverse transcription and amplification. Reactions were performed in 20 µL RT-qPCR mixture containing PrimeDirect™ Probe RT-qPCR Mix (1x), 250 nM of each primer and probe, and 2 µL RNA. The RT-qPCR reaction was set up in a different room from nucleic acid preparation. The 1x RT-qPCR reaction mixture included 10 µL of 2x buffer, 0.2 µL of ROX Reference Dye (50X conc), 0.5 µL of 10 µM forward primer, 0.5 µL of 10 µM reverse primer and 1.0 µL of 5 µM Probe, 2 µL RNA and 5.8 µL of nuclease-free water. The standard graph was prepared based on the 10-fold serial dilutions of viral RNA (Figure A-26) and each dilution series was tested in quadruplicate. All samples were tested in duplicate along with appropriate positive and negative controls. A negative control was prepared with nuclease-free water in place of ϕ6 RNA to ensure that there was no nucleic acid contamination introduced in the run. A positive control was included in each run to confirm the successful amplification of ϕ6 RNA with the master mix. The inclusion of positive and negative controls ensured the validity of each run to prevent false negative or false positive reactions. The reaction conditions included initial denaturation (30 s at 95 °C), reverse transcription (5 min at 60 °C), and 45 cycles of 5 s denaturation at 95 °C and 30 s annealing/extension at 60 °C. All RT-qPCR amplification reactions

were performed in a ABI 7500-Fast Real-Time PCR system (Applied Biosystems, CA). It is emphasized that this procedure targets a very short RNA target (70 nucleotides) of the entire ϕ6 genome (13385 nucleotides) representing a coverage of only 0.5%.

A seven log-linear dynamic range of the amplification assay for the quantitative PCR analysis was obtained when C_T values were regressed against the starting ϕ6 phage standard concentrations with an R^2 value of 1.0 and a slope of −3.39 (SI Section S2). This corresponds to calculated PCR efficiencies of 97.3% and the detection limit of the TaqMan assay was 4 viral particles per reaction. In short, the developed method was highly sensitive, specific, and rapid for detecting viral RNA.

Microscopy and spectroscopy

Phages were negative stained with 5 μL of 2% uranyl acetate solution without pH adjustment and imaged using TEM (F20 Thermo Fisher Scientific) at an accelerating voltage of 200 keV on a K2 camera or a Gatan Tridiem GIF-CCD camera. The stock suspension was used to image native viruses. For coagulated viruses, flocs were harvested from the sludge after sedimentation and directly imaged without separating viruses from iron precipitates. 5 μL of sample was applied to a glow-discharged 300 mesh formvar-coated carbon grid and stained as mentioned above. ATR-FTIR spectra (Nicolet iS10, ThermoFisher) were collected directly by mounting samples on a diamond iTX accessory (Section A26 has more details).

Coagulation

Batch coagulation experiments were conducted in duplicate using a baffled 450 mL custom-built cell [16, 134] at an iron dosage of 10 mg/L and initial virus concentration of ~10^8 plaque forming units (PFU)/mL. A solution containing monovalent and divalent cations and alkalinity (3 mM $NaHCO_3$ and 1 mM $CaCl_2$ at pH 6.4±0.2) was employed based on our earlier

results with a non-enveloped phage (MS2) [134, 135]. Electrochemical dosing was accomplished using a 99.95% pure Fe(0) cylindrical anode surrounded by a dimensionally stable perforated annular 316 stainless steel cathode at current density of 2.8 mA/cm^2 for 2.6 minutes (the Faraday time to release 10 mg/L Fe). $FeCl_3$ was used for conventional coagulation. The system was well-mixed for the first 2.6 minutes during both electrocoagulation and conventional coagulation after which it was slowly stirred (flocculated) for 2-hours. Ten mL of suspension was carefully pipetted out at 2.6, 10, 20, 30, 60, and 120 minutes, transferred to a 50 mL centrifuge tube, and centrifuged at 10,000 g for 20 minutes. (Sodium sulfite was added to quench H_2O_2 and prevent further inactivation during analysis for electrocoagulated samples.) The supernatant (i.e. bulk water) was gently decanted and the pelletized flocs were resuspended in beef extract. Direct addition of $FeCl_3$ results in fast Fe(III) precipitation during conventional coagulation [36, 136] whereas electrocoagulation releases soluble Fe(II) which slowly oxidizes to insoluble Fe(III) at pH 6.4 [134].

Iron and hydrogen peroxide measurement

Sample aliquots were first filtered with 0.1 μm PES syringe filters and 7.2 mM of citrate was added to eliminate Fe(II) interferences [137]. H_2O_2 concentration was measured by monitoring absorbance at 454 nm after an orange-colored complex of Cu(I) and 2,9-dimethyl-1,10-phenanthroline (DMP) was formed upon the reduction of Cu(II) by H_2O_2 in the presence of DMP (DR-6000, HACH) [138, 139]. Total iron and Fe(II) concentrations were measured by HACH methods 8112 and 8146 respectively. For total iron, Fe(III) was reduced to Fe(II) by sodium metabisulfite to form a complex with 2,4,6-Tris(2-pyridyl)-s-triazine which was quantified by absorbance at 590 nm (DR-6000, HACH). Fe(II) concentration was determined by quantifying the light absorbance at 510 nm when Fe(II) was chelated with 1,10-phenanthroline at pH 3 adjusted

with HCl.

Results and discussion

Infective virus control by conventional- and electrocoagulation

Virus concentrations were constant when iron was not added (black line in Figure III-1) ensuring insignificant losses within the apparatus or aggregation under initial solution conditions. As seen, both coagulation approaches decreased infective ϕ6 concentrations (i.e. PFU) from the bulk water column by ~5-logs at 20 minutes (the minimum flocculation residence time during conventional treatment [140]), exceeding USEPA requirements by ~1-log (Surface Water Treatment Rule (54 FR 27486) [141]) even without filtration or disinfection. Electrocoagulation removed/inactivated more than 3-logs of viruses from the water column in 2.6 minutes, which continued to increase over time exceeding 6-log in 1-hour. In contrast, conventional coagulation sharply reduced viruses in bulk water to > 5-log in 2.6 minutes remaining relatively constant thereafter.

Different decay kinetics between the two coagulation methods potentially arose from dissimilar modes of iron addition. Soluble Fe(II) dosed in electrocoagulation [134] would have oxidized relatively slowly to Fe(III) at pH 6.4 [97] but Fe(III) precipitation is fast during conventional $FeCl_3$ coagulation [36, 136]. The viral envelope's hydrophobicity [114, 125, 142] facilitated ϕ6 sorption onto the rapidly precipitated iron (hydr)oxides during conventional treatment enabling its facile sweep coagulation resulting in the steep decline measured at short times (~5 logs in just 2.6 minutes, purple line in Figure III-1A).

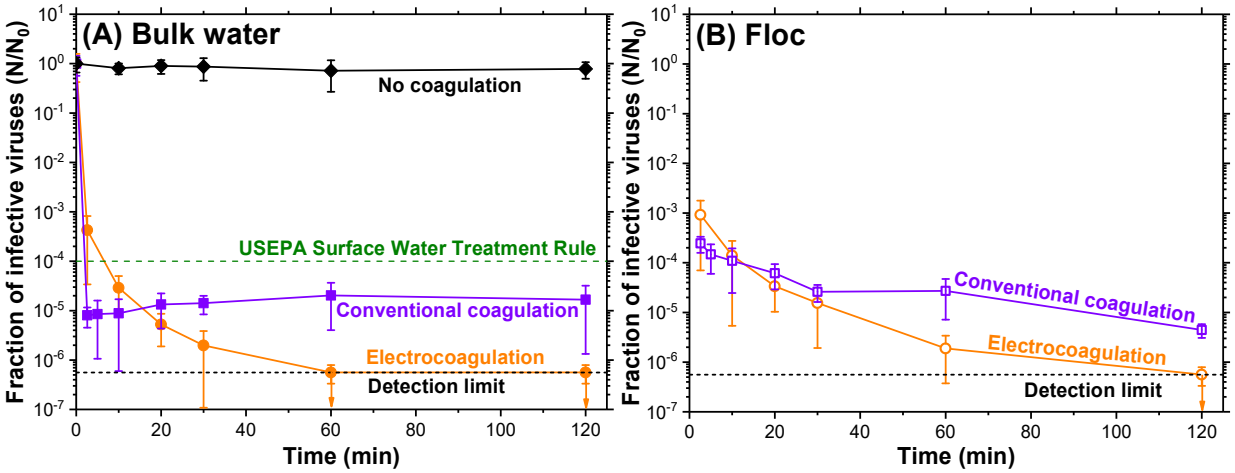

Figure III-1. Facile reduction of ϕ6 by both electrocoagulation and conventional chemical coagulation at 10 mg Fe/L, pH 6.4, and N_0 ~10^8 PFU/mL. Error bars represent one standard deviation of a minimum of four measurements. The left panel (A) denotes viruses in the bulk water. Very few infective viruses were recovered from the flocs, which continuously declined over time (B, right panel).

Attempts were also made to elute viruses from flocs after centrifugation (10,000 g for 20 min), adding 6% beef extract, and adjusting the pH to 7.5 [126, 142]. As seen in Figure III-1B, only a very small fraction of ϕ6 was recovered by this procedure even though viruses would have remained infective at this pH [143]. This is consistent with enveloped viruses being notoriously difficult to recover after they partition onto solid surfaces [126, 130]. Nevertheless, the recovery of (a small number of) infective phages from the flocs demonstrates that viruses were physically removed by both forms of coagulation and a fraction of them continued to be active even after uptake on flocs. More details of ϕ6 attenuation (i.e. both removal and inactivation) by conventional- and electrocoagulation are pursued next.

Conventional coagulation and electrocoagulation damage ϕ6 structure

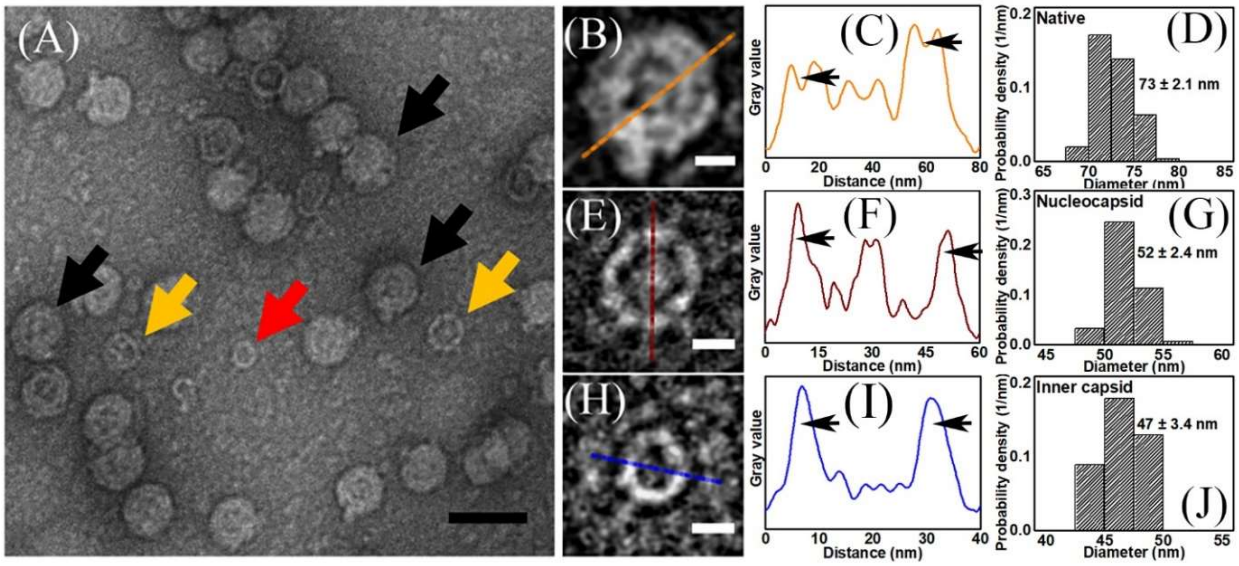

Figure III-2. (A) TEM of complete native ϕ6 (black arrows), nucleocapsids (yellow arrows) and innermost capsid (red arrow) in the left panel. (B) boxed-out images of a native ϕ6, (E) the nucleocapsid and (H) the innermost capsid. The gray scale plots show the density distribution along the lines drawn through the boxed-out particles (C, F, I). The black arrowheads represent the edges of the particles providing us their size shown in (B, E, H). Size distributions of native viruses (n=100), nucleocapsids (n=32), and inner capsids (n=30) are shown on the rightmost panels (D), (G), and (J), respectively, where n is the number of particles analyzed. The mean and standard deviation are shown in each panel. Scale bars: (A) 100 nm and (B, E, H) 20 nm.

Figure III-2A is an electron micrograph of native ϕ6 particles where nucleocapsids and the inner capsid were seen in close vicinity of fully matured phages (Figure III-2B, E and H) followed by their respective gray scale profiles (Figure III-2C, F and I). Measured sizes of these particles from this and other images shown in Figures 2D, G and J (mature virions 73 ± 2.1 nm, nucleocapsid 52 ± 2.4 nm, and inner capsid 47 ± 3.4 nm) agreed well with literature values [127]. We imaged and screened three batches of flocs containing ϕ6 particles (after 2.6 minutes of mixing during conventional and electrocoagulation) that visually divulged approximately 80% of them to have suffered significant structural damages. Some were even fragmented beyond recognition as to which portion of the capsid they belonged to and appeared like "empty bowls." The diameter of the damaged virions (55 ± 3 nm) was close to the nucleocapsid size [127] indicating that both

coagulation types had completely damaged the outer lipid layer similar to montmorillonite clay [132]. Figure III-3A shows iron flocs without viruses (negative control). Most phages were embedded in flocs after both forms of coagulation (consistent with Figure III-1A) and were damaged appearing as dark patches with lighter patches of protein complexes sticking out (Figure III-3B).

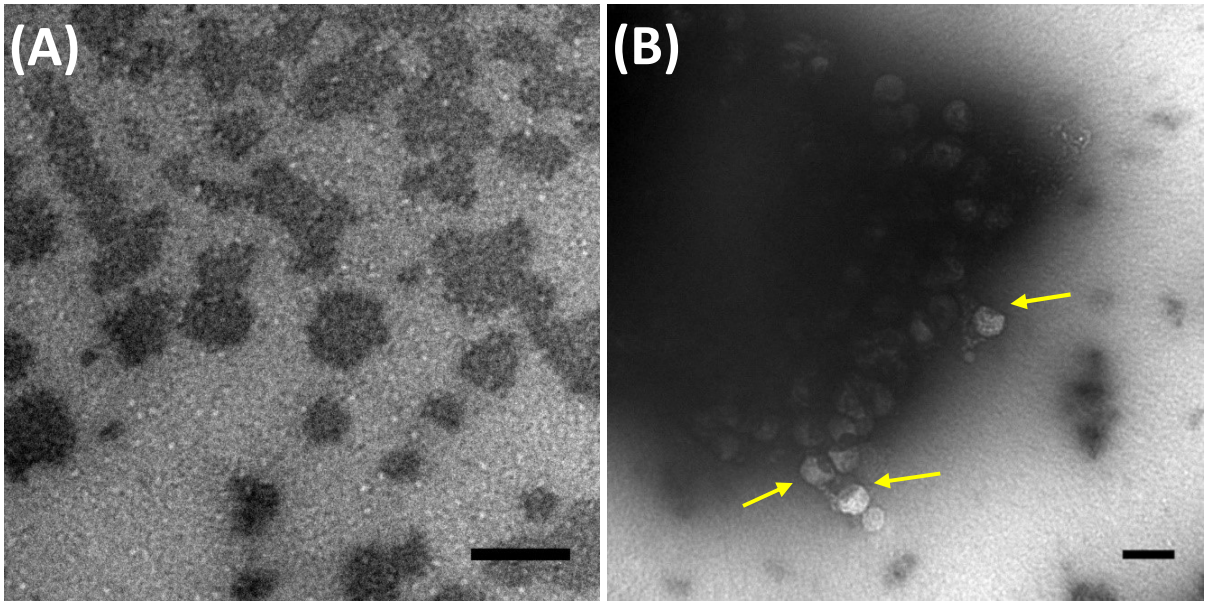

Figure III-3. (A) Image of iron flocs distributed on the TEM grid surface. (B) TEM image of a group of damaged ϕ6 particles trapped in the iron floc after 2.6 minutes appearing in lighter color with yellow arrows pointing to damaged phages. Scale bars: 100 nm.

A novel approach was implemented to estimate the degree of damage by generating computationally altered 3D electron density maps of ϕ6 using the map EMD-1301 [127, 144]. Eight 3D maps were created by computationally modifying portions of the nucleocapsid starting from one of the 5-fold regions in small increments. A total of 42 projections from each of the computationally modified maps were generated and correlated with each of the boxed-out damaged ϕ6 particle images to find the best matches. The altered maps showing the best match with the boxed out damaged particles were further analyzed to determine the remaining volume of the capsid. More details are in Section A28 and results are summarized in Figure III-4.

Figure III-4A is a representative micrograph of native ϕ6, a single boxed out virion is shown in (B) and its gray scale profile along the line drawn across the particle length is in (C). The valleys in the gray scale profile indicated by the black arrows (C) correspond to the inner procapsid and nucleocapsid. Note that since the boundaries of the outermost lipid layer could not be precisely distinguished it was excluded from computational analysis. The electron density map of native ϕ6 with the lipid layer intentionally removed is also shown (D) [127, 144]. We selected two damaged ϕ6 virions, one each from the images belonging to conventional coagulation and electrocoagulation (E and I). Our choices of the single damaged particle from each of the two micrographs are shown in (F and J) with their gray scale profiles (G and K). It is interesting to note that the valleys in the gray scale profile are still visible in both damaged particles at least on one of the edges (marked by black arrows in G and K). This suggested that the nucleocapsid and the inner capsid, although damaged, were still associated together for the portion that is left behind, confirmed by the measured size of the virions that were in close proximity to the nucleocapsids. Hence, it appeared that the two coagulation types damaged the phage in-whole and not layer-by-layer (or else the inner capsid would have been present along with damaged exterior nucleocapsid).

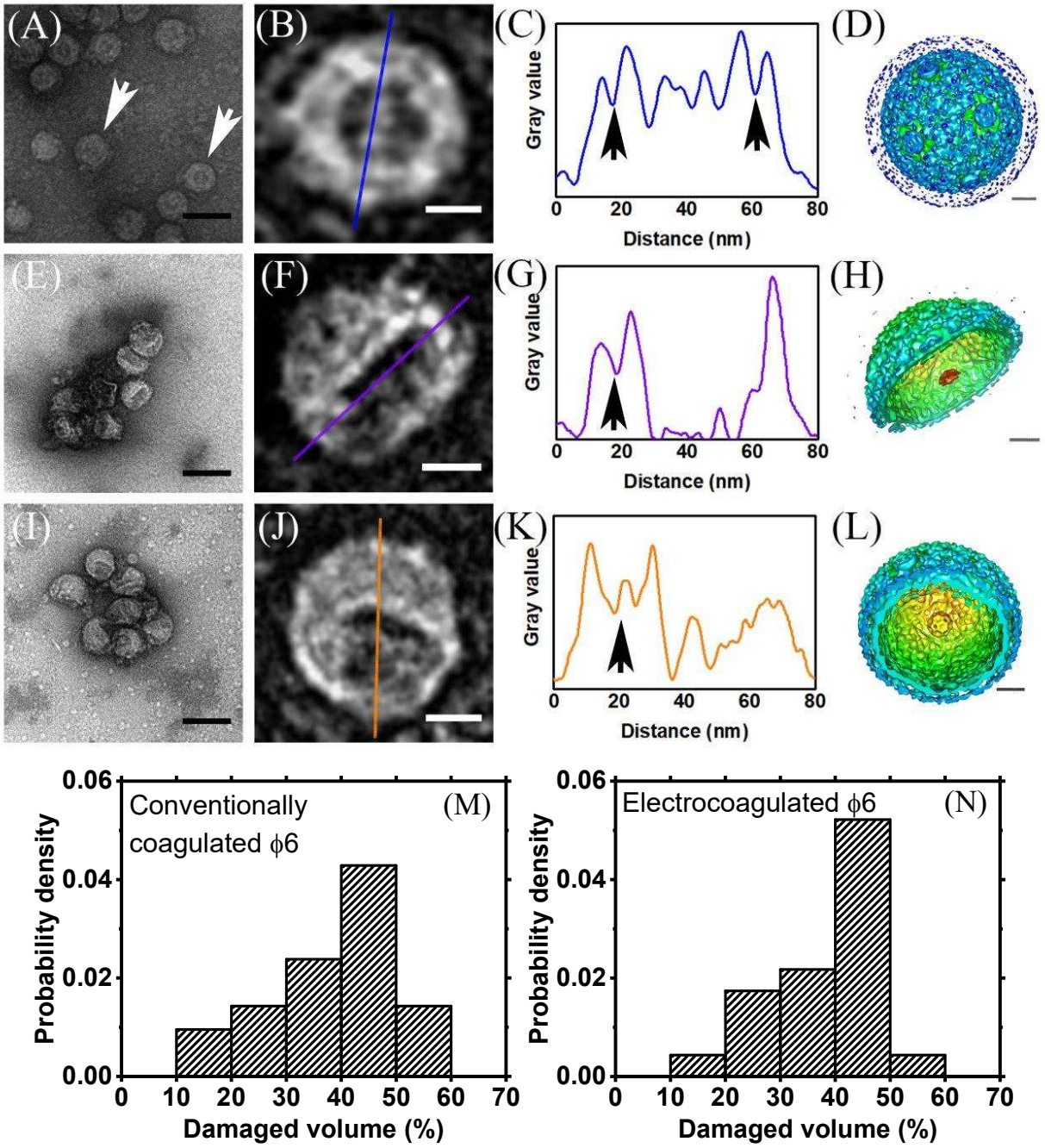

Figure III-4. TEM images of native, conventionally coagulated, and electrocoagulated damaged ϕ6 particles are shown in (A), (E) and (I), respectively (coagulation was performed for 2.6 minutes). The image on the top left shows the multi-layer structure of intact virions (marked with white arrows). Scale bar: 100 nm. (B), (F) and (J) represent the boxed out native, conventionally coagulated and electrocoagulated damaged ϕ6 particles with lines drawn across them showing the position the gray scale profiles generated. Scale bar: 20 nm. (C), (G) and (K) represent gray scale profiles corresponding to the boxed out particle on their left. The two valleys, marked with black arrows confirm the presence of nucleocapsid and inner capsid layers. (D) Iso-surface representation of electron density map of native bacteriophage ϕ6 (EMD-1301). Altered electron density maps of ϕ6 shown in (H) and (L) represent the 3D structures that matches best to (F) and (J)

respectively. Scale bar: 10 nm. (M) and (N) shows computationally analyzed capsid volume damage induced by conventional and electrocoagulation, respectively obtained by analyzing 70 viruses in each case.

We further constructed the 3D structure of the damaged phages for (F) and (J) as shown in (H) and (L) respectively. The volume of (H) was measured to be lower than (L) revealing that particle (F) was more damaged that (J), suggesting that conventional coagulation inflicted more damage to ϕ6 than electrocoagulation at early time, which is consistent with its higher removal/inactivation in Figure III-1A. However, a statistically significant number of virions need to be analyzed to generalize relative effects of different coagulation types via this procedure.

Analysis of damaged particles after both coagulation approaches showed that two-thirds of conventionally coagulated phages and three-quarters of electrocoagulated phages lost 30 to 50% of capsids as summarized in (M) and (N). Damage <15 % was not statistically recognizable due to the limited resolution of the micrographs after negatively staining the specimens. Assessment of capsids showing >60% damage is also difficult with the current approach as there are artifacts in the preparation, which can be misinterpreted as damaged capsids. Cryo-electron microscopy followed by intense computational image analysis is necessary to quantitatively assess these capsids. Since coagulation destroyed all capsid layers, the genomic dsRNA located within the procapsid core presumably could not be sheltered, resulting in inactivation.

Coagulation alters ϕ6 biochemical composition

The mid-IR region (3000-2800 cm^{-1} and 1800-900 cm^{-1}) was used to examine viral components after accurately resolving peaks and shoulders using second derivatives and comparing with previously reported ϕ6 composition, model biomolecules, and microorganism-iron interactions [145-150]. Peak assignments are summarized in Table A-7 and Figure III-5 depicts spectra for native, conventionally coagulated, and electrocoagulated viruses after 2.6

minutes (same as Figure III-3 and 4). Spectral interpretations for a complex structure such as ϕ6 should be considered as being suggestive rather than definitive.

For native phages (top brown colored curve in Figure III-5), bands associated with major viral envelope components i.e. phosphatidylethanolamine and phosphatidylglycerol [146, 147] were detected. These include $\nu_{as}(CH_3)$, $\nu_{as}(CH_2)$, and $\nu_s(CH_2)$ (2966, 2937, and 2851 cm^{-1}), $\nu(C=O)$, $\delta_{as}(CH_3)$ (1749, 1732, and 1457 cm^{-1}), *cis* C=C (3013 cm^{-1}) in hydrocarbon chains, as well as $\nu_{as}(C\text{-}O\text{-}C)$ (1169 cm^{-1}) in head groups [151-153]. Strong signals attributable to specific capsid proteins were also obtained including $\nu_s(CH_3)$ (2871 cm^{-1}) of threonine, alanine, valine, and leucine (P5, P3, P8, P6 proteins) and methionine (P3, P8, P6 proteins), amide I (1654 cm^{-1}), amide II (1585 cm^{-1} and 1542 cm^{-1}), and amide III (1290 cm^{-1}) bands, δ(CN), δ(CH), and δ(NH) of tryptophan (1507 cm^{-1}) (spike protein P3, fusion protein P6, capsid protein P1), as well as $\delta_{as}(CH_3)$ and $\delta_s(CH_3)$ (1457 cm^{-1} and 1408 cm^{-1}, respectively) [145, 152, 154]. $\nu(C_2=O)$ (1697 cm^{-1}), C=C (1488 cm^{-1}), ν(C-N) (1326 cm^{-1}) were assigned to guanine and adenine in dsRNA [152]. Phosphate moieties, $\nu_{as}(PO_2^-)$ and $\nu_s(PO_2^-)$ (1236 cm^{-1} and 1080 cm^{-1}, respectively) were variably assigned to lipids and/or proteins [152, 153].

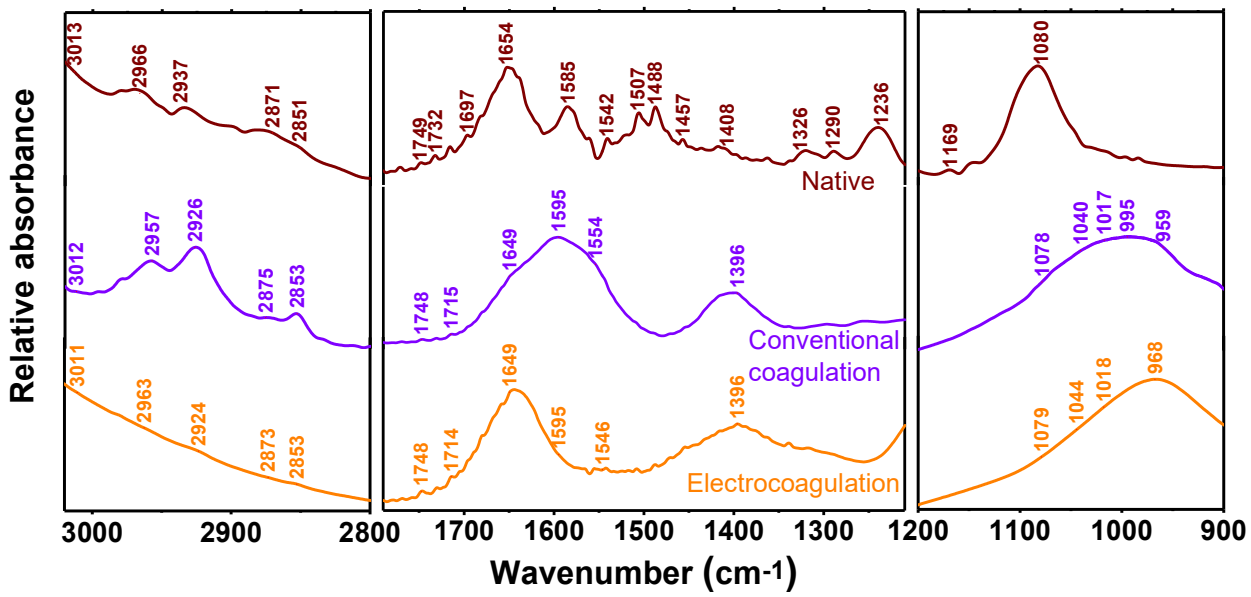

Figure III-5. FTIR spectra of native (top, brown color), conventionally coagulated (middle purple color), and electrocoagulated (bottom, orange color) ϕ6 after 2.6 minutes. See Table A-7 for comprehensive peak assignment.

Conventionally coagulated ϕ6 (middle purple colored curve in Figure III-5) exhibited significant changes in 1800 cm^{-1} - 900 cm^{-1} region compared with native phages while bands of hydrocarbon chains in phospholipids (3000 cm^{-1} - 2800 cm^{-1}) remained largely intact. A strong new band appeared at 1595 cm^{-1} (C-O-Fe) and peaks between 1044 cm^{-1} - 995 cm^{-1} (ν(P-OH, P-O-Fe)) suggesting iron complexation via carbonyl groups [155, 156] and phospholipids [149] respectively during enmeshment. Emergence of the 1396 cm^{-1} peak also implies soluble Fe(III) species interacted with ϕ6 [156]. Hence, specific Fe-O-P and Fe-O-C interactions appeared to have contributed to virus uptake during conventional coagulation, similar to bacterial adhesion onto iron [149, 150]. The shoulder at 959 cm^{-1} was assigned to PO_2^- stretching [149].

Electrocoagulated viruses also displayed intense peaks at 1044 cm^{-1} and 1018 cm^{-1} (ν(P-OH, P-O-Fe)) as seen in the bottom orange colored curve in Figure III-5. The C-O-Fe peak at 1595 cm^{-1} was substantially weakened compared with conventional coagulation suggesting the relative importance of phospholipids [149] in iron complexation of viral components by

electrocoagulation. Importantly, lipid hydrocarbon chains lack *trans* double bonds but they appear upon oxidative rearrangement of their *cis* counterparts [157-159]. We used two indices of this phenomenon to monitor oxidation in our experiments. The first was the intensity ratio of *trans* double bond (at 968 cm^{-1} denoting =C-H out of plane deformation) [160, 161] and lipid hydrocarbon chain markers (CH_3 and CH_2 stretching bands in 3000 ~ 2800 cm^{-1}). This index was zero for native and conventionally coagulated viruses as expected but 8.2 for electrocoagulated viruses [159]. The second index was the intensity ratio of *trans* to *cis* C=C, which was also zero for native and conventionally coagulated viruses but was 10.6 after electrocoagulation. Both these observations indicate electrocoagulation oxidized lipids. Oxidative stresses can also transition the *gauche* CH_2 rotamer in lipids to the *trans* form, which can be monitored by the band near 2850 cm^{-1} [159, 162]. (Note that the *trans* geometric isomer is different from the *trans* rotational isomer.) The intensity ratio of the 2850 cm^{-1} band and lipid markers was 0.24 for native viruses (and 0.22 for conventionally coagulated viruses), which reduced to 0.13 after electrocoagulation further evidencing oxidative damages to lipids [160, 161]. Oxidation was further validated by monitoring the intensity ratio of carbonyl groups (1749-1705 cm^{-1}) and lipid markers, which increased from 0.81 for native viruses to 1.51 after electrocoagulation. These various lines of evidence cumulatively establish lipid oxidation during electrocoagulation strongly suggesting the presence of reactive intermediates and a separate chemical inactivation pathway absent in conventional $FeCl_3$ coagulation (that is pursued later).

Protein secondary structures were estimated using relative peak areas in the amide I region (1700 – 1600 cm^{-1}) revealing the dominance of α-helices in native viruses consistent with them being major components of ϕ6 membrane and nucleocapsid [148] (Section A29). Both coagulation methods substantially reduced relative amounts of α-helices with an opposite trend for aggregated

strands/intermolecular β-sheets consistent with the compromised architecture of destabilized ϕ6 revealed by electron microscopy earlier in Figure III-4. Damages to α-helices, which comprise ~35% of the spike protein [148] potentially led to phage's failure to properly bind to its bacterial host, which manifested as loss of infectivity. Alterations to α-helices and other secondary structures indicates that coagulation unfolded, disordered, and ruptured viral proteins [86].

Viral RNA loss during coagulation

Figure III-6 shows time series of ϕ6 RNA extracted from the bulk water (left panel) and flocs (right panel). Similar to infectious viruses measured via the plaque assay (Figure III-1A), the targeted genome region was quantitatively detected over the 2 hours of slow mixing without iron addition (black lines in Figure III-1A and 6A). Therefore, any measured changes during coagulation experiments were reliably assigned to virus-iron interactions.

As seen in Figure III-6A, the fraction of intact RNA in the bulk water during conventional coagulation (purple line) declined sharply initially but remained stable at longer times which is similar to the trend observed for infective viruses in Figure III-1A. However, infective viruses measured with the plaque assay were reduced by 5-logs compared with only 3-logs as monitored by RT-qPCR beyond 20 minutes. The shape of the time series trend of RNA decrease for electrocoagulation (orange line) in Figure III-6A was similar to infective viruses in Figure III-1A but again differed quantitatively (exceeding 6-logs for plaque assay but only achieving 2-logs with RT-qPCR $\geq$ 60 minutes).

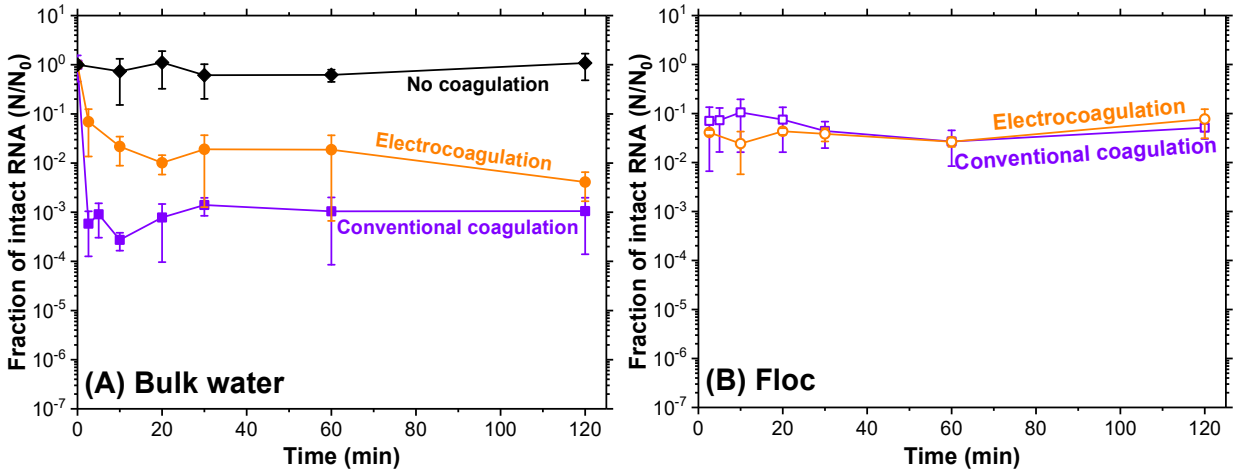

Figure III-6. Coagulation (10 mg Fe/L at pH 6.4) effects on RNA recovery from bulk water (left panel, A) and flocs (right panel, B). Error bars represent one standard deviation of a minimum of four measurements. Our RT-qPCR assay only targets a short region (0.5%) of the ϕ6 genome. N_0 is the number of viral particles (expressed as RNA copies) in the bulk water initially spiked to the experimental set-up.

Figure III-6B shows that viral RNA was consistently recovered from flocs over the entire 2-hours of experimentation remaining steady with only ~1-log reduction compared with the initial amount in the bulk water. This was in contrast to the behavior of infective viruses on floc surfaces, where plaque assays were reduced by 3-6 logs and also continuously declined over time after enmeshment (Figure III-1B). Hence, ϕ6 behavior both in the bulk water and after being taken up by flocs was substantially different depending on whether it was assayed by RT-qPCR or by infectivity.

Significant differences in virus quantitation by the two methods highlight that RNA detection did not closely correspond to the presence of infective particles. Hence, RNA degradation in our targeted amplicon region measured by RT-qPCR was not well-suited to assess overall viral infectivity agreeing with earlier reports of false-positive PCR results [163-165]. Further, since RT-qPCR underestimated ϕ6 inactivation compared with the plaque assay both in bulk water (2-logs lower at 2-hours) and on floc surfaces (3.5-logs lower at 2-hours), coagulation appears to have damaged capsid proteins and/or the lipid envelope significantly more than the viral

genome.

Electro-Fenton reactions during electrocoagulation

Lipid oxidative damage only detected in electrocoagulated viruses (Figure III-5) pointed to the presence of reactive chemical intermediates during electrolytic treatment (and not during conventional coagulation). Anodic Fe(0) oxidation to Fe(II) coupled to cathodic O_2 reduction to H_2O_2 during electrolysis suggested electro-Fenton reactions [89]. $^{\bullet}OH$ and high-valent ferryl ion (e.g.. FeO^{2+}) [90, 91] thus generated have been implicated in inactivation of the MS2 phage [42, 88] and therefore by analogy ϕ6 in the current study. We measured 7.0±0.4 mg/L of Fe(II) and 785±121 µg/L of H_2O_2 at the end of electrolysis (dissolved oxygen reduced from 8.3 mg/L to 7.1 mg/L in this timeframe) verifying the existence of Fenton's reagents. Our choice of pH 6.4 is common for coagulation [36], significantly extended Fe(II) lifetime [97, 134] having generated higher amounts of peroxide [89], prolonged Fenton's reactions, and better inactivated viruses without impacting sweep coagulation [36].

Conclusions

Facile control of ϕ6 by conventional coagulation (5-logs in 20 minutes) suggests that surface water treatment plants using iron might be already well-equipped to meet primary drinking water virus regulations (total 4-logs removal/inactivation) vis-à-vis enveloped viruses. Additional barriers implemented for surface water treatment such as media filtration and disinfection will further attenuate enveloped viruses, alleviate associated health risks, and facilitate regulatory compliance. Specific Fe-O-P and Fe-O-C interactions appears to have contributed to ϕ6 uptake on iron (hydr)oxides, which was accompanied by severe morphological damages similar to its sorption on clay [125, 132] also partially explaining the poor recovery of enveloped viruses after

they partitioned onto solids [20, 126, 130]. Data reported herein add to our body of knowledge on electrocoagulation, with past work exclusively focusing on non-enveloped viruses [4, 134] extending the potential applicability of this technology for small-scale, distributed water treatment. Importantly, orders of magnitude greater ϕ6 attenuation measured by infectivity assay compared with RT-qPCR demonstrated that both techniques are necessary to mechanistically monitor virus removal/inactivation during water treatment and that relying solely on PCR may overstate human health risks from other enveloped viruses. It is emphasized that experiments reported herein were performed in the absence of natural organic matter (NOM) and suspended solids although NOM, turbidity, and other constituents impact virus behavior. Also, any surrogate is imperfect by definition and ϕ6 does not mimic all enveloped viruses equally, particularly since it is known that these viruses do not behave identically during conventional water treatment [22, 123, 134]. Additionally, the RT-qPCR assay developed herein targeted only a very small portion of the viral genome thereby underestimating inactivation measured by the plaque assay (i.e. appearance of false-positives). Further, the persistence of dsRNA genome of ϕ6 in the aquatic environment may differ from ssRNA of coronaviruses. Consequently, our bench-scale results need to be verified with actual surface water containing pathogenic enveloped viruses and other suspended, macromolecular, and dissolved constituents before our results can be quantitatively extrapolated to full-scale water treatment.

CHAPTER IV

VIRUS MITIGATION USING CONVENTIONAL COAGULATION AND ELECTROCOAGULATION: COMPARISION OF NON-ENVELOPED AND ENVELOPED VIRUS

Introduction

Waterborne viral pathogens have been major target pollutants in drinking water treatment as they can be introduced to drinking water sources through multiple routes such as discharge of insufficiently-treated wastewater, urban and agricultural run-off, and leaking sewage network [1, 166], and potentially cause clinical symptoms even at low digestion dose [167]. Hence, as an effort to assure the safe drinking water, the United States Environmental Protection Agency (USEPA) mandates drinking water treatment facilities to achieve at least 99.99 % removal/inactivation (4-log credit) of viruses, and several enteric viruses have been listed on Contaminant Candidate List 4 as microbial contaminants known to occur in public water systems [168].

Although coagulation/flocculation is not directly given a credit for a virus control, understanding virus behavior during this process is essential because conventional filtration and (micro)membrane filtration may to fail to serve as an effective barrier without proper practice of coagulation/flocculation due to their large pore size compared to that of viruses [13, 15, 169, 170]. In this context, virus coagulation/flocculation has been extensively investigated [49, 171], but mostly with non-enveloped pathogenic enteric viruses and bacteriophages. In addition to these non-enveloped viruses, enveloped viruses such as influenza virus [172], severe acute respiratory syndrome (SARS) coronavirus [173], and Ebola virus [174] have been drawing attention as a newly emerging concern in water treatment as they were found to be able to survive in aqueous

phase. Despite the importance of coagulation/flocculation process and necessity of investigation on enveloped virus behavior during this process, there is only limited work available [26], especially in comparison of both types of viruses.

The objectives of this study is 1) to evaluate conventional coagulation with $Al_2(SO_4)_3$ and $FeCl_3$, and Al and Fe electrocoagulation performance against non-enveloped and enveloped viruses, 2) to investigate morphological modifications using transmission electron microscopy (TEM) and computational electron micrograph analysis, and 3) to elucidate biochemical transformation of viral components induced by coagulation processes using Attenuated total reflection Fourier transformed infrared spectroscopy (ATR-FTIR). MS2 and ϕ6 bacteriophage were chosen as a model virus to represent non-envelope and envelope virus, respectively.

Materials and methods

Virus stock preparation

Bacteriophage MS2 (ATCC 15597-B1) and ϕ6 were chosen as surrogates for non-enveloped and enveloped viral pathogens, respectively [175-177]. ϕ6 and its host *Pseudomonas syringae* were kindly provided by Dr. M. Worth Calfee at USEPA. Both phages were propagated and purified following the previous literature with slight modifications [20, 38, 178-180].

For MS2 phage, its bacterial host, *Escherichia coli* (*E. coli*, ATCC 15597), was grown in tryptic soy broth (TSB; tryptone 17 g/L, soytone 3 g/L, dextrose 2.5 g/L, NaCl 5 g/L, K_2HPO_4 2.5 g/L, pH 7.5) at 37 °C until its optical density at 600 nm wavelength (OD_{600}) reached 0.3 (mid-log phase). Then, bacterial cells were inoculated with MS2 phage at multiplicity of infection (MOI) of 0.1 with 1 mM $MgSO_4$ followed by further incubation for next 16 hours. Afterwards, bacterial cell debris were removed by centrifugation at 13,500 g for 20 min at 4°C and serial filtration with

0.2 and 0.1 μm polyethersulfone (PES) filter. MS2 phages were pelletized by ultracentrifugation at 104,000 g for 9 hours at 4 °C, and the pellet was resuspended overnight in 1 mL of phosphate buffer saline (PBS; 4.8 mM of NaH_2PO_4, 17.6 mM of Na_2HPO_4, 145.4 mM of NaCl, pH 7.5). The titer of infective MS2 in resulting stock was routinely obtained as 10^{12} PFU/mL determined following a double-agar layer method [181].

For ϕ6 stock, the host, *Pseudomonas syringae,* was grown in Luria-Bertani medium (LB; tryptone 10 g/L, yeast extract 1g/L, NaCl 8 g/L, pH 7.5) supplemented with 1g/L dextrose, 1 g/L $MgCl_2$ and 0.22 g/L $CaCl_2$ at 26 °C until OD_{640} reached 0.1 followed by ϕ6 inoculation at MOI of 2 and further incubation for next 9 hours. Afterwards, bacterial debris were removed by centrifugation at 12,000 g for 20 min and filtration with 0.2 μm polyether sulfone (PES) filters. The pellet of ϕ6 phages in the resulting suspension was obtained by ultracentrifugation at 104,000 g for 2 hours at 4 °C, and was resuspended overnight in 1 ml of SM buffer (10 mM Tris-HCl, 100 mM NaCl, 50 mM $MgSO_4$, pH 7.5), which was further purified by sucrose gradient purification (10 – 40 %) at 104,000 g for 1 hour at 4 °C. The phage band was recovered and the sucrose medium was replaced with SM buffer using the centrifugal filter (Amicon Ultra-15, 100 kDa Millipore). The titer of final stock resulted in the order of 10^{11} PFU/mL following a double-agar layer method.

Coagulation experiment

Both conventional (chemical) and electrochemical coagulation were performed in a same cylindrical batch reactor with a 450 mL of synthetic water containing 3 mM $NaHCO_3$ and 1 mM $CaCl_2$. The initial pH was adjusted using HCl and maintained at 6.4±0.2 throughout the experiment. The same molar concentration of 0.18 mM Al or Fe was used. All experiments were duplicated.

For conventional Al and Fe coagulation, $Al_2(SO_4)_3$ and $FeCl_3$ were used, respectively. The coagulant was spiked to reach the target dose of 0.18 mM Al or Fe in the beginning of the experiment with a rapid mixing for 2.6 min followed by a slow mixing (flocculation) until the total coagulation/flocculation duration reached 120 min. For electrocoagulation, a concentric assembly of a rod-shaped Al(0) or Fe(0) anode and a perforated annular 316 stainless steel cathode was employed. The gap between electrodes was 2 mm. The anode was electrolyzed for 2.6 min with a rapid mixing followed by flocculation same as for conventional coagulation. It is noted that, in order to electrolyze Al(III) or Fe(II) from the anode at the same rate (1.15 μM/s), different current densities were applied; 4.2 and 2.8 mA/cm^2 for Al and Fe, respectively (see Section A30).

In the course of coagulation/flocculation, 10 mL of suspension was sampled at pre-determined time intervals and sodium sulfite (25 mM) was immediately added to quench hydrogen peroxide. Then the sample aliquot was centrifuged for 20 min at 10,000 g to separate supernatant and flocs. Infectivity assay was performed for supernatant as it was, and for flocs after dissolving them in 9.5 % beef extract solution (pH 9.5 for MS2, and pH 7.5 for ϕ6) following a double-agar layer method. At least two plates showing more than 10 plaques from each replicate were counted and their average and standard deviation are presented in figures.

Transmission electron microscopy.

Untreated and coagulated viruses were negatively stained with 2% uranyl acetate solution without pH adjustment and imaged using FEI Tecnai G2 F20 TEM (Thermo Fisher Scientific) at an accelerating voltage of 200 keV with a Gatan K2 or a Gatan Tridiem GIF-CCD camera. Formvar-coated carbon grids (300 mesh) were glow-discharged. For untreated virus imaging, stock was directly used. For coagulated viruses, the suspension was sampled and directly mounted on the grids without any attempt to dislodge viruses from flocs.

Fourier-transformed infrared spectroscopy

ATR-FTIR spectra of untreated and coagulated viruses were obtained using Nicolet iS10 spectrometer (Thermo Fisher Scientific) with an Ever-Glo MIR source, KBr beam splitter, DTGS detector. In order to amplify the signal from the virus, samples pelletized and directly mounted on the iTX accessory for the measurement. Intact MS2 and ϕ6 pellet was formed by centrifuging the prepared stock at 104,000 g for 9 hours and 2 hours, respectively. For coagulated virus, coagulation experiment was performed at an elevated initial virus concentration (~10^{11} PFU/mL) and 35 mL of the suspension was centrifuged at 104,000 g for 30 min to form a pellet of mixture of viruses and Al or Fe precipitates. The spectrum was acquired by coadding and averaging 128 scans at 4 cm^{-1} resolution. Afterwards, the original spectrum was processed with ATR-correction, auto-base line correction, 9-point Savitzky-Golay smoothing and normalizing by the largest peak intensity [182]. In order to confirm the minimal contribution of biochemical residues and contaminants possibly remaining in virus stock to the spectrum, a control pellet sample was prepared by following the stock preparation protocol without virus inoculation, which yielded a negligible spectral profile as shown as gray-dashed lines in Figure IV-6A and 6B.

Results and discussion

Al and Fe (electro)coagulation of non-enveloped and enveloped virus

Virus attenuations by four different coagulation approaches were compared using MS2 and ϕ6 at the same molar concentration of 0.18 mM Al or Fe and pH 6.4. Following coagulation under a rapid mixing for initial 2.6 minutes, the suspension was slowly stirred for an extended duration (120 minutes in total) to clarify the impact of coagulant-virus interaction on virus infectivity. Figure IV-1 summarizes infective virus fractions in bulk water over time. The results of negative

controls (i.e., no coagulation, black solid lines in Figure IV-1A and 1B) demonstrated that suspended virions remained infective and colloidally-stable in the absence of coagulant addition.

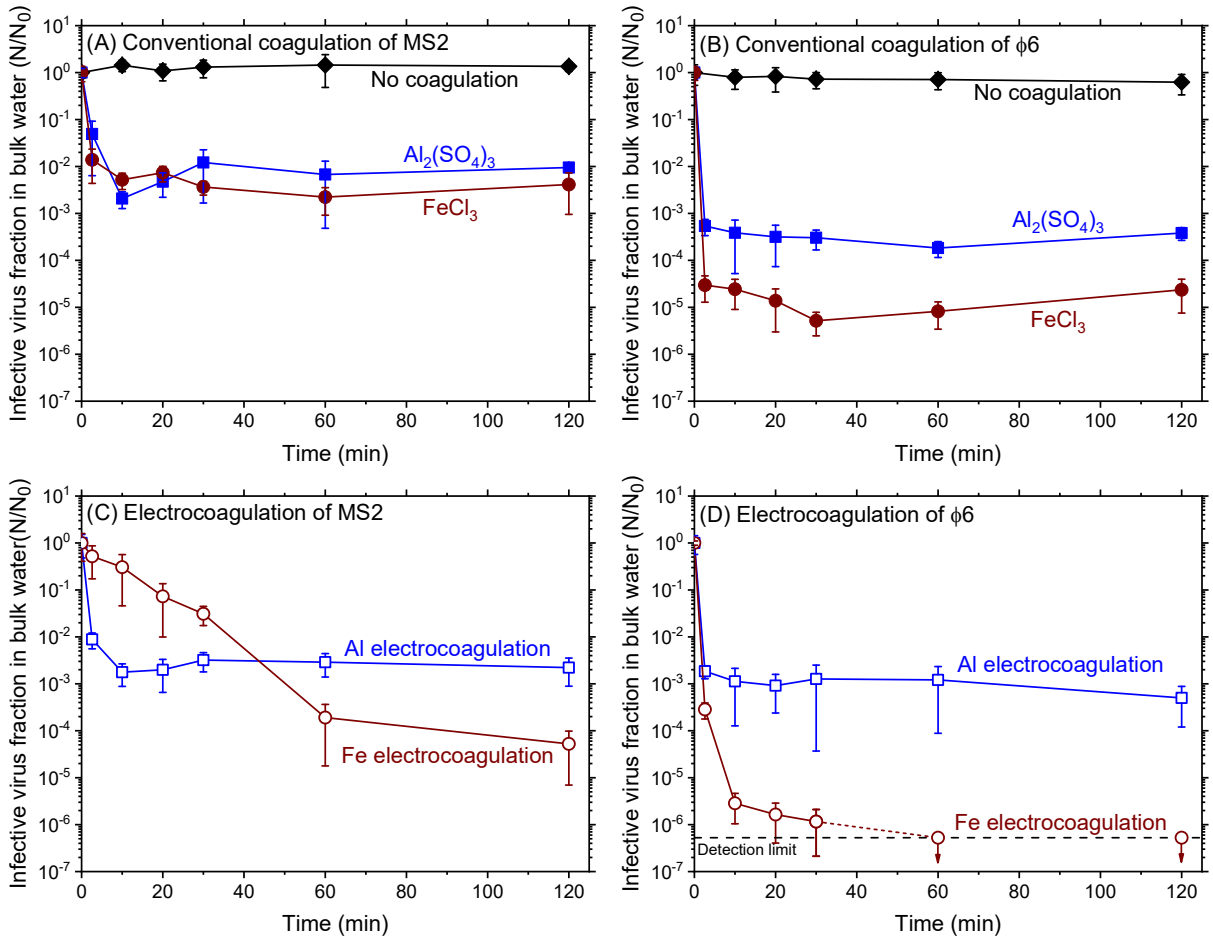

Figure IV-1. Coagulation of MS2 and ϕ6 with $Al_2(SO_4)_3$, $FeCl_3$, Al electrocoagulation, and Fe electrocoagulation at 0.18 mM Al or Fe and pH 6.4. Infective virus concentration in bulk water was normalized by initial bulk concentration, N_0. Negative controls (black solid lines) ensured that only coagulant addition was attributed to decline of infective virus fraction.

Both $Al_2(SO_4)_3$ and $FeCl_3$ coagulation resulted in a sharp decline of infective virus fraction in bulk water followed by a relatively constant profile for both MS2 (Figure IV-1A) and ϕ6 (Figure IV-1B). This trend signifies that 1) virus adsorption onto Al and Fe flocs during the flocculation is negligible, 2) adsorption of soluble Al(III) and Fe(III) species such as $Al(OH)_2^+$ and $Fe(OH)_2^+$ to virions during the flocculation insignificantly contributes to virus mitigation, and 3) hence, a

long detention time of flocculation may not be required for virus control using conventional chemical coagulation.

Meanwhile, $Al_2(SO_4)_3$ and $FeCl_3$ coagulation showed a statistically insignificant difference ($p > 0.05$) in MS2 phage attenuation from bulk water achieving 2.2±0.1 and 2.4±0.1 log reduction (calculated from data points at t= 10 ~ 120 min), respectively (Figure IV-1A). Similar result for other non-enveloped viruses such as adenovirus type 40 and poliovirus type1 was reported in a previous study [183]. In contrast, as seen in Figure IV-1B, $FeCl_3$ coagulation outperformed its Al counterpart for ϕ6 phage resulting in a higher log reduction by 1.4±0.2 log consistently throughout flocculation (t= 2.6 ~ 120 min). In addition, attenuation of ϕ6 by both Al and Fe chemical coagulant was to a greater extent compared to that of MS2 by 1.3±0.2 and 2.5±0.2 log during t= 10 ~ 120 min, respectively. Given that the presence of lipid envelope is the major structural difference between these two viruses, these results suggest that viruses can behave differently in response to the chemical coagulant type, and it may arise from the difference in the viral components.

Al electrocoagulation resulted in a similar temporal trend of infective virus fraction to that of $Al_2(SO_4)_3$ coagulation for both MS2 and ϕ6; an initial decline was followed by a stationary profile. Also, attenuation extent turned out to be similar for MS2 (0.4±0.2 log difference calculated from t= 10 ~ 120 min) and statistically same for ϕ6 ($p \geq 0.05$ from t= 2.6 ~ 120 min) compared with that of $Al_2(SO_4)_3$ coagulation. This is attributed to the fact that the chemistries of both approaches are essentially identical. As proven in Figure A-32, Al(III) is dissolved into the aqueous phase during the electrolysis of Al^0 anode in Al electrocoagulation. Hence, it is expected that Al speciation following an instantaneous hydrolysis of Al^{3+} would be same regardless of the dosing mechanisms under controlled pH condition [184].

Interestingly, MS2 and ϕ6 responded differently to Fe electrocoagulation. A gradual decrease of infective MS2 fraction in bulk water was observed, overtaking $FeCl_3$ coagulation around 40 minutes. However, Fe electrocoagulation yielded a rapid drop of infective ϕ6 fraction similar to $FeCl_3$ coagulation, but it was followed by a continuous decline, and also outperformed $FeCl_3$ coagulation during the entire course of coagulation and flocculation. Aforementioned results again indicate the possible impact of viral structure on coagulation efficiency depending on coagulant type and approach.

Virus removal and inactivation during coagulation.

In general, virions in aqueous phase are expected to be physically destabilized and removed during the coagulation via two mechanisms; charge neutralization by positively-charged soluble coagulant species followed by aggregation and sweep coagulation by insoluble precipitates [185]. Nonetheless, inactivation of non-enveloped viruses during (electro)coagulation has also been reported [14-16, 48, 49] while enveloped viruses have been scarcely investigated. Total infective virus fraction (bulk water + flocs) of MS2 and ϕ6 during each coagulation process is summarized in Figure IV-2 (see Section A31 for floc concentration only).

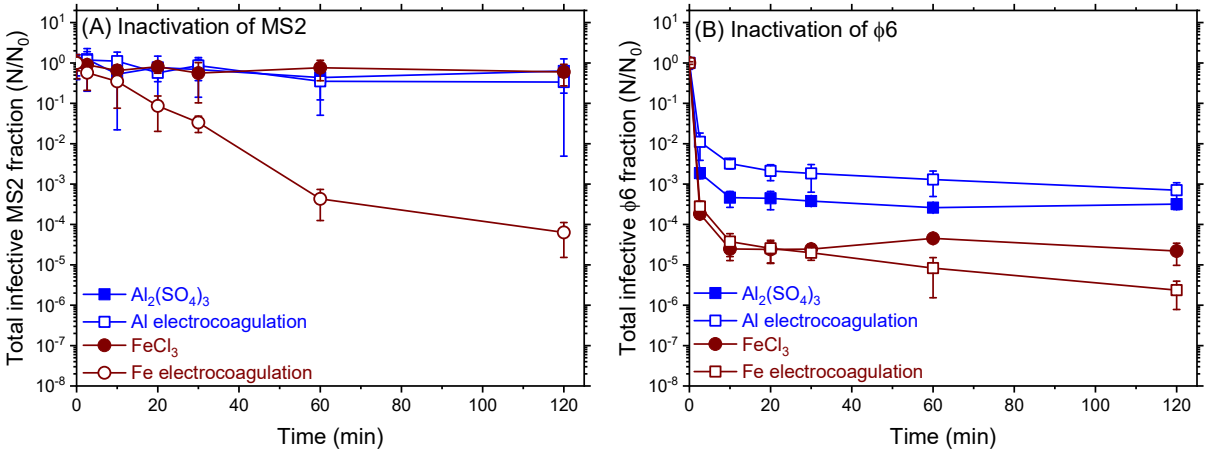

Figure IV-2. Inactivation of MS2 ϕ6 during the course of coagulation process. Total infective virus concentration (bulk water + flocs) was normalized by initial bulk concentration, N_0.

As seen in Figure IV-2A, MS2 phages maintained their infectivity during the entire course of treatment with $Al_2(SO_4)_3$, $FeCl_3$, and Al electrocoagulation. Constant recovery of MS2 phages from Al and Fe precipitates at the concentration close to the initially-spiked concentration (~10^8 PFU/mL) during these three coagulation approaches (Figure A-33A and 33C) directly proves that most of the phages were physically removed by flocs and these flocs did not compromise MS2 infectivity. Moreover, as observed in Figure IV-1A and 1C, soluble Al/Fe species did not inactivate the phages because the bulk concentration showed a plateau during the flocculation. Therefore, during these three coagulation processes, physical removal of bulk MS2 phage was predominated by sweep coagulation by flocs and any coagulant species did not induce virus inactivation. Virus inactivation during Al electrocoagulation due to anodic generation of free chlorine has been reported elsewhere [16], but it was not observed in this study probably because of low chloride concentration.

In contrast, a gradual decrease of total infective MS2 fraction during Fe electrocoagulation clearly indicated that MS2 was inactivated contrasting to $FeCl_3$ coagulation. This is attributed to the fundamental difference in Fe dosing mechanism between these two processes. As shown in Figure A-32B, Fe^{2+} is dissolved from Fe^0 anode during the electrolysis for the Fe electrocoagulation while Fe^{3+} are directly added in $FeCl_3$ coagulation. During Fe electrocoagulation, it has been suggested that Fenton's reaction can be triggered by Fe(II) in combination with dissolved O_2 producing •OH and/or Fe(IV) [186-188] which are virucidal [88, 92, 189]. A continuous decrease in infective MS2 fraction in Fe flocs (Figure A-33C) directly demonstrated the virus inactivation on the surface of flocs.

Similar to Fe electrocoagulated MS2, ϕ6 phages were seemingly inactivated by all types of coagulation processes as shown in Figure IV-2B. A poor recovery of infective ϕ6 phages from

Al and Fe precipitates may indicate viral inactivation upon contact with these precipitates (Figure A-33B and 33D). However, unlike MS2 cases, a complete recovery of infective ϕ6 phages from flocs was not achieved in any sets of coagulation experiment, which raises the possibility of imperfect virus extraction from the flocs [190, 191]. Hence, direct observation of coagulated ϕ6 as well as MS2 was made using electron micrography to elucidate the consequence of virus-coagulant interaction as follows.

Viral morphology alteration induced by coagulation

Impact of each coagulation treatment on virus structure was investigated by visualizing treated viruses and comparing them with untreated ones. Intact MS2 capsid is characterized by its icosahedral shape with a maturation protein (A-protein) connected to a single-stranded RNA encapsulated in the capsid [192]. Figure IV-3A shows intact MS2 virions measuring a size of 26±0.6 nm (50 virions analyzed in total), close to the values presented in previous studies [57, 193, 194]. A well-defined hexagonal outline of the selected MS2 virions confirms the icosahedral nature of capsid structure (Figure IV-3A1-3A3). Note that A-protein was not able to be visualized. Meanwhile, intact ϕ6 is composed of three layers; from the exterior, a lipid envelope with spike (receptor) proteins embedded, a nucleocapsid, and a procapsid packaging three segments of double-stranded RNA [127]. Figure IV-3B shows spherical intact ϕ6 virions whose size was measured as 73±2.2 nm (50 virions analyzed) showing a good agreement with previously reported values [127, 195]. As pronounced in Figure IV-3B1-3B3, a layered-structure of ϕ6 was confirmed with a hexagonal capsid inside [196]. Nonetheless, the inner boundary of lipid envelope was not clearly discernible, and embedded spike proteins were not identifiable. Morphological changes of MS2 and ϕ6 after each coagulation approach is presented in the following separate sections.

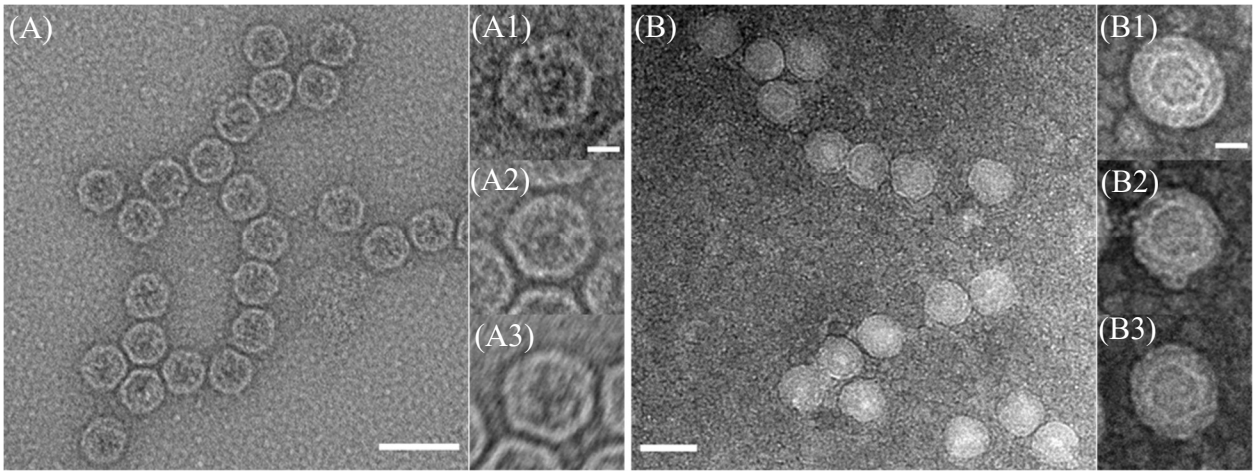

Figure IV-3. Electron micrographs of untreated viruses. Intact MS2 virions show a single layer of protein capsid (A, scale: 50 nm). Hexagonal structure of representative MS2 virions confirm their icosahedral capsids (A1-A3, shared scale: 10 nm). Intact ϕ6 virions appear to have a layered-structure (B, scale: 100 nm) with a hexagon inside (B1-B3, shared scale: 25 nm).Non-enveloped phage MS2

MS2 virions after conventional coagulation and electrocoagulation (t= 20 min, 0.18 mM Al or Fe) are shown in Figure IV-4A-4D. Severe aggregation of virions was found in common after all coagulation processes demonstrating effective destabilization of virions. However, a noticeable morphological alteration was observed exclusively in Fe electrocoagulated viruses. As seen in Figure IV-4A-4C, MS2 particles appeared to be morphologically intact maintaining their continuous viral capsid boundary. Note that the capsid may appear thicker than untreated phages due to the presence of Al or Fe precipitate in contact with the capsid, confirming the presence of Al/Fe precipitates around the phage particles. In contrast, Fe electrocoagulation resulted in irregular-shaped virus particles (Figure IV-4D) explicitly demonstrating the loss of structural integrity of protein capsids. Figure IV-4E enlarges the yellow-boxed area in Figure IV-4D to highlight discontinuous/open-ring or irregular boundary of capsid layers as pointed with yellow arrows. Computer-assisted analysis to match the electron density maps to the architecture of Fe electrocoagulated MS2 particles shown in electron micrographs was performed to further elaborate protein capsid deformation. Briefly, a publicly available electron density map of intact MS2 virion

(accession number EMD-1431) was modified to find the best-matching 3-dimensional structure with capsid damage to a selected virus particle in electron micrographs (see Section A34 for detailed protocol). For example, a yellow-circled damaged MS2 particle in Figure IV-4E shows a capsid shell with angled corners in its upper part and an empty density (dark area) in lower part. The best-matching electron density map was found as shown in Figure IV-4F, which demonstrates a capsid shell maintaining the icosahedral structure with an opening as a result of the damage.

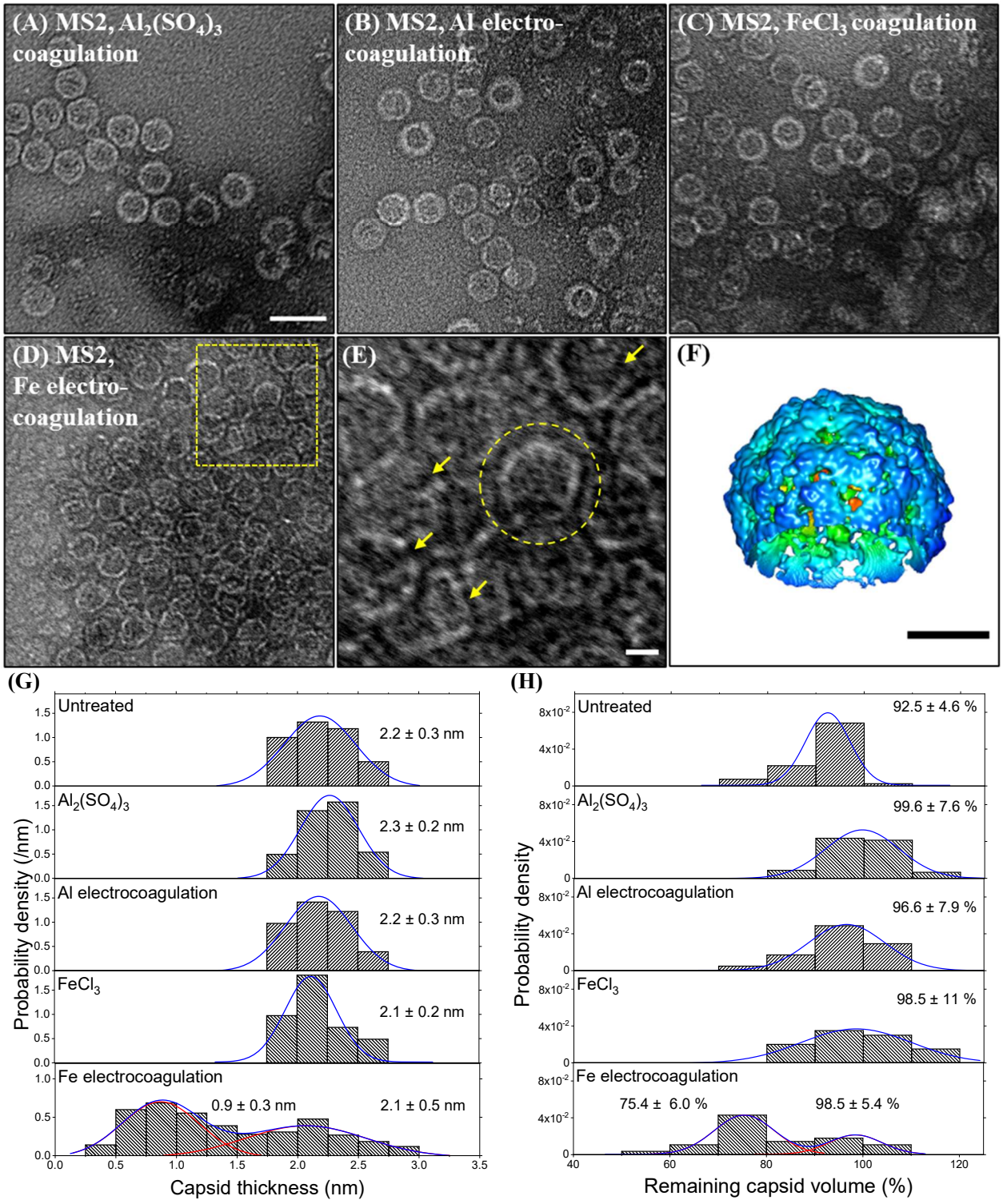

Figure IV-4. (A-D) Electron micrographs of MS2 virions after each coagulation treatment as labeled (scale bar equals 50 nm and shared with A-D). (E) enlarges the yellow-boxed area in (D), and is followed by (F) which is a computationally-simulated damaged structure of a yellow-circled MS2 particle in (E). Scale bars in (E) and (F) equal 10 nm. (G) and (H) depict capsid thickness (20 ~ 30 virions analyzed for each case) and

remaining capsid volume distribution of untreated and coagulated MS2 (15 ~ 25 virions analyzed for each case), respectively.

Quantitative image analysis was performed for the selected MS2 particles in the electron micrographs to investigate changes in capsid thickness and volume. It is noted that coagulated MS2 virions with abnormally thick capsids due to interference of Al or Fe precipitates, and with open-ring structures significantly deviated from a spherical shell were excluded from the analysis. Capsid thickness distribution was computationally obtained using MATLAB code developed to load a boxed-out MS2 virion micrograph, band-pass filter it, read the gray-scale profile across the capsid, fit it to Gaussian distribution, and read its full width at half maximum values as capsid thickness [56]. For untreated and coagulated MS2 with $Al_2(SO_4)_3$, Al electrocoagulation and $FeCl_3$, capsid volumes were calculated assuming a spherical shape without any damages as they were below the minimum volume change (~10 %) that could be computationally recognizable. The remaining capsid volume of Fe electrocoagulated MS2 was obtained from the best-matching electron density map generated via computational analysis as explained above. Calculated volumes were normalized by the value of the reconstructed MS2 (EMD-1431). As shown in Figure IV-4G and 4H, changes in capsid thickness and volume after coagulation showed a similar trend to overall morphological alterations; only Fe electrocoagulated MS2 resulted in noticeably different distributions with an extra population of a thinner capsid thickness and a smaller capsid volume while the other coagulation approaches yielded distributions similar to intact ones.

Aforementioned visual observations and quantitative assessments on morphological changes after each coagulation approach indirectly support infectivity assay results shown in Figure IV-2A. Uncompromised structural integrity of MS2 virions after coagulation with $Al_2(SO_4)_3$, Al electrocoagulation, and $FeCl_3$ rationalizes a negligible loss of viral infectivity when MS2 was coagulated via these coagulation approaches. In contrast, a continuous decline in

infective MS2 fraction during Fe electrocoagulation (Figure IV-2B) can be explained by altered structures shown in Figure IV-4D. Although A-protein was not visually discernible, the loss of a portion of capsid infers the possibility of A-protein displacement since it is a part of a whole capsid shell replacing a copy of capsid protein [192]. Given the role of A-protein to recognize and bind to host bacterium, MS2 particle missing A-protein would not be able to successfully anchor to the surface of bacterial pilus. Also, MS2 particle with an open-ring or a discontinuous capsid may not be able to deliver its RNA to host bacterium cell because internal stress required to inject RNA into the cell might have dissipated [57] or RNA might have been released from the capsid [197].

Enveloped virus ϕ6

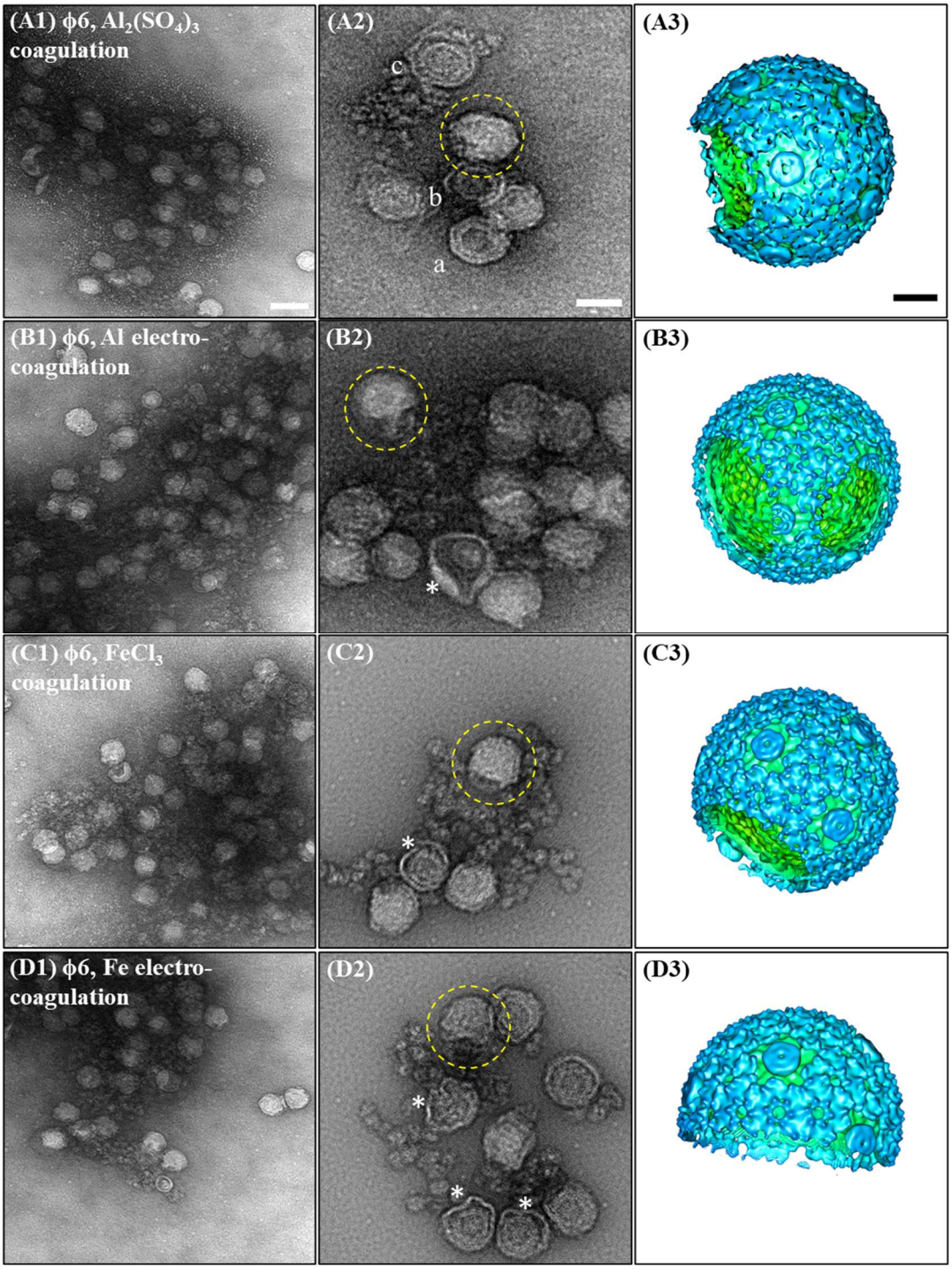

Figure IV-5. Large-view electron micrographs of ϕ6 particles after each coagulation treatment as labeled (first column, A1-D1, shared scale: 100 nm) followed by enlarged-view to probe morphological changes (second column, A2-D2, shared scale: 50 nm) and computationally-generated best-matching damaged particles circled in yellow in A2-D2 to confirm and quantify nucleocapsid damage (third column, A3-D3, shared scale: 10 nm).

Similar to MS2, ϕ6 particles formed large agglomerations after treated by all coagulation approaches (images in the first column of Figure IV-5). However, morphological modifications were accompanied in all cases, not only by Fe electrocoagulation. After all types of coagulation treatment, observed particles measured in a size ranging from 55 nm ~ 60 nm which is close to that of nucleocapsid [195], indicating that these particles lack lipid envelopes. In addition, nucleocapsid damage was also found. In Figure IV-5A2, three particles showing internal details are presented. An intact double-layered particle (labeled as 'a') measured about 55 nm and 40 nm of outer and inner layer, respectively. Based on the hexagonal cross-sectional shape and the size of each layer, this particle was presumed to be an icosahedral nucleocapsid with a procapsid (or polymerase complex) inside [196, 198]. Above this particle, two other double-layered particles are shown with less structural integrity, e.g. discontinuous (labeled as 'b') or irregular (labeled as 'c') outer layer, demonstrating that nucleocapsid of ϕ6 can be damaged by $Al_2(SO_4)_3$ coagulation. Meanwhile, the particle in the yellow circle does not reveal its internal structure, but it was also considered as a damaged nucleocapsid lacking a lipid envelope based on its comparable size to the other particles labeled as 'a', 'b' and 'c', angled right corners, and seemingly missing density on the left corner. Our computational analysis confirmed the presence of the damaged corner as shown in Figure IV-5A3. The other coagulation approaches yielded similar features of ϕ6 nucleocapsid; Al electrocoagulation resulted in ϕ6 nucleocapsid particles (Figure IV-5B2) missing a portion of capsid shell (yellow circled, simulated as shown in Figure IV-5B3) or appearing as a shell with a large opening (white asterisk), ruptured/deformed nucleocapsid layers (white asterisks) and damaged nucleocapsid shells (yellow circled particles, simulated particle shown in the next column) after $FeCl_3$ and Fe electrocoagulation as seen in Figure IV-5C2 and 5D2, respectively. As seen in Figure A-35, a quantitative analysis on ϕ6 nucleocapsid volume change confirmed that all

coagulation approaches induced the damages showing portions of the volumes less than 90% of intact nucleocapsid.

Observed morphological changes in virus structure can possibly bring inactivation of ϕ6. Although alteration or detachment of spike proteins from the lipid layer was not explicitly visualized, the nucleocapsid missing its lipid envelope is likely to lack spike proteins as well since they are embedded in the envelope [199]. Hence, such particles (bare nucleocapsids) would fail in docking onto host bacterial cells [105]. In addition, the lipid bilayer fusion with host cell outer membrane to deliver the nucleocapsid encapsulating dsRNA segments into periplasmatic area [200] would not be triggered as the process requires catalytic function of spike proteins [105, 201]. Nucleocapsid breakage can also bring infectivity loss because lytic enzyme proteins on its surface is necessary for local digestion of peptidoglycan layer of the host cell and subsequent entry to the cell cytosol [202]. Lastly, the possibility of RNA release from the capsid cannot be excluded [203].

Spectral investigation of viral deformation/transformation upon coagulation

FTIR spectra of untreated and coagulated viruses were obtained to probe molecular alterations in viral compositions induced by coagulation. Peak locations were identified by taking second derivatives of the spectrum [153]. For the relative amount of protein secondary structures, amide I region was decomposed into separate peaks whose relative areas were measured assuming Lorentzian distribution [80] (see Section A36). Given a complexity of viral structure, it should be noted that interpretation on spectral changes is only suggestive [74, 204]. Figure IV-6A and 6B summarize the results in the range of 3050 cm^{-1} ~ 2800 cm^{-1} and 1800 cm^{-1} ~ 950 cm^{-1} of MS2 and ϕ6, respectively. Assignments and contributors of identified peaks are shown in Table A-9.

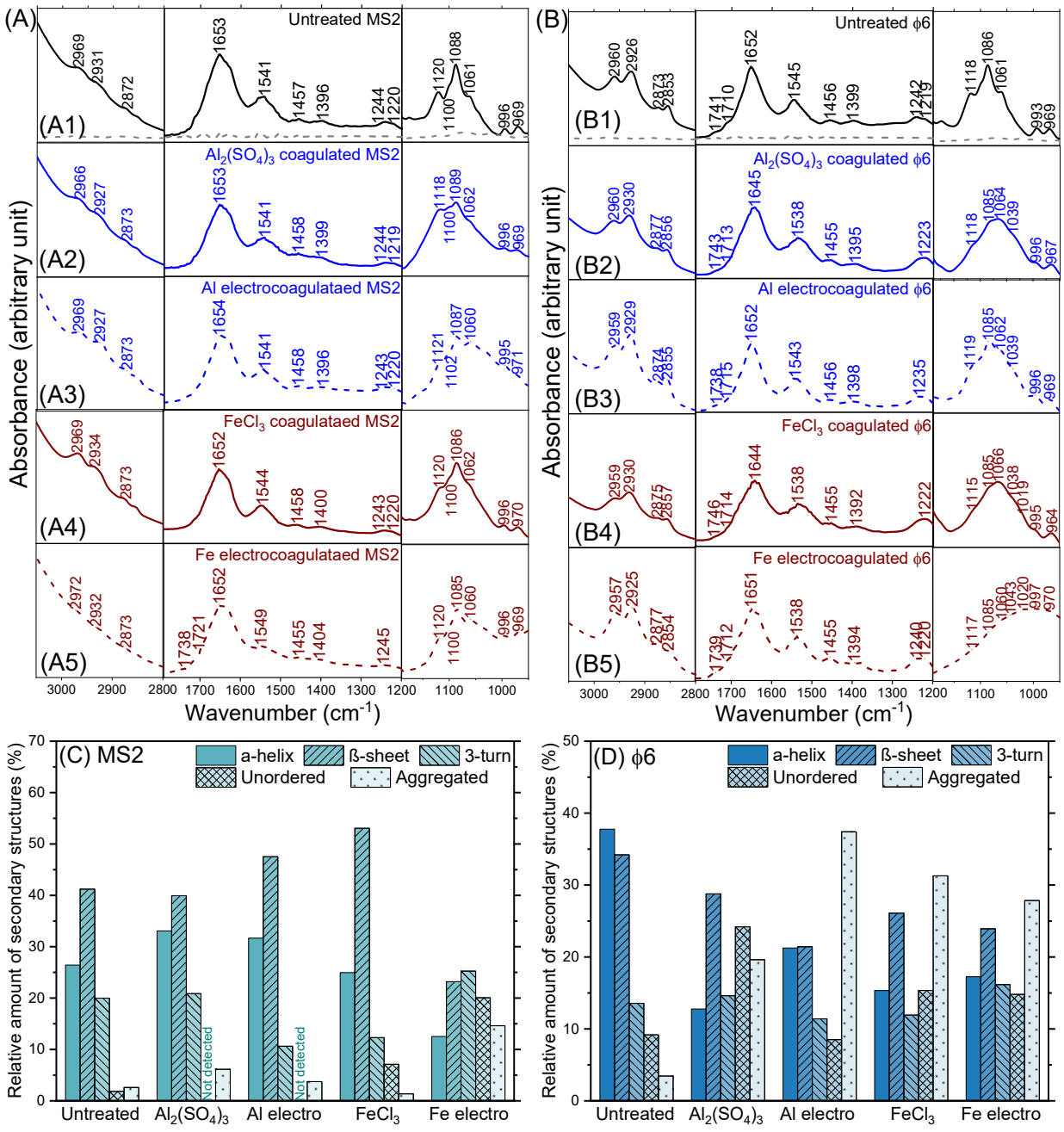

Figure IV-6. FTIR spectra of untreated and coagulated viruses, MS2 (A) and ϕ6 (B). Changes in relative amount of secondary structures of MS2 (C) and ϕ6 (D).

Untreated MS2 showed component-associated peaks (Figure IV-6A1). Two wide bands appeared at 1653 cm^{-1} (amide I, ν(C=O)) and 1541 cm^{-1} (amide II, δ(NH) and ν(C-N)) indicating the presence of protein backbone structure [73] along with hydrocarbon peaks (2969 cm^{-1} ~ 2872

cm^{-1}, 1457 cm^{-1} and 1396 cm^{-1}) of amino acid side chains, while characteristic peaks of genomic materials such as $\nu_{as}(PO_2^-)$ at 1244 and 1220 cm^{-1}, ν_s(C-O) at 1120 cm^{-1}, $\nu_s(PO_2^-)$ at 1100 and 1088 cm^{-1}, ν_s(C-O) at 1061 cm^{-1}, C-O and/or C-C of ribose at 996 cm^{-1}, and $\nu(PO_4^{2-})$ at 969 cm^{-1} confirming RNA. Similarly, untreated ϕ6 spectrum (Figure IV-6B1) displayed characteristic peaks of its compositions: acyl chains (2960 ~ 2853 cm^{-1}) and carbonyl groups (1741 and 1710 cm^{-1}) of lipid envelope, amide I/II (1652 and 1545 cm^{-1}, respectively) and hydrocarbon chains (1456 and 1399 cm^{-1}) of protein capsids, and moieties/bondings such as PO_2^-, PO_4^{2-}, and C-O/C-C associated with RNA (1242 ~ 969 cm^{-1}).

Figure IV-6A2-A5 depict spectral profiles of the coagulated MS2. It is noted that the peaks associated with amorphous Al precipitates such as AlO_4 tetrahedra at 992 and 967 cm^{-1} [205] were not pronounced while amorphous Fe precipitates has been shown to not yield any peaks in the investigated spectral range [206]. In overall, infrared spectral profiles of all coagulated MS2 except Fe electrocoagulation resembled that of untreated phage indicating that there was only marginal biochemical alteration induced by these three coagulation approaches. A noticeable increase of a peak at 1118 cm^{-1} in $Al_2(SO_4)_3$ coagulation was attributed to the adsorption of sulfate to Al flocs [207]. In contrast, Fe electrocoagulation appeared to have caused spectral changes potentially indicative of capsid protein oxidation and its structural deformation. Several new peaks arising above 1700 cm^{-1} were assigned to the carbonyl group which can be formed as a result of protein oxidation [208]. Also, decrease in amide II region can be attributed to protein structure alteration [76]. Changes in relative amount of protein secondary structures further pronounced the oxidative environment and consequent capsid deformation during Fe electrocoagulation. As depicted in Figure IV-6C, aggregated and unordered structures notably increased after Fe electrocoagulation compared to other coagulation approaches.

After both conventional coagulation of ϕ6 with $Al_2(SO_4)_3$ and $FeCl_3$, and Al electrocoagulation, a blue-shift of $\nu_{as}(CH_2)$ and $\nu_s(CH_2)$ was observed (2926 cm^{-1} to 2930/2929 cm^{-1}, and 2853 cm^{-1} to 2855~2857 cm^{-1}, respectively) indicating a conformational change of acyl chains of lipid into a disordered structure [209, 210], which indirectly explains bare ϕ6 nucleocapsids without lipid envelopes observed in electron micrographs (Figure IV-6B2, 6B3, and 6B4). New peaks at 1064 and 1039 cm^{-1} after $Al_2(SO_4)_3$ coagulation were attributable to the inner-sphere P-O-Al complex [211] possibly due to the adsorptive interaction between hydroxyl groups on amorphous $Al(OH)_3$ and viral phosphate moieties in lipid envelop via ligand exchange [212]. Similarly, $FeCl_3$ coagulation resulted in several new peaks centered at 1066, 1038, 1019, and 995 cm^{-1} which can be assigned to inner-sphere P-O-Fe coordination [212-215] suggesting adhesion of Fe flocs and viral lipid. As a result of Fe electrocoagulation of ϕ6, oxidative impact was pronounced with arise of peak centered at 970 cm^{-1}, which can be assigned to trans double bond indicative of lipid oxidation [160]. In addition, changes in amide I band shape are indicative of protein secondary structure alterations. Band decomposition in amide I region revealed that all types of coagulation increased the unordered and aggregated structures (Figure IV-6D). This result is accordance with morphological changes in nucleocapsid found in electron microscopic images shown in Figure IV-5.

Conclusions

Virus mitigating efficiency of four different coagulation approaches was evaluated using MS2 and ϕ6 phage, as a model virus with a non-enveloped and enveloped structure, respectively, in a synthetic water. $Al_2(SO_4)_3$ and $FeCl_3$ rapidly attenuated both phages from bulk water suggesting that a long contact time between virus and coagulant is not necessary when these

coagulants are adopted. Meanwhile, Al electrocoagulation resulted in a similar virus attenuation for both phages to $Al_2(SO_4)_3$ chemical coagulation. Therefore, Al electrocoagulation for virus control as an alternative to its conventional counterpart should be carefully considered taking account of water chemistry like chloride content to expect additional contribution from inactivation mechanism by anodically-generated free chlorine [16, 216]. Fe electrocoagulation was found to be more effective against both phages than any other coagulation approaches. However, it should be noted that MS2 phage only showed a gradual decline of infective bulk concentration necessitating a sufficient contact time for Fe electrocoagulation, whereas ϕ6 phage resulted in a steep decline similar to chemical coagulations.

Divergent behavior of MS2 and ϕ6 phage in each coagulation approach estimated by infectivity assay may arise from the structural difference (i.e., lipid envelope). The protein capsid of MS2 phage was found to be resistant to contact with both flocs. In contrast, the lipid envelope of ϕ6 phage was completely ruptured and removed during the chemical coagulations hinting that the envelope may make the phage relatively more vulnerable compared to MS2 phage. In addition, nucleocapsid of ϕ6 phage was also damaged by both flocs indicating that different protein capsid properties may also play a role in capsid damage. The results presented in this study can be carefully extended to predict the behavior of other pathogenic viruses. Non-enveloped viruses with a similar capsid thickness and/or size to MS2 may be persistent during conventional coagulation and Al electrocoagulation whereas they are subject to oxidative damage during the Fe electrocoagulation. Similarly, enveloped animal virus may be readily inactivated during the all coagulation processes due to lipid layer damage.

CHAPTER V

REJECTION AND FOULING OF *ACHOLEPLASMA LAIDLAWII* DURING MICROFILTRATION

Introduction

Microfiltration has been extensively applied in various areas including water treatment, pharmaceutical industry, food production, and biotechnology [217]. Membrane fouling has been a critical concern as it diminishes the filtration performance overtime [218]. Hence, as an effort to understand the fundamentals of fouling, mathematical models have been developed to describe different modes of fouling namely complete blocking (or pore sealing), standard blocking (or pore constriction), intermediate blocking, and cake filtration [219-222]. Successful application of the models have been demonstrated for proteins [223] and humic acids [224] providing insights into fouling behaviors of these particles. However, relatively less attention has been paid to soft or deformable particles.

Meanwhile, mycoplasma, a trivial name of *Mollicutes*, is a particular concern in biopharmaceutical industry as it has been identified as a prevailing contaminant of the products manufactured with plant and animal sources [225]. Owing to its distinguishable characteristic of cell-wall deficiency, thus lack of rigidity, the use of sterilizing grade filters rated at 0.2 and 0.1 μm has been reported to fail to prevent the contamination [225-228].

Given the value as a target contaminant as well as a model particle with a high deformability, *A. laidlawii* is selected in this study. The aim of this study is to investigate the effect of particle flexibility during the microfiltration. *A. laidlawii* was chosen as a model soft particle

and its retention and fouling were evaluated with polycarbonate track-etched membrane filters in comparison with spherical silica colloid in a similar size as a rigid counterpart.

Materials and methods

Preparation and quantification of A. laidlawii and silica particles

A. laidlawii (ATCC 23206) was cultured following a protocol presented in [225] with slight modifications. A basal medium containing polypeptide (40 g/L), trizma-base (5 g/L), and glucose (7 g/L) was sterilized by autoclaving at 121 ℃ for 15 min and cooled down to ambient temperature, to which bovine serum albumin (BSA, 4 g/L) in deionized water was aseptically added after being filtered with 0.2 μm polyether sulfone (PES) syringe filter. Afterwards, oleic acid and palmitic acid stock that were separately prepared in 99.5 % ethanol (both at 50 mg/mL) were supplemented at 0.04 % (v/v). After adjusting its pH to 7.2±0.2, the final medium was filtered with 0.1 μm polyvinylidene difluoride (PVDF) membrane filter.

A. laidlawii cells were cultured in the final medium for approximately 72 hours under aerobic condition at 37 °C with gentle shaking followed by dialyzing with 12-14 kDa dialysis tube for 7 hours to remove soluble substances. The final stock routinely showed the titer of ~10^9 CFU/mL. Electron micrograph of the stock depicts a spherical morphology of bacterial cells in size of 329±12 nm (Figure V-1A). For viable cell assay, agar plates containing agar (12 g/L), peptone (10 g/L), trizma-base (5 g/L), beef heart infusion (6 g/L), glucose (7 g/L), BSA (4 g/L), oleic acid (0.02 g/L), and palmitic acid (0.02 g/L) were prepared. Similar to the liquid medium, following autoclave at 121 ℃ for 15 min, agar base was cooled down to 45 ℃ and separately prepared BSA, oleic acid, and palmitic acid were supplemented.

Silica suspension was prepared with 300 nm silica nanosphere standard (NanoXact, nanoComposiz) as a stock (Figure V-1B). It is noted that silica particle concentrations were determined based on the stock concentration (3.5×10^{11} particles/mL) provided by the manufacturer.

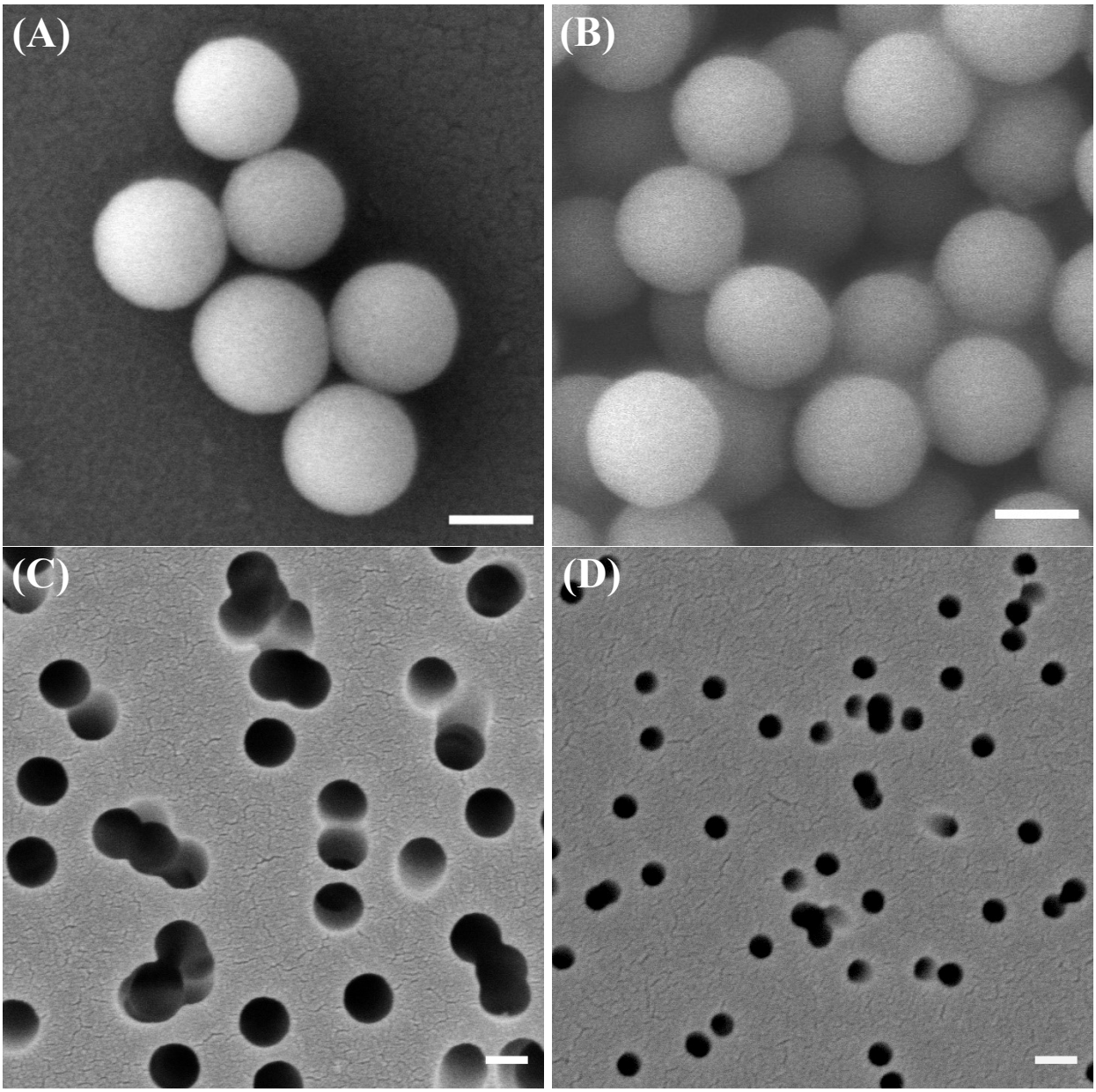

Figure V-1. Scanning electron micrograph of unpressurized A. laidlawii cells (A), silica particles (B), and 0.2 (C) and 0.1 µm rated track-etched membrane filters (D). All scale bars equal 200 nm. It is noted that the fraction of multiples are exaggerated in these micrographs. See Table 1 for the pore characterization results.

Membranes

Polycarbonate track-etched (PCTE) membranes with pores nominally rated at 0.1 and 0.2 μm (Isopore™ Membrane Filters, Millipore Corporation, Bedford, MA) were used. However, electron micrographs of membrane surfaces revealed the existence of multiplets or intersecting pores (Figure V-1C and 1D) forming larger entries than rated pore sizes. 4439 and 2622 pores in total for 0.1 and 0.2 μm membrane, respectively, were analyzed for pore characterization. Table V-1 summarizes the fraction of multiplets and pore density. Pore size distributions as equivalent diameter (d_e) and the longest dimension (d_l), which is the distance between two extrema of a multiplet, were also obtained as shown in Figure V-2.

Table V-1. Summary of membrane characterization.

Nominal pore size (μm)	Fraction of multiplets (%)				Pore density ($\times 10^8$ /cm^2)
	Singlet	Doublet	Triplet	Quadruplet	
0.1	84.7	12.6	2.4	0.3	4.6 ± 0.2
0.2	79.4	15.3	4.2	1.1	3.7 ± 0.1

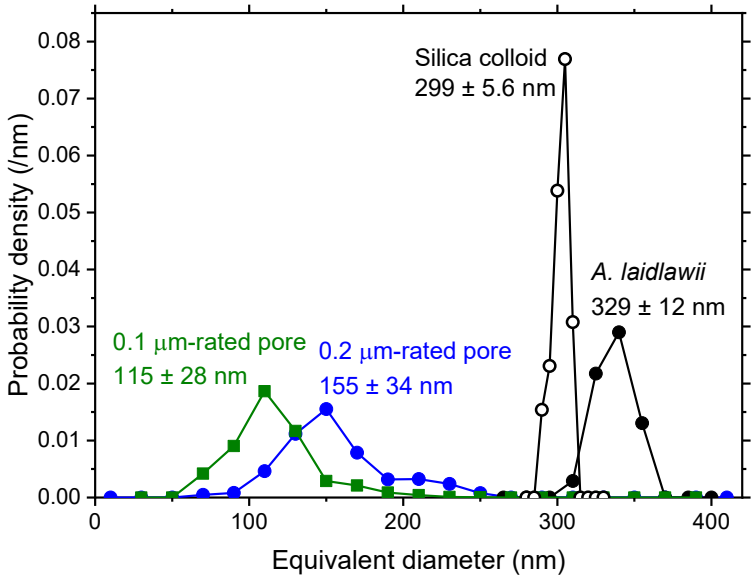

Figure V-2. Distribution of equivalent pore diameter of membranes (4439 and 2622 pores were analyzed for 0.1 and 0.2 μm-rated membrane, respectively) and particles (55 and 100 particles were analyzed for A. laidlawii and silica colloid, respectively). Both types of particles were found to be virtually bigger than pores.

Filtration experiment

All filtration experiments were conducted in a commercially available dead-end cell (Model 8010, Millipore Corporation, Bedford, MA) with an effective filtration area of 4.1 cm^2 at room temperature. The pressure and cumulative permeate mass were measured by a pressure transducer (P598, Johnson Controls) and a weighing balance (Navigator, OHAUS), respectively, and were computationally recorded using a laboratory-developed data acquisition program written in LabVIEW (National Instruments, Austin, TX). Prior to each filtration, membrane pores were saturated with 0.1 μm filtered phosphate buffer saline (PBS, pH 7.2) by passing it through the membrane at the pressure for the actual filtration experiment with bacterial or silica suspension. Feed suspension of bacterial cells and silica particles was prepared by diluting stocks in 0.1 μm filtered PBS to reach desired concentrations. Viable bacterial cells in the feed suspension and permeate were quantified by aerobically incubating 1 mL of the serial dilution aliquots on the agar plates prepared as described above at 37 °C for 7 days. Bacterial cell retention was estimated in a log removal as shown below.

$$Log\ removal = log_{10}\left(\frac{viable\ cell\ concentration\ in\ feed\ suspension}{viable\ cell\ concentration\ in\ permeate}\right) \quad (1)$$

Silica particle rejection was assessed based on the light extinction at wavelength of 600 nm in a cell with a 5 cm path length (DR 6000, Hach).

Data process for blocking laws analysis

During the course of filtration experiment, cumulative mass of permeate and corresponding time was computationally recorded. Due to the interfacial discordance of electronic signal communication between a personal computer for recording and a weighing balance, raw mass data tended to erroneously contain zero values, which were omitted from the data analysis. Specific

gravity of the permeate with respect to water at room temperature was assumed to be 1 to convert mass to volume.

For blocking laws analysis using integrated form models (Eqs. 1-9 in Table V-3), these data were directly used for the model fitting with Minitab without any further processing. For two sequential blocking mechanism scenario, transition time from one mechanism to another was varied until the minimal sum of squared residuals (SSR) was yielded. Membrane blocking mechanisms were also probed using a differential form (equation 10), for which the smoothing of experimental data has been routinely involved. In this study, first and second derivative (dt/dV and d^2t/dV^2) was obtained via numerical differentiation using "diffxy" routine in MATLAB. The characteristic curve (d^2t/dV^2 versus dt/dV) was examined for the blocking mechanism index (n in Eq. 10), and, if necessary, the first derivative was smoothed using "moving" routine in MATLAB with a span size of 10 % of data points.

Sample preparation for SEM analysis

Conformational changes of *A. laidlawii* and silica particles before and after filtration were examined using scanning electron microscopy (JEOL JSM-7500F). The sample of unpressurized bacterial cells was prepared by directly putting the stock on the silicon wafer substrate. The membrane after bacterial cell filtration was recovered and used for the imaging. To both samples, 2.5 % glutaraldehyde prepared in PBS (pH 7.2) was added to fix the cells followed by a gentle rising with PBS and deionized water, and dewatering with increasing ethanol concentration (30, 50, 70, 90 and 100 % v/v). Silica samples were prepared following a same protocol, but without fixing, rinsing, and dewatering. All samples were coated with Pt(80%)/Pd(20%).

Results and discussion

Penetration of A. laidlawii cells through sterilizing-grade filters

Retention of bacterial cells by 0.2 and 0.1 µm-rated membrane was estimated under 34.5 and 345 kPa in a dead-end microfiltration system. Log-removal during the course of filtration was plotted in Figure V-3A, and the values were compared with previously-reported results in Figure V-3B. It is noted that our log-removal results shown in Figure V-3B (black symbols) are the average of values recorded during the filtration shown in Figure V-3A.

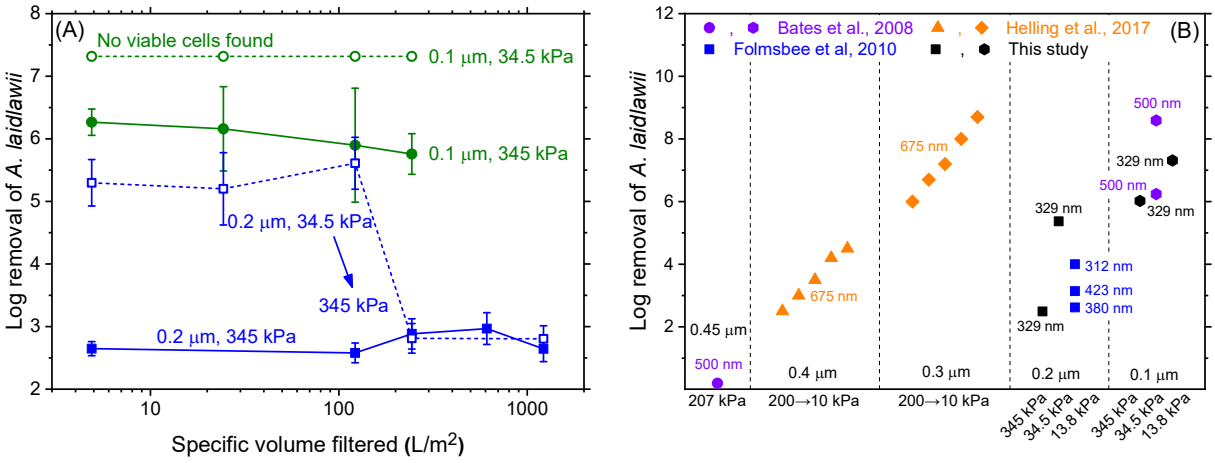

Figure V-3. Log removal of A. laidlawii cells under various filtration conditions (A), and a comparison of log-removal values in this study with previous results (B). The results of this study (black symbols) in (B) are the average of log removals during the filtration shown in (A). In (B), filtration pressures and pore sizes are denoted in units of kPa and µm, respectively. Also, the average size of *A. laidlawii* cells are presented near the symbols in matching colors.

With a 0.2 µm-rated membrane, 2.5±0.2 log removal was measured throughout the course of filtration at 345 kPa (solid blue line in Figure V-3A) demonstrating incomplete retention of *A. laidlawii*. SEM images of the permeate-side of the membranes showed morphologically deformed bacterial cells, which may explain the penetration mechanism (Figure V-4A). At a lower pressure of 34.5 kPa, higher log removal (5.4±0.2 log) was achieved (dotted blue line in Figure V-3A, up to 122 L/m^2 of specific volume filtered) indicating that the bacterial cell retention was affected by

transmembrane pressure. This was further confirmed by the immediate decline in log removal when the pressure was elevated back to 345 kPa in the middle of the filtration (dotted blue line in Figure V-3A from 244 ~ 1220 L/m^2 of specific volume filtered). Viable *A. laidlawii* cells in the permeate after filtration with 0.1 µm at 345 kPa (green solid line in Figure V-3A) emphasized a highly deformable nature of the cells (also see Figure V-4B). Only at a lower pressure of 34.5 kPa, no viable cells were measured in the permeate (green dotted line in Figure V-3A).

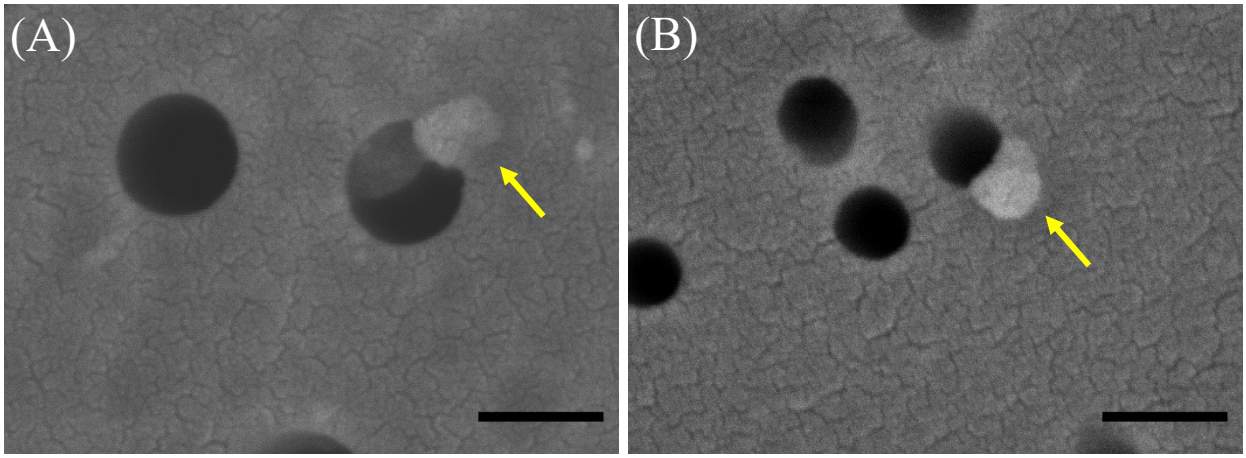

Figure V-4. Scanning electron micrographs of the permeate side of 0.2 µm (A) and 0.1 µm rated (B) membranes. Severely deformed bacterial cells near the pores (yellow arrows) were observed. Scale bars equal 200 nm.

As summarized in Figure V-3B, penetration of *A. laidlawii* cells through the filters with pores smaller than *A. laidlawii* cells have been reported. The result by Bates et al. clearly depicted the inverse proportionality of log removal to pore size and pressure [225]. Nonetheless, the overall trend is not evident indicating that other factors may influence the retention result. First of all, *A. laidlawii* cells cultured in each study may possess different characteristics. It is seen that the average size of *A. laidlawii* cells significantly varies over the studies ranging from 312 nm to 675 nm, presumably due to different nutrient conditions [229]. Consistently higher log-removals with a 0.3 µm filter (orange diamonds) in a wide range of applied pressures compared with the removal with a 0.2 µm filter (black and blue squares) can be simply due to the bigger cell size relative to

the pore size. Second, the other cell characteristic such as lipid layer composition is also affected by nutrient condition, which may further influence cell flexibility. It has been shown that the composition of lipid layer varied depending on the saturation and the length of acyl chain of fatty acid sources suggesting different rigidities of the layer [230]. This may explain the wide fluctuation of log-removals of cells grown in different culture media when the cell sizes were similar (blue squares) [226]. Lastly, the extent of cell retention can be affected by the membrane pore structure. In this study, we employed track-etched membranes which is characterized to have (ideally) cylindrical pores, in other words, a low tortuosity. Membranes with a higher tortuosity or interconnected pores are expected to provide higher retention facilitating internal pore surface deposition.

Worsened fouling by A. laidlawii cells compared with silica particle

Normalized flux decline profiles of representative *A. laidlawii* filtration experiments in comparison with those of silica particles are depicted in Figure V-5. In all cases, the membrane filters were more severely fouled by bacterial cells than silica particles although they were challenged at the similar number concentrations demonstrating contrasting behaviors of these two particles possibly due to the different deformability. The deleterious effect of particle flexibility on flux decline has been reported. Tung et al. [231] observed increase in filtration resistance to a greater extent with "softer" *Saccharomyces cerevisiae* (yeast) particles. Also, dextran-MnO_2 particle with a higher deformability showed the consistent result [232].

Moreover, unlike silica particles with which the flux decline resulted in similar profiles under both pressures of 345 and 34.5 kPa with 0.2 μm-rated membrane (brown circles in Figure V-5A and 5B), pressure dependency of the flux was observed with *A. laidlawii* cells; they showed a more rapid decline in flux at a lower pressure (black squares in Figure V-5A and 5B), which is

opposed to the common observation. Typically, higher pressure tend to lead a higher extent of flux decline owing to the cake compression via particle rearrangement and deformation [232]. However, in our case with *A. laidlawii* cells, the opposite phenomenon was observed which can be attributed to the extent of conformational change depending on the pressure which allows the cells pass through the pores [233, 234]. Insignificant difference in flux decline profiles of bacterial cells with 0.1 μm-rated membrane might be due to the severe confinement of cells at the pore entrance which lead cell deposition rather than cell penetration regardless of the pressure [234]. In order to further elucidate the contrasting behavior of these particles, investigation on membrane blocking mechanisms is followed.

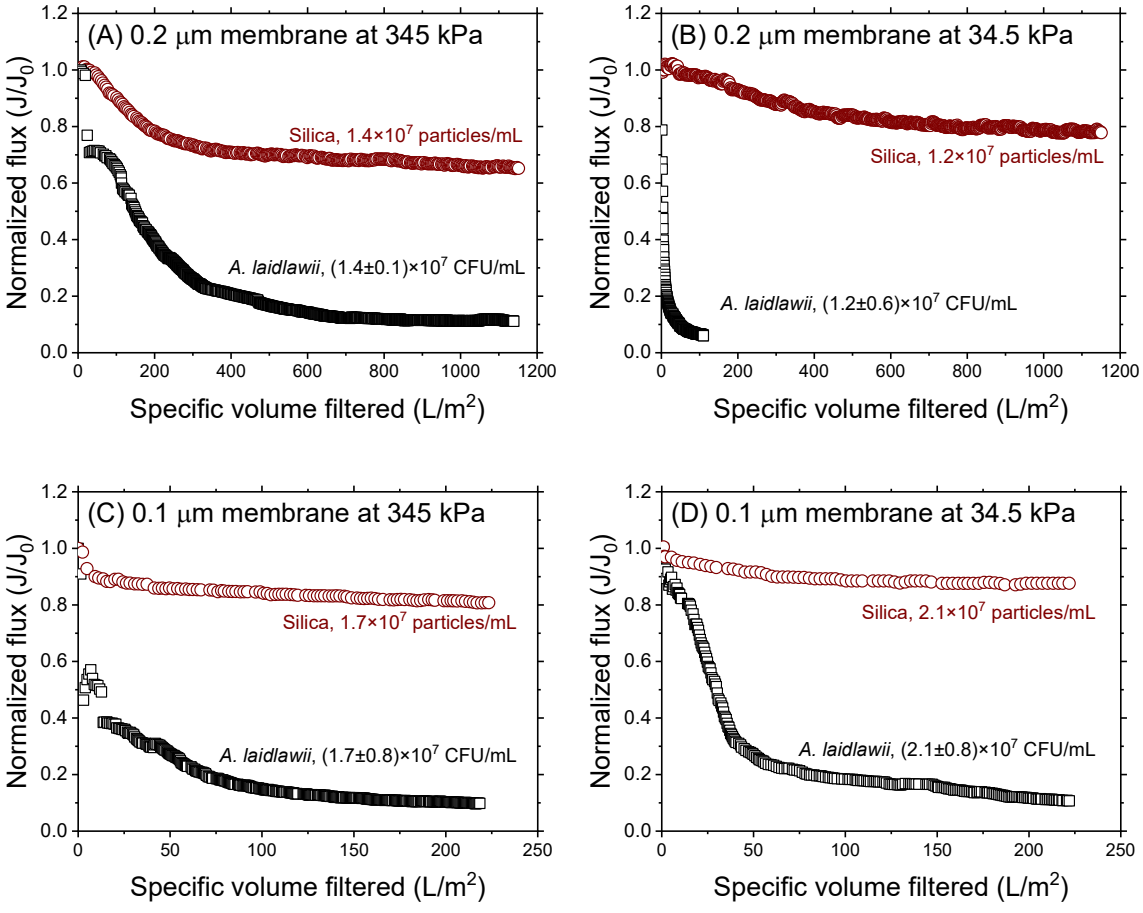

Figure V-5. Normalized flux decline profiles of *A. laidlawii* and silica particles under different conditions.

Identification of blocking mechanisms using integrated blocking models

Membrane blocking mechanisms during the filtration of both particles were investigated using the previously developed theoretical models for constant-pressure filtration mode. The classical blocking model (differential approach) derived in a unified differential form [219] probes four different blocking mechanisms depending on the blocking index (n); 2, 1.5, 1, and 0 for complete blocking, standard blocking, intermediate blocking, and cake filtration, respectively (Eq. 11 in Table V-2). Another approach is to use the models in integrated forms (integral approach) that directly predict the filtered volume according to filtration time. In this study, three scenarios were considered for this approach; single blocking mechanisms (Eqs. 2-5 in Table V-2), two sequential blocking mechanisms (combinations of Eqs. 2-5 in Table V-2), and two combined (simultaneous) blocking mechanisms (Eqs. 6-10 in Table V-2). It is noted that the combined models were adopted from Bolten's study [220] as these models assume the non-permeable particles and include all four classical blocking mechanisms. Table V-2 summarizes the employed models and the fitting parameters.

First, the approaches using integrated forms were compared. The models were fitted to experimental data (i.e. filtrate volume (mL) as a function of time (s)) to minimize the sum of squared residuals (SSR) as model fit errors where the residuals was the difference between the values of experimental data and model predictions. The best-fitting blocking mechanism of each scenario is summarized in Table V-3, and the modeled filtrate volumes according to filtration time are shown in comparison with experimental data in Figure V-6.

Table V-2. Summary of blocking laws models used in this study.

Model		Mechanism	Fitting parameters	Reference
Integrated forms of individual mechanism				
$V = \frac{J_0}{K_b}(1 - \exp(-K_b t))$	(2)	Complete blocking	K_b (/s)	[220]
$V = \left(\frac{1}{J_0 t} + \frac{K_s}{2}\right)^{-1}$	(3)	Standard blocking	K_s (/m)	
$V = \frac{1}{K_i}\ln(1 + K_i J_0 t)$	(4)	Intermediate blocking	K_i (/m)	
$V = \frac{1}{K_c J_0}\left(\sqrt{1 + 2K_c J_0^2 t} - 1\right)$	(5)	Cake filtration	K_c (s/m^2)	
Integrated forms of combined mechanism				
$V = \frac{J_0}{K_b}\left(1 - exp\left(\frac{-K_b}{K_c J_0^2}\left(\sqrt{1 + 2K_c J_0^2 t} - 1\right)\right)\right)$	(6)	Complete blocking + Cake filtration	K_b (/s) K_c (s/m^2)	[220]
$V = \frac{1}{K_i}\ln\left(1 + \frac{K_i}{K_c J_0}((1 + 2K_c J_0^2 t)^{0.5} - 1)\right)$	(7)	Intermediate blocking + Cake filtration	K_i (/m) K_c (s/m^2)	
$V = \frac{J_0}{K_b}\left(1 - exp\left(\frac{-2K_b t}{2 + K_s J_0 t}\right)\right)$	(8)	Complete blocking + Standard blocking	K_b (/s) K_s (/m)	
$V = \frac{1}{K_i} ln\left(1 + \frac{2K_i J_0 t}{2 + K_s J_0 t}\right)$	(9)	Standard blocking + Intermediate blocking	K_s (/m) K_i (/m)	
$V = \frac{2}{K_s}\left(\beta \cos\left(\frac{2\pi}{3} - \frac{1}{3}\arccos(\alpha)\right) + \frac{1}{3}\right)$, $\alpha = \frac{8}{27\beta^3} + \frac{4K_s}{3\beta^3} + \frac{4K_s}{3\beta^3 K_c J_0} - \frac{4K_s^2 t}{3\beta^3 K_c}$, $\beta = \sqrt{\frac{4}{9} + \frac{4K_s}{3K_c J_0} + \frac{2K_s^2 t}{3K_c}}$	(10)	Standard blocking + Cake filtration	K_s (/m) K_c (s/m^2)	
Differential form				
$\frac{d^2 t}{dV^2} = K\left(\frac{dt}{dV}\right)^n$	(11)	n = 2 for complete blocking n = 1.5 for standard blocking n = 1 for intermediate blocking n = 0 for cake filtration	- - - -	[219]

Table V-3. Summary of blocking laws analysis results using integrated form models.

Filtration	Particle	Single mechanism (SSR)	Combined mechanism (SSR)	Sequential mechanism (SSR)
0.2 μm, 345 kPa	A. laidlawii	Cake (71174)	Intermediate + Cake (57973)	Intermediate then Cake (27617)
	Silica	Cake (3264)	Complete + Cake (3259)	Intermediate then Cake (394)
0.2 μm, 34.5 kPa	A. laidlawii	Cake (82)	Intermediate + Cake (75)	Intermediate then Cake (3.5)
	Silica	Cake (971)	Intermediate + Cake (1305)	Intermediate then Cake (79)
0.1 μm, 345 kPa	A. laidlawii	Cake (2815)	Intermediate + Cake (2856)	Intermediate then Cake (870)
	Silica	Cake (93201)	Intermediate + Cake (93227)	Intermediate then Cake (9914)
0.1 μm, 34.5 kPa	A. laidlawii	Cake (5727)	Intermediate + Cake (5734)	Intermediate then Cake (1536)
	Silica	Cake (367)	Intermediate + Cake (373)	Intermediate then Cake (118)

For all investigated sets, cake filtration as a single fouling mechanism was found to be the best-fitting indicating the dominance of cake filtration. However, it does not necessarily mean that cake filtration was the only blocking mechanism throughout the filtration because the single mechanism approach can be easily biased depending on the relative number of data points of each fouling mechanism. The best-fitting combined (simultaneous) mechanism turned out to be an intermediate blocking and a cake filtration for all cases except silica filtration with 0.2 μm-rated membrane at 345 kPa. However, with a few exceptions, the SSRs were comparable with those of single fouling mechanism results indicating that the contribution of cake filtration was dominantly accounted although the model considered two mechanisms simultaneously. Interestingly, when a sequential two mechanism scenario was assumed, SSRs appeared to significantly improve for all the tested sets. Hence, it can be concluded that membrane fouling for all cases was dominated by intermediate blocking and cake filtration in a sequential manner rather than simultaneous one.

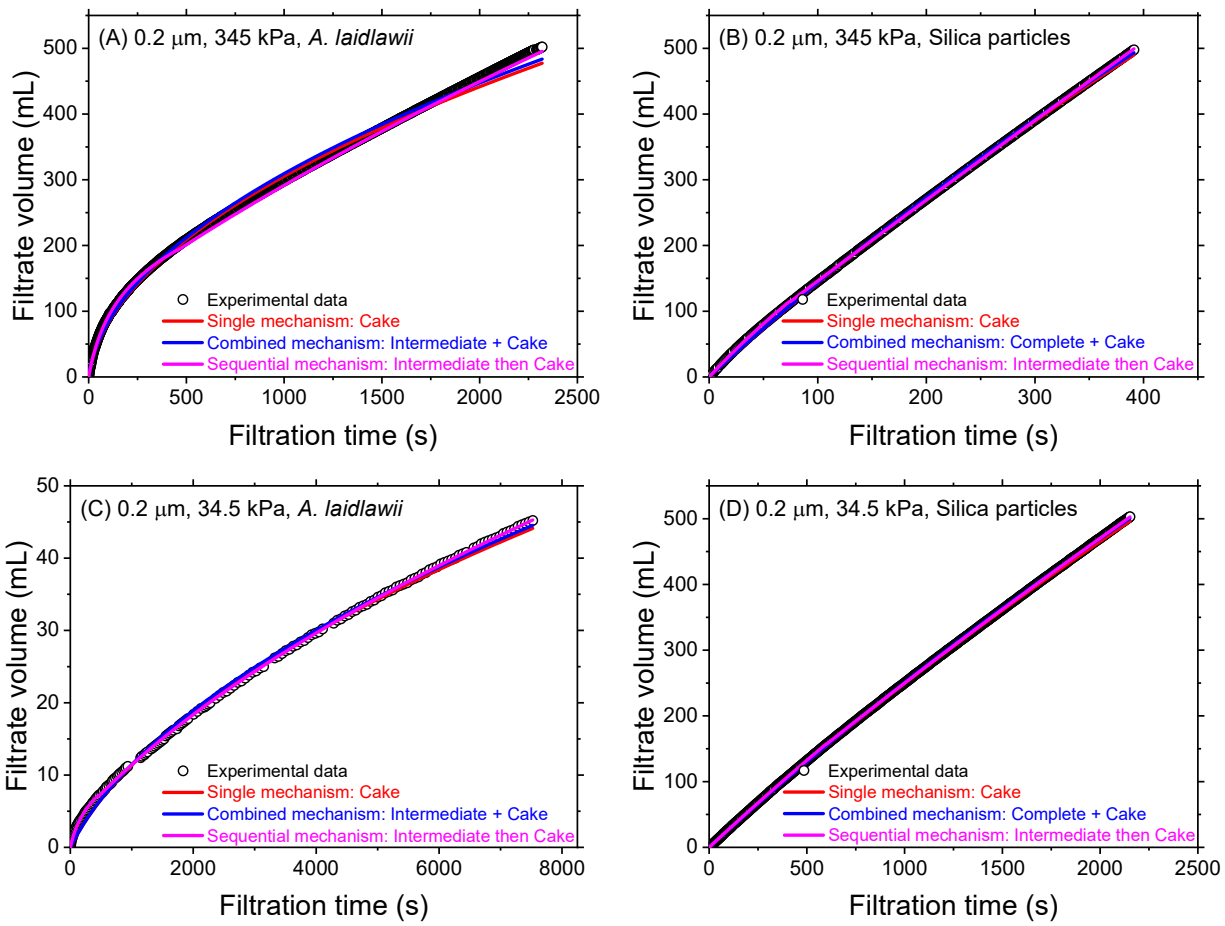

Figure V-6. Model predictions on filtrate volume using integrated form models in three different scenarios in comparison with experimental data.

Further, the results of two sequential mechanism approach (as a representative integral approach) were compared with those of differential approach. Figure V-7 depicts chronology of blocking mechanisms of bacterial cells and silica particles under different filtration conditions identified by two approaches.

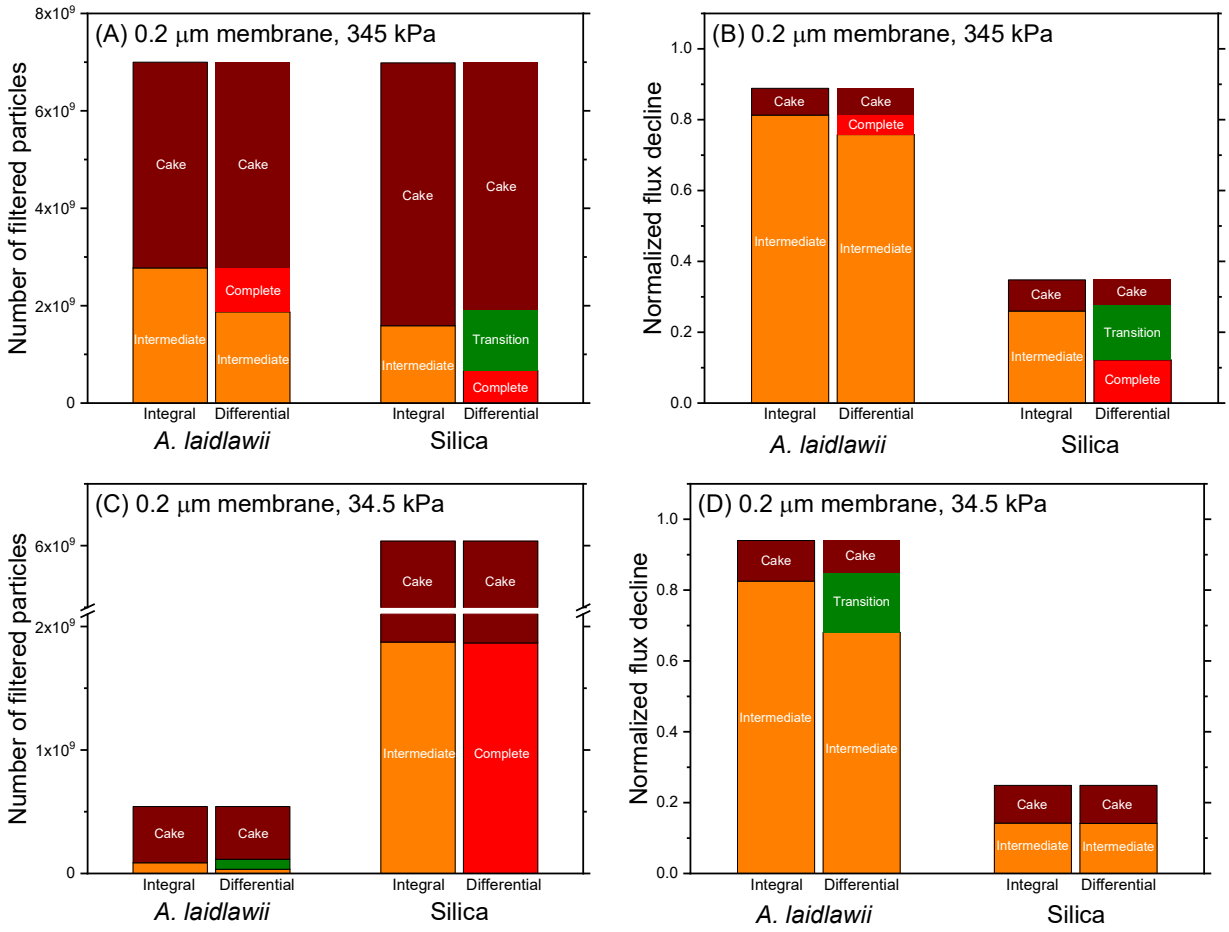

Figure V-7. Comparison of blocking laws analysis using integral and differential approaches.

As discussed earlier, two sequential mechanism model resulted in intermediate blocking followed by cake filtration for all the investigated sets. However, differential approach yielded somewhat different blocking mechanisms. For bacterial cell filtration with 0.2 μm membrane at 345 kPa, differential approach predicted a serial blocking mechanism of intermediate blocking, complete blocking, cake filtration demonstrating that blocking mechanism may appear differently depending on the approach. Complete blocking in between the two other mechanisms can be rationalized by the presence of a low fraction of multiplets. During the initial stage of the filtration, bacterial cells are likely to aggregate near the average-sized pores and deposit onto each other resulting in intermediate blocking as a dominant mechanism, while large multiplets tend to allow

the cells to pass through them. As bacterial cells accumulates on the membrane surface and flux declines, those multiplets may be blocked before transition to cake filtration. A qualitative explanation on sequential blocking mechanisms accounting for the pore size distribution has been proposed in several previous studies [235, 236]. Another noticeable discordance between the results via two approaches is the complete blocking mechanism captured by differential approach in silica particle filtration experiments. Given the relative size of the silica particles and their rigidity, complete blocking of pores can also be rationalized. Despite aforementioned differences, the number of particles filtered at transition to cake filtration identified using these two approaches was in reasonable agreement in all cases demonstrating that both approaches are equally suitable for capturing cake filtration mechanism.

In addition, the number of particles required to reach cake filtration for *A. laidlawii* cells and silica particles showed different behavior under two different applied pressures. Regardless of the pressure, silica particles formed a cake when approximately 2×10^9 particles were filtered whereas significantly less number of particles was required for *A. laidlawii* cells at a lower pressure ($\sim1\times10^8$ particles) compared with one at a higher pressure (3×10^9 particles) demonstrating the pressure-dependent behavior of these bacterial cells.

Blocking parameters by these two approaches were also compared as shown in Figure V-8, and filtrate volume predicted by sequential integral approach and differential approach are depicted in comparison with experimental data of selected sets.

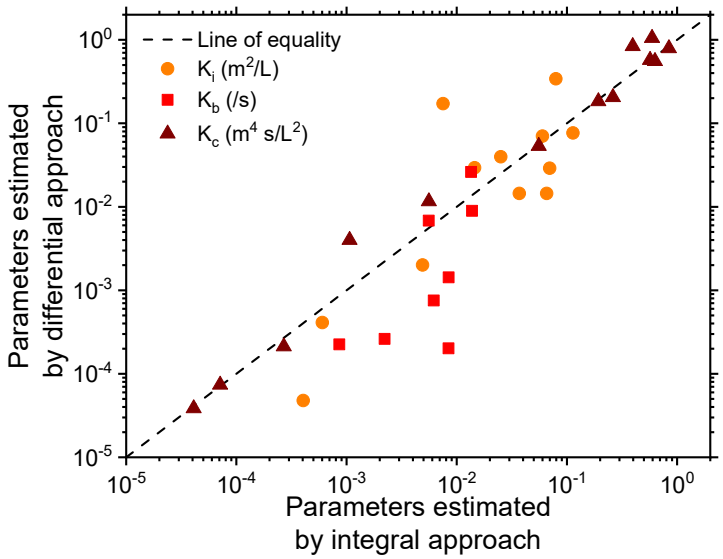

Figure V-8. Comparison of blocking parameters obtained by integral approach and differential approach.

As seen in Figure V-8, parameters estimated by two different approaches show a good agreement in general when plotted in a log-log scale except K_b. However, when filtrate volume versus time plot was reconstructed based on the parameters estimated by differential approach, a large deviation from the experimental data especially in cake filtration zone was observed for A. laidlawii filtration (purple lines in Figure V-9A and 9B) whereas integral approach model consistently showed a good agreement for all cases (magenta lines in Figure V-9). This result suggests that integral approach may be preferred over the other for the accurate estimation of blocking parameters.

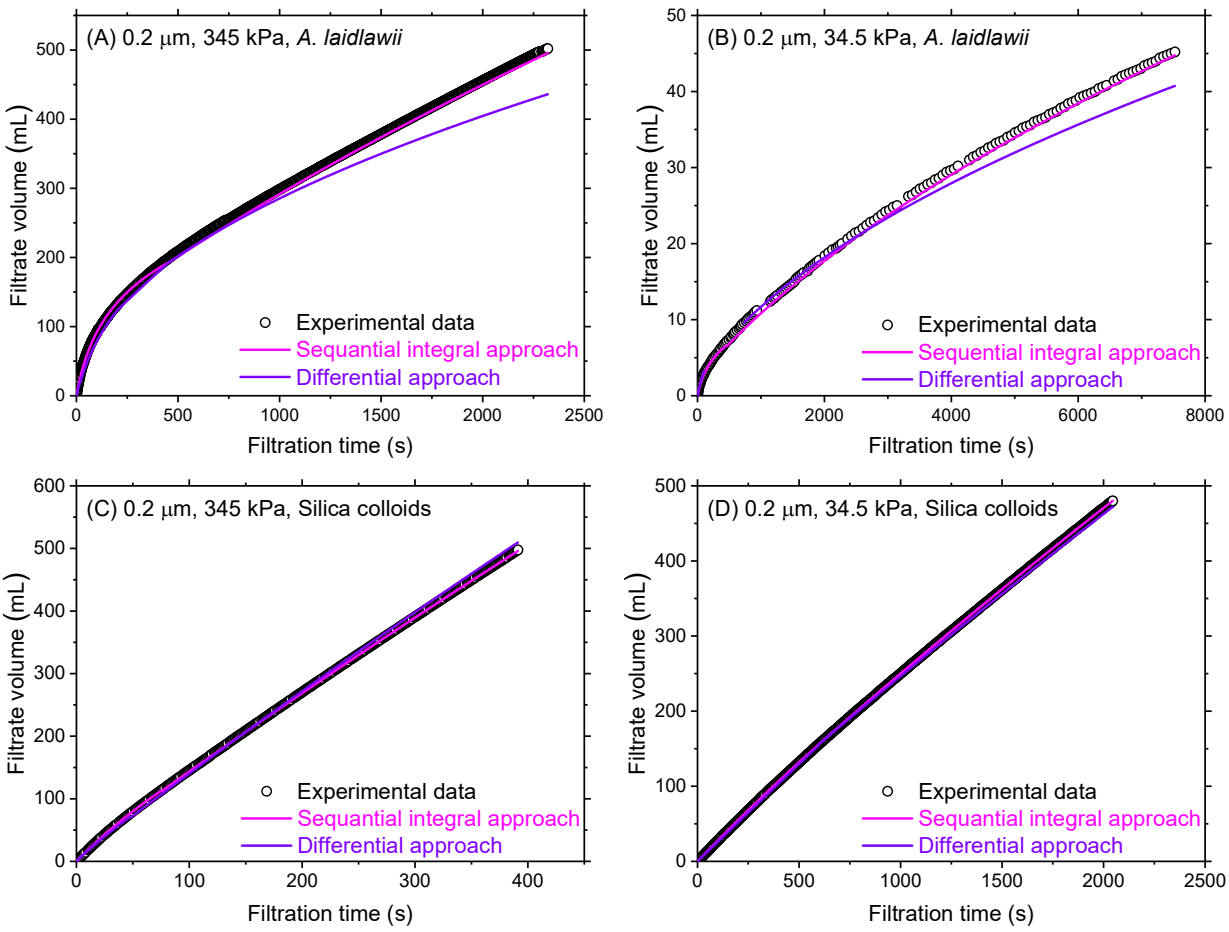

Figure V-9. Model predictions on filtrate volume using sequential integral and differential approaches in comparison with experimental data.

Conclusively, the differential approach is less laborious as it (ideally) enables us to capture all the blocking mechanisms in a single plot of d^2t/dV^2 versus dt/dV whereas the integral approach requires extensive computational work to investigate all the possible blocking scenarios. However, the blocking mechanism identification using differential approach may be significantly affected by the noise of the experimental data, which forces smoothing of raw data with care. In addition, it was also observed that more accurate parameters were obtained with integral approach. Therefore, it can be suggested that differential approach is taken with care for a rapid identification blocking mechanisms and transition times while integral approach is employed for the parameter estimation.

Compressible cake of A. laidlawii cells

Compressibility of *A. laidlawii* cells and silica particles was measured by filtering PBS (prefiltered with 0.1 μm PVDF membrane) at various pressures ranging from 34.5 to 345 kPa through the preformed cakes on 0.2 μm PTCE membranes. Specific cake resistant (α^*, m/kg) was calculated based on the equations shown below.

$$J = \frac{\Delta P}{\mu(R_m + R_c)} \tag{12}$$

$$R_c = \alpha^* W / A \tag{13}$$

where J is the permeate flux ($m^3/s/m^2$), ΔP is the transmembrane pressure (kPa), μ is the viscosity of the feed water (kPa·s), R_m is the clean membrane resistance (/m), R_c is the cake resistance (/m), α^* is the specific cake resistance (m/kg), W is the dry mass of cake (kg), and A is the membrane surface area (m^2). It is noted that μ was assumed to be equal to that of clean water at room temperature. R_m was measured by filtering PBS prefiltered with 0.1 μm PVDF filter at different pressures (34.5 ~ 345 kPa) and averaged value was used for the calculation of R_c. Figure V-10 shows the specific cake resistance of both particles along with electron micrographs of the cakes.

As seen in Figure V-10A, the specific cake resistance of silica cakes appeared to be incompressible showing constant values at order of 10^{13} m/kg independent of the transmembrane pressure. This is consistent with previous results [237]. Although rigid particles can show a cake compression owing to particle rearrangement, that is only due to the migration of finer particles which requires a relatively wide particle size distribution. Hence, highly monodispersed silica colloids used in this study (coefficient of variation of particle size= 1.9 %) are not expected to be compressible, and electron micrograph of silica cake (Figure V-10C) also qualitatively supports the result.

In contrast, *A. laidlawii* cells showed a non-linear behavior of cake resistance in response to the applied pressure obeying a power law. A linear proportionality of specific cake resistance to applied pressure has been reported for microorganisms such as *Escherichia coli* [238] and yeast [239] demonstrating 'linearly' compressible nature of the cakes formed by these particles. Unlike these microorganisms, *A. laidlawii* appeared to have non-linear concave-down behavior similar to natural colloidal materials although the specific cake resistance values were within the range of those found for other bacterial species, which may be attributed to the exceptionally high flexibility of *A. laidlawii* cells.

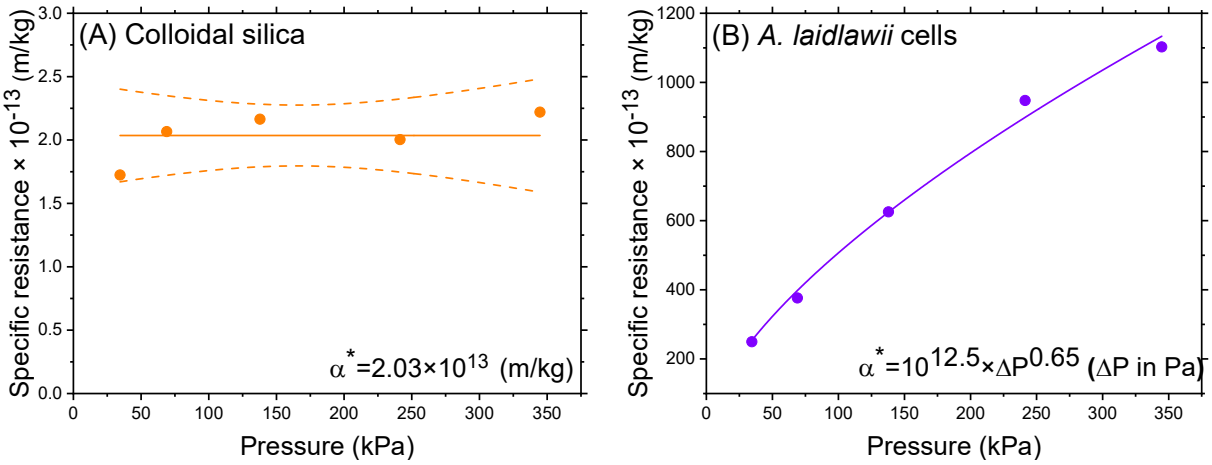

Figure V-10. Characterization of cakes formed by A. laidlawii cells and silica particles. Specific cake resistance of silica colloids (A) and A. laidlawii cells (B). The dashed-lines shown in (A) represent the 95 % confidence band.

Conclusions

Microfiltration of *A. laidlawii* was investigated in contrast with silica colloidal particles. *A. laidlawii* lacks a typical cell wall structure presumably making them highly deformable. In this study, penetration of viable *A. laidlawii* cells through the pores smaller than their size were observed, and the extent of retention was influenced by applied pressure. This results demonstrate

the role of particle flexibility on filter penetration and urges further emphasis on re-evaluating the validity of 0.2 or 0.22 μm rated filters as sterilization grade.

It was also shown that *A. laidlawii* cells foul the membrane filter more severely compared with rigid silica particles under identical filtration conditions demonstrating the role of particle deformability on the membrane fouling. The flux decline by *A. laidlawii* cells was influenced by the applied pressure whereas the flux profiles of colloidal silica particles under various pressures resulted in a similar extent of declines, further emphasizing the flexible nature of *A. laidlawii* cells.

Membrane blocking mechanisms during the filtration of these two types of particles were examined with various blocking laws models. Integrated form models suggested the sequential intermediate blocking and cake filtration mechanisms for all cases whereas the unified differential form model captured complete blocking mechanism prior to cake filtration especially for colloidal silica filtration experiments, demonstrating a potential discordance in a blocking mechanism analysis result depending on the approach taken. Given the advantages and disadvantages of both approaches observed in this study, the use of these approaches in combination is suggested.

CHAPTER VI

CONCLUSIONS AND RECOMMENDATIONS FOR FUTURE WORK

Conclusions

Iron EC simultaneously disinfects and coagulates viruses and appears to be a promising technology especially for small-scale distributed water treatment enhancing the robustness of multiple barriers necessary for public health protection. A highly effective virus control by iron EC was demonstrated with both non-enveloped (MS2, 5-log reduction at 20 mg/L and pH 6.4 in 30 minutes) and enveloped virus surrogates (ϕ6, 5.9-log reduction at 10 mg/L and pH 6.4 in 30 minutes) outperforming convention chemical coagulation with $FeCl_3$ (3.7-log reduction of MS2 at 20 mg/L and pH 6.4 in 30 minutes, and 5.0-log reduction of ϕ6 at 10 mg/L and pH 6.4 in 30 minutes). In contrast, aluminum EC showed similar performance to conventional $Al_2(SO_4)_3$ coagulation indicating that the application of aluminum EC as an alternative to conventional counterpart may be determined by non-technical reasons such as cost.

As evidenced by ATR-FTIR spectrum of iron-electrocoagulated MS2 phage, oxidative stress possibly imposed by reactive oxygen species such as •OH and/or oxoiron(IV) produced during iron EC is capable of alternating viral capsid structures indicating that this technology is potentially suitable to treat a wide range of non-enveloped pathogenic viruses.

Both iron coagulation types appear to be highly effective in controlling enveloped viruses (unlike the MS2 phage) during surface water treatment. Therefore, surface water treatment facilities utilizing iron coagulant might be already providing a sufficient barrier against enveloped viruses.

Particle deformability was shown to worsen the membrane fouling. Compared with rigid silica particles, highly flexible *Acholeplasma laidlawii* cells caused a more rapid flux decline. These bacteria penetrated/blocked pores that were even smaller than their sizes (shown by the presence of viable cells in the permeate) and forming a compressible cake (shown by increasing specific cake resistance with increasing applied pressure).

Recommendations for future work

Based on the results of this research, the following ideas can be pursued in the future:

Optimization of iron EC process in complex water matrices

Electro-Fenton reaction triggered by *in-situ* generated Fe(II) and H_2O_2 during iron EC additionally contributes to virus attenuation on top of physical removal (i.e. sweep flocculation). Hence, it is a rational attempt to promote a cathodic production of H_2O_2 to improve the overall performance of iron EC towards virus attenuation, for which several approaches can be considered. One possible way is to carefully choose a cathodic material to effectively reduce O_2 to H_2O_2. For example, carbon-based electrode such as activated carbon [240] may promote the H_2O_2 production. In addition, operating parameters to maximize such reaction should be investigated as it has been shown that electrode potential and/or current may affect the H_2O_2 production efficiency [240-242].

Investigation on other viruses

In this research, only two bacteriophages were used as model viruses with different viral components/structures. Although these model viruses were well-contrasted with respect to their behaviors during the various coagulation processes, there is still a need of investigating other viruses such as pathogenic mammalian viruses with structural differences to better understand the

viral behavior during the coagulation. Specifically, it was shown in this research that MS2 capsid maintains its structural integrity in contact with Al and Fe precipitates whereas ϕ6 nucleocapsid is damaged under the identical conditions. This observation indicates that physicochemical properties of viral capsids (such as mechanical strength) can be used to predict the viral alteration and thus, infectivity during the coagulation.

REFERENCES

1. Fong, T.T. and E.K. Lipp, *Enteric viruses of humans and animals in aquatic environments: health risks, detection, and potential water quality assessment tools.* Microbiology and Molecular Biology Reviews, 2005. **69**(2): p. 357-371.

2. Craun, G.F., et al., *Causes of outbreaks associated with drinking water in the United States from 1971 to 2006.* Clinical Microbiology Review, 2010. **23**(3): p. 507-528.

3. Reynolds, K.A., K.D. Mena, and C.P. Gerba, *Risk of waterborne illness via drinking water in the United States*, in *Reviews of Environmental Contamination and Toxicology*, D.M. Whitacre, Editor. 2008, Springer New York: New York, NY. p. 117-158.

4. Heffron, J. and B.K. Mayer, *Emerging investigators series: virus mitigation by coagulation: recent discoveries and future directions.* Environmental Science-Water Research & Technology, 2016. **2**(3): p. 443-459.

5. USEPA, *Drinking Water Contaminant Candidate List 4 - Final*. 2016, Federal Register. p. 81099-81114.

6. Shirasaki, N., et al., *Comparison of removal performance of two surrogates for pathogenic waterborne viruses, bacteriophage Qβ and MS2, in a coagulation–ceramic microfiltration system.* Journal of Membrane Science, 2009. **326**(2): p. 564-571.

7. Zhu, B., D.A. Clifford, and S. Chellam, *Comparison of electrocoagulation and chemical coagulation pretreatment for enhanced virus removal using microfiltration membranes.* Water Research, 2005. **39**(13): p. 3098-3108.

8. Hendricks, D.W., et al., *Filtration removals of microorganisms and particles.* Journal of Environmental Engineering, 2005. **131**(12): p. 1621-1632.

9. Mollah, M.Y., et al., *Fundamentals, present and future perspectives of electrocoagulation.* Journal of Hazardous Materials, 2004. **114**(1-3): p. 199-210.

10. Chellam, S. and M.A. Sari, *Aluminum electrocoagulation as pretreatment during microfiltration of surface water containing NOM: A review of fouling, NOM, DBP, and virus control.* Journal of Hazardous Materials, 2016. **304**: p. 490-501.

11. Canizares, P., et al., *Electrodissolution of aluminum electrodes in electrocoagulation processes.* Industrial & Engineering Chemistry Research, 2005. **44**(12): p. 4178-4185.

12. Barrera-Díaz, C., et al., *Physicochemical aspects of electrocoagulation.* Separation & Purification Reviews, 2011. **40**(1): p. 1-24.

13. Tanneru, C.T., J.D. Rimer, and S. Chellam, *Sweep flocculation and adsorption of viruses on aluminum flocs during electrochemical treatment prior to surface water microfiltration.* Environmental Science & Technology, 2013. **47**(9): p. 4612-4618.

14. Tanneru, C.T. and S. Chellam, *Mechanisms of virus control during iron electrocoagulation-microfiltration of surface water.* Water Research, 2012. **46**(7): p. 2111-2120.

15. Heffron, J., et al., *Mechanisms of virus mitigation and suitability of bacteriophages as surrogates in drinking water treatment by iron electrocoagulation.* Water Research, 2019. **163**: p. 114877.

16. Tanneru, C.T., et al., *Relative insignificance of virus inactivation during aluminum electrocoagulation of saline waters.* Environmental Science & Technology, 2014. **48**(24): p. 14590-14598.

17. Heffron, J., B. McDermid, and B.K. Mayer, *Bacteriophage inactivation as a function of ferrous iron oxidation.* Environmental Science-Water Research & Technology, 2019. **5**(7): p. 1309-1317.

18. McDonnell, G.E., *Antisepsis, disinfection, and sterilization: Types, action, and resistance*. 1st ed. 2007: ASM Press.

19. Weber, D.J., et al., *Emerging infectious diseases: Focus on infection control issues for novel coronaviruses (Severe Acute Respiratory Syndrome-CoV and Middle East Respiratory Syndrome-CoV), hemorrhagic fever viruses (Lassa and Ebola), and highly pathogenic avian influenza viruses, A(H5N1) and A(H7N9).* American Journal of Infection Control, 2016. **44**(5): p. e91-e100.

20. Wood, J.P., et al., *Evaluating the environmental persistence and inactivation of MS2 bacteriophage and the presumed Ebola virus surrogate Phi6 using low concentration hydrogen peroxide vapor.* Environmental Science & Technology, 2020. **54**(6): p. 3581-3590.

21. Bibby, K., et al., *Persistence of Ebola virus in sterilized wastewater.* Environmental Science & Technology Letters, 2015. **2**(9): p. 245-249.

22. Casanova, L., et al., *Survival of surrogate coronaviruses in water.* Water Research, 2009. **43**(7): p. 1893-1898.

23. Casanova, L.M. and S.R. Weaver, *Inactivation of an enveloped surrogate virus in human sewage.* Environmental Science & Technology Letters, 2015. **2**(3): p. 76-78.

24. de Carvalho, N.A., et al., *Evaluation of phi6 persistence and suitability as an enveloped virus surrogate.* Environmental Science & Technology, 2017. **51**(15): p. 8692-8700.

25. Kim, K., et al., *Virus Removal and Inactivation Mechanisms during Iron Electrocoagulation: Capsid and Genome Damages and Electro-Fenton Reactions.* Environmental Science & Technology, 2021.

26. Kim, K., et al., *Removal and inactivation of an enveloped virus surrogate by iron conventional coagulation and electrocoagulation.* Environmental Science & Technology, 2021. **55**(4): p. 2674-2683.

27. Colford, J.M., Jr., et al., *A review of household drinking water intervention trials and an approach to the estimation of endemic waterborne gastroenteritis in the United States.* Journal of Water and Health, 2006. **4**(S2): p. 71-88.

28. Messner, M., et al., *An approach for developing a national estimate of waterborne disease due to drinking water and a national estimate model application.* Journal of Water and Health, 2006. **4**(S2): p. 201-240.

29. Bain, R., et al., *Global assessment of exposure to faecal contamination through drinking water based on a systematic review.* Tropical Medicine & International Health, 2014. **19**(8): p. 917-927.

30. Clasen, T., et al., *Estimating the impact of unsafe water, sanitation and hygiene on the global burden of disease: evolving and alternative methods.* Tropical Medicine & International Health, 2014. **19**(8): p. 884-893.

31. Gibson, K.E., *Viral pathogens in water: occurrence, public health impact, and available control strategies.* Current Opinion in Virology, 2014. **4**: p. 50-57.

32. Julian, T.R. and K.J. Schwab, *Challenges in environmental detection of human viral pathogens.* Current Opinion in Virology, 2012. **2**(1): p. 78-83.

33. Gall, A.M., et al., *Waterborne viruses: A barrier to safe drinking water.* PLOS Pathogens, 2015. **11**(6).

34. Allaire, M., H. Wu, and U. Lall, *National trends in drinking water quality violations.* Proceedings of the National Academy of Sciences, 2018. **115**(9): p. 2078-2083.

35. USEPA, *25 years of the Safe Drinking Water Act: History and trends EPA/816/R/99/007*. 1999.

36. Benjamin, M.M. and D.F. Lawler, *Water Quality Engineering: Physical-Chemical Treatment Processes*. 2013, Hoboken, NJ: John Wiley & Sons, Inc.

37. Pecson, B.M., L.V. Martin, and T. Kohn, *Quantitative PCR for determining the infectivity of bacteriophage MS2 upon inactivation by heat, UV-B radiation, and singlet oxygen: Advantages and limitations of an enzymatic treatment to reduce false-positive results.* Applied and Environmental Microbiology, 2009. **75**(17): p. 5544-5554.

38. Dunkin, N., et al., *Comparative inactivation of murine Norovirus and MS2 bacteriophage by peracetic acid and monochloramine in municipal secondary wastewater effluent.* Environmental Science & Technology, 2017. **51**(5): p. 2972-2981.

39. Cho, M., et al., *Visible light sensitized inactivation of MS-2 bacteriophage by a cationic amine-functionalized C_{60} derivative.* Environmental Science & Technology, 2010. **44**(17): p. 6685-6691.

40. Wigginton, K.R., et al., *Virus inactivation mechanisms: impact of disinfectants on virus function and structural integrity.* Environmental Science & Technology, 2012. **46**(21): p. 12069-12078.

41. Pham, M., E.A. Mintz, and T.H. Nguyen, *Deposition kinetics of bacteriophage MS2 to natural organic matter: role of divalent cations.* Journal of Colloid and Interface Science, 2009. **338**(1): p. 1-9.

42. Nieto-Juarez, J.I., et al., *Inactivation of MS2 coliphage in Fenton and Fenton-like systems: Role of transition metals, hydrogen peroxide and sunlight.* Environmental Science & Technology, 2010. **44**(9): p. 3351-3356.

43. Badireddy, A.R., et al., *Inactivation of bacteriophages via photosensitization of fullerol nanoparticles.* Environmental Science & Technology, 2007. **41**(18): p. 6627-6632.

44. Müller, S., T. Behrends, and C.M. van Genuchten, *Sustaining efficient production of aqueous iron during repeated operation of Fe(0)-electrocoagulation.* Water Research, 2019. **155**: p. 455-464.

45. van Genuchten, C.M., et al., *Controls on the formation of Fe(II,III) (hydr)oxides by Fe(0) electrolysis.* Electrochimica Acta, 2018. **286**: p. 324-338.

46. Dubrawski, K.L., et al., *Production and transformation of mixed-valent nanoparticles generated by Fe(0) electrocoagulation.* Environmental Science & Technology, 2015. **49**(4): p. 2171-2179.

47. Pan, C., et al., *Dynamics of Chromium(VI) Removal from Drinking Water by Iron Electrocoagulation.* Environmental Science & Technology, 2016. **50**(24): p. 13502-13510.

48. Matsui, Y., et al., *Virus inactivation in aluminum and polyaluminum coagulation.* Environmental Science & Technology, 2003. **37**(22): p. 5175-5180.

49. Kreißel, K., et al., *Inactivation of F-specific bacteriophages during flocculation with polyaluminum chloride - A mechanistic study.* Water Research, 2014. **51**: p. 144-151.

50. Connell, K.P., et al., *Real-time fluorogenic reverse transcription-PCR assays for detection of bacteriophage MS2.* Applied and Environmental Microbiology, 2006. **72**(1): p. 478-483.

51. Raynor, P.C., et al., *Comparison of samplers collecting airborne influenza viruses: 1. Primarily impingers and cyclones.* PLoS One, 2021. **16**(1): p. e0244977.

52. Unnithan, V.V., A. Unc, and G.B. Smith, *Enzymatic Pre-treatment of Wastewater to Minimize Recovery by Reverse Transcriptase PCR of RNA from Inactive Bacteriophages.* Current Microbiology, 2015. **71**(1): p. 49-53.

53. Koning, R., et al., *Visualization by Cryo-electron Microscopy of Genomic RNA that Binds to the Protein Capsid Inside Bacteriophage MS2.* Journal of Molecular Biology, 2003. **332**(2): p. 415-422.

54. Dent, K.C., et al., *The asymmetric structure of an icosahedral virus bound to its receptor suggests a mechanism for genome release.* Structure, 2013. **21**(7): p. 1225-1234.

55. Toropova, K., et al., *The three-dimensional structure of genomic RNA in bacteriophage MS2: Implications for assembly.* Journal of Molecular Biology, 2008. **375**(3): p. 824-836.

56. Lisjak, M., et al., *AQP4e-based orthogonal arrays regulate rapid cell volume changes in astrocytes.* The Journal of Neuroscience, 2017. **37**(44): p. 10748-10756.

57. Kuzmanovic, D.A., et al., *The MS2 coat protein shell is likely assembled under tension: A novel role for the MS2 bacteriophage A protein as revealed by small-angle neutron scattering.* Journal of Molecular Biology, 2006. **355**(5): p. 1095-1111.

58. Kuzmanovic, D.A., et al., *Bacteriophage MS2: Molecular weight and spatial distribution of the protein and RNA components by small-angle neutron scattering and virus counting.* Structure, 2003. **11**(11): p. 1339-1348.

59. Heymann, J.B. and D.M. Belnap, *Bsoft: Image processing and molecular modeling for electron microscopy.* Journal of Structural Biology, 2007. **157**(1): p. 3-18.

60. Pettersen, E.F., et al., *UCSF Chimera - A visualization system for exploratory research and analysis.* Journal of Computational Chemistry, 2004. **25**(13): p. 1605-1612.

61. Wang, J.C., S. Mukhopadhyay, and A. Zlotnick, *Geometric Defects and Icosahedral Viruses.* Viruses, 2018. **10**(1).

62. Baxter, W.T., et al., *Determination of signal-to-noise ratios and spectral SNRs in cryo-EM low-dose imaging of molecules.* Journal of Structural Biology, 2009. **166**(2): p. 126-132.

63. Earl, T., et al. *Accuracy and speed assessment of 3D cross-correlation algorithms for two-frame and multi-frame PIV*. in *11TH INTERNATIONAL SYMPOSIUM ON PARTICLE IMAGE VELOCIMETRY - PIV15*. 2015. Santa Barbara, United States.

64. Rath, B.K., et al., *Fast 3D motif search of EM density maps using a locally normalized cross-correlation function.* Journal of Structural Biology, 2003. **144**(1): p. 95-103.

65. Losdorfer Bozic, A., A. Siber, and R. Podgornik, *Statistical analysis of sizes and shapes of virus capsids and their resulting elastic properties.* Journal of Biological Physics, 2013. **39**(2): p. 215-228.

66. Vargas, C.A., et al., *Integrated Capture and Spectroscopic Detection of Viruses.* Applied and Environmental Microbiology, 2009. **75**(20): p. 6431-6440.

67. Valegard, K., et al., *The three-dimensional structure of the bacterial virus MS2.* Nature, 1990. **345**(6270): p. 36-41.

68. Stuart, B.H., *Infrared Spectroscopy : Fundamentals and Applications*. 2004, Hoboken, United Kingdom: John Wiley & Sons, Incorporated.

69. Barth, A., *The infrared absorption of amino acid side chains.* Progress in Biophysics and Molecular Biology, 2000. **74**(3-5): p. 141-173.

70. Davies, M.J., *Protein oxidation and peroxidation.* Biochemical Journal, 2016. **473**(7): p. 805-825.

71. Wigginton, K.R., et al., *Oxidation of virus proteins during UV_{254} and singlet oxygen mediated inactivation.* Environmental Science & Technology, 2010. **44**(14): p. 5437-5443.

72. Sano, D., et al., *Detection of oxidative damages on viral capsid protein for evaluating structural integrity and infectivity of human norovirus.* Environmental Science & Technology, 2010. **44**(2): p. 808-812.

73. Barth, A., *Infrared spectroscopy of proteins.* Biochimica et Biophysica Acta, 2007. **1767**(9): p. 1073-1101.

74. Schmitt, J. and H.-C. Flemming, *FTIR-spectroscopy in microbial and material analysis.* International Biodeterioration & Biodegradation, 1998. **41**(1): p. 1-11.

75. Pulgarin, C., J. Kiwi, and V. Nadtochenko, *Mechanism of photocatalytic bacterial inactivation on TiO2 films involving cell-wall damage and lysis.* Applied Catalysis B: Environmental, 2012. **128**: p. 179-183.

76. Kiwi, J. and V. Nadtochenko, *Evidence for the mechanism of photocatalytic degradation of the bacterial wall membrane at the TiO_2 interface by ATR-FTIR and laser kinetic spectroscopy.* Langmuir, 2005. **21**(10): p. 4631-4641.

77. Santos, A.L., et al., *Effects of UV radiation on the lipids and proteins of bacteria studied by mid-infrared spectroscopy.* Environmental Science & Technology, 2013. **47**(12): p. 6306-6315.

78. Amici, A., et al., *Conversion of amino acid residues in proteins and amino acid homopolymers to carbonyl derivatives by metal-catalyzed oxidation reactions.* The Journal of Biological Chemistry, 1989. **264**(6): p. 3341-3346.

79. Stadtman, E.R. and R.L. Levine, *Free radical-mediated oxidation of free amino acids and amino acid residues in proteins.* Amino Acids, 2003. **25**(3-4): p. 207-218.

80. Byler, D.M. and H. Susi, *Examination of the secondary structure of proteins by deconvolved FTIR spectra.* Biopolymers, 1986. **25**(3): p. 469-487.

81. Jackson, M. and H.H. Mantsch, *The Use and Misuse of FTIR Spectroscopy in the Determination of Protein Structure.* Critical Reviews in Biochemistry and Molecular Biology, 1995. **30**(2): p. 95-120.

82. Badireddy, A.R., et al., *Spectroscopic characterization of extracellular polymeric substances from Escherichia coli and Serratia marcescens: Suppression using sub-inhibitory concentrations of bismuth thiols.* Biomacromolecules, 2008. **9**(11): p. 3079-3089.

83. Buijs, J., W. Norde, and J.W.T. Lichtenbelt, *Changes in the secondary structure of adsorbed IgG and F(ab')(2) studied by FTIR spectroscopy.* Langmuir, 1996. **12**(6): p. 1605-1613.

84. Yu, P.Q., et al., *Using synchrotron-based FTIR microspectroscopy to reveal chemical features of feather protein secondary structure: Comparison with other feed protein sources.* Journal of Agricultural and Food Chemistry, 2004. **52**(24): p. 7353-7361.

85. Mirzaei, H. and F. Regnier, *Protein:protein aggregation induced by protein oxidation.* Journal of Chromatography B: Analytical Technologies in the Biomedical and Life Sciences, 2008. **873**(1): p. 8-14.

86. Blanch, E.W., et al., *Molecular structures of viruses from Raman optical activity.* Journal of General Virology, 2002. **83**(10): p. 2593-2600.

87. Meng, R., et al., *Structural basis for the adsorption of a single-stranded RNA bacteriophage.* Nature Communications, 2019. **10**(1): p. 3130.

88. Kim, J.Y., et al., *Inactivation of MS2 coliphage by ferrous ion and zero-valent iron nanoparticles.* Environmental Science & Technology, 2011. **45**(16): p. 6978-6984.

89. Brillas, E., I. Sirés, and M.A. Oturan, *Electro-Fenton process and related electrochemical technologies based on Fenton's reaction chemistry.* Chemical Reviews, 2009. **109**(12): p. 6570-6631.

90. Wiegand, H.L., et al., *Investigation of the iron-peroxo complex in the Fenton reaction: Kinetic indication, decay kinetics, and hydroxyl radical yields.* Environmental Science & Technology, 2017. **51**(24): p. 14321-14329.

91. Wardman, P. and L.P. Candeias, *Fenton chemistry: An introduction.* Radiation Research, 1996. **145**(5): p. 523-531.

92. Kim, J.Y., et al., *Inactivation of MS2 coliphage by Fenton's reagent.* Water Research, 2010. **44**(8): p. 2647-2653.

93. Buxton, G.V., et al., *Critical review of rate constants for reactions of hydrated electrons, hydrogen atoms and hydroxyl radicals (·OH/·O⁻) in aqueous solution.* Journal of Physical and Chemical Reference Data, 1988. **17**(2): p. 513-886.

94. Huang, X. and J.T. Groves, *Beyond ferryl-mediated hydroxylation: 40 years of the rebound mechanism and C–H activation.* Journal of Biological Inorganic Chemistry, 2017. **22**(2): p. 185-207.

95. Bataineh, H., O. Pestovsky, and A. Bakac, *pH-induced mechanistic changeover from hydroxyl radicals to iron(IV) in the Fenton reaction.* Chemical Science, 2012. **3**(5): p. 1594-1599.

96. Badireddy, A.R., et al., *Bacteriophage inactivation by UV-A illuminated fullerenes: Role of nanoparticle-virus association and biological targets.* Environmental Science & Technology, 2012. **46**(11): p. 5963-5970.

97. Stumm, W. and G.F. Lee, *Oxygenation of ferrous iron.* Industrial and Engineering Chemistry, 1961. **53**(2): p. 143-146.

98. Sigstam, T., et al., *Subtle differences in virus composition affect disinfection kinetics and mechanisms.* Applied and Environmental Microbiology, 2013. **79**(11): p. 3455–3467.

99. Kohn, T., et al., *Association with natural organic matter enhances the sunlight-mediated inactivation of MS2 coliphage by singlet oxygen.* Environmental Science & Technology, 2007. **41**(13): p. 4626-4632.

100. Zhu, B., D.A. Clifford, and S. Chellam, *Virus removal by iron coagulation-microfiltration.* Water Research, 2005. **39**(20): p. 5153-5161.

101. Lee-Montiel, F.T., K.A. Reynolds, and M.R. Riley, *Detection and quantification of poliovirus infection using FTIR spectroscopy and cell culture.* Journal of Biological Engineering, 2011. **5**(1): p. 16.

102. Santos, M.C.D., et al., *ATR-FTIR spectroscopy coupled with multivariate analysis techniques for the identification of DENV-3 in different concentrations in blood and serum: a new approach.* RSC Advances, 2017. **7**(41): p. 25640-25649.

103. Barauna, V.G., et al., *Ultrarapid On-Site Detection of SARS-CoV-2 Infection Using Simple ATR-FTIR Spectroscopy and an Analysis Algorithm: High Sensitivity and Specificity.* Analytical Chemistry, 2021. **93**(5): p. 2950-2958.

104. Costa, L., et al., *SDS-PAGE and IR spectroscopy to evaluate modifications in the viral protein profile induced by a cationic porphyrinic photosensitizer.* Journal of Virological Methods, 2014. **209**: p. 103-109.

105. Li, T., et al., *Structural studies of the enveloped dsRNA bacteriophage ϕ6 of Pseudomonas syringae by Raman spectroscopy: I. The virion and its membrane envelope.* Journal of Molecular Biology, 1993. **230**(2): p. 461-472.

106. Overman, S.A. and G.J. Thomas Jr, *Structural studies of viruses by Raman spectroscopy. Novel vibrational assignments for proteins from Raman spectra of viruses.* Journal of Raman Spectroscopy, 1998. **29**(1): p. 23-29.

107. Tsuboi, M., et al., *Protein and DNA Residue Orientations in the Filamentous Virus Pf1 Determined by Polarized Raman and Polarized FTIR Spectroscopy.* Biochemistry, 2003. **42**(4): p. 940-950.

108. Perez-Berna, A.J., et al., *The role of capsid maturation on adenovirus priming for sequential uncoating.* Journal of Biological Chemistry, 2012. **287**(37): p. 31582-31595.

109. Liu, H., et al., *Atomic Structure of Human Adenovirus by Cryo-EM Reveals Interactions Among Protein Networks.* Science, 2010. **329**(5995): p. 1038.

110. Medema, G., et al., *Presence of SARS-Coronavirus-2 RNA in Sewage and Correlation with Reported COVID-19 Prevalence in the Early Stage of the Epidemic in The Netherlands.* Environmental Science & Technology Letters, 2020. **7**(7): p. 511-516.

111. Peccia, J., et al., *Measurement of SARS-CoV-2 RNA in wastewater tracks community infection dynamics.* Nature Biotechnology, 2020. **39**: p. 1164–1167.

112. World Health Organization, *Water, sanitation, hygiene, and waste management for SARS-CoV-2, the virus that causes COVID-19: Interim guidance*. 2020, WHO reference number: WHO/2019-nCoV/IPC_WASH/2020.4.

113. Kitajima, M., et al., *SARS-CoV-2 in wastewater: State of the knowledge and research needs.* Science of the Total Environment, 2020. **739**: p. 139076.

114. Gundy, P.M., C.P. Gerba, and I.L. Pepper, *Survival of Coronaviruses in Water and Wastewater.* Food and Environmental Virology, 2009. **1**(1): p. 10-14.

115. Peiris, J.S., et al., *Clinical progression and viral load in a community outbreak of coronavirus-associated SARS pneumonia: a prospective study.* Lancet, 2003. **361**(9371): p. 1767-72.

116. National Research Council, *Water Reuse: Potential for Expanding the Nation's Water Supply Through Reuse of Municipal Wastewater*. 2012, Washington, DC: The National Academies Press. 276.

117. Wigginton, K.R., Y. Ye, and R.M. Ellenberg, *Emerging investigators series: the source and fate of pandemic viruses in the urban water cycle.* Environmental Science-Water Research & Technology, 2015. **1**(6): p. 735-746.

118. Garcia-Segura, S., et al., *Electrocoagulation and advanced electrocoagulation processes: A general review about the fundamentals, emerging applications and its association with other technologies.* Journal of Electroanalytical Chemistry, 2017. **801**: p. 267-299.

119. Ye, Y.Y., et al., *Reactivity of Enveloped Virus Genome, Proteins, and Lipids with Free Chlorine and UV_{254}* Environmental Science & Technology, 2018. **52**(14): p. 7698-7708.

120. Silverman, A.I. and A.B. Boehm, *Systematic Review and Meta-Analysis of the Persistence and Disinfection of Human Coronaviruses and Their Viral Surrogates in Water and Wastewater.* Environmental Science & Technology Letters, 2020. **7**(8): p. 544-553.

121. Rice, E.W., et al., *Chlorine Inactivation of Highly Pathogenic Avian Influenza Virus (H5N1).* Emerging Infectious Disease Journal, 2007. **13**(10): p. 1568.

122. Bibby, K., et al., *Disinfection of Ebola Virus in Sterilized Municipal Wastewater.* PLOS Neglected Tropical Diseases, 2017. **11**(2): p. e0005299. doi:10.1371/journal.pntd.0005299.

123. Lenes, D., et al., *Assessment of the removal and inactivation of influenza viruses H5N1 and H1N1 by drinking water treatment.* Water Research, 2010. **44**(8): p. 2473-2486.

124. Templeton, M.R., R.C. Andrews, and R. Hofmann, *Particle-associated viruses in water: Impacts on disinfection processes.* Critical Reviews in Environmental Science and Technology, 2008. **38**(3): p. 137-164.

125. Katz, A., et al., *Heteroaggregation of an enveloped bacteriophage with colloidal sediments and effect on virus viability.* Science of the Total Environment, 2018. **637**: p. 104-111.

126. Ye, Y.Y., et al., *Survivability, Partitioning, and Recovery of Enveloped Viruses in Untreated Municipal Wastewater.* Environmental Science & Technology, 2016. **50**(10): p. 5077-5085.

127. Jäälinoja, H.T., J.T. Huiskonen, and S.J. Butcher, *Electron cryomicroscopy comparison of the architectures of the enveloped bacteriophages ϕ6 and ϕ8.* Structure, 2007. **15**(2): p. 157-167.

128. Mindich, L., *Precise Packaging of the Three Genomic Segments of the Double-Stranded-RNA Bacteriophage φ6.* Microbiology and Molecular Biology Reviews, 1999. **63**(1): p. 149-160.

129. Grabow, W.O.K., *Bacteriophages: Update on application as models for viruses in water.* Water SA, 2001. **27**(2): p. 251-268.

130. Whitworth, C., et al., *Persistence of Bacteriophage Phi 6 on Porous and Nonporous Surfaces and the Potential for Its Use as an Ebola Virus or Coronavirus Surrogate.* Applied and Environmental Microbiology, 2020. **86**(17): p. e01482-20.

131. Gallandat, K., M.K. Wolfe, and D. Lantagne, *Surface Cleaning and Disinfection: Efficacy Assessment of Four Chlorine Types Using Escherichia coli and the Ebola Surrogate Phi6.* Environmental Science & Technology, 2017. **51**(8): p. 4624-4631.

132. Block, K.A., et al., *Disassembly of the cystovirus phi 6 envelope by montmorillonite clay.* Microbiology open, 2014. **3**(1): p. 42-51.

133. Hill, V.R., et al., *Development of a Nucleic Acid Extraction Procedure for Simultaneous Recovery of DNA and RNA from Diverse Microbes in Water.* Pathogens, 2015. **4**(2): p. 335-354.

134. Tanneru, C.T. and S. Chellam, *Mechanisms of virus control during iron electrocoagulation - Microfiltration of surface water.* Water Research, 2012. **46**(7): p. 2111-2120.

135. Zhu, B., D.A. Clifford, and S. Chellam, *Virus removal by iron coagulation–microfiltration.* Water Research, 2005. **39**(20): p. 5153-5161.

136. Pham, A.N., et al., *Kinetics of Fe(III) precipitation in aqueous solutions at pH 6.0-9.5 and 25 degrees C.* Geochimica Et Cosmochimica Acta, 2006. **70**(3): p. 640-650.

137. Smith, G.F. and W.H. Mccurdy, *2,9-Dimethyl-1,10-phenanthroline - New specific in spectrophotometric determination of copper.* Analytical Chemistry, 1952. **24**(2): p. 371-373.

138. Baga, A.N., et al., *A simple spectrophotometric determination of hydrogen-peroxide at low concentrations in aqueous solution.* Analytica Chimica Acta, 1988. **204**(1-2): p. 349-353.

139. Kosaka, K., et al., *Comparison among the methods for hydrogen peroxide measurements to evaluate advanced oxidation processes: Application of a spectrophotometric method using copper(II) ion and 2.9 dimethyl-1,10-phenanthroline.* Environmental Science & Technology, 1998. **32**(23): p. 3821-3824.

140. Texas Commission on Environmental Quality, *Rules and Regulations for Public Water Systems (TCEQ Publication RG-195)*. 2012.

141. USEPA, *40 CFR Parts 141 and 142 Drinking Water; National Primary Drinking Water Regulations; Filtration, Disinfection; Turbidity, Giardia lamblia, Viruses, Legionella, and Heterotrophic Bacteria; Final Rule (Federal Register; 54 FR 27486, June 29, 1989)*.

142. Pitol, A.K., et al., *Virus Transfer at the Skin-Liquid Interface.* Environmental Science & Technology, 2017. **51**(24): p. 14417-14425.

143. Lamarre, A. and P.J. Talbot, *Effect of pH and temperature on the infectivity of human coronavirus 229E.* Canadian Journal of Microbiology, 1989. **35**(10): p. 972-974.

144. https://www.emdataresource.org/ (Accessed October 10 2020). Accessed October 10, 2020.

145. Santos, M.C.D., et al., *Spectroscopy with computational analysis in virological studies: A decade (2006-2016).* Trends in Analytical Chemistry: TRAC, 2017. **97**: p. 244-256.

146. Laurinavičius, S., D.H. Bamford, and P. Somerharju, *Transbilayer distribution of phospholipids in bacteriophage membranes.* Biochimica et Biophysica Acta (BBA) - Biomembranes, 2007. **1768**(10): p. 2568-2577.

147. Laurinavičius, S., et al., *The origin of phospholipids of the enveloped bacteriophage phi6.* Virology, 2004. **326**(1): p. 182-190.

148. Li, T., et al., *Structural Studies of the Enveloped dsRNA Bacteriophage ϕ6 of Pseudomonas syringae by Raman Spectroscopy: I. The Virion and Its Membrane Envelope.* Journal of Molecular Biology, 1993. **230**(2): p. 461-472.

149. Parikh, S.J. and J. Chorover, *ATR-FTIR spectroscopy reveals bond formation during bacterial adhesion to iron oxide.* Langmuir, 2006. **22**(20): p. 8492-500.

150. Parikh, S.J., F.N.D. Mukome, and X. Zhang, *ATR-FTIR spectroscopic evidence for biomolecular phosphorus and carboxyl groups facilitating bacterial adhesion to iron oxides.* Colloids and surfaces. B, Biointerfaces, 2014. **119**: p. 38-46.

151. Mantsch, H.H., A. Martin, and D.G. Cameron, *Characterization by infrared spectroscopy of the bilayer to nonbilayer phase transition of phosphatidylethanolamines.* Biochemistry, 1981. **20**(11): p. 3138-3145.

152. Movasaghi, Z., S. Rehman, and I.U. Rehman, *Fourier Transform Infrared (FTIR) spectroscopy of biological tissues.* Applied Spectroscopy Reviews, 2008. **43**(2): p. 134-179.

153. Stuart, B., *Infrared Spectroscopy: Fundamentals and Applications*. 2004: John Wiley & Sons, Ltd.

154. Sinclair, J.F., et al., *Proteins of bacteriophage phi6.* Journal of Virology, 1975. **16**(3): p. 685-695.

155. Debnath, S., et al., *Reductive Dissolution of Ferrihydrite by Ascorbic Acid and the Inhibiting Effect of Phospholipid.* Journal of Colloid and Interface Science, 2010. **341**(2): p. 215-223.

156. Ha, J., et al., *Adsorption of Organic Matter at Mineral/Water Interfaces: 7. ATR-FTIR and Quantum Chemical Study of Lactate Interactions with Hematite Nanoparticles.* Langmuir, 2008. **24**(13): p. 6683-6692.

157. Chatgilialoglu, C., et al., *cis−trans Isomerization of Monounsaturated Fatty Acid Residues in Phospholipids by Thiyl Radicals.* Journal of the American Chemical Society, 2000. **122**(19): p. 4593-4601.

158. Niki, E., et al., *Membrane damage due to lipid oxidation.* The American Journal of Clinical Nutrition, 1991. **53**(1): p. 201S-205S.

159. Borchman, D. and M.C. Yappert, *Age-related lipid oxidation in human lenses.* Investigative Ophthalmology & Visual Science, 1998. **39**(6): p. 1053-1058.

160. Cebi, N., et al., *Prediction of peroxide value in omega-3 rich microalgae oil by ATR-FTIR spectroscopy combined with chemometrics.* Food Chemistry, 2017. **225**: p. 188-196.

161. Daoud, S., et al., *Fast and direct analysis of oxidation levels of oil-in-water emulsions using ATR-FTIR.* Food Chemistry, 2019. **293**: p. 307-314.

162. Borchman, D., et al., *Temperature-induced conformational changes in human tearlipids hydrocarbon chains.* Biopolymers, 2007. **87**(2-3): p. 124-133.

163. Shin, G.A. and M.D. Sobsey, *Reduction of Norwalk virus, poliovirus 1, and bacteriophage MS2 by ozone disinfection of water.* Applied and Environmental Microbiology, 2003. **69**(7): p. 3975-3978.

164. Bhattacharya, S.S., et al., *Use of reverse transcription and PCR to discriminate between infectious and non-infectious hepatitis A virus.* Journal of Virological Methods, 2004. **116**(2): p. 181-187.

165. Duizer, E., et al., *Inactivation of caliciviruses.* Applied and Environmental Microbiology, 2004. **70**(8): p. 4538-4543.

166. Boehm, A.B., et al., *Systematic review and meta-analysis of decay rates of waterborne mammalian viruses and coliphages in surface waters.* Water Research, 2019. **164**: p. 114898.

167. Haas, C.N., et al., *Risk assessment of virus in drinking water.* Risk Analysis, 1993. **13**(5): p. 545-552.

168. USEPA, *Drinking Water Contaminant Candidate List 4.* Federal Register, 2016. **81**: p. 81099-81114.

169. Sriramula, N. and M. Chaudhuri, *Virus removal by filtration.* Water Science and Technology, 1982. **14**(4-5): p. 253-256.

170. Nasser, A., et al., *Removal of hepatitis A virus (HAV), poliovirus and MS2 coliphage by coagulation and high rate filtration.* Water Science and Technology, 1995. **31**(5): p. 63-68.

171. Brooke K. Mayer, Hodon Ryu, and M. Abbaszadegan, *Treatability of U.S. Environmental Protection Agency Contaminants Candidate List viruses: Removal of coxsackievirus and echovirus using enhanced coagulation.* Environmental Science & Technology, 2008. **42**: p. 6890–6896.

172. David, E.S., et al., *Avian influenza virus in aquatic habitats: What do we need to learn?* Avian Diseases, 2010. **54**(s1): p. 461-465.

173. Rabenau, H.F., et al., *Stability and inactivation of SARS coronavirus.* Medical Microbiology and Immunology, 2005. **194**(1): p. 1-6.

174. Bibby, K., N. Aquino de Carvalho, and K. Wigginton, *Research Needs for Wastewater Handling in Virus Outbreak Response.* Environmental Science & Technology, 2017. **51**(5): p. 2534-2535.

175. Leclerc, H., et al., *Bacteriophages as indicators of enteric viruses and public health risk in groundwaters.* Journal of Applied Microbiology, 2000. **88**(1): p. 5-21.

176. Gallandat, K. and D. Lantagne, *Selection of a Biosafety Level 1 (BSL-1) surrogate to evaluate surface disinfection efficacy in Ebola outbreaks: Comparison of four bacteriophages.* PLoS One, 2017. **12**(5): p. e0177943.

177. Whitworth, C., et al., *Persistence of Bacteriophage Phi 6 on Porous and Nonporous Surfaces and the Potential for Its Use as an Ebola Virus or Coronavirus Surrogate.* Appl Environ Microbiol, 2020. **86**(17).

178. Ye, Y., et al., *Reactivity of enveloped virus genome, proteins, and lipids with free chlorine and UV_{254}.* Environmental Science & Technology, 2018. **52**(14): p. 7698-7708.

179. Sinclair, J.F., et al., *Proteins of bacteriophage ϕ6.* Journal of Virology, 1975. **16**(3): p. 685-695.

180. Qiao, Z., et al., *Nucleic acid photolysis by UV_{254} and the impact of virus encapsidation.* Environmental Science & Technology, 2018. **52**(18): p. 10408-10415.

181. APHA, AWWA, and WEF, *Standard Methods for the Examination of Water & Wastewater*. 21st Edition ed. 2005, Washington, D.C.: American Public Health Association, American Water Works Association and Water Environment Federation.

182. Mariey, L., et al., *Discrimination, classification, identification of microorganisms using FTIR spectroscopy and chemometrics.* Vibrational Spectroscopy, 2001. **26**(2): p. 151-159.

183. Shirasaki, N., et al., *Investigation of enteric adenovirus and poliovirus removal by coagulation processes and suitability of bacteriophages MS2 and φX174 as surrogates for those viruses.* Science of The Total Environment, 2016. **563-564**: p. 29-39.

184. Canizares, P., et al., *Comparison of the aluminum speciation in chemical and electrochemical dosing processes.* Industrial & Engineering Chemistry Research, 2006. **45**(26): p. 8749-8756.

185. Benjamin, M.M. and D.F. Lawler, *Water quality engineering : physical/chemical treatment processes*. 2013, Wiley: Hoboken, New Jersey.

186. Qian, A., et al., *Oxidizing capacity of iron electrocoagulation systems for refractory organic contaminant transformation.* Environmental Science & Technology, 2019. **53**(21): p. 12629-12638.

187. Li, L., et al., *Modeling As(III) oxidation and removal with iron electrocoagulation in groundwater.* Environmental Science & Technology, 2012. **46**(21): p. 12038-12045.

188. Bicudo, B., et al., *Low voltage iron electrocoagulation as a tertiary treatment of municipal wastewater: removal of enteric pathogen indicators and antibiotic-resistant bacteria.* Water Research, 2021. **188**: p. 116500.

189. Rattanakul, S. and K. Oguma, *Analysis of hydroxyl radicals and inactivation mechanisms of bacteriophage MS2 in response to a simultaneous application of UV and chlorine.* Environmental Science & Technology, 2017. **51**(1): p. 455-462.

190. Ye, Y., et al., *Survivability, partitioning, and recovery of enveloped viruses in untreated municipal wastewater.* Environmental Science & Technology, 2016. **50**(10): p. 5077-5085.

191. Whitworth, C., et al., *Persistence of bacteriophage Phi 6 on porous and non-porous surfaces; Potential for use as Ebola or coronavirus surrogate.* Applied and Environmental Microbiology, 2020: p. AEM.01482-20.

192. Koning, R.I., et al., *Asymmetric cryo-EM reconstruction of phage MS2 reveals genome structure in situ.* Nature Communications, 2016. **7**(1): p. 12524.

193. Nguyen, T.H., et al., *The RNA core weakly influences the interactions of the bacteriophage MS2 at key environmental interfaces.* Soft Matter, 2011. **7**(21): p. 10449-10456.

194. Watts, S., et al., *Colloidal transformations in MS2 virus particles: Driven by pH, influenced by natural organic matter.* ACS Nano, 2020. **14**(2): p. 1879-1887.

195. Block, K.A., et al., *Disassembly of the cystovirus ϕ6 envelope by montmorillonite clay.* MicrobiologyOpen, 2014. **3**(1): p. 42-51.

196. Steely, H.T. and D. Lang, *Electron microscopy of bacteriophage ϕ6 nucleocapsid: two-dimensional image analysis.* Journal of Virology, 1984. **51 2**: p. 479-483.

197. Škubník, K., et al., *Capsid opening enables genome release of iflaviruses.* Science Advances, 2021. **7**(1): p. eabd7130.

198. Sun, X., D.H. Bamford, and M.M. Poranen, *Probing, by self-assembly, the number of potential binding sites for minor protein subunits in the procapsid of double-stranded RNA bacteriophage Phi6.* Journal of Virology, 2012. **86**(22): p. 12208-12216.

199. Kenney, J.M., et al., *Bacteriophage ϕ6 envelope elucidated by chemical cross-linking, immunodetection, and cryoelectron microscopy.* Virology, 1992. **190**(2): p. 635-644.

200. Huiskonen, J.T., et al., *Structure of the bacteriophage ϕ6 nucleocapsid suggests a mechanism for sequential RNA packaging.* Structure, 2006. **14**(6): p. 1039-1048.

201. Harrison, S.C., *Viral membrane fusion.* Virology, 2015. **479-480**: p. 498-507.

202. Poranen, M.M., et al., *A novel virus–host cell membrane interaction: Membrane voltage–dependent endocytic-like entry of bacteriophage ϕ6 nucleocapsid.* Journal of Cell Biology, 1999. **147**(3): p. 671-682.

203. Akhavan, O., M. Choobtashani, and E. Ghaderi, *Protein degradation and RNA efflux of viruses photocatalyzed by graphene–tungsten oxide composite under visible light irradiation.* The Journal of Physical Chemistry C, 2012. **116**(17): p. 9653-9659.

204. Stuart, B.H., *Infrared spectroscopy of biological applications.* Encyclopedia of Analytical Chemistry, 2006.

205. Su, C. and D.L. Suarez, *In situ infrared speciation of adsorbed carbonate on aluminum and iron oxides.* Clays and Clay Minerals, 1997. **45**(6): p. 814-825.

206. Su, C. and D.L. Suarez, *Coordination of adsorbed boron: A FTIR spectroscopic study.* Environmental Science & Technology, 1995. **29**(2): p. 302-311.

207. Muller, K. and G. Lefevre, *Vibrational characteristics of outer-sphere surface complexes: example of sulfate ions adsorbed onto metal (hydr)oxides.* Langmuir, 2011. **27**(11): p. 6830-6835.

208. Davies, M.J., *Singlet oxygen-mediated damage to proteins and its consequences.* Biochemical and Biophysical Research Communications, 2003. **305**(3): p. 761-770.

209. Moore, D.J., et al., *Quantitative IR studies of acyl chain conformational order in fatty acid homogeneous membranes of live cells of Acholeplasma laidlawii B.* Biochemistry, 1993. **32**(24): p. 6281-6287.

210. Wang, T., et al., *Cellular uptake of nanoparticles by membrane penetration: A study combining confocal microscopy with FTIR spectroelectrochemistry.* ACS Nano, 2012. **6**(2): p. 1251-1259.

211. Hong, Z.-N., et al., *Preferential adhesion of surface groups of Bacillus subtilis on gibbsite at different ionic strengths and pHs revealed by ATR-FTIR spectroscopy.* Colloids and Surfaces B: Biointerfaces, 2018. **165**: p. 83-91.

212. Liu, Z., et al., *Adhesion of Escherichia coli and Bacillus subtilis to amorphous Fe and Al hydroxides and their effects on the surface charges of the hydroxides.* Journal of Soils and Sediments, 2015. **15**(11): p. 2293-2303.

213. Elzinga, E.J., et al., *ATR-FTIR spectroscopy study of the influence of pH and contact time on the adhesion of Shewanella putrefaciens bacterial cells to the surface of hematite.* Environmental Science & Technology, 2012. **46**(23): p. 12848-12855.

214. Omoike, A., et al., *Adhesion of bacterial exopolymers to α-FeOOH: Inner-sphere complexation of phosphodiester groups.* Langmuir, 2004. **20**(25): p. 11108-11114.

215. Parikh, S.J. and J. Chorover, *ATR-FTIR spectroscopy reveals bond formation during bacterial adhesion to iron oxide.* Langmuir, 2006. **22**(20): p. 8492-8500.

216. Feng, Y.J., et al., *Electrochemical technologies for wastewater treatment and resource reclamation.* Environmental Science-Water Research & Technology, 2016. **2**(5): p. 800-831.

217. Anis, S.F., R. Hashaikeh, and N. Hilal, *Microfiltration membrane processes: A review of research trends over the past decade.* Journal of Water Process Engineering, 2019. **32**.

218. Howe, K.J. and M.M. Clark, *Fouling of Microfiltration and Ultrafiltration Membranes by Natural Waters.* Environmental Science & Technology, 2002. **36**(16): p. 3571-3576.

219. Hermia, J., *Constant Pressure Blocking Filtration Laws - Application to Power-Law Non-Newtonian Fluids.* Transactions of the Institution of Chemical Engineers, 1982. **60**(3): p. 183-187.

220. Bolton, G., D. LaCasse, and R. Kuriyel, *Combined models of membrane fouling: Development and application to microfiltration and ultrafiltration of biological fluids.* Journal of Membrane Science, 2006. **277**(1-2): p. 75-84.

221. Ho, C.C. and A.L. Zydney, *A Combined Pore Blockage and Cake Filtration Model for Protein Fouling during Microfiltration.* Journal of Colloid and Interface Science, 2000. **232**(2): p. 389-399.

222. Shirato, M., T. Aragaki, and E. Iritani, *Blocking Filtration Laws for Filtration of Power-law Non-Newtonian Fluids.* Journal of Chemical Engineering of Japan, 1979. **12**(2): p. 162-164.

223. Palacio, L., C.C. Ho, and A.L. Zydney, *Application of a pore-blockage--cake-filtration model to protein fouling during microfiltration.* Biotechnol Bioeng, 2002. **79**(3): p. 260-70.

224. Yuan, W., A. Kocic, and A.L. Zydney, *Analysis of humic acid fouling during microfiltration using a pore blockage-cake filtration model.* Journal of Membrane Science, 2002. **198**(1): p. 51-62.

225. Bates, S., N. Nguyen, and K.R. Lentine, *Development of serum-free media for the cultivation and recovery of Acholeplasma laidlawii used for challenge testing sterilizing-*

grade filters in biopharmaceutical applications. PDA Journal of Pharmaceutical Science and Technology, 2008. **62**: p. 402-420.

226. Folmsbee, M., G. Howard, and M. McAlister, *Nutritional effects of culture media on mycoplasma cell size and removal by filtration.* Biologicals, 2010. **38**(2): p. 214-7.

227. Cronholm, K., et al., *Validation of a Microbiological Method Using Acholeplasma laidlawii for Assessing Performance of Microporous Membranes for Mycoplasma Clearance.* PDA Journal of Pharmaceutical Science and Technology, 2009. **63**: p. 438-461.

228. Folmsbee, M., et al., *The Development of a Microbial Challenge Test with Acholeplasma laidlawii To Rate Mycoplasma-Retentive Filters by Filter Manufacturers.* PDA Journal of Pharmaceutical Science and Technology, 2014. **68**(3): p. 281-96.

229. Helling, A., et al., *Retention of Acholeplasma laidlawii by Sterile Filtration Membranes: Effect of Cultivation Medium and Filtration Temperature.* PDA Journal of Pharmaceutical Science and Technology, 2018. **72**(3): p. 264-277.

230. Wieslander, A., et al., *Membrane Lipid-Composition and Cell-Size of Acholeplasma-Laidlawii Strain-a Are Strongly Influenced by Lipid Acyl-Chain Length.* European Journal of Biochemistry, 1995. **227**(3): p. 734-744.

231. Tung, K.L., et al., *Effects of Soft Particle Deformability and Particle/Pore Size Ratio on the Blocking Mechanism in Dead-End Microfiltration.* Chemical Engineering & Technology, 2010. **33**(8): p. 1341-1348.

232. Hwang, K.-J., et al., *Effects of porous gel particle compression properties on microfiltration characteristics.* Journal of Membrane Science, 2009. **341**(1-2): p. 286-293.

233. Hendrickson, G.R. and L.A. Lyon, *Microgel translocation through pores under confinement.* Angew Chem Int Ed Engl, 2010. **49**(12): p. 2193-7.

234. Holden, D.A., et al., *Electrical signature of the deformation and dehydration of microgels during translocation through nanopores.* Soft Matter, 2011. **7**(18).

235. Wang, F. and V.V. Tarabara, *Pore blocking mechanisms during early stages of membrane fouling by colloids.* Journal of Colloid and Interface Science, 2008. **328**(2): p. 464-9.

236. Bowen, W.R., J.I. Calvo, and A. Hernandez, *Steps of Membrane Blocking in Flux Decline during Protein Microfiltration.* Journal of Membrane Science, 1995. **101**(1-2): p. 153-165.

237. Chellam, S. and W. Xu, *Blocking laws analysis of dead-end constant flux microfiltration of compressible cakes.* Journal of Colloid and Interface Science, 2006. **301**(1): p. 248-57.

238. Nakanishi, K., T. Tadokoro, and R. Matsuno, *On the Specific Resistance of Cakes of Microorganisms.* Chemical Engineering Communications, 2007. **62**(1-6): p. 187-201.

239. McCarthy, A.A., et al., *The effect of pressure on the specific resistance of yeast filter cakes during dead-end filtration in the range 30–500kPa.* Biotechnology Techniques, 1998. **12**(12): p. 909-912.

240. Zhou, W., et al., *Activated carbon as effective cathode material in iron-free electro-Fenton process: Integrated H_2O_2 electrogeneration, activation, and pollutants adsorption.* Electrochimica Acta, 2019. **296**: p. 317-326.

241. Qiang, Z., J.H. Chang, and C.P. Huang, *Electrochemical generation of hydrogen peroxide from dissolved oxygen in acidic solutions.* Water Research, 2002. **36**(1): p. 85-94.

242. Liu, Y., et al., *High-yield electrosynthesis of hydrogen peroxide from oxygen reduction by hierarchically porous carbon.* Angewandte Chemie International Edition, 2015. **54**(23): p. 6837-6841.

243. Darling, A.J., J.A. Boose, and J. Spaltro, *Virus Assay Methods: Accuracy and Validation.* Biologicals, 1998. **26**(2): p. 105-110.

244. Shi, C.J., et al., *Removal of viruses and bacteriophages from drinking water using zero-valent iron.* Separation and Purification Technology, 2012. **84**: p. 72-78.

245. Brie, A., et al., *The impact of chlorine and heat on the infectivity and physicochemical properties of bacteriophage MS2.* FEMS Microbiology Ecology, 2018. **94**(8).

246. You, Y., et al., *Removal and Inactivation of Waterborne Viruses Using Zerovalent Iron.* Environmental Science & Technology, 2005. **39**(23): p. 9263-9269.

247. Heffron, J., D.R. Ryan, and B.K. Mayer, *Sequential electrocoagulation-electrooxidation for virus mitigation in drinking water.* Water Research, 2019. **160**: p. 435-444.

248. Delaire, C., et al., *Escherichia coli attenuation by Fe electrocoagulation in synthetic Bengal groundwater: Effect of pH and natural organic matter.* Environmental Science & Technology, 2015. **49**(16): p. 9945-9953.

249. Delaire, C., et al., *Bacteria attenuation by iron electrocoagulation governed by interactions between bacterial phosphate groups and Fe(III) precipitates.* Water Research, 2016. **103**: p. 74-82.

250. Chen, M., et al., *Boron removal by electrocoagulation: Removal mechanism, adsorption models and factors influencing removal.* Water Research, 2020. **170**: p. 115362.

251. Isa, M.H., et al., *Boron removal by electrocoagulation and recovery.* Water Research, 2014. **51**: p. 113-123.

252. Durante, C., et al., *Advanced oxidation processes coupled with electrocoagulation for the exhaustive abatement of Cr-EDTA.* Water Research, 2011. **45**(5): p. 2122-2130.

253. Pan, C., et al., *Effect of Humic Acid on the Removal of Chromium(VI) and the Production of Solids in Iron Electrocoagulation.* Environmental Science & Technology, 2017. **51**(11): p. 6308-6318.

254. Bandaru, S.R.S., et al., *Rapid and Efficient Arsenic Removal by Iron Electrocoagulation Enabled with in Situ Generation of Hydrogen Peroxide.* Environmental Science & Technology, 2020. **54**(10): p. 6094-6103.

255. van Genuchten, C.M., et al., *Removing arsenic from synthetic groundwater with iron electrocoagulation: an Fe and As K-edge EXAFS study.* Environmental Science & Technology, 2012. **46**(2): p. 986-994.

256. Bandaru, S.R.S., et al., *Long-term electrode behavior during treatment of arsenic contaminated groundwater by a pilot-scale iron electrocoagulation system.* Water Research, 2020. **175**: p. 115668.

257. Roy, M., et al., *Integrating biological As(III) oxidation with Fe(0) electrocoagulation for arsenic removal from groundwater.* Water Research, 2021. **188**: p. 116531.

258. Wan, W., et al., *Effects of water chemistry on arsenic removal from drinking water by electrocoagulation.* Water Research, 2011. **45**(1): p. 384-392.

259. Li, P., et al., *Highly efficient interception and precipitation of uranium(VI) from aqueous solution by iron-electrocoagulation combined with cooperative chelation by organic ligands.* Environmental Science & Technology, 2017. **51**(24): p. 14368-14378.

260. Dubrawski, K.L. and M. Mohseni, *Standardizing electrocoagulation reactor design: iron electrodes for NOM removal.* Chemosphere, 2013. **91**(1): p. 55-60.

261. McBeath, S.T., et al., *In-situ determination of current density distribution and fluid modeling of an electrocoagulation process and its effects on natural organic matter removal for drinking water treatment.* Water Research, 2020. **171**: p. 115404.

262. Dubrawski, K.L. and M. Mohseni, *In-situ identification of iron electrocoagulation speciation and application for natural organic matter (NOM) removal.* Water Research, 2013. **47**(14): p. 5371-5380.

263. Devlin, T.R., et al., *Removal of Soluble Phosphorus from Surface Water Using Iron (Fe-Fe) and Aluminum (Al-Al) Electrodes.* Environmental Science & Technology, 2017. **51**(23): p. 13825-13833.

264. Tian, Y., et al., *Effective phosphate removal for advanced water treatment using low energy, migration electric-field assisted electrocoagulation.* Water Research, 2018. **138**: p. 129-136.

265. Liang, S., et al., *One-Step Treatment of Phosphite-Laden Wastewater: A Single Electrochemical Reactor Integrating Superoxide Radical-Induced Oxidation and Electrocoagulation.* Environmental Science & Technology, 2019. **53**(9): p. 5328-5336.

266. Cañizares, P., et al., *Coagulation and electrocoagulation of wastes polluted with dyes.* Environmental Science & Technology, 2006. **40**(20): p. 6418-6424.

267. Bocos, E., et al., *Electrocoagulation: Simply a phase separation Technology? The case of bronopol compared to its treatment by EAOPs.* Environmental Science & Technology, 2016. **50**(14): p. 7679-7686.

268. Lin, H., et al., *Efficient sorption and removal of perfluoroalkyl acids (PFAAs) from aqueous solution by metal hydroxides generated in situ by electrocoagulation.* Environmental Science & Technology, 2015. **49**(17): p. 10562-10569.

269. Ryan, D.R., P.J. McNamara, and B.K. Mayer, *Iron-electrocoagulation as a disinfection byproduct control strategy for drinking water treatment.* Environmental Science: Water Research & Technology, 2020. **6**(4): p. 1116-1124.

270. Lakshmanan, D., D.A. Clifford, and G. Samanta, *Ferrous and ferric ion generation during iron electrocoagulation.* Environmental Science & Technology, 2009. **43**(10): p. 3853-3859.

271. Bagga, A., S. Chellam, and D.A. Clifford, *Evaluation of iron chemical coagulation and electrocoagulation pretreatment for surface water microfiltration.* Journal of Membrane Science, 2008. **309**(1-2): p. 82-93.

272. Goeller, L.J. and M.R. Riley, *Discrimination of Bacteria and Bacteriophages by Raman Spectroscopy and Surface-enhanced Raman Spectroscopy.* Applied Spectroscopy, 2007. **61**(7): p. 679-685.

273. Hill, V.R., et al., *Multistate evaluation of an ultrafiltration-based procedure for simultaneous recovery of enteric microbes in 100-liter tap water samples.* Applied and Environmental Microbiology, 2007. **73**(13): p. 4218-4225.

274. Johnson, I. and M.T.Z. Spence, *The Molecular Probes Handbook. A Guide to Fluorescent Probes and Labeling Technologies*. 11 ed. 2010, Carlsbad, CA: Invitrogen Corp.

275. Chen, N.-d., et al., *Discrimination and similarity evaluation of tissue-cultured and wild Dendrobium species using Fourier transform infrared spectroscopy.* Journal of Molecular Structure, 2015. **1086**: p. 255-265.

276. Jiang, Y., et al., *Qualification of FTIR spectroscopic method for protein secondary structural analysis.* Journal of Pharmaceutical Sciences, 2011. **100**(11): p. 4631-4641.

277. Siebert, F., *[20] Infrared spectroscopy applied to biochemical and biological problems*, in *Methods in Enzymology*. 1995, Academic Press. p. 501-526.

278. Elliott, A. and E.J. Ambrose, *Structure of Synthetic Polypeptides.* Nature, 1950. **165**(4206): p. 921-922.

279. Surewicz, W.K. and H.H. Mantsch, *New insight into protein secondary structure from resolution-enhanced infrared spectra.* Biochimica et Biophysica Acta (BBA) - Protein Structure and Molecular Enzymology, 1988. **952**: p. 115-130.

280. Dovbeshko, G.I., et al., *FTIR spectroscopy studies of nucleic acid damage.* Talanta, 2000. **53**(1): p. 233-246.

281. Theis, T.L. and P.C. Singer, *Complexation of iron(ll) by organic matter and its effect on iron(ll) oxygenation.* Environmental Science & Technology, 1974. **8**(6): p. 569–573.

282. Adewuyl, Y.G. and G.R. Carmlchae, *Kinetics of oxidation of dimethyl sulfide by hydrogen peroxide in acidic and alkaline medium.* Environmental Science & Technology, 1986. **20**: p. 1017-1022.

283. Nahar, S. and H.A. Tajmirriahi, *A comparative study of Fe(II) and Fe(III) ions complexation with proteins of the light-harvesting complex of chloroplast thylakoid membranes.* Journal of Inorganic Biochemistry, 1994. **54**(2): p. 79-90.

284. Kinsela, A.S., et al., *Influence of dissolved silicate on rates of Fe(II) oxidation.* Environmental Science & Technology, 2016. **50**(21): p. 11663-11671.

285. Meneghini, R., *Iron homeostasis, oxidative stress, and DNA damage.* Free Radical Biology & Medicine, 1997. **23**(5): p. 783-792.

286. Loeb, S.K., et al., *Sunlight inactivation of human norovirus and bacteriophage MS2 using a genome-wide PCR-based approach and enzyme pretreatment.* Environmental Science & Technology, 2021. **55**(13): p. 8783-8792.

287. Leifels, M., et al., *Capsid integrity quantitative PCR to determine virus infectivity in environmental and food applications - A systematic review.* Water Research X, 2021. **11**: p. 100080.

288. De Vries, T.A. and M.A. Hamilton, *Estimating the Antimicrobial Log Reduction: Part 1. Quantitative Assays.* Quantitative Microbiology, 1999. **1**(1): p. 29-45.

289. Liu, W., et al., *Optimal Methods for Quenching H_2O_2 Residuals Prior to UFC Testing.* Water Research, 2003. **37**(15): p. 3697-703.

290. Olsztyńska-Janus, S., et al., *ATR-IR study of skin components: Lipids, proteins and water. Part I: Temperature effect.* Spectrochimica Acta Part A: Molecular and Biomolecular Spectroscopy, 2018. **188**: p. 37-49.

291. Ruan, X., et al., *Comparison of the Effects of Triton X-100 Treatment on the Protein Secondary Structure of Photosystem I and Photosystem II Studied by FT-IR Spectroscopy.* Journal of Molecular Structure, 2000. **525**(1): p. 97-106.

292. Jung, C., *Insight into Protein Structure and Protein-ligand Recognition by Fourier Transform Infrared Spectroscopy.* Journal of Molecular Recognition, 2000. **13**(6): p. 325-351.

293. Cagnasso, M., et al., *ATR-FTIR studies of phospholipid vesicle interactions with α-FeOOH and α-Fe_2O_3 Surfaces.* Colloids and Surfaces B: Biointerfaces, 2010. **76**(2): p. 456-467.

294. Ojeda, J.J., et al., *Characterization of the Cell Surface and Cell Wall Chemistry of Drinking Water Bacteria by Combining XPS, FTIR Spectroscopy, Modeling, and Potentiometric Titrations.* Langmuir, 2008. **24**(8): p. 4032-4040.

APPENDICES

Supporting information for chapter II

Section A1. Phage preparation, enumeration, and analysis

MS2 bacteriophage was purified and concentrated in many steps. *Escherichia coli* was cultured in 10 mL tryptic soy broth solution (TSB; Difco) at 37 ℃ until reaching a mid-log phase. Next, 1 mL of the cultured *E. coli* suspension was inoculated to 100 ml of fresh TSB solution and cultured again at 37 ℃ until mid-log phase, which was inoculated with MS2 at multiplicity of infection of 0.1. After 16 hours of incubation, the suspension was centrifuged at 13,500 g for 20 min, subsequently filtered with 0.2 μm and then with a 0.1 μm polyethersulfone (PES) syringe filter. The resulting filtrate was rinsed and concentrated with phosphate buffer solution (PBS, 4.8 mM of NaH_2PO_4, 17.6 mM of Na_2HPO_4, 145.4 mM of NaCl, pH 7.4±0.1) using a 100 kDa PES membrane centrifugal filter (Spin-X UF, Corning) at 5,900 g for 20 min to remove soluble and low molecular weight impurities [37]. MS2 retained on the membrane filter was resuspended in 1 mL of PBS and stored at 4 ℃. Infective MS2 phages were quantified following double-agar layer method [37, 38, 181]. The titer of final MS2 stock was of the order of 10^{12} PFU/mL.

Section A2. Electrocoagulation

Prior to each experiment, the anode was scrubbed with a 220 grit sandpaper, cleaned with HCl solution (pH 2.5), and rinsed with ultrapure water to remove any impurities and the outer layers. After each experiment, the cell was soaked in HCl solution (pH 2.5) overnight and rinsed with ultrapure water to remove iron residues (and other acid-soluble contamination). The total iron dosage was controlled by adjusting electrolysis time at a fixed current density of 2.8 mA/cm^2 (see Section A4). For phage infectivity assay, Na_2SO_3 was added to the collected samples as a

scavenger of H_2O_2 to prevent further inactivation and, thus to avoid overestimating infective viruses [92]. Afterwards, samples were centrifuged to separate flocs at 12,000 g for 30 min. After centrifugation, infective MS2 remaining in supernatant was enumerated representing the bulk water concentration. Collected iron flocs were re-dissolved in beef extract solution (pH 9.5) to extract MS2 phages representing the floc concentration. The procedure for phage extraction was validated as explained below in Section A5. The detection limit of infectivity assay in both bulk water and flocs was 100 PFU/mL, which was determined based on the linearity between logarithm of dilution factor and PFU count [243], and the volume of phage samples plated (0.1 mL). As shown in Figure A-11, a linear behavior was observed among averages of plaque counts at different dilution factors when plaque counts were more than 10 PFU for both bulk water and floc concentration counting (R^2= 0.994 and 0.996, respectively). Hence, only plates showing more than 10 plaques were used for assay which is the same protocol as in earlier literature [244-246]. The detection limit for both assays (i.e. in flocs and bulk water) was determined as 10 PFU/0.1 mL = 100 PFU/mL [244].

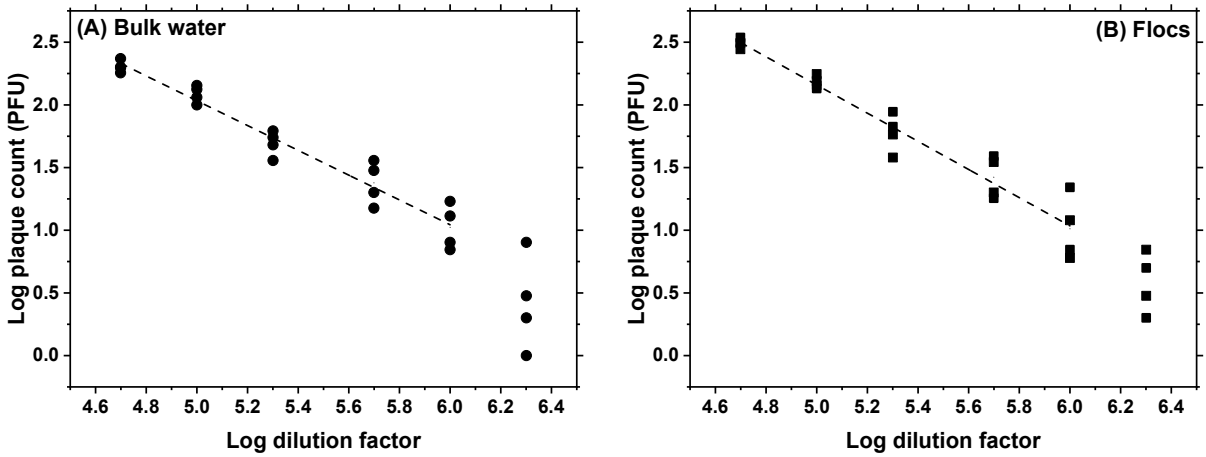

Figure A-1. Linear relation between log plaque counts and log dilution factors was only valid when plaque count was more than 10 PFU for both assays. The bulk water data are shown on the left panel and results from the flocs are on the right panel. Individual symbols represent plaque counts from different plates.

Section A3. Comparison of electrocoagulation experiments

Table A-1 summarizes electrocoagulation system set-ups and experimental conditions for various target contaminants. As seen, the key experimental conditions such as pH, current density and iron dosage in this study (pH 6.4 and 8.2, 2.8 mA/cm^2, and 5 ~ 2500 mg/L Fe, respectively) are within the range of previously employed values (pH 4 ~ 11, 0.02 ~ 250 mA/cm^2, and 0.7 ~ 500 mg/L Al or Fe).

Table A-1. Comparison of experimental set-ups and conditions for electrocoagulation of various target contaminant.

Target contaminant	Solution composition	pH	Electrode material (anode/cathode)	Electrode geometry (anode/cathode)	Current density (mA/cm^2)	Dose (mg/L Al or Fe)	Reference
Bacteriophage MS2	Synthetic water ($NaHCO_3$, $CaCl_2$)	6.4, 8.2	Fe/stainless steel	Rod/hollow cylinder 0.2 cm gap	2.8	5, 10, 20	This study
Bacteriophage MS2	Natural water, Synthetic water ($NaHCO_3$, $CaCl_2$)	6.4, 7.5	Fe/stainless steel	Not specified	0.8, 2.1, 2.7	~ 12	[14]
Bacteriophage MS2	Natural water	6.4	Al/stainless steel	Rod/ not specified	20	~ 30	[13]
Bacteriophage MS2	Synthetic water ($NaHCO_3$, NaCl)	6.2, 8.2	Al/stainless steel	Rod/hollow cylinder	20	~ 30	[16]
Bacteriophage MS2 Bacteriophage ϕX174 Human echovirus 12	Synthetic water ($NaHCO_3$) Natural water	6, 7, 8	Fe/Fe	Plate/plate	1.1	~ 30	[247]
Bacterial indicators Bacteriophage ϕX174	Synthetic effluent water Secondary effluent	7.3	Fe/Fe	Plate/plate 1 cm gap	1.3 ~ 19	2.9 ~ 116.1	[188]
Mammalian viruses Bacteriophages	Synthetic water ($NaNO_3$, $NaHCO_3$)	6, 7, 8	Fe/Fe	Plate/plate 1 cm gap	1.7	2.3	[15]
Escherichia coli	Synthetic groundwater	6.6, 7.5	Fe/Fe	Plate/plate 0.5 cm gap	0.33 ~ 10	6 ~ 140	[248]
Escherichia coli *Enterococcus faecalis*	Synthetic groundwater	7	Fe/Fe	Plate/plate 0.5 cm gap	10	28	[249]
Boron	Natural water	7.8	Al/Al	Rod/rod 2.5 cm gap	18 ~ 250	~ 2500	[250]
Boron	Synthetic produced water	7.8	Al/Al	Plate/plate 0.5 cm gap	6.25 ~ 18.8	36 ~ 320	[251]
Cr-EDTA	Synthetic wastewater	7.8	Fe/Fe	Rod/rod	64	~ 300	[252]
Cr(IV)	Synthetic water	6, 7, 8	Fe/Fe	Rod/rod	0.99	~ 10	[47]

	($NaNO_3$,Na_2HPO_4, Na_2SiO_3, Na_2SO_4)			2 cm gap			
Cr(IV)	Synthetic water ($NaNO_3$,Na_2HPO_4, Na_2SiO_3, Na_2SO_4)	6 ~ 9	Fe/Fe	Rod/rod 2 cm gap	0.99	~ 10	[253]
As(III)	Synthetic groundwater	7	Fe/Fe	Plate/plate 7.5 cm gap	0.15 ~ 3.6	~ 43	[187]
As(III)	Synthetic groundwater	7	Fe/Fe Fe/carbon	Plate/plate or cloth 0.7, 2.5 cm gap	0.14 ~ 56	174	[254]
As(III)	Synthetic groundwater	7	Fe/Cu	Wire/mesh 1 cm gap	0.02 ~ 100	22, 51	[255]
As	Natural groundwater	7.1	Fe/Fe	Plate/plate 5 cm gap	0.3	130	[256]
As(III)/(V)	Synthetic water (NaCl)	7 ~ 8	Fe/Fe	Plate/plate 1 cm gap	3.5 ~ 40	3.5 ~ 70	[257]
As(III)/(V)	Synthetic water (Na_2HPO_4, Na_2SiO_3 Na_2SO_4, $NaHCO_3$)	5 ~ 9	Fe/Fe	Rod/rod 2 cm gap	0.39	50	[258]
U(VI)	Synthetic water (Na_2SO_4)	3.0 ~ 9.0	Fe/graphite	Plate/plate 5 cm gap	0.6 ~ 1.4	~ 100	[259]
Natural organic matter	Synthetic water (Na_2SO_4)	7	Fe/stainless steel	Plate/plate 0.2 cm gap	2.5 ~ 27	300	[260]
Natural organic matter	Natural water Synthetic water (NaCl)	6.6, 7.9	Fe/stainless steel	Plate/plate 0.1, 0.2, 1 cm gap	3.6 ~ 28	25.7 ~ 51.1	[261]
Natural organic matter	Natural water	6 ~ 9	Fe/Pt	Foil/foil 1 cm gap	1 ~ 25	6 ~ 12	[262]
Soluble phosphorous	Natural water	7.8 ~ 8.3	Fe/Fe or Al/Al	Plate/plate 2.5 cm gap	1 ~ 10 (Fe) 2 ~ 15 (Al)	2.6 ~ 16 (Fe) 0.7 ~ 4.3 (Al)	[263]
Phosphate	Wastewater	6.8 ~ 7.1	Fe or Al/activated carbon	Mesh/air cathode	1	-	[264]
Phosphite	Synthetic water (Na_2SO_4)	4	Fe/stainless steel	Plate/plate 1 cm gap	12.5 ~ 50	500	[265]
Erochrome Black T	Synthetic water (NaCl or Na_2SO_4)	4 ~ 11	Al/Al	Plate/plate 0.9 cm gap	1.4	12 ~ 14	[266]
Bronopol	Synthetic wastewater	6.5	Fe, Al/stainless steel	Plate/plate 1 ~ 4 cm gap	11 ~ 66	-	[267]
Perfluoroalkyl acids	Synthetic water (NaCl)	5	Fe, Al, Mg, Zn /stainless steel	Plate/plate or Sheet/rod	0.5	~ 150	[268]
Total trihalomethane	Synthetic water ($NaHCO_3$, KCl, NaBr)	6 ~ 9	Fe/Fe	Not specified	5.55	6.4	[269]

Section A4. Dosage control using Faraday's law

Electrolysis was performed for predetermined time durations calculated using Faraday's law (both sides were divided by volume to obtain concentration, Eq. A1) to add targeted total iron dosages (78 s, 156 s, and 312 s for 5 mg/L, 10 mg/L, and 20 mg/L, respectively), and total iron concentration was measured in the middle and at the end of electrolysis. Figure A-2 compares purely theoretical predictions of total iron concentration with experimentally measured concentrations when the number of electrons transferred (z) is assumed to be 2. As seen, experimentally measured total iron concentrations agreed extremely well with theoretical Faraday's law prediction with no fitting parameters for z = 2 at both pH values providing strong evidence that Fe(II) is generated during electrolysis as shown earlier [253, 262, 270].

$$\frac{m}{V} = \frac{A_W \cdot I \cdot t}{z \cdot F \cdot V} \tag{A1}$$

where, m is mass of total iron (g), V is the electrolytic cell volume (0.45 L), A_w is an atomic mass of iron (55.85 g/mol), I is electrical current (0.1 A), t is electrolysis time (s), z is the number of electrons transferred (=2 here), and F is Faraday's constant (96,486 C/eq).

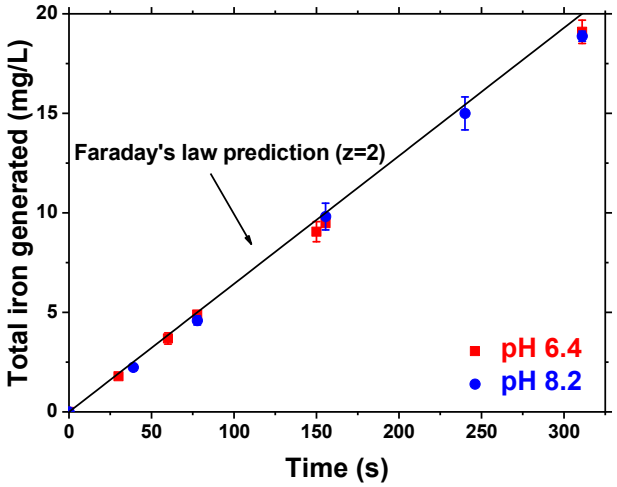

Figure A-2. Strong evidence of Fe(II) production during electrocoagulation via excellent agreement between Faraday's law and experimental measurements of total iron in all cases. A 2-electron transfer quantitatively explains our experimental observations without any fitting demonstrating anodic oxidation produces Fe(II).

Section A5. Recovery of MS2 from iron flocs

The procedure for MS2 phage recovery from iron flocs using 6 % beef extract solution (pH 9.5) was validated. Conventional chemical coagulation with Fe(III) at pH 6.4 and 8.2 was performed to avoid inactivation of MS2 phages, which makes it a suitable condition to verify that all MS2 phages sorbed in flocs are recoverable if not inactivated following the protocol. MS2 phages were spiked in the cell to achieve an initial concentration of O(10^8) PFU/mL. Afterwards, Fe(III) coagulant was added at three target dosages (5 mg/L, 10 mg/L, and 20 mg/L). The solution was rapidly mixed for 2 min followed by a slow mixing for a total time of 120 min. Sorbed MS2 phage concentration was calculated by subtracting bulk water concentration at t=120 min from initial concentration and compared to that of MS2 phages recovered from flocs (Figure A-3). Statistical comparison (*t* test, n= 3 ~ 5, $p < 0.05$ for statistically significant difference) of sorbed and recovered MS2 phages resulted in insignificant differences between two concentrations indicating that phages were fully recovered from iron flocs at all dosages and pH conditions. Hence, the recovery procedure is valid and, thus, any reduction in virus floc concentration during electrocoagulation is solely due to inactivation. In addition, phage recovery during the course of experiment is shown in Figure A-4. At all time points, insignificant difference between sorbed and recovered MS2 concentration was obtained (*t* test, n= 4, $p < 0.05$ for statistically significant difference).

These results correspond with earlier reports from our group using aluminum electrocoagulation and conventional coagulation [13, 49, 100]. Further, this is the basis of the "Standard Method" for concentrating viruses from water and wastewater samples [181]. In other words, our results fully agree with conventional chemical coagulation with alum and iron salts solely removing microorganisms without inactivating them.

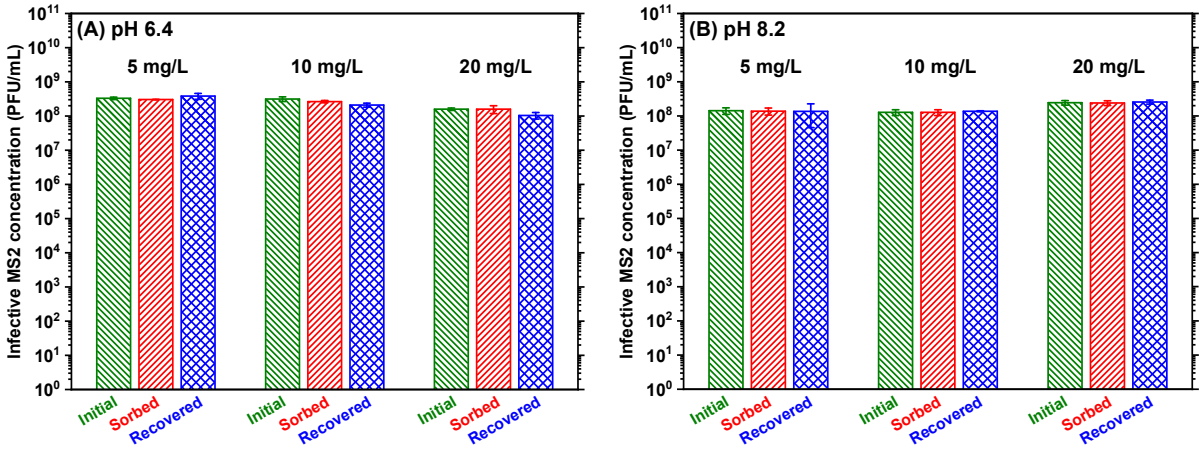

Figure A-3. Complete recovery of MS2 phages using 6 % beef extract solution from iron flocs generated with $FeCl_3$ at all dosages used in this study at pH 6.4 (A) and 8.2 (B). It is noted that the phages were extracted at the end of flocculation (t= 120 min). *t* test between sorbed and recovered phage concentrations indicated insignificant differences at all conditions.

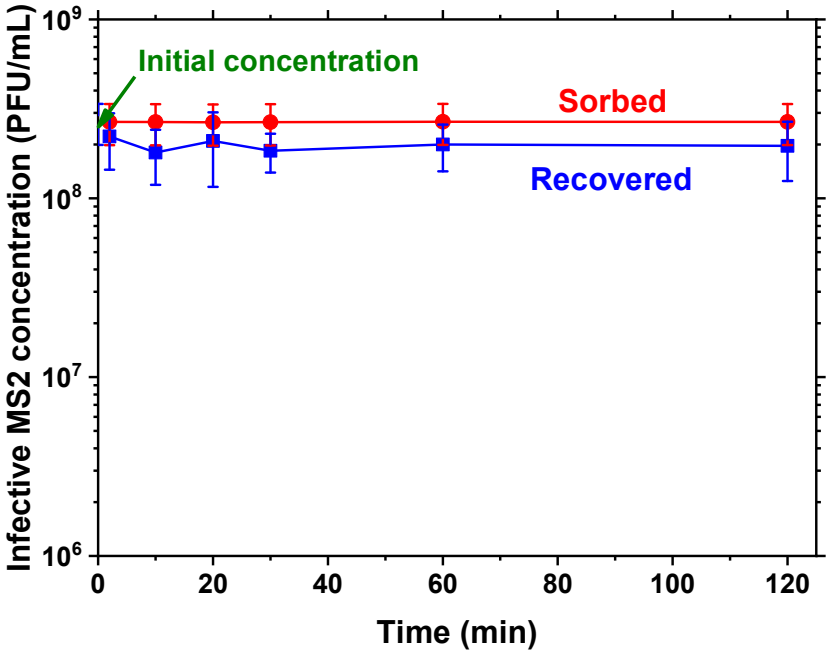

Figure A-4. Time series of MS2 recovery from the flocs at pH 6.4 when 10 mg/L Fe was added as $FeCl_3$. t test between sorbed and recovered phage concentrations indicated insignificant differences at all time points.

Section A6. Analytical methods

Total iron and Fe(II) concentration were measured with a spectrophotometer (DR6000, HACH). Total iron was measured following HACH method 8112 in which Fe(III) is reduced by sodium metabisulfite to Fe(II), and Fe(II) forms a complex with 2,4,6-Tris(2-pyridyl)-s-triazine.

Violet-colored complex was quantified by light absorption at 590 nm. Ferrous iron concentration was determined using HACH method 8146 where 1,10-phenanthroline is used as a chelating agent for Fe(II) after adding HCl to adjust pH to 3. The complex of Fe(II) and 1,10-phenanthrolie was quantified by light absorption at 510 nm [88, 270, 271].

H_2O_2 was measured based on the reduction of Cu(II) to Cu(I) by H_2O_2 and the formation of Cu(I)-2,9-dimethyl-1,10-phenanthroline complex [138, 139]. Samples were filtered with 0.1 μm syringe filter followed by citrate (7.2 mM) addition in order to prevent the reduction of Cu(II) by Fe(II) [137]. Orange-colored complex was quantified by light absorption at 454 nm (DR-6000, HACH).

Section A7. ATR-FTIR

ATR-FTIR spectra were collected using Nicolet iS10 spectrometer (Thermo Fisher Scientific) equipped with an Ever-Glo MIR source, DTGS detector, KBr beam splitter and Omnic 9 software. Samples were directly mounted on a diamond iTX accessory and spectra were obtained in ATR mode. Each spectrum reported herein is an average of three to five measurements consisting of 128 coadded scans at 4 cm^{-1} resolution. ATR-correction was conducted followed by auto-base line correction and 9-point Savitzky-Golay smoothing. The spectra were normalized by the largest peak intensity [182]. Peak positions were identified by taking the second derivatives of the spectra.

A control was performed to prove these ATR-FTIR signals were not due to residuals (e.g. bacterial debris or other chemicals) or contamination in the virus stock. In addition to “regular” MS2 stock prepared as described in Section A1, a “control” stock was prepared by following the same procedure except for the virus inoculation to bacterial cells. This control stock was expected

to only contain residues that might be also in the regular stock.

Untreated MS2 spectrum was obtained by subtracting the spectrum of a freeze-dried control stock from that of freeze-dried regular stock. This subtraction procedure is expected to minimize the interference of potential chemical and biological residues carried over to MS2 stock during its preparation [16, 66, 272]. Similarly, for the spectrum of coagulated MS2, coagulation was separately performed with regular and control stock followed by spectrum subtraction to ensure that any changes in spectrum were due to MS2 transformation, not modifications of other residues if there were any. The entire suspension was vacuum-filtered with a glass fiber membrane (1.2 μm nominal pore size) followed by vacuum-drying for 6 ~ 9 hours. The spectrum of each sample was obtained from 3 different locations on the membrane and averaged, and then difference spectrum was obtained.

Section A8. RT-qPCR Protocol

The sample volume of 400 μL was added to an equal volume of UNEX lysis buffer [273] (Microbiologics, St. Cloud, MN), mixed vigorously and incubated at room temperature for 15 min. After incubation, the entire volume of the mixture was added to a silica spin column (Omega Biotek, Norcross, GA) and centrifuged at 10,000 g for 1 min. After discarding the flow through, the column was washed with 500 μL of 100% ethanol and centrifuged at 10,000 g for 1 min. The column was washed again with 70% ethanol at 10,000 g for 1 min followed by an extra centrifugation to remove excess ethanol. The RNA was eluted in a clean microcentrifuge tube with 70 μL of 10 mM Tris-1 mM EDTA (pH 8.0) by centrifugation at 10,000 g for 1 min.

Viral RNA was quantified by one-step real-time RT-qPCR [16, 50] with a forward primer 632F, GTCGCGGTAATTGGCGC, a reverse primer 708R, GGCCACGTGTTTTGATCGA, and a fluorescent probe 650P, 5′-AGGCGCTCCGCTACCTTGCCCT-3′ labeled on 5′ end with FAM

(6-carboxy-fluorecein) and 3′ end labeled with black hole quencher in duplicate. RNA was reverse transcribed into complementary DNA (cDNA) and thermocycling comprised 45 cycles of amplification consisting of denaturation at 95 ℃ for 5 s, annealing at 60 ℃ for 30 s, and acquiring the fluorescence signal, which was used to obtain the cycling threshold (values > 40 were considered negative). Each TaqMan mixture for the reaction consisted of 5 µL of 4X TaqMan Fast Virus 1-Step Mastermix (Life Technologies), 0.8 µL of 250 nM each primer, 1 µL of 100 nM probe, 10.4 µL of nuclease free water and 2 µL of RNA sample to a final reaction volume of 20 µL. All reactions were performed in duplicate on ABI 7500 (Applied Biosystems) with slight modifications to a previously reported protocol [50].

Duplicates of 2 µL sample extract were run along with a positive control and no-template negative control to verify the protocol and check for contamination. Duplicates of the samples were assayed, and the detection limit was determined by the lowest concentration samples resulting in a positive signal. A standard curve was constructed with 10-fold dilution series of MS2 stock of known concentrations. qPCR efficiency was calculated as 91.6 % from the slope of a linear regression curve with 0.99 of R^2 (Figure A-5).

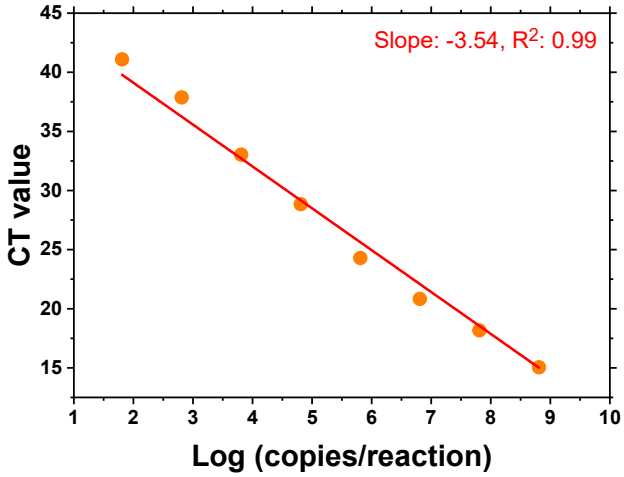

Figure A-5. Standard curve of MS2 RNA RT-qPCR.

Section A9. Indirect evidence of virus inactivation

A set of controls was performed to probe the possibility of electrocoagulation inactivating at pH 6.4 by comparing with conventional $FeCl_3$ coagulation. Total reductions of MS2 in bulk water by electrocoagulation and $FeCl_3$ chemical coagulation at different pH and doses are summarized in Figure A-6A and 6B. Also, relative reductions were calculated by dividing EC reductions by $FeCl_3$ reductions and plotted in Figure A-6C. Note that MS2 is not inactivated by conventional $FeCl_3$ coagulation at pH 6.4 (Section A5) [15, 49, 100]. Importantly, as shown in Section A5 and Figure A-6, infective MS2 was reduced in bulk water to a substantially greater extent (8 ~ 500 times) by EC than $FeCl_3$ (red line in Figure A-6C) demonstrating bulk inactivation at pH 6.4. In flocs, unlike $FeCl_3$ coagulation where infective viruses were completely recovered from flocs (i.e. only removal), MS2 was only partially extracted from EC flocs by the plaque assay indicating loss of infectivity showing monotonic decrease over time (Figure II-1 in the main manuscript text) suggesting progressive inactivation. Hence, EC at pH 6.4 removed and inactivated viruses. However, at pH 8.2, total virus reduction in bulk water by EC and $FeCl_3$ coagulation were similar as evidenced by overlapping total reduction curves and relative reduction values close to 1 (Figure A-6B and blue line in Figure II-1C of the main manuscript) validating negligible inactivation during EC as well as $FeCl_3$ coagulation at the higher pH.

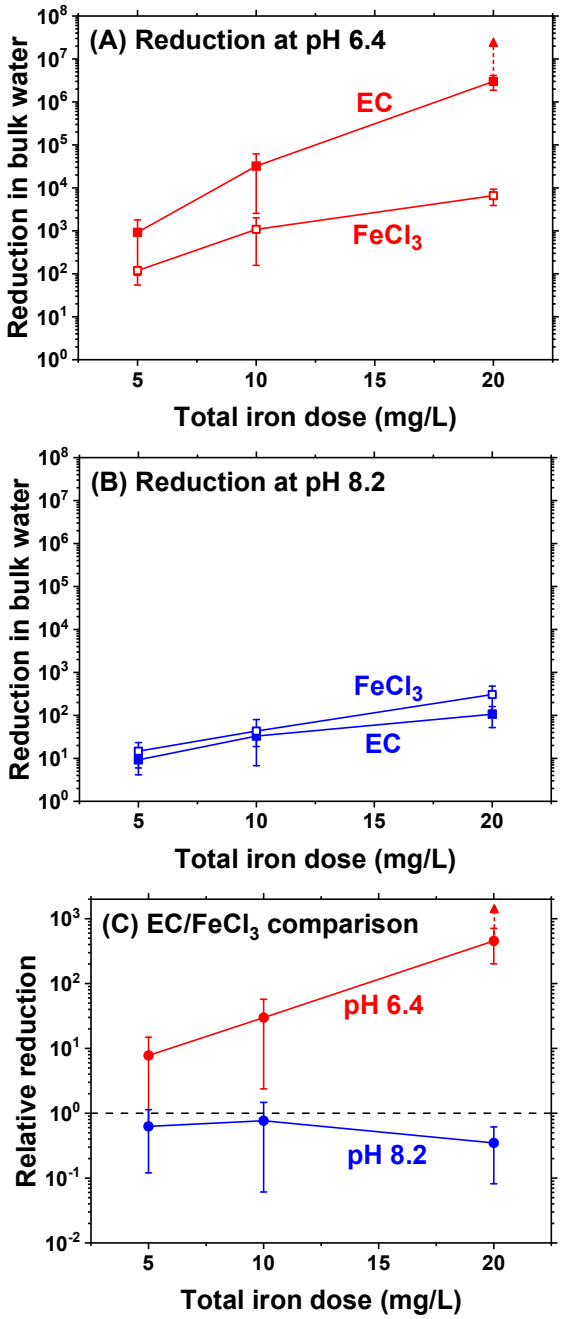

Figure A-6. Comparison of log-reduction in bulk water at the end of flocculation (t= 120 min) in EC and $FeCl_3$ coagulation at pH 6.4 (A), at pH 8.2 (B), and the relative reduction between EC and $FeCl_3$ calculated by dividing EC reductions by $FeCl_3$ reductions (C). The *t* test performed between EC and $FeCl_3$ (n= 3 ~ 6, $p < 0.05$ for statistically significant difference) at each dose revealed that mean reductions were statistically different at all doses at pH 6.4 whereas EC and $FeCl_3$ did not show significant differences at pH 8.2.

Section A10. Visualization of MS2 sorbed onto iron flocs

MS2 phages were conjugated with fluorescein isothiocyanate isomer 1 (FITC) as described previously [274]. Briefly, 1 mL of phage stock prepared in 0.1 M borate buffer (pH 9.2) was mixed

with 5 mL of dimethylformamide and 21 mg of FITC. The solution was stored at 4°C overnight and dialyzed with 12-14 kDa membrane tube against PBS for 5 days. The end product was further purified by rinsing MS2 phages several time with PBS using a 100 kDa centrifugal filter unit (Spin-X UF, Corning). Upon electrocoagulation of FITC-labeled phages, images were taken with Olympus BX 53. In addition, control experiments were performed to ensure that only FITC-tagged phages were responsible for the fluorescence signal [13]. Free FITC solution was prepared by following the procedure described above without adding MS2.

Brightfield transmission mode **Fluorescence mode**

(A) Floc with labelled MS2

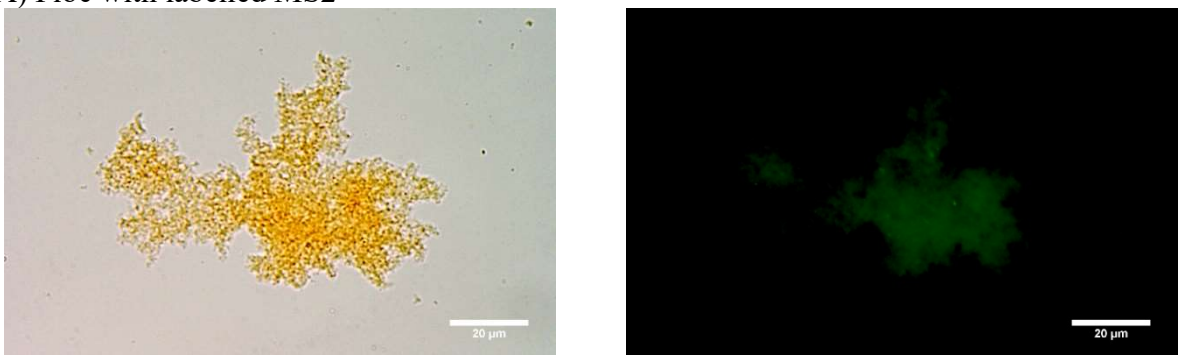

(B) Floc (control)

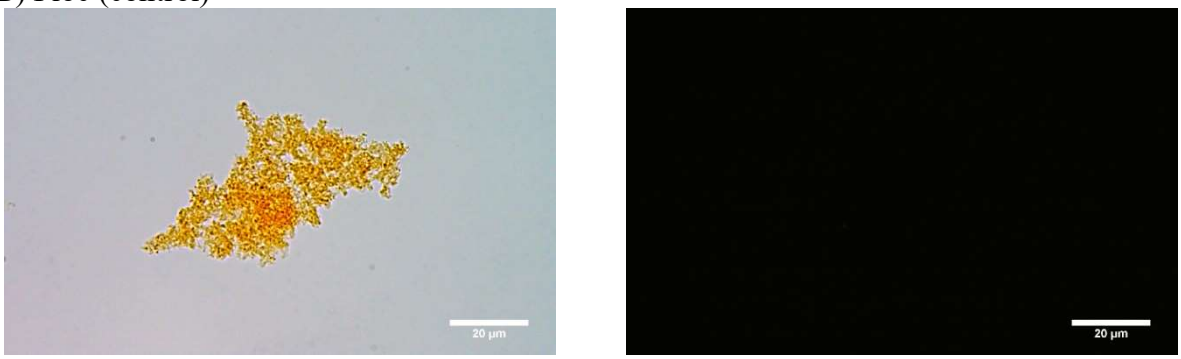

(C) Floc with unlabeled MS2 (control)

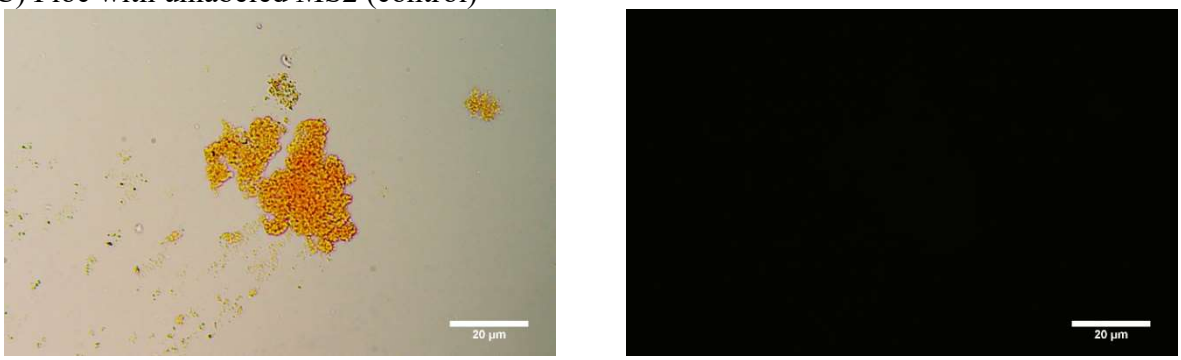

(D) Floc with free FITC (control)

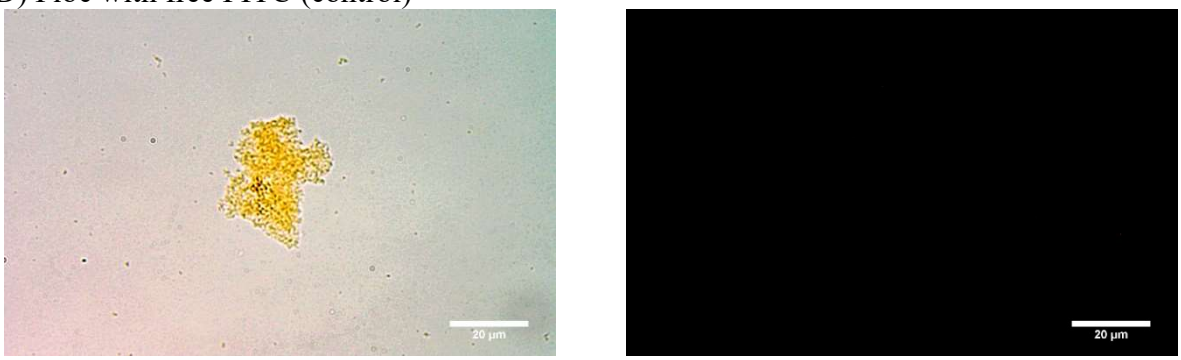

Figure A-7. Visualization of phages captured by iron flocs at 10 mg/L total iron and pH 6.4 (A) along with various controls (B), (C), and (D). Bright field images and corresponding fluorescence images (excitation at 480 nm and emission at 510 nm, exposure time 200 ms) are shown next each other.

Bright-field transmission mode **Fluorescence mode**

(A) Floc with labelled MS2

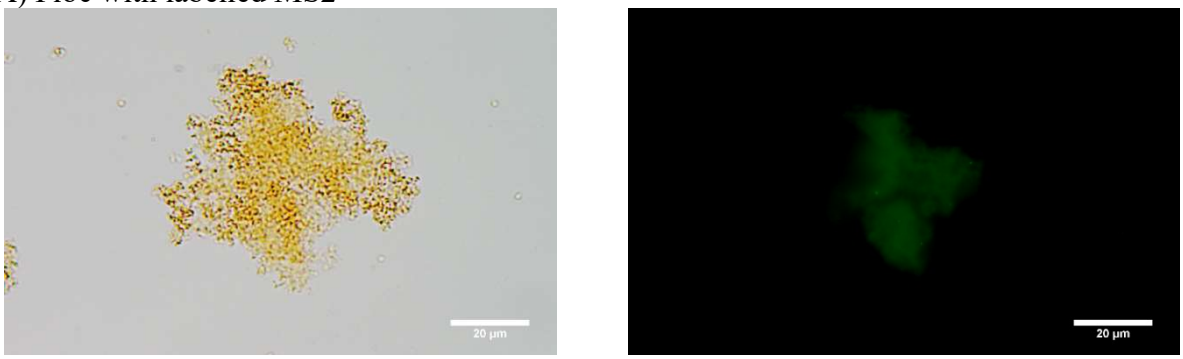

(B) Floc (control)

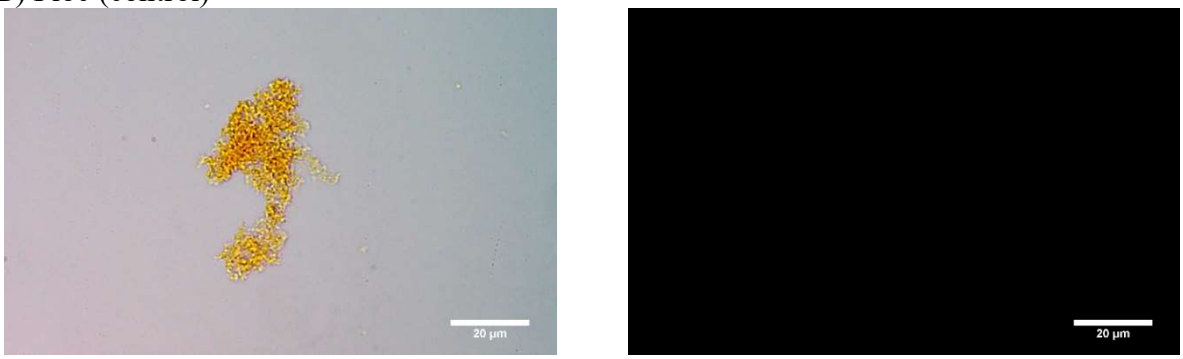

(C) Floc with unlabeled MS2 (control)

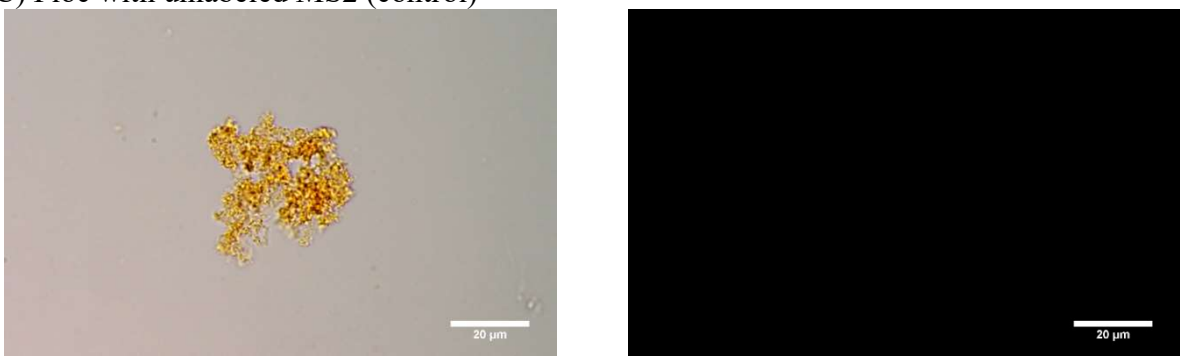

(D) Floc with free FITC (control)

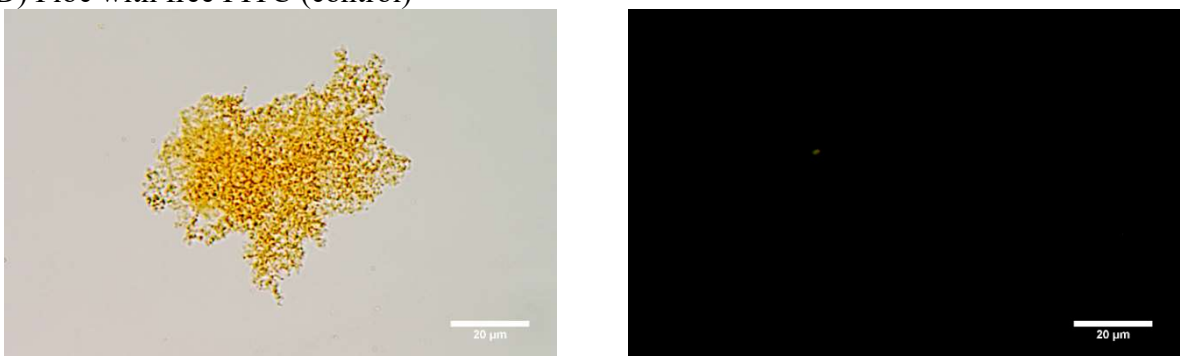

Figure A-8. Duplication of Figure A-7 at 10 mg/L total iron and pH 8.2. Microscopic analysis details are same as the previous figure.

Section A11. Original TEM of untreated and electrocoagulated MS2.

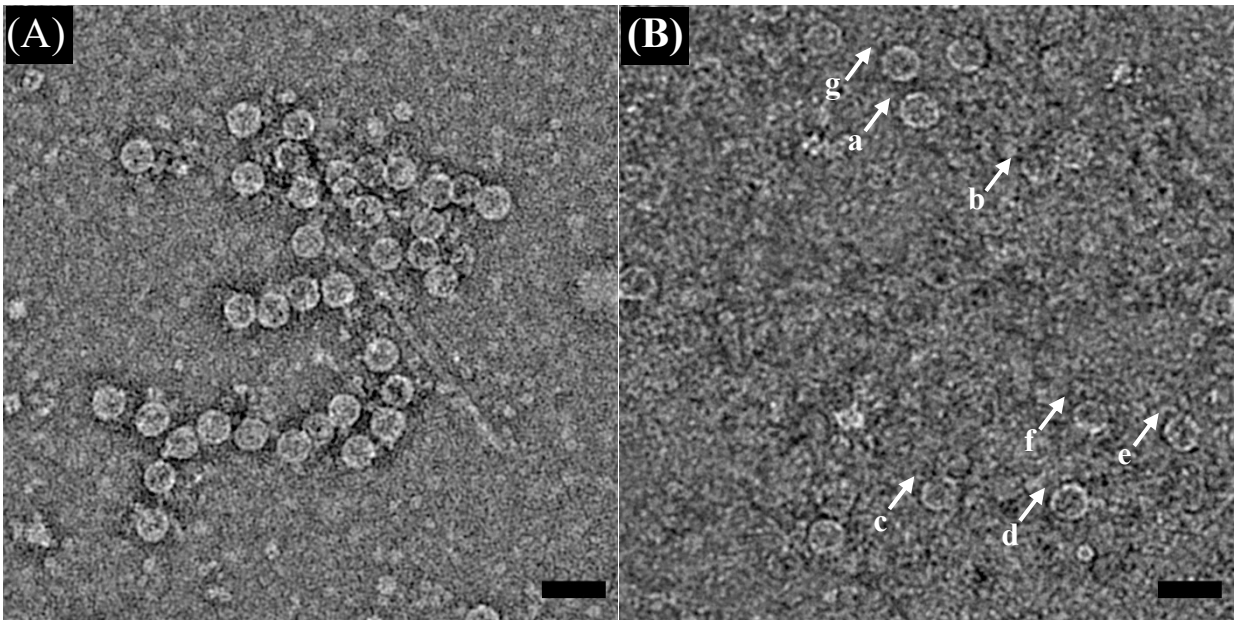

Figure A-9. Representative TEMs of untreated (A) and electrocoagulated MS2 (B). Scale bars equal 50 nm. The white arrows with labels in Figure A-9B depict the particles that were chosen to be represented in the main manuscript. Particle 'b' is represented in Figure II-3B, and particles 'a-g' were used for the boxed-out images in Figure II-4A-4G matching the alphabetical sequence.

Section A12. Discussion on viral capsid damage

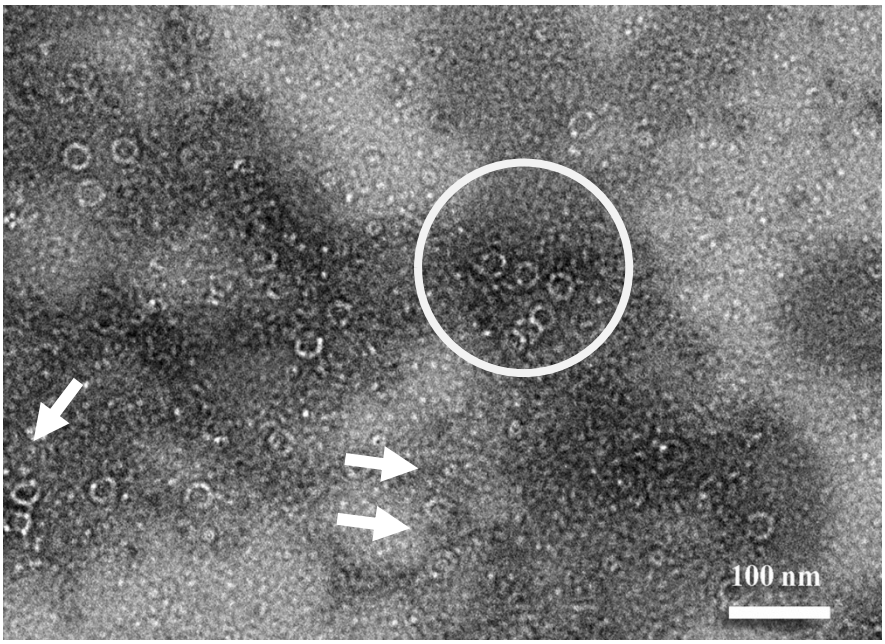

Figure A-10. Electron micrograph of electrocoagulated MS2 phages. MS2 particles with deformed/damaged capsids are shown in the white circle while severely damaged particles are pointed by white arrows.

Section A13. Visualizing MS2 embedded in iron flocs with defocusing

Unlike untreated MS2 phages imaged on a clean carbon grid, electrocoagulated phages were intrinsically embedded in iron flocs thus making it difficult to achieve enough contrast between viral capsid and iron flocs under the same instrumental condition for untreated phages. As seen in Figure A-11A, due to the presence of numerous electron-dense iron flocs, the contrast of these images was too low to clearly outline damaged phages and their structural deformation. Nonetheless, it should be noted that such images were used for capsid thickness measurement which justified the capsid thickness comparison shown in Figure II-4H and 4I in the main manuscript.

Meanwhile, higher defocusing provided more contrast between viral capsid and iron floc background clearly depicting capsid damages (Figure A-11B). However, it also resulted in a large shift of intact capsid thickness from 2.4 nm to 4.0 nm

Figure A-12) demonstrating its artifactual influence on quantitative measurement.

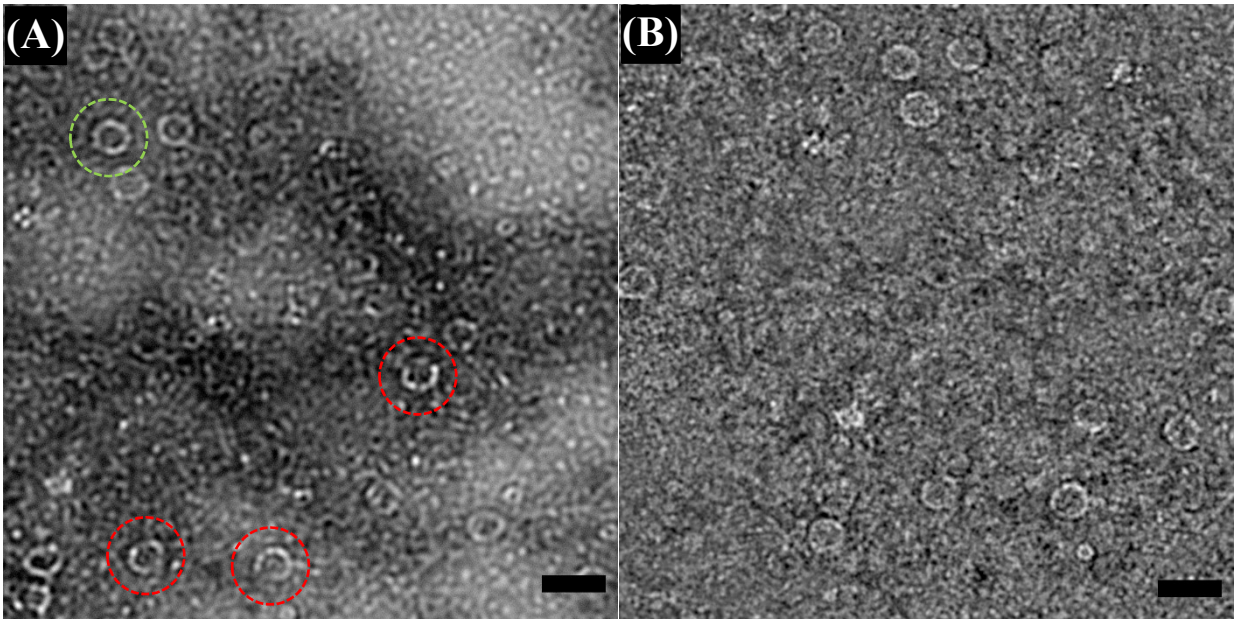

Figure A-11. Visualization of phages in iron flocs with low (A) and high defocusing (B). The use of high defocusing generated electron micrographs that clearly differentiated relatively intact virion (green-dotted circle) and structurally-deformed virions (red-dotted circles). Scale bars equal 50 nm.

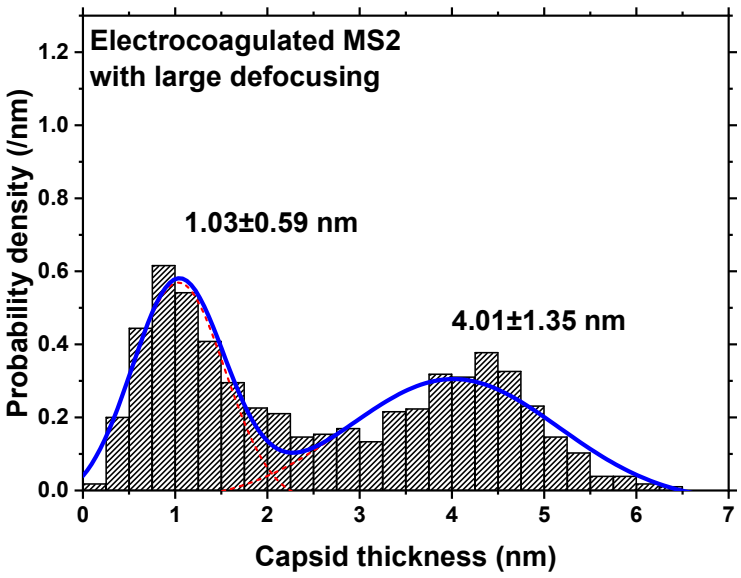

Figure A-12. Artifactual effect of defocusing on capsid thickness measurement.

Section A14. FTIR analysis of untreated and coagulated MS2

Experiments and instrumental measurements were replicated and reproducibility was estimated by calculating correlation coefficients using QCheck function embedded in OMNIC software (Thermo Scientific) at 4 cm^{-1} resolution (Figure A-13) [275, 276]. Although visually recognizable local discrepancies (e.g. shape of the shoulder of untreated MS2 spectrum around 1550 cm^{-1}) were found, replicate spectra were statistically similar resulting in correlation coefficients of 0.88-0.96 (among triplicates of untreated MS2), 0.78 (between duplicates after $FeCl_3$), and 0.73 (between duplicates after EC) according to the criteria by Thermo Scientific (https://kb.unitylabservices.com/kb/article?ArticleId=349327&source=Article&c=13142&cid=12825). Importantly, the replicated spectra featured common important characteristics. For example, electrocoagulated MS2 resulted in a slightly different spectrum in each trial, but all spectra showed a significant decrease in amide II region and evolution of new peaks above 1700 cm^{-1} compared with untreated and chemically

coagulated MS2. Therefore, the average of replicate spectra was presented in Figure II-5 of the main manuscript Figure A-14 shown below.

For probing secondary structure changes, the amide I region was exclusively analyzed as it has been known to be dominantly affected by the structure of the protein backbone and, thus, by characteristics of hydrogen bonds between C=O and N-H groups (not by the types of the side chain) which largely determine protein secondary structures [73, 81, 153, 277]. Peak positions (within amide I region) of different secondary structures have been examined and documented based on empirical/experimental data with known structure protein molecules with a support of theoretical calculation [277-279]. In this study, amide I region was decomposed into individual peaks that were identified by taking a second derivative. Revealed peaks were assigned to specific secondary structures based on literature values (see Table A-2 and A-3).

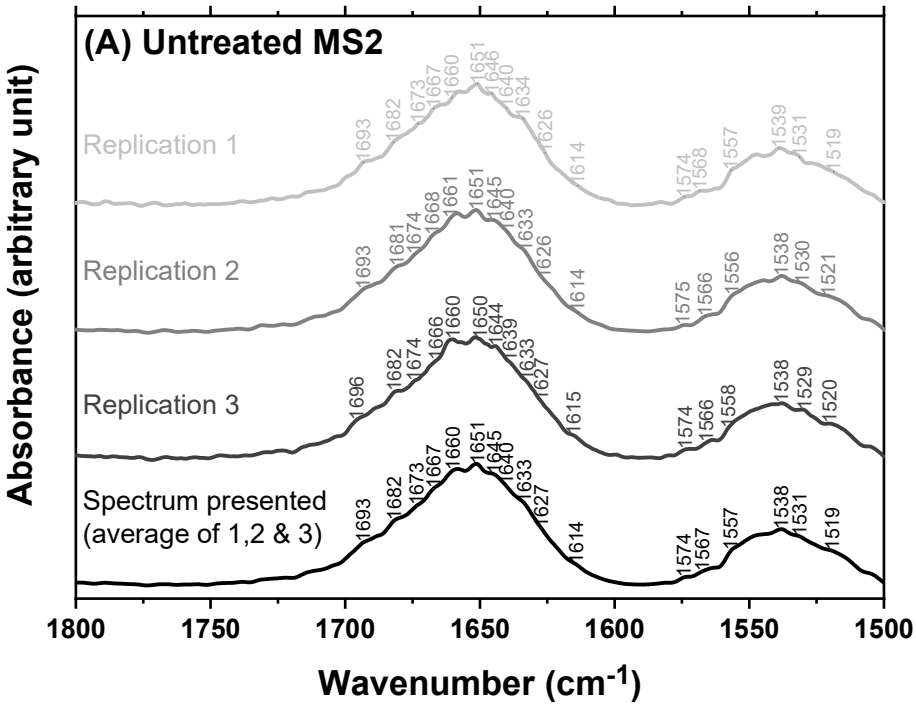

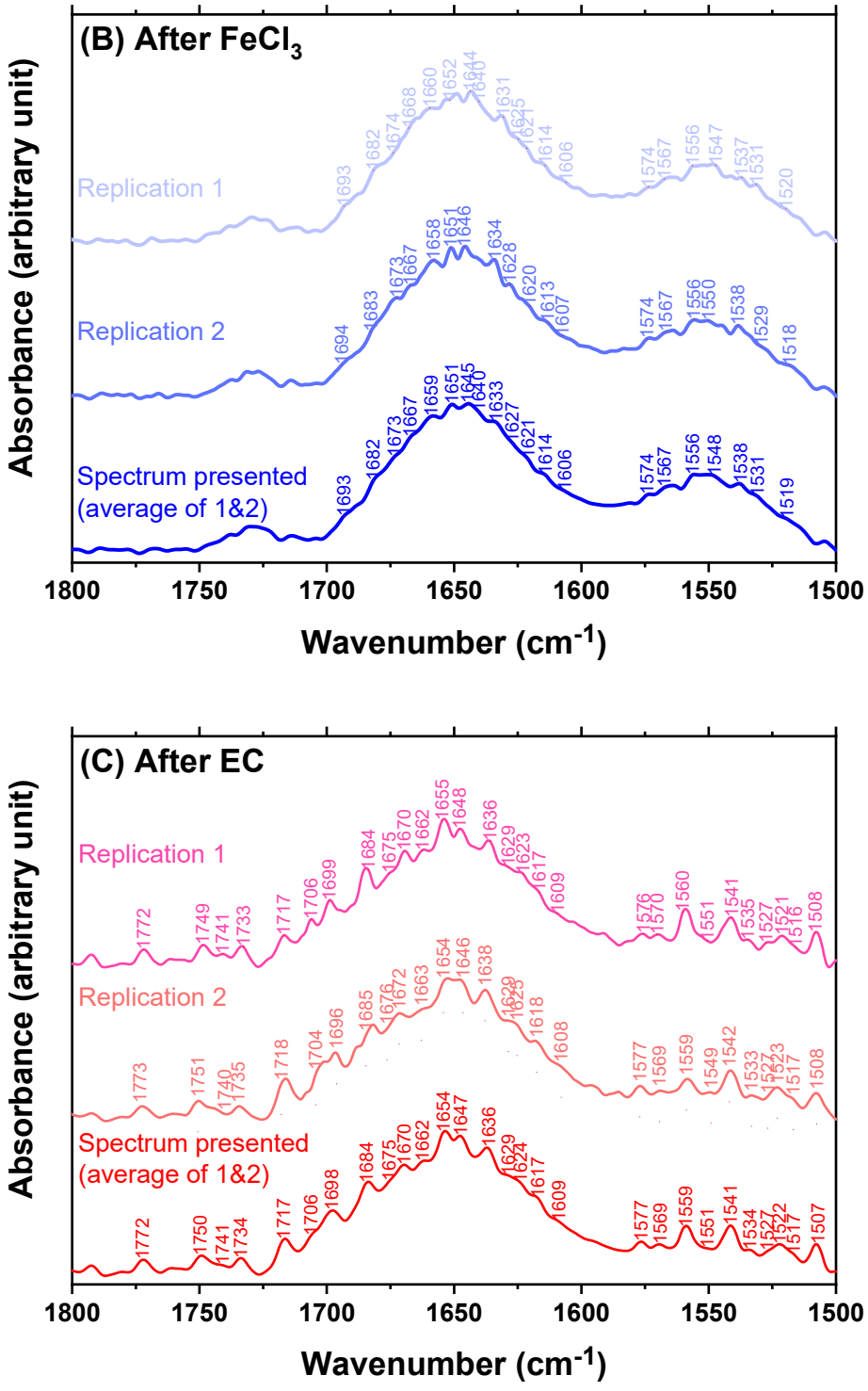

Figure A-13. Reproducibility of FTIR spectrum of untreated (A), chemically coagulated (B), and electrocoagulated MS2 (C). Correlation coefficient among replicated spectra were found to be 0.88-0.96, 0.78, and 0.73 for untreated MS2, after $FeCl_3$, and after EC, respectively.

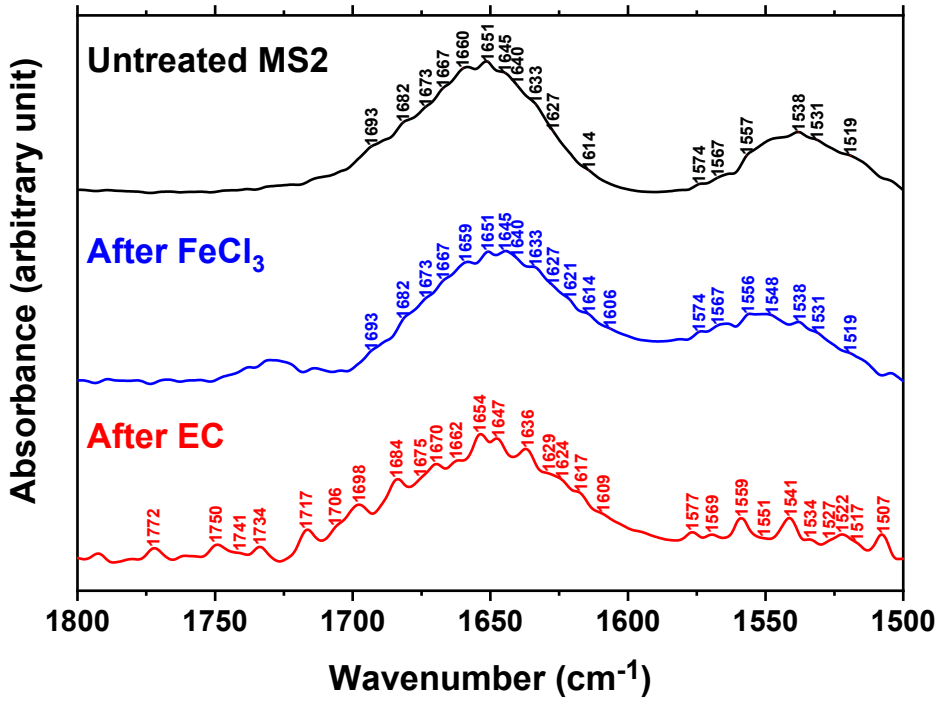

Figure A-14. Comparison of untreated and coagulated MS2 with complete peak identifications.

Table A-2. Identified FTIR band positions and corresponding assignments.

Wavenumber (cm^{-1})	Assignment [69, 73, 81, 152, 153, 280]
1772	Carbonyl groups
1750	Carbonyl groups
1743, 1740, 1734	Aliphatic aldehyde
1717, 1706	Aliphatic ketone
1700	Aromatic ketone
1698	C_2=O Guanine
1693	High frequency of β-sheet
1684	Disordered structure, non-hydrogen bonded
1682	Unordered random coils and turns
1675 ~ 1667	Turns
1662	Disordered structure
1660 ~ 1651	α-helix
1647, 1645	Random coils and turns
1640 ~ 1627	β-sheet
1624 ~ 1614	Aggregated strand, intermolecular β-sheet
1609	Gln, $\delta(NH_2)$
1579 ~ 1574	Asp $\nu_{as}(COO^-)$
1577, 1574	C=N Adenine

1569, 1567	Ring base
1559	Ring base or Glu, $\nu_{as}(COO^-)$
1557 ~ 1551	Ring base
1548	Amide II
1541	Amide II, β-sheet, ν(N-H)
1538	Stretching C=N, C=C
1534	Amide II, modified guanine, ν(C=N), ν(C=C)
1531	Stretching C=N, C=C
1527	Lys, $\delta_s(NH_3^+)$
1522	Stretching C=N, C=C
1519	Tyr–OH, ν(CC), δ(CH)
1517	Amide II
1507	Trp, ν(CN), δ(CH), δ(NH)

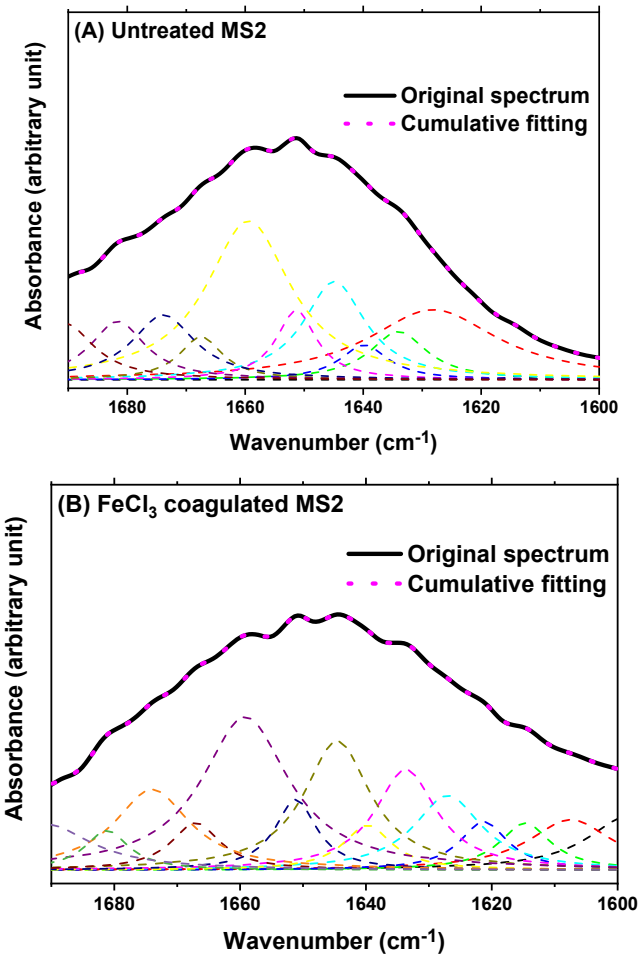

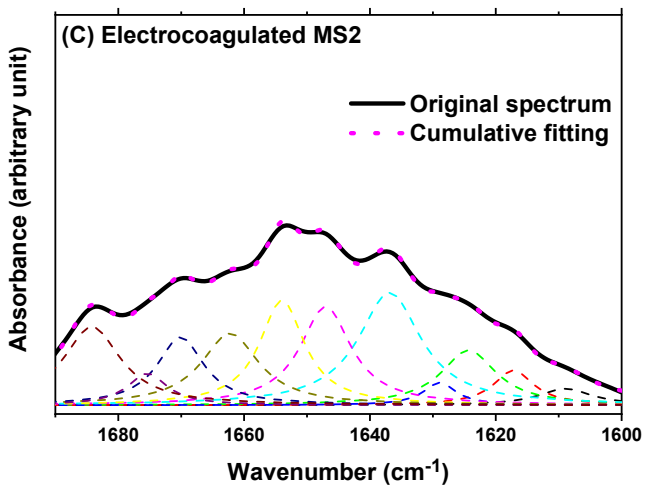

Figure A-15. Decomposition of FTIR spectrum of untreated (A), $FeCl_3$ coagulated (B), and electrocoagulated MS2 (C).

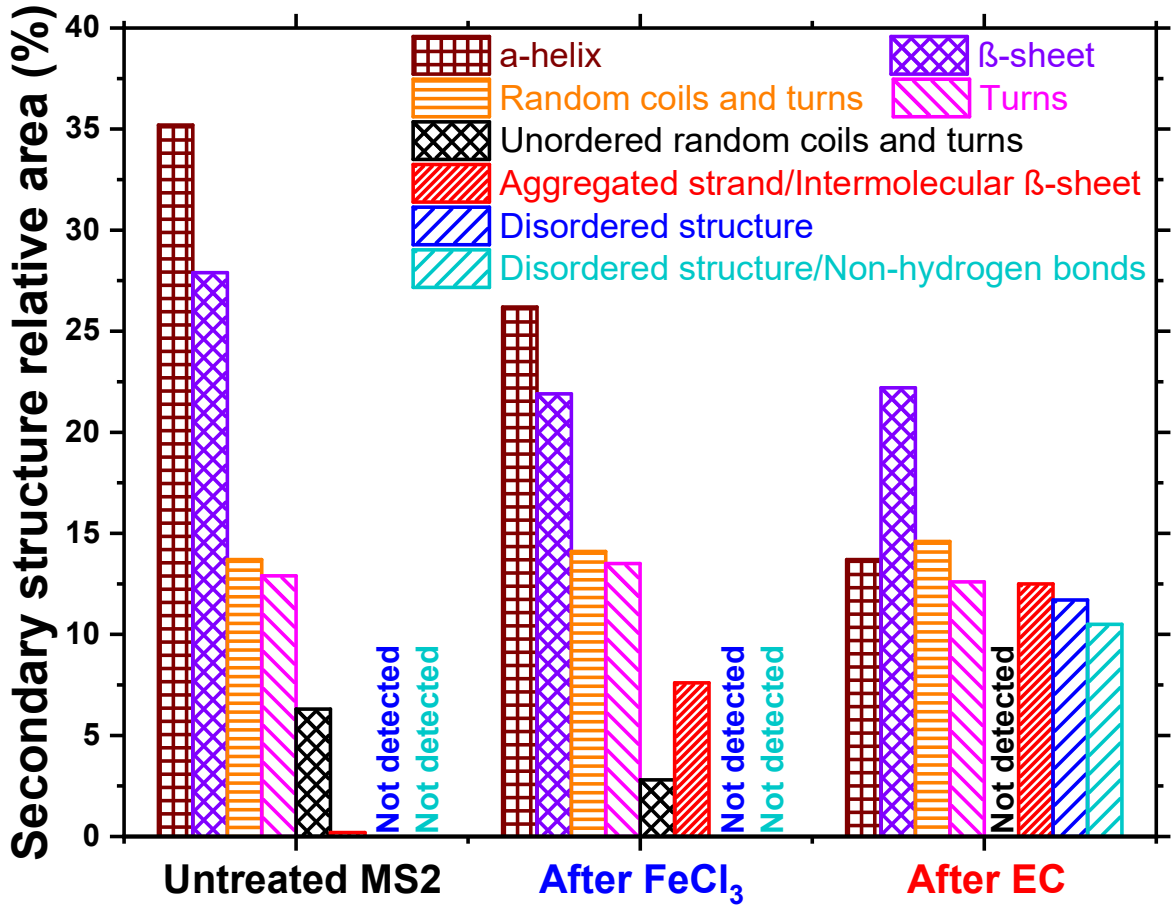

Figure A-16. Comparison of relative secondary structure areas before and after conventional coagulation and electrocoagulation.

Table A-3. Comparison of secondary structure relative areas of untreated and coagulated MS2 phage.

Secondary structure	Untreated MS2		Fe(III) or $FeCl_3$-coagulated MS2		Electrocoagulated MS2	
	Wavenumber (cm^{-1})	Relative area (%)	Wavenumber (cm^{-1})	Relative area (%)	Wavenumber (cm^{-1})	Relative area (%)
Aggregated strand, Intermolecular β-sheet	1614	0.2	1614 1621	3.8 3.8	1617 1624	4.0 8.5
β-sheet	1627 1633 1640	17.8 6.2 3.9	1627 1633 1640	8.1 10.1 3.7	1629 1636	2.2 20.0
Random coils and turns	1645	13.7	1645	14.1	1647	14.6
α-helix	1651 1660	6.5 28.7	1651 1659	5.0 21.2	1654	13.7
Disordered structure	-	-	-	-	1662	11.7
Turns	1667 1673	4.2 8.7	1667 1673	3.9 9.6	1670 1675	9.0 3.6
Unordered random coils and turns	1682	6.3	1682	2.8	-	-
Disordered structure, non-hydrogen bonded	-	-	-	-	1684	10.5
Etc.	1693	3.8	1598 1606 1691	3.2 5.3 5.4	1609	2.2

Section A15. Temporal profile of infective virus in bulk water and floc during electro-, $FeCl_2$, and $FeCl_3$ coagulation

In $FeCl_3$ coagulation, nearly all (> 8-log) of the phages sorbed onto iron flocs (red line in Figure A-17B), which we could completely extract and enumerate using the plaque assay (also see Figure A-3 and A-4). Corresponding infective virus concentrations in the bulk water were 100 – 1,000 times lower ranging between 10^5 – 10^6 PFU/mL in Figure A-17A demonstrating highly effective coagulation. This corresponds to a total iron dosage of 10 mg/L and solution pH of 6.4. Since the sum of infective viruses in the flocs and water column was the same as what was added at the beginning of the experiment it can be concluded that viruses were not inactivated during direct $FeCl_3$ coagulation.

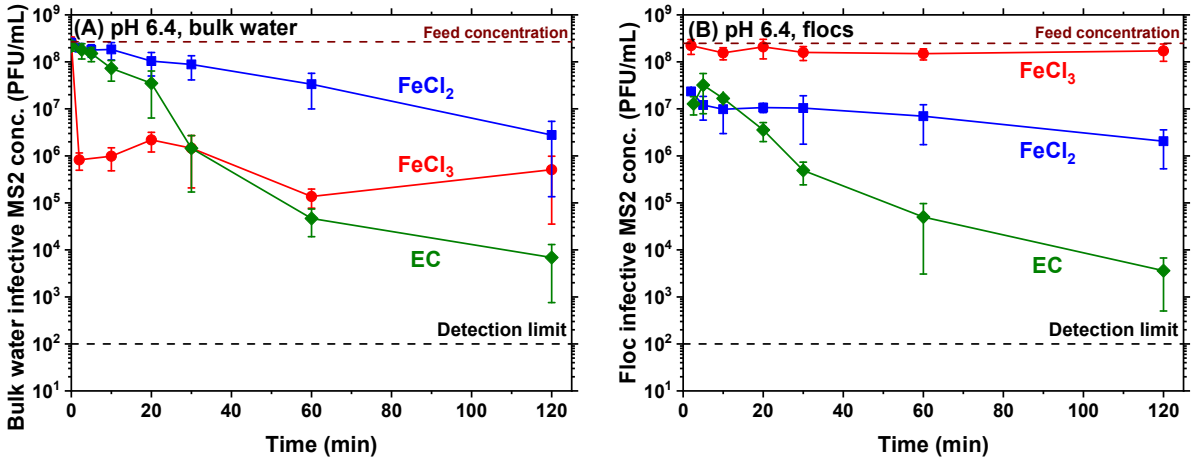

Figure A-17. Comparison of infective virus concentration profiles by $FeCl_2$, $FeCl_3$, and electrocoagulation. Experimental conditions were pH 6.4 and 10 mg/L total iron dosage.

Section A16. Additional dissolved oxygen (DO) consumption due to H_2O_2 production during electrolysis

Figure A-18 shows dissolved oxygen (DO) changes over time under various conditions when total 10 mg/L of iron was dosed either by external chemical addition or via electrolysis, in the presence and absence of a chelating agent (1,10-phenanthroline), and at two pH values of interest (6.4 and 8.2). When $FeCl_2$ was added at pH 6.4, DO was gradually consumed

demonstrating only a slow oxidation of Fe(II) (black solid line). However, when Fe(II) was complexed at the same pH by adding 1,10-phenathroline (4.4 mM, black dotted line), DO concentration remained unchanged [281]. When EC was performed at pH 8.2 (blue solid line), a rapid decrease of DO during the electrolysis was observed, similar to $FeCl_2$ at pH 8.2. Considering that H_2O_2 was not detected at pH 8.2 (Figure II-7B in the main manuscript), this behavior is indicative of fast oxidation of Fe(II) released during electrolysis by DO at high pH [97] as expected. In contrast, additional DO consumption was observed in EC at pH 6.4 (red solid line) indicating that DO was consumed by cathodic H_2O_2 production as well. Addition of 1,10-phenanthroline to EC at pH 6.4 further confirms the extra DO consumption during the electrolysis. Even when this chelating agent was added (red dotted line), approximately 15 % of the DO was consumed.

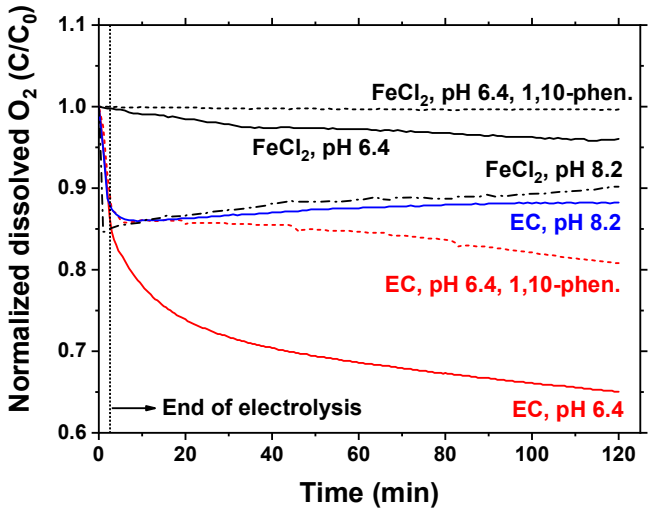

Figure A-18. Dissolved oxygen consumption under various conditions at total iron dosage of 10 mg/L.

Section A17. Only ˙OH/Fe(IV) in the close vicinity of MS2 may be responsible for inactivation

Figure A-19 compares the infective MS2 concentration in bulk water and flocs when EC was performed with and without addition of dimethyl sulfoxide (DMSO). DMSO is known to

scavenge •OH and Fe(IV) [95], but not H_2O_2 [282]. In our experiments, the effect of DMSO was found to be negligible in bulk phase which is consistent with previous studies where inactivation of MS2 by Fenton's and Fenton-like reaction was investigated separate from electrolysis [42, 92]. This result indicates that only •OH/Fe(IV) present in the close proximity near and/or on the surface of MS2 are effective in bulk inactivation. This can be attributed to a rapid consumption of •OH/Fe(IV) by reacting with other species such as Fe(II) (Eqs. A11 and A12 in Table A-4 below), and to possible complexation of Fe(II) with coat protein of MS2 [283]. DMSO also did not affect inactivation on floc surfaces. This might be because floc inactivation is triggered by Fe(II) adsorbed on the floc as it has been shown that Fe(II) adsorbs onto iron (oxy)hydroxide [284].

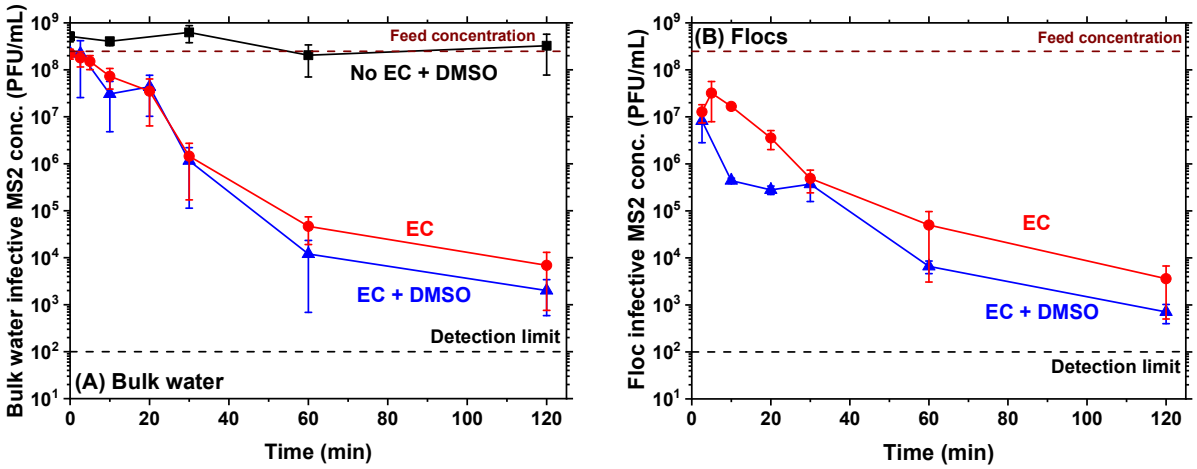

Figure A-19. Negligible effect of DMSO (25 mM) on MS2 control by EC at pH 6.4 and 10 mg/L total iron.

Section A18. Total inactivation at different pH

In order to clarify pH dependence of virus inactivation during EC, total inactivation at each pH and dose over time was determined by dividing the initial concentration (N_0) by the sum of infective virus concentrations in bulk water and flocs (N). These results are shown below in Figure A-20. The left panel shows a continuous increase in total inactivation at pH 6.4 demonstrating that viruses lost infectivity during the entire 2-hour flocculation period. In contrast at pH 8.2 (right

panel), inactivation was not only significantly lower, but was only observed during electrolysis and the initial period of flocculation consistent with Fenton's chemistry.

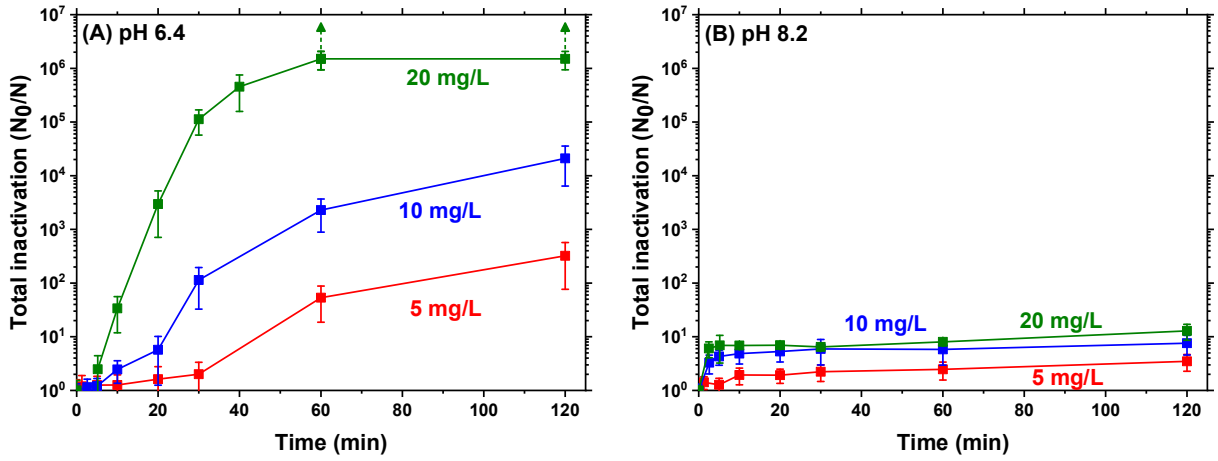

Figure A-20. Total inactivation of MS2 phages during EC at pH 6.4 and pH 8.2.

Section A19. Control experiments to obtain clues underlying chemical inactivation

Several other controls were also performed, and measurements were made to identify potentially responsible species in the context of Fe(II) and Fenton's chemistry. For example, H_2O_2 alone did not impact MS2 viability over the 2-hour duration of experiments (Figure A-22). Further, inactivation was completely suppressed during $FeCl_2$ coagulation and EC at pH 6.4 by (i) chelating Fe(II) using 1,10-phenanthroline [285] or (ii) N_2 purging to deoxygenate the feed water [270] and consequently prevent Fe(II) oxidation (Figure A-23). These controls demonstrate unequivocally that both Fe(II) and dissolved oxygen species needed to be present simultaneously to inactivate MS2 at pH 6.4. A role of H_2O_2 was further clarified by adding sodium sulfite as a H_2O_2 scavenger at the end of electrolysis (Figure A-24). Negligible inactivation solely by 25 μM of H_2O_2 at both pH and significant inhibition of inactivation due to sodium sulfite signifies the involvement of additionally generated H_2O_2 in inactivation along with Fe(II) enhancing Fenton's reaction.

Insignificant impact of $^{\bullet}O_2^-$ on MS2 inactivation in EC

The addition of 5 U/mL superoxide dismutase (SOD) as a scavenger for superoxide radical ($^{\bullet}O_2^-$) [92] resulted only in a marginal difference in infective MS2 concentration in bulk water and flocs. In other words, the superoxide radical was not an effective disinfectant in our experiments.

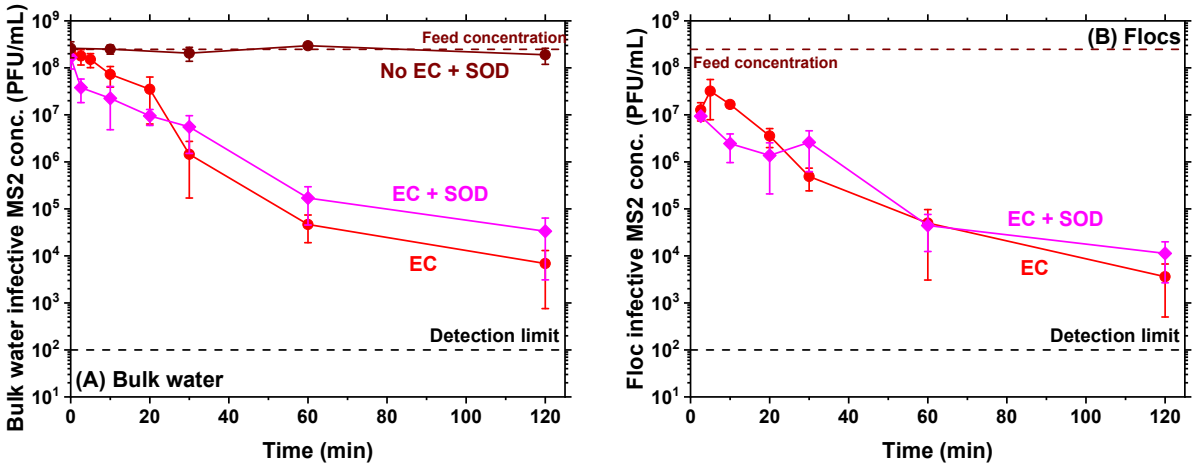

Figure A-21. Negligible effect of $^{\bullet}O_2^-$ on MS2 inactivation during EC (pH 6.4, 10 mg/L total iron) proven by addition of superoxide dismutase.

Negligible inactivation of MS2 by H_2O_2

Changes in infective MS2 concentrations solely by adding ~850 µg/L of H_2O_2 was monitored at both pH values. As shown below as blue lines in Figure A-22, inactivation was not observed at pH 6.4 and 8.2, as expected from previous publications [42, 92]. Also, in the absence of Fe(II), H_2O_2 concentrations remained relatively constant as shown as green lines corresponding to the second (right hand side) y-axis.

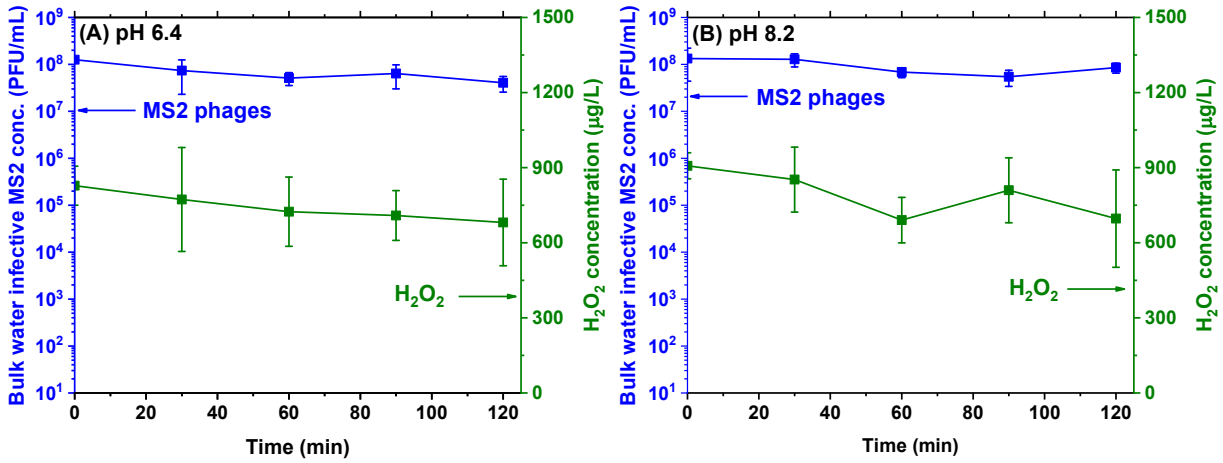

Figure A-22. Negligible effect of H_2O_2 on MS2 phage inactivation.

Combined role of Fe(II) and O_2 in MS2 inactivation

Viruses were monitored after adding $FeCl_2$ and EC at pH 6.4 and 10 mg/L total iron in the presence of 1,10-phenanthroline [88, 92] or deaeration [88] to screen out the role of Fe(II) and dissolved oxygen , respectively. As seen in Figure A-23, inactivation of MS2 phage was substantially inhibited by addition of 1,10-phenanthroline and deaeration in $FeCl_2$ and EC. This result indicates that virus inactivation by $FeCl_2$ and EC requires both Fe(II) and dissolved oxygen to be present concurrently.

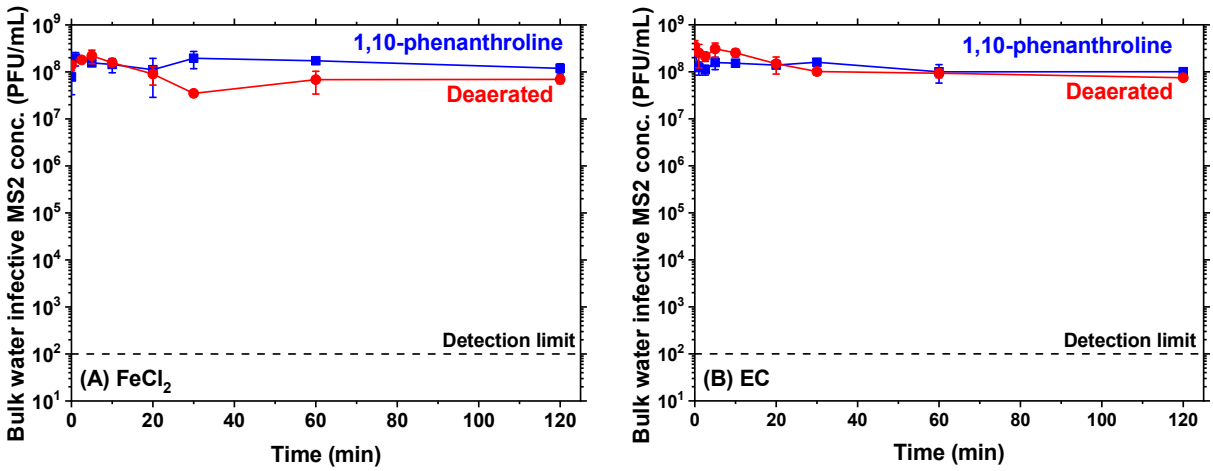

Figure A-23. Suppression of virus inactivation due to Fe(II) complexation with 1,10-phenanthroline (4.4 mM) and deaeration in (A) $FeCl_2$ and (B) EC.

Important role of H_2O_2 in inactivation

The addition of 25 mM Na_2SO_3 as a H_2O_2 scavenger at the end of electrolysis inhibited virus inactivation both in bulk solution and floc surfaces. This result signifies the involvement of additionally generated H_2O_2 in inactivation along with Fe(II), i.e. Fenton's reaction.

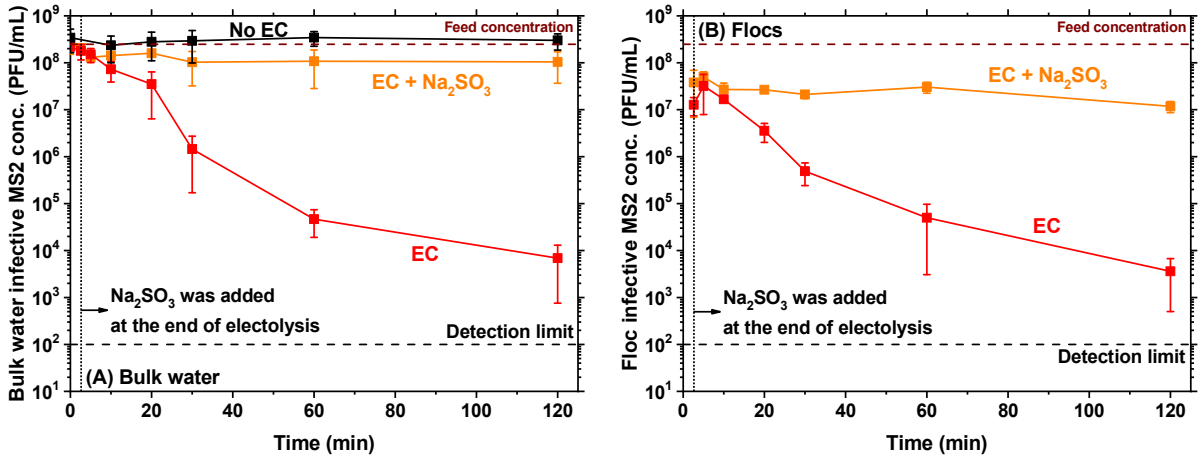

Figure A-24. Inhibition of MS2 inactivation by Na_2SO_3 in EC when 10 mg/L total iron was targeted at pH 6.4.

Free chlorine was not detected

In our previous study using aluminum EC of saline solutions, free chlorine was detected and was attributed to minor amounts of inactivation.[16] Therefore, the possibility of free chlorine production during electrolysis in these experiments and its potential contributions to inactivation was also investigated. In order to avoid interference by other oxidants, the indophenol method was used to detect free chlorine where free chlorine is converted to chloramine (HACH method 10241). In all experiments, free chlorine was not detected during the electrolysis and flocculation presumably because chloride ion concentrations were low unlike our earlier study [16].

Section A20. Lower viral RNA loss compared with plaque assay

Figure A-25 depicts temporal profiles of viral RNA extracted from the bulk water (left panel) and flocs (right panel) at different total iron doses and pH. The targeted genomic region was quantitatively measured via RT-qPCR in the negative control (no electrolysis, black line in Figure

A-25A) similar to the plaque assay in Figure II-1 in the manuscript. Therefore, any genomic changes measured during EC could be reliably assigned to electrolysis products.

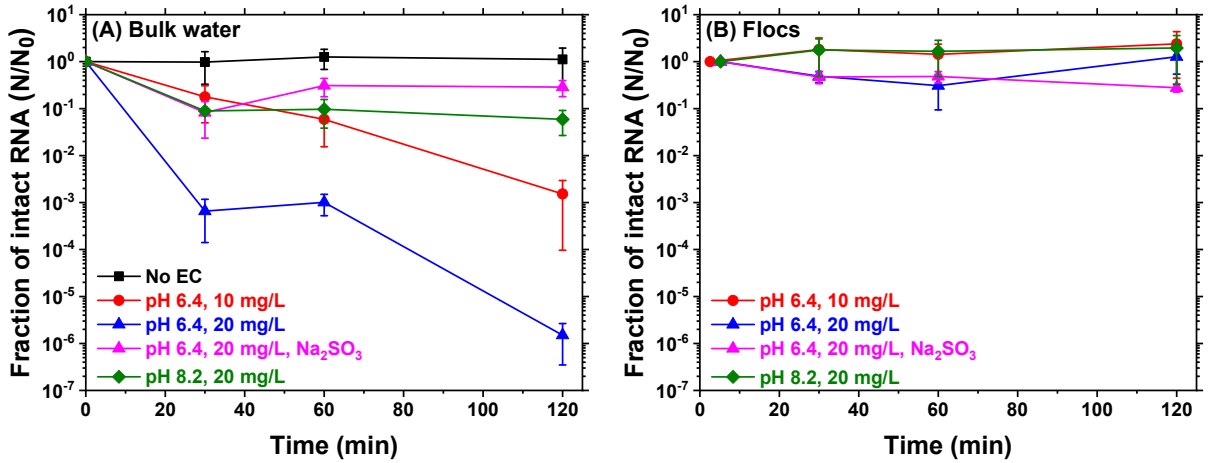

Figure A-25. RNA measured in bulk water (left panel, A) and flocs (right panel, B) during EC. Error bars are one standard deviation of at least four measurements. N_0 is the number of RNA copies measured immediately after adding viruses to the EC apparatus.

Electrocoagulation at pH 6.4 reduced the fraction of intact RNA extracted from the bulk water over time and with total iron dosage (red and blue curves in Figure A-25A). However, at pH 8.2 and 20 mg/L total iron, RNA decreased by only ~1-log in the first 30 minutes (green curve) remaining constant later on. As shown, significantly more RNA was lost at pH 6.4 compared with 8.2. These trends for viral RNA in the water column obtained via RT-qPCR are qualitatively similar to those of plaque assays but exhibit large differences in magnitude. For example, Figure A-25A depicts a decrease of only 1.2-log RNA compared with 3.7-logs of total infectivity loss in Figure II-1A for 10 mg/L total iron at 60 minutes and pH 6.4 in the manuscript. Substantially lower RNA loss compared with the plaque assay demonstrates that RT-qPCR targeting only a short fragment (77 bp amplicon) underestimated trends obtained with infective virions [16, 165, 286, 287].

In contrast to the bulk water, viral ssRNA was consistently and quantitatively recovered from the flocs showing only relatively minor changes throughout the 2-hour duration of all

experiments (Figure A-25B). This suggests relatively stable behavior of the targeted genome region even following MS2 uptake on iron flocs. In contrast, Figure II-1B in the manuscript depicts significant virus inactivation on flocs at pH 6.4 using the plaque assay because lower amounts of phages were recovered with time, i.e. all three curves had negative slopes. Therefore, virus behavior trends during EC differed substantially depending on whether it was monitored by RT-qPCR or infectivity assay both quantitatively and qualitatively. Presumptive oxidative modifications inferred from Figure II-5 in the manuscript and RNA loss in Figure A-25A point to the presence of chemical intermediates in solution.

Section A21. Electrochemical reactions during EC

Table A-4. Summary of electrochemical reactions in EC.

Description	Reaction [90, 92, 187]	
Dissolution of ferrous iron from anode	$\mathrm{Fe(0) \rightarrow Fe(II) + 2e^-}$	(A2)
Ferrous iron oxidation by dissolved O_2	$\mathrm{Fe(II) + O_2 \rightarrow Fe(III) + {\cdot}O_2^-}$	(A3)
Ferrous iron oxidation by $\cdot O_2^-$	$\mathrm{Fe(II) + {\cdot}O_2^- + 2H^+ \rightarrow Fe(III) + H_2O_2}$	(A4)
Ferric iron reduction by $\cdot O_2^-$	$\mathrm{Fe(III) + {\cdot}O_2^- \rightarrow Fe(II) + O_2}$	(A5)
Fenton's reaction	$\mathrm{Fe(II) + H_2O_2 \rightarrow Fe(III) + {\cdot}OH + OH^-}$	(A6)
	$\mathrm{Fe(II) + H_2O_2 \rightarrow Fe(IV)O^{2+} + H_2O}$	(A7)
$H_{2(g)}$ production on cathode	$\mathrm{2H^+ + 2e^- \rightarrow H_{2(g)}}$	(A8)
H_2O_2 production on cathode	$\mathrm{2H^+ + O_2 + 2e^- \rightarrow H_2O_2}$	(A9)
Iron floc formation	$\mathrm{Fe(III) + 3H_2O \rightarrow Fe(OH)_{3(am)} + 3H^+}$	(A10)
Consumption of Fenton's reaction products	$\mathrm{{\cdot}OH + Fe(II) \rightarrow OH^- + Fe(III)}$	(A11)
	$\mathrm{Fe(IV)O^{2+} + Fe(II) + 2H^+ \rightarrow 2Fe(III) + H_2O}$	(A12)

Supporting information for chapter III

Section A22. ϕ6 preparation and assay

The ϕ6 phage and its bacterial host *Pseudomonas syringae* were graciously provided by Dr. M. Worth Calfee, microbiologist with the United States Environmental Protection Agency. They were stored at -80 °C upon receipt, taken before experimentation, and grown with well accepted methods (with minor variations). Bacterial host was grown in nutrient broth (tryptone 10 g/L, yeast extract 1 g/L, dextrose 1 g/L, NaCl 8 g/L, $MgCl_2$ 1 g/L, $CaCl_2$ 0.22 g/L) at 26 °C until its optical density at 640 nm wavelength reached 0.1 followed by phage inoculation at multiplicity of infection of 2 and subsequent incubation at 26 ℃ for 9 hours [178]. Bacterial cell debris were centrifuged out at 10,000 g for 20 min at 4 ℃ and collected supernatant was filtered with 0.2 μm PES filter. Phages were concentrated by ultracentrifugation at avg. 104,000 g for 2 hours at 4 ℃. Collected phage pellet was resuspended in SM buffer (10 mM Tris-HCl, NaCl 100 mM, $MgSO_4$ 50 mM, gelatin 0.01%, pH 7.5) which was then passed through a sucrose gradient layer (10 % - 40 %) prepared in SM buffer at avg. 104,000 g for 1 hour at 4℃. Recovered phage band was subject to centrifugal filtration (100 kDa, Amicon Ultra-15, Millipore) to replace sucrose solution to SM buffer. The titer of final stock was $O(10^{11})$ PFU/mL. Infective ϕ6 was enumerated using double top layer method resulting in 30 – 300 plaques. Along with plates from actual experiments, a plate without any inoculation and a plate only with host bacterial inoculation were incubated to screen plate contamination, false-negative, and false positive results. The arithmetic mean and standard deviation were calculated using the concentrations across all replicates, following appropriate error propagation rules.

Section A23. RT-qPCR standard curve and efficiency

A standard curve was obtained using 10-fold dilutions of known concentration stock. Slope, R^2, and efficiency were calculated as -3.39, 1.00, and 97.3 %, respectively. The arithmetic mean and standard deviation of intact RNA concentration were calculated using the concentrations across all replicates, following appropriate error propagation rules.

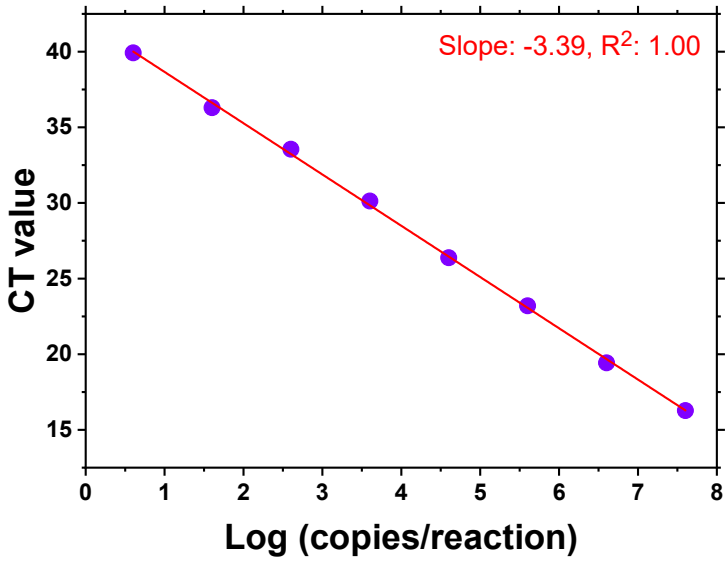

Figure A-26. Standard curve of RT-qPCR.

Section A24. Log reduction calculation

Comparison of log reductions in infectivity and RT-qPCR assay using two different approaches was performed [288]. Log reduction 1 (LR1) was calculated based on the logarithmic difference of mean concentrations (used in this study) while log reduction 2 (LR2) was the difference of the mean of log-transformed concentrations. Errors represent standard deviation. Similarity between two approaches was evaluated based on Pearson's r value at slope = 1 using the log reduction values at all time points except those below detection limit.

$$LR1 = \log\left[\frac{1}{A}\sum_{m=1}^{A} C_{m,t=0} \div \frac{1}{B}\sum_{n=1}^{B} C_{n,t}\right] \quad \text{(A13)}$$

$$LR2 = \frac{1}{A}\cdot\sum_{m=1}^{A}\log\left(C_{m,t=0}\right) - \frac{1}{B}\sum_{n=1}^{B}\log\left(C_{n,t}\right) \quad \text{(A14)}$$

Table A-5. Similarity between two approaches to calculate log reductions. High linearities (r ≥ 0.94) demonstrated that both approaches generate statistically identical log reduction values in this study.

No coagulation, pH 6.4, infectivity assay			No coagulation, pH 6.4, RT-qPCR assay		
Time (min)	Bulk water		Time (min)	Bulk water	
	LR1	LR2		LR1	LR2
0	0.00±0.15	0.00±0.14	0	0.00±0.06	0.00±0.05
10	0.09±0.11	0.08±0.10	10	0.13±0.34	0.28±0.40
20	0.05±0.14	0.04±0.12	20	-0.05±0.30	0.05±0.32
30	0.06±0.21	0.08±0.18	30	0.21±0.29	0.30±0.30
60	0.19±0.34	0.26±0.43	60	0.21±0.12	0.22±0.11
120	0.11±0.16	0.11±0.15	120	-0.04±0.24	0.02±0.24
r	0.9496		r	0.9645	

Electrocoagulation, 10 mg/L Fe, pH 6.4, infectivity assay					Electrocoagulation, 10 mg/L Fe, pH 6.4, RT-qPCR assay				
Time (min)	Bulk water		Floc		Time (min)	Bulk water		Floc	
	LR1	LR2	LR1	LR2		LR1	LR2	LR1	LR2
0	0.00±0.25	0.00±0.28	0.00±0.25	0.00±0.28	0	0.00±0.04	0.00±0.03	0.00±0.04	0.00±0.03
2.6	3.37±0.40	3.49±0.45	3.03±0.40	3.12±0.39	2.6	1.16±0.35	1.41±0.61	1.39±0.05	1.39±0.40
10	4.54±0.32	4.57±0.32	3.85±0.42	3.92±0.35	10	1.67±0.26	1.73±0.26	1.61±0.33	1.74±0.35
20	5.28±0.28	5.30±0.31	4.47±0.30	4.48±0.27	20	2.00±0.18	2.03±0.17	1.36±0.07	1.37±0.60
30	5.70±0.41	5.76±0.34	4.81±0.38	4.91±0.43	30	1.72±0.41	1.93±0.47	1.42±0.13	1.43±0.12
60	> 6.25	> 6.21	5.72±0.35	5.78±0.36	60	1.73±0.42	1.98±0.53	1.57±0.09	1.58±0.08
120	> 6.25	> 6.21	> 6.25	> 6.21	120	2.37±0.24	2.43±0.33	1.11±0.26	1.18±0.25
r	0.9999		0.9998		r	0.9994		0.9998	

Conventional coagulation, 10 mg/L Fe, pH 6.4, infectivity assay					Conventional coagulation, 10 mg/L Fe, pH 6.4, RT-qPCR assay				
Time (min)	Bulk water		Floc		Time (min)	Bulk water		Floc	
	LR1	LR2	LR1	LR2		LR1	LR2	LR1	LR2
0	0.00±0.19	0.00±0.17	0.00±0.19	0.00±0.17	0	0.00±0.24	0.00±0.22	0.00±0.24	0.00±0.22
2.6	5.10±0.19	5.10±0.18	3.61±0.15	3.60±0.14	2.6	3.23±0.34	3.30±0.34	1.15±0.39	1.28±0.43
5	5.07±0.38	5.16±0.33	3.83±0.26	3.86±0.25	5	3.04±0.29	3.07±0.28	1.14±0.34	1.20±0.34
10	5.06±0.41	5.18±0.39	3.96±0.33	4.04±0.34	10	3.56±0.17	3.54±0.16	0.98±0.37	1.07±0.38
20	4.87±0.29	4.93±0.29	4.21±0.23	4.23±0.21	20	3.11±0.38	3.22±0.40	1.12±0.34	1.19±0.34
30	4.85±0.18	4.84±0.16	4.59±0.16	4.58±0.15	30	2.85±0.17	2.83±0.16	1.36±0.24	1.36±0.22
60	4.69±0.35	4.80±0.37	4.57±0.32	4.65±0.35	60	2.98±0.40	3.12±0.44	1.57±0.30	1.61±0.29
120	4.78±0.40	4.94±0.44	5.36±0.13	5.34±0.12	120	2.98±0.38	3.09±0.40	1.29±0.18	1.27±0.16
r	0.9998		0.9999		r	0.9992		0.9965	

Section A25. Reproducibility estimation

Variability in duplicated results of infectivity and RT-qPCR assay was estimated using log reductions at all time points except those below detection limit. It is noted that log reduction values of each replicate (LR-R1 and LR-R2) were the logarithmic difference of mean concentrations, and errors represent standard deviation. Linearity was assessed based on Pearson's r value at slope = 1. Statistical estimation (r ≥ 0.92) demonstrates that experiments were reproducible.

Table A-6. Summary of reproducibility estimation.

No coagulation, pH 6.4, infectivity assay		No coagulation, pH 6.4, RT-qPCR assay	
	Bulk water		Bulk water

Time (min)	LR-R1	LR-R2	Time (min)	LR-R1	LR-R2
0	0.00±0.26	0.00±0.02	0	0.00±0.06	0.00±0.08
10	0.07±0.18	0.12±0.02	10	0.13±0.34	0.13±0.48
20	0.09±0.18	0.01±0.11	20	-0.05±0.31	-0.05±0.43
30	0.11±0.21	0.07±0.18	30	0.17±0.32	0.26±0.39
60	0.00±0.18	0.03±0.08	60	0.21±0.12	0.21±0.17
120	0.14±0.24	0.08±0.12	120	0.00±0.31	-0.07±0.27
r	**0.9276**		r	**0.9715**	

Electrocoagulation, 10 mg/L Fe, pH 6.4, infectivity assay					**Electrocoagulation, 10 mg/L Fe, pH 6.4, RT-qPCR assay**				
Time (min)	Bulk water		Floc		Time (min)	Bulk water		Floc	
	LR-R1	LR-R2	LR-R1	LR-R2		LR-R1	LR-R2	LR-R1	LR-R2
0	0.00±0.31	0.00±0.04	0.00±0.31	0.00±0.04	0	0.00±0.01	0.00±0.03	0.00±0.01	0.00±0.03
2.6	3.23±0.45	3.47±0.48	2.67±0.30	3.56±0.14	2.6	1.21±0.57	1.12±0.28	1.35±0.06	1.43±0.04
10	4.34±0.45	4.70±0.13	3.56±0.46	4.18±0.15	10	1.96±0.01	1.50±0.02	1.38±0.01	2.09±0.04
20	5.05±0.27	5.48±0.34	4.20±0.32	4.75±0.07	20	1.85±0.01	2.20±0.05	1.34±0.07	1.38±0.09
30	5.37±0.39	6.11±0.08	4.68±0.50	4.91±0.35	30	1.78±0.45	1.68±0.50	1.30±0.01	1.56±0.04
60	> 6.09	> 6.37	5.51±0.42	5.88±0.33	60	1.71±0.51	1.75±0.51	1.49±0.03	1.67±0.03
120	> 6.09	> 6.37	> 6.09	> 6.37	120	2.36±0.29	2.38±0.29	1.08±0.32	1.15±0.30
r	**0.9997**		**0.9980**		**r**	**0.9446**		**0.9546**	

Conventional coagulation, 10 mg/L Fe, pH 6.4, infectivity assay					**Conventional coagulation, 10 mg/L Fe, pH 6.4, RT-qPCR assay**				
Time (min)	Bulk water		Floc		Time (min)	Bulk water		Floc	
	LR-R1	LR-R2	LR-R1	LR-R2		LR-R1	LR-R2	LR-R1	LR-R2
0	0.00±0.19	0.00±0.27	0.00±0.19	0.00±0.27	0	0.00±0.26	0.00±0.31	0.00±0.26	0.00±0.31
2.6	5.20±0.19	5.02±0.21	3.59±0.16	3.63±0.21	2.6	3.22±0.41	3.24±0.42	1.14±0.48	1.16±0.48
5	5.45±0.15	4.87±0.30	3.83±0.26	3.83±0.37	5	3.03±0.34	3.06±0.36	1.11±0.41	1.16±0.41
10	4.87±0.32	5.40±0.37	3.97±0.37	3.95±0.44	10	3.55±0.19	3.58±0.23	0.97±0.45	0.98±0.45
20	4.83±0.32	4.93±0.38	4.21±0.23	4.21±0.32	20	3.09±0.46	3.12±0.47	1.11±0.39	1.14±0.44
30	4.85±0.18	4.85±0.25	4.58±0.16	4.59±0.23	30	2.84±0.19	2.87±0.22	1.34±0.29	1.37±0.29
60	4.69±0.36	4.69±0.48	4.54±0.30	4.59±0.47	60	2.96±0.48	3.00±0.50	1.55±0.33	1.59±0.40
120	4.83±0.47	4.73±0.49	5.35±0.13	5.36±0.19	120	2.97±0.45	2.99±0.47	1.28±0.20	1.30±0.23
r	**0.9901**		**0.9999**		**r**	**0.9999**		**0.9997**	

Section A26. ATR-FTIR spectroscopy

ATR-FTIR spectra were obtained in ATR mode using Nicolet iS10 spectrometer (Thermo Fisher Scientific) equipped with an Ever-Glo MIR source, KBr beam splitter, DTGS detector. Samples were directly mounted on a diamond iTX accessory. An average of 128 coadded scans at 4 cm^{-1} resolution was obtained for each sample followed by ATR-correction, auto-base line correction using Omnic 9 software. Spectra were further processed by 9-point Savitzky-Golay smoothing and normalized by the largest peak intensity [182]. Band positions were identified by second derivative method. Samples were prepared was as follows.

A control sample was prepared and its spectrum was subtracted from that of actual sample to minimize the interference of possible residuals remaining in the phage stock [16, 66, 272]. For

native phage spectrum, the actual sample was prepared by freeze-drying a phage stock, and a corresponding control sample was obtained following phage stock preparation protocol except bacterial host inoculation (blank stock) followed by freeze-drying. For coagulated phages, conventional coagulation and electrocoagulation experiments were separately performed with phage stock and blank stock. Afterwards, the suspension was vacuum-filtered through a 1.2 μm glass fiber membrane and the membrane was vacuum-dried for 6-9 hours until spectra of three different locations of the membrane were obtained.

Section A27. Addition of sodium sulfite as a hydrogen peroxide quencher

At the end of electrolysis, 785±121 μg/L of H_2O_2 was detected accompanied with 1.2 mg/L of dissolved oxygen decline (LDO101, HACH). H_2O_2 was quenched using 25 mM of Na_2SO_3. We used an even higher molar ratio of Na_2SO_3 to H_2O_2 (~1,000) compared to what was previously recommended (~1.1) [289]. In addition, a control experiment result showed that 25 mM of Na_2SO_3 did not impact ϕ6 infectivity over the duration of our experiments.

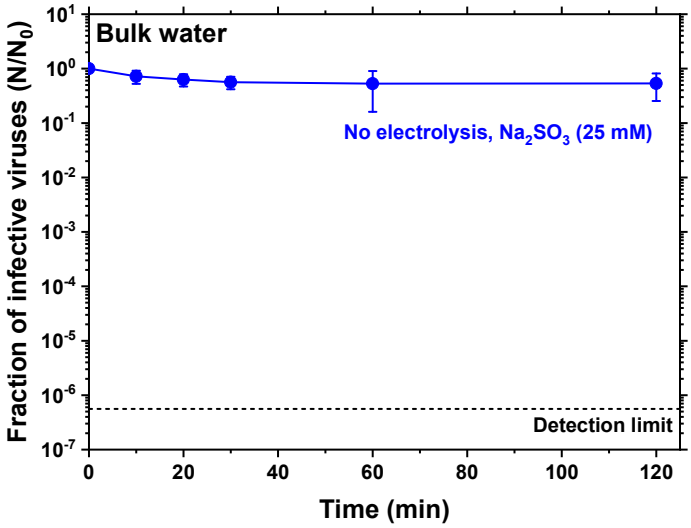

Figure A-27.Negligible impact of Na_2SO_3 on ϕ6 infectivity.

Section A28. Quantitative analysis of damages on virus

This section explains the computational procedure to estimate damages on viral capsids. Figure A-28 demonstrates how damaged viral capsid were computationally simulated. Figure A-28A depicts electron density map of intact ϕ6 (with the outer phospholipid layer computationally removed) from which portions of the density map from one of the 5-fold region in steps of ~4 nm [59, 60]. Side views and tilted views (rotated by an angle of 40°) of some of the resultant maps are shown in Figure A-28B.

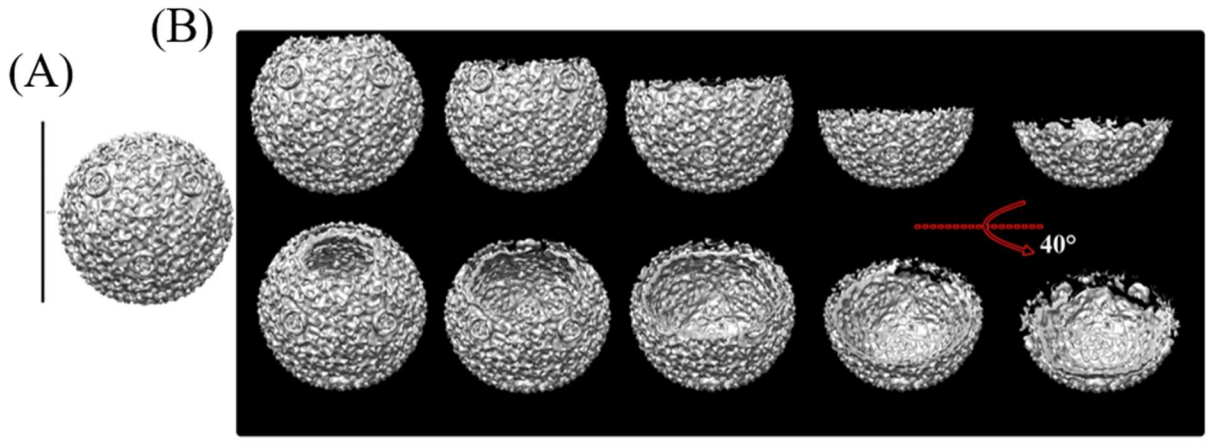

Figure A-28. Segmentation of electron density map of intact ϕ6 (after computationally removing the outermost lipid layer) with accession number EMD-1301 (https://www.emdataresource.org/). (A) Electron density map of intact ϕ6 nucleocapsid (vertical scale bar: 60 nm). (B) Side views and tilted views of computationally altered maps.

Multiple projections were generated from density maps altered to different extents [59]. Each of the projection images was then matched to the boxed out damaged ϕ6 capsid images and the best fit was determined. The map that gave the best fit was then analyzed to determine the remaining capsid matter, which allowed us to estimate the range of damage (15 to 60 % of the actual volume) of the 80 % of the virion particles suffered from the effects of conventional chemical coagulation and electrocoagulation.

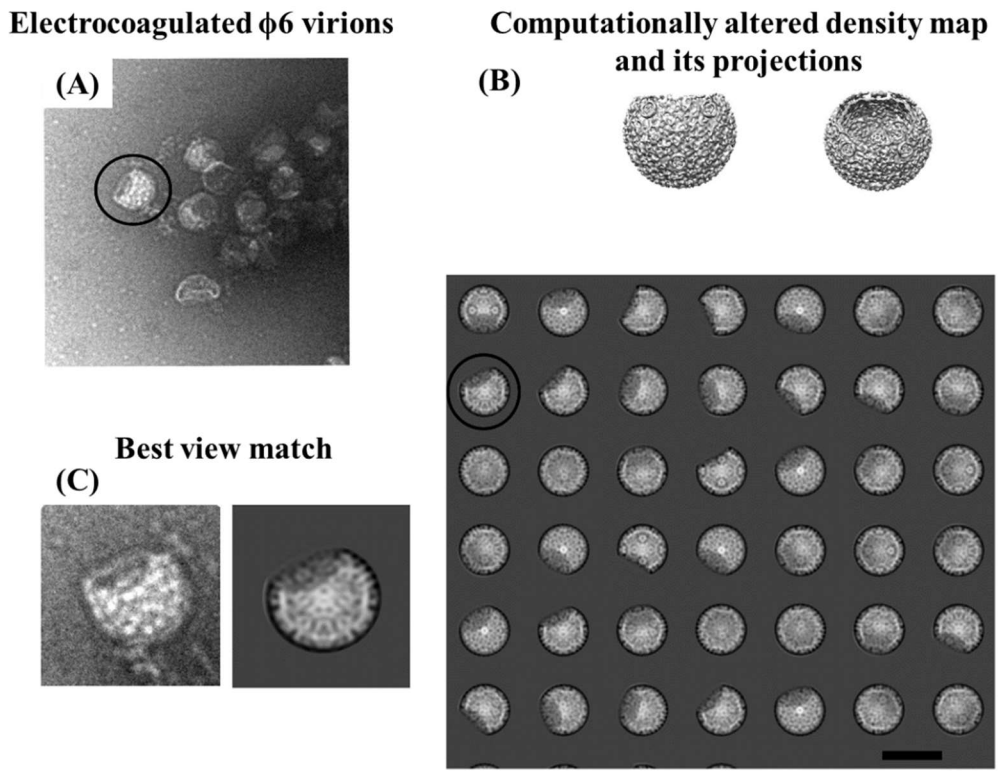

Figure A-29.Example of computational image analysis to quantitatively assess damages induced by electrocoagulation (black scale bar in bottom panel of (B): 100 nm).

We first selected a ϕ6 virion particle damaged by electrocoagulation shown inside the black circle in the micrograph as an example (Figure A-29A, top left). We then generated projections from various computationally altered electron density maps of the ϕ6 virion and looked for the best matched view. In Figure A-29B, we show the side and inclined view of the altered ϕ6 density map whose projection matched best with the selected virion particle shown in Figure A-29C. The computationally altered density map misses ~25% of its density. Thus, the analysis reveals that electrocoagulation damaged about a quarter of the capsid for the encircled virion particle in Figure A-29A.

Table A-7. Summary of FTIR band identification, assignments, and contributors.

Wavenumber (cm^{-1})	Assignment	Contributor
3013 - 3011	*cis* C=C	Hydrocarbon chains in lipid [161]
2966	$\nu_{as}(CH_3)$	Lipid [152, 153]
2963 - 2957	$\nu_{as}(CH_3)$	Acyl chain of lipid [151-153, 290], protein [290]
2937	$\nu_{as}(CH_2)$	Lipid[152]
2926 - 2924	$\nu_{as}(CH_2)$	Mainly lipid [152, 153, 290], protein [290]
2875 - 2871	$\nu_s(CH_3)$	Mainly protein [290], lipid [151-153, 290]
2853 - 2851	$\nu_s(CH_2)$	Mainly acyl chain of lipid [151-153, 290]
1749 - 1705	ν(C=O)	Lipids [151-153]
1697	ν (C_2=O)	RNA (guanine) [152]
1654 - 1649	Amide I , mainly ν(C=O)	Protein [152, 153, 290]
1595	C-O-Fe	Fe(III)-carbonyl group complex [155, 156]
1585	Amide II, δ(NH), ν(C-N)	Protein [291]
1554	Amide II, δ(NH), ν(C-N)	Protein [152]
1546, 1542	Amide II, δ(NH), ν(C-N)	Protein [152, 290]
1507	δ(CN), δ(CH), δ(NH)	Tryptophan [73]
1488	C=C	RNA [152, 280]
1457	$\delta_{as}(CH_3)$	Protein [152, 290], lipid [152, 153, 290]
1408	$\delta_s(CH_3)$	Protein [152]
1396	-	Soluble Fe(III) complex [156]
1326	ν(C-N)	Adenine [152]
1290	Amide III, δ(NH), ν(C-N)	Protein [153, 292]
1236	$\nu_{as}(PO_2^-)$	RNA [152, 153], phospholipid [152]
1169	ν_{as}(C-O-C)	Lipid [153]
1080 - 1078	$\nu_s(PO_2^-)$	RNA [152, 153], phospholipid [152, 153, 290]
1044 - 1040	ν(P-OH, P-OFe)	Iron adsorption on lipid [213, 215]
1018, 1017	ν(P-OFe)	Iron adsorption on lipid [213, 215]
995	ν(P-OFe)	Iron adsorption on lipid [293]
968	C-H out of plane deformation of trans double bond (-HC=CH-)	Lipid oxidation [160, 161]
959	$\nu_{as}(PO_2^-)$, $\nu_s(PO_2^-)$	Possibly [213, 215, 294] lipid, RNA

Section A29. Relative amount of protein secondary structures

Amide I band decomposition was performed to quantitatively estimate changes in secondary structures upon electro- and conventional coagulation. Assignment of each band to secondary structure can be found in Table A-7.

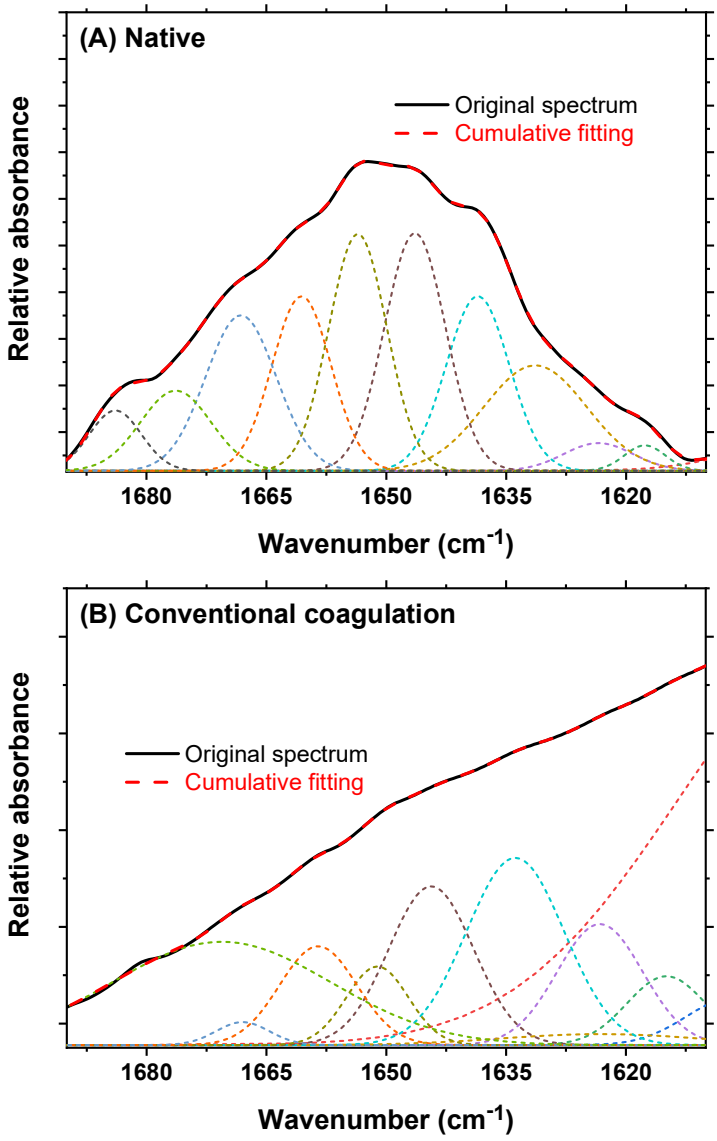

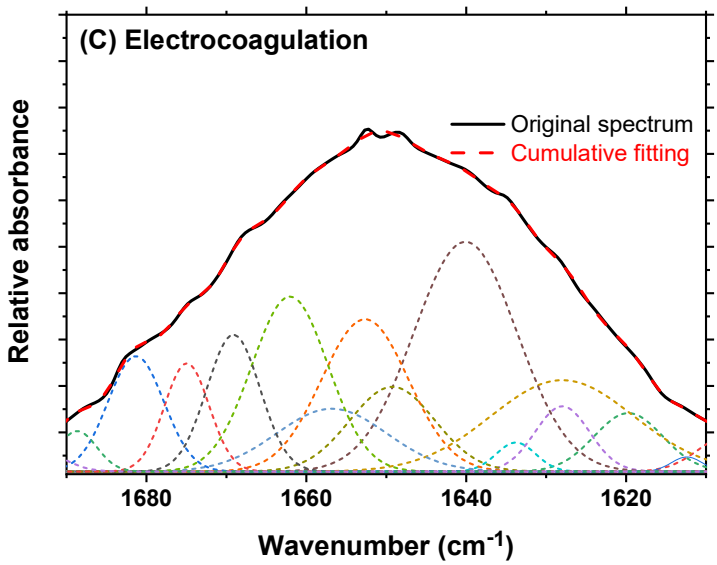

Figure A-30. Decomposition of amide I region for protein secondary structure relative amount of native (A), and after conventional coagulation (B) and electrocoagulation (C).

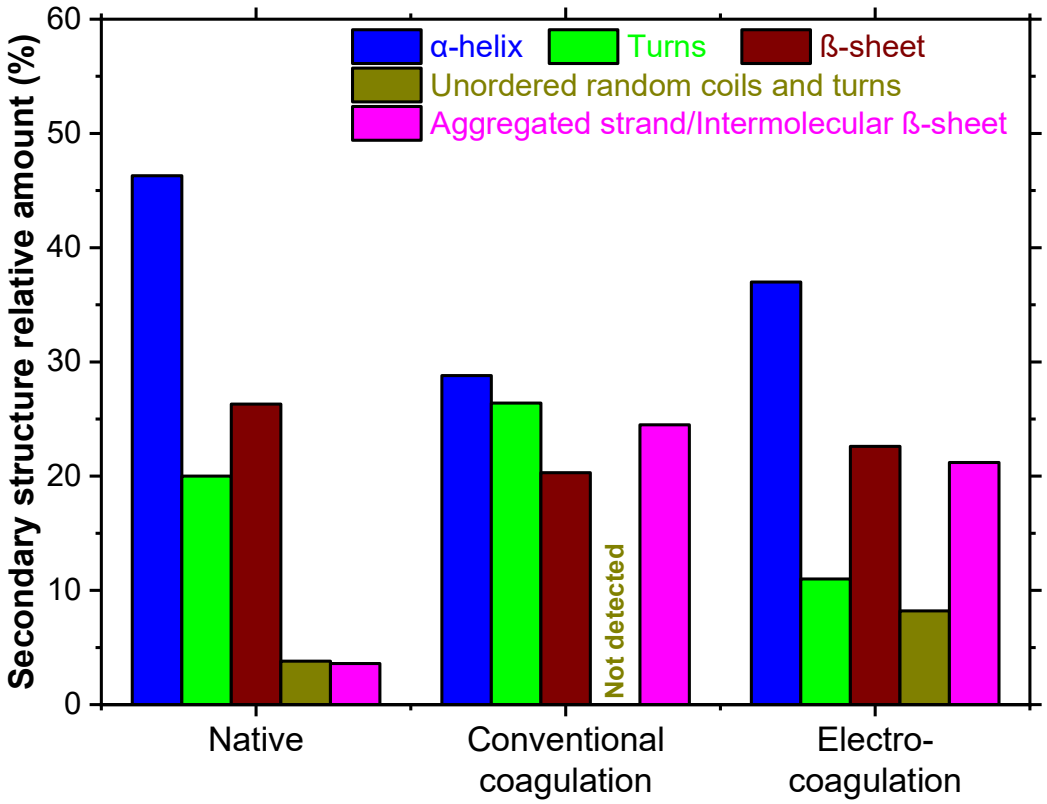

Figure A-31. Comparison of relative amount of protein secondary structure before and after conventional coagulation and electrocoagulation.

Table A-8. Comparison of secondary structure relative areas of native and coagulated ϕ6.

Secondary structure [73, 81]	Native ϕ6		Conventional coagulation		Electrocoagulation	
	Wavenumber (cm^{-1})	Relative area (%)	Wavenumber (cm^{-1})	Relative area (%)	Wavenumber (cm^{-1})	Relative area (%)
Aggregated strand, Intermolecular β-sheet	1618 1623	1.3 2.3	1607 1615 1623	4.5 6.0 13.9	1607 1612 1620 1628	2.0 0.4 3.6 15.1
β-sheet	1631 1639	13.1 13.2	1634	20.3	1634 1640	1.0 21.5
α-helix	1646 1654 1661	17.4 16.5 12.4	1644 1651 1659	14.9 5.4 8.5	1649 1653 1657 1662	6.5 12.0 6.3 12.1
Turns	1668 1676	13.2 6.8	1668 1671	1.4 25.1	1669 1675	6.6 4.4
Unordered random coils and turns	1684	3.8	-	-	1681 1689 1693	5.9 1.4 1.2

Supporting information for chapter IV

Section A30. Electrocoagulation dosing control

For electrocoagulation, electrolysis time for targeted Al and Fe dose was determined based on the Faraday's law shown below.

$$\frac{m}{A_W \cdot V} = \frac{I \cdot t}{zF} \tag{A15}$$

where, m is the mass of total Al or Fe (g), A_W is the atomic weight (27.0 g/mol for Al and 55.9 g/mol for Fe), V is the total volume of solution (L), I is the current (A), t is the electrolysis time (s), z is the number of electrons transferred, and F is the Faraday's constant (96,486 C/eq). Total Al and Fe concentration was measured using HACH method 8012 and 8112, respectively, and compared to the theoretical prediction (Figure A-32).

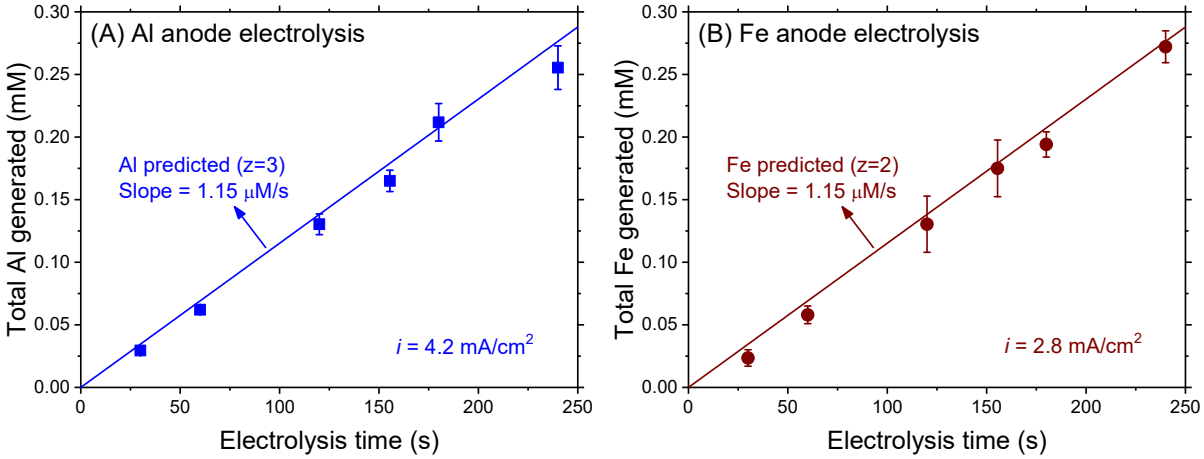

Figure A-32. Al(III) and Fe(II) generation during the electrolysis of Al^0 and Fe^0 anode for electrocoagulation. It is noted that the different current density of 4.2 and 2.8 mA/cm2 was applied for Al and Fe electrocoagulation, respectively to introduce Al(III) and Fe(II) at the same molar concentration rate of 1.15 μM/s.

Due to the different number of electrons to transfer (z) to generate the equal amount of Al and Fe in molar concentration, the current density (i, mA/cm^2) was differed as denoted in Figure A-32. A good agreement between predicted and measured concentration validates that Al(III) and Fe(II) species was generated during the electrolysis of Al^0 and Fe^0 anode, respectively, and the dosing was well-controlled.

Section A31. Floc concentration of MS2 and ϕ6

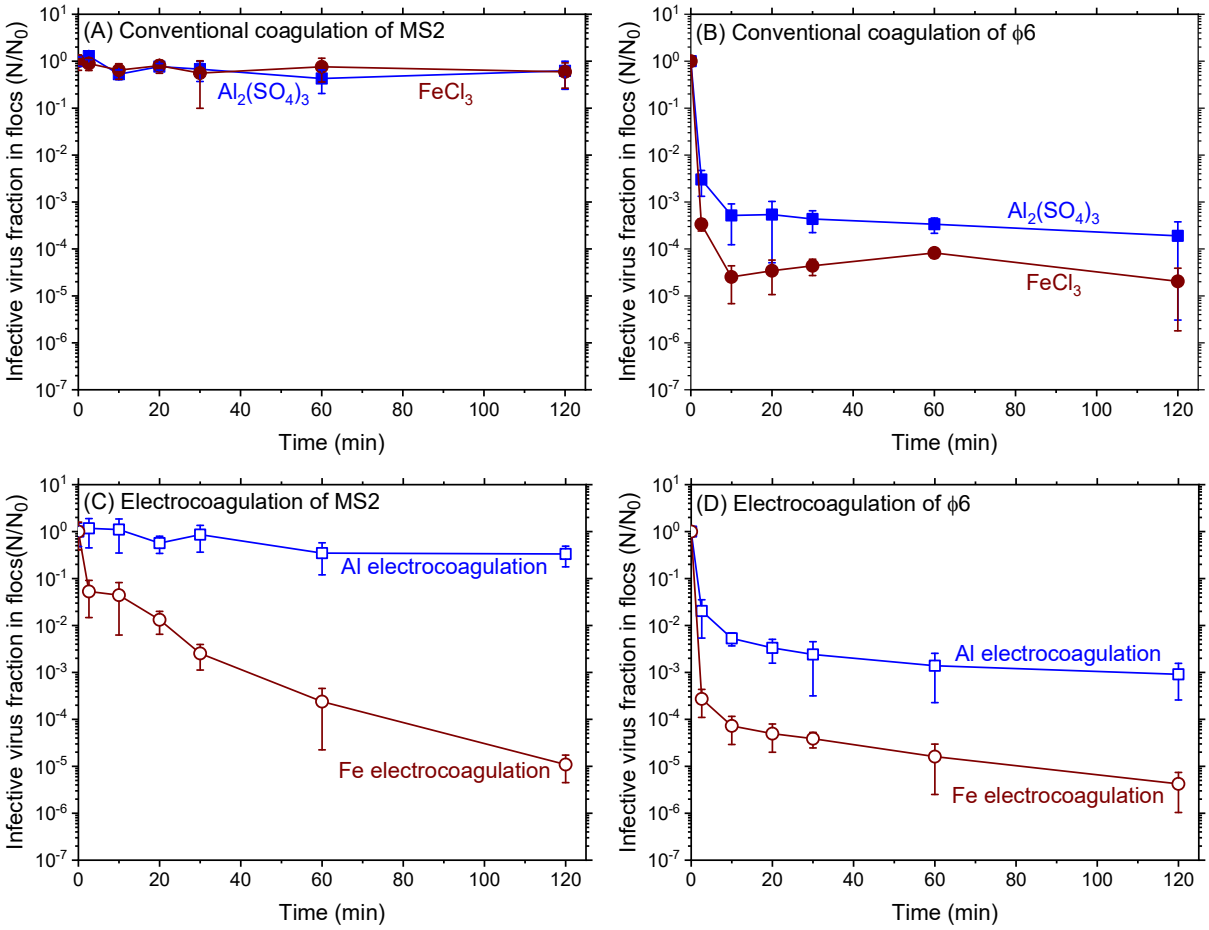

Figure A-33. Temporal profiles of infective virus fractions extracted from Al or Fe flocs

Section A32. Free chlorine measurement

Free chlorine was measured using HACH method 10214 to avoid possible interference by any oxidants. In both Al and Fe electrocoagulation, free chlorine was not detected.

Section A33. MS2 capsid thickness measurement

Capsid thickness of MS2 capsid was computationally obtained using the code written in MATLAB. The code was constructed to 1) employ an electron micrograph of a single virion, 2) bandpass filter it, 3) read gray-value profile across the virion particle, 4) fit the peaks corresponding to the capsids to Gaussian distribution, and 5) read full-width at half maximum

(FWHM) values as the thicknesses [56]. A series of figures are shown in Figure A-34 to visualize the protocol.

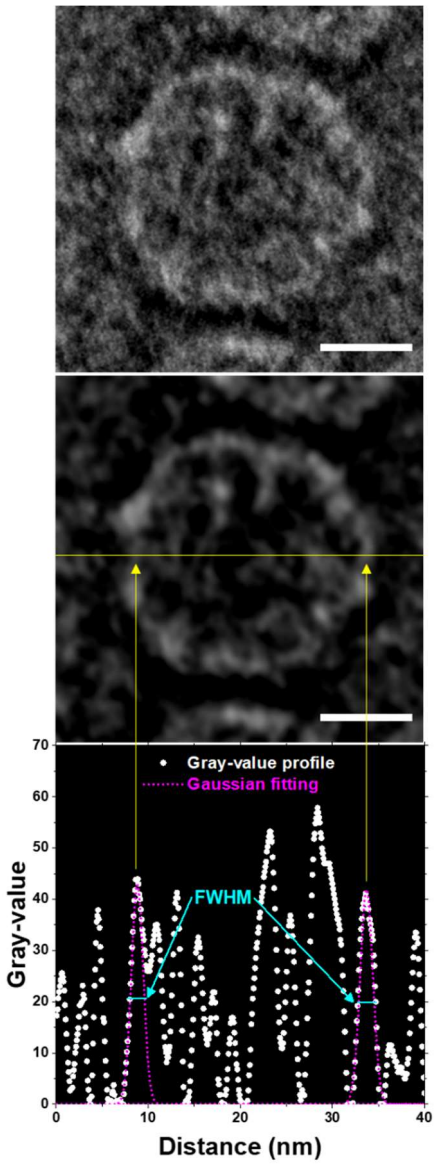

Figure A-34. MS2 capsid thickness measurement protocol.

Section A34. Capsid volume damage estimation

Viral capsid damages of MS2 and ϕ6 were quantitively estimated following the computational protocol described in the previous literature [26]. First, electron density map of intact MS2 (accession number EMD-1431) and ϕ6 (accession number EMD-1301, note that lipid layer was removed prior to the analysis) was computationally altered by removing a portion from the 5-fold region by increment of approximately 4 nm [59, 60]. This step resulted in numerous simulated virus particles with a different extent of capsid damage. Next, each of these 3-dimentional simulated virus particles was projected on a plane at different angles yielding 45 images in 2-dimension. Then, each of 2D images were compared to the boxed-out TEM image of damaged virus particle to find the best-matching projection from which the remaining capsid volume was obtained.

Section A35. Remaining capsid volume of ϕ6 phage after each coagulation process.

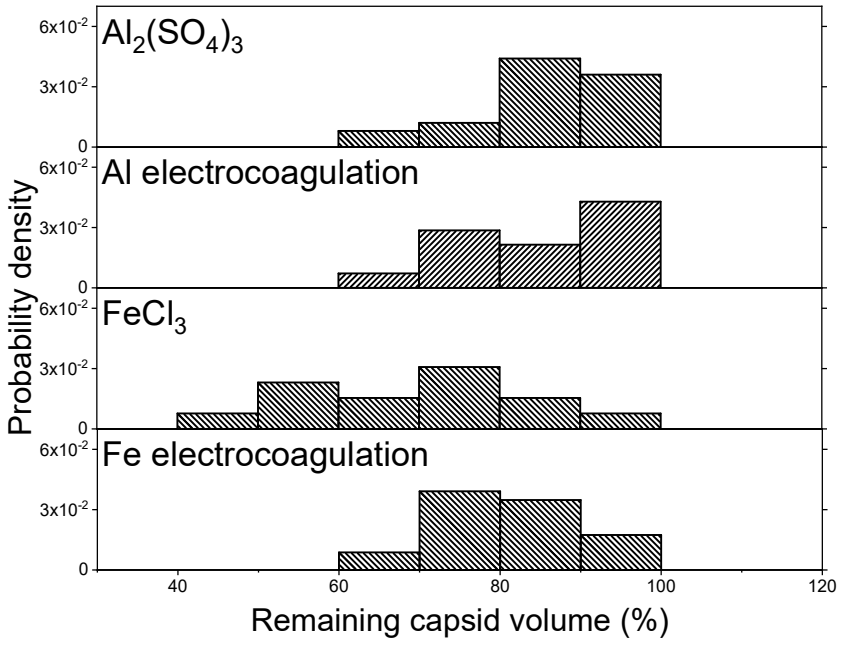

Figure A-35. Computationally analyzed remaining capsid volume after each coagulation approach. 20~25 virions were used for each case.

Section A36. Spectroscopic analysis of untreated and coagulated viruses.

Table A-9. Summary of FTIR peak assignment and contributor.

Wavenumber (cm^{-1})	Assignment	Contributor
2972, 2969, 2966, 2960, 2955	$\nu_{as}(CH_3)$	Acyl chain of lipid [151-153, 290] and protein [290]
2927, 2931, 2918	$\nu_{as}(CH_2)$	Mainly lipid [152, 153, 290], protein [290]
2873, 2872	$\nu_s(CH_3)$	Mainly protein [290], lipid [151-153, 290]
2854, 2849	$\nu_s(CH_2)$	Mainly acyl chain of lipid [151-153, 290]
1741	ν(C=O)	Lipid [152]
1710	ν(C=O)	Lipid
1652, 1653	Amide I , mainly ν(C=O)	Protein [152, 153, 290]
1545, 1541	Amide II, δ(NH), ν(C-N)	Protein [152, 290]
1456, 1457	$\delta_{as}(CH_3)$	Protein [152, 290], lipid [152, 153, 290]
1399, 1396	$\delta_s(CH_3)$	Protein [152]
1242, 1244	$\nu_{as}(PO_2^-)$	RNA [152]
1219, 1220	$\nu_{as}(PO_2^-)$	RNA [152]
1118, 1120	ν_s(C-O) or ν(SO)	RNA [152] SO_4^{2-} adsorption [207]
1100	$\nu_s(PO_2^-)$	RNA[152, 153], phospholipid[152, 153, 290]
1086, 1088	$\nu_s(PO_2^-)$	RNA[152, 153], phospholipid[152, 153, 290]
1061	ν_s(C-O)	RNA [152]
1038	ν(P-OH, P-OFe)	Iron adsorption on lipid[213, 215]
1019	ν(P-OFe)	Iron adsorption on lipid[213, 215]
996	C-O, C-C of ribose	RNA [152, 280]
995	ν(P-OFe)	Iron adsorption on lipid[293]
970, 969	$\nu(PO_4^{2-})$	RNA [152]
968	C-H out of plane deformation of trans double bond (-HC=CH-)	Lipid oxidation[160, 161]

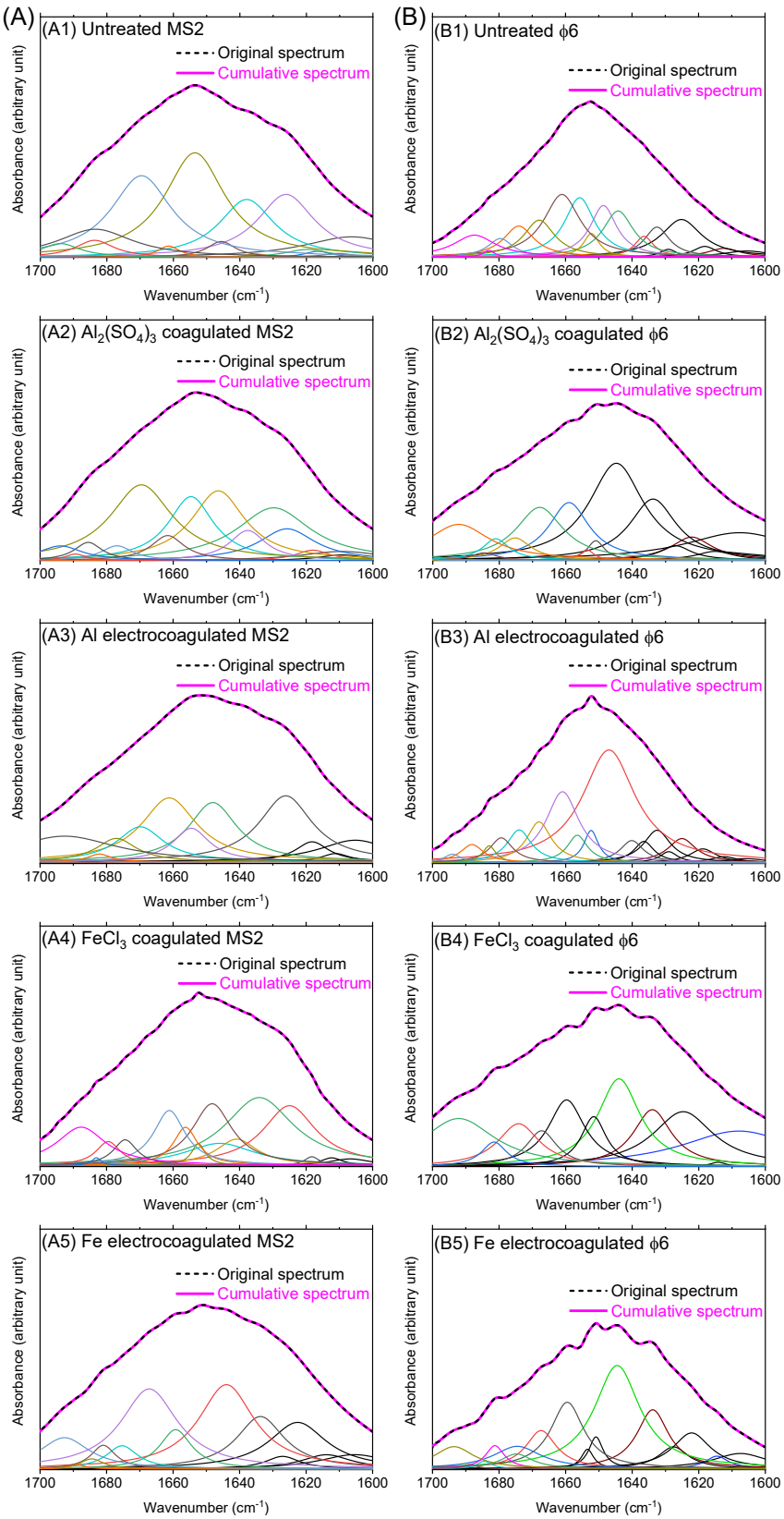

Figure A-36. Amide I peak decomposition to calculate relative amount of protein secondary structures.